ScuDo

Scuola di Dottorato ~ Doctoral School

WHAT YOU ARE, TAKES YOU FAR

Doctoral Dissertation

PhD in Electrical, Electronics and Communications Engineering (30^{th}cycle)

Statistical and Graph-Based Signal Processing: Fundamental Results and Application to Cardiac Electrophysiology

By

Francesco Grassi

******

Supervisor:

Prof. Lorenzo Galleani

Doctoral Examination Committee:

Prof. P. Frossard, Referee, École Polytechnique Fédérale de Lausanne

Prof. M. Grangetto, Referee, University of Turin

Dott. M. Anselmino, University of Turin

Prof. A. Coluccia, University of Salento

Prof. E. Magli, Politecnico di Torino

Politecnico di Torino

2018

Contents

List of Figures

List of Tables

Nomenclature

Abbreviations

AF	Atrial Fibrillation
AP	Action Potential
BMI	Body-Mass Index
CM	Cardiomyopathy
CF	Contact Force
CS	Coronary Sinus
CV	Conduction Velocity
DFT	Discrete Fourier Transform
ECG	Electrocardiogram
EGM	Electrogram
EP(S)	Electrophysiology (Study)
FIRM	Focal Impulse Rotor Modulation
FTI	Force-Time Integral
GSP	Graph Signal Processing
GFT	Graph Fourier Transform
IIR	Image Intensity Ratio
JFT	Joint Time-Vertex Fourier Transform
LA	Left Atrium
LAT	Local Activation Time
LGE	Late-Gadolinium Enhancement
LIPV	Left Inferior Pulmonary Vein
LSPV	Left Superior Pulmonary Vein
MGSP	Multidimensional Graph Signal Processing
MRI	Magnetic Resonance Imaging

PCL	Pacing Cycle Length
PDE	Partial Differential Equation
PSD	Power Spectral Density
PV	Pulmonary Vein
PVI	Pulmonary Veins Isolation
RA	Right Atrium
RF	Radiofrequency
RIPV	Right Inferior Pulmonary Vein
RMN	Remote Magnetic Navigation
RMT	Remote Magnetic ThermoCool
RSPV	Right Superior Pulmonary Vein
SNR	Signal-to-Noise Ratio
SpC	Spectral Centroid
ST	SmartTouch
STFT	Short Time Fourier Transform
STVFT	Short Time-Vertex Fourier Transform
STVWT	Spectral Time-Vertex Wavelet Transform
TF	Time-Frequency
TK	Teager-Kaiser

Symbols

$\mathbb{R}$	Field of Real numbers
$\mathscr{V}$	Vertex set
$\mathscr{E}$	Edge set
N	Number of vertices $\lvert\mathscr{V}\rvert$
T	Number of time steps
$\otimes$	Kronecker product between graphs, matrices, vectors
$\times$	Cartesian product between graphs, matrices, vectors
$\boldsymbol{W}, W$	Weight matrix and function
$\boldsymbol{D}, \boldsymbol{d}, d$	Degree matrix, vector and function
∇	Gradient operator
div	Divergence operator
$\boldsymbol{L}$	Laplacian matrix

$\boldsymbol{U}$	Eigenvectors matrix
$\boldsymbol{x}$	Graph signal
$\vec{\boldsymbol{x}}, \vec{\boldsymbol{X}}$	Edge signal
$\boldsymbol{X}$	Multidimensional graph signal or time-vertex signal
$\widetilde{\boldsymbol{X}}$	Graph Fourier transform of $\boldsymbol{X}$
$\dot{\boldsymbol{X}}$	Discrete Fourier transform of $\boldsymbol{X}$
$\widehat{\boldsymbol{X}}$	Joint time-vertex Fourier transform of $\boldsymbol{X}$
t, τ	Time indices
n, m	Vertex indices
ℓ	Eigenvalue index
k	Angular frequency index
$\boldsymbol{\Lambda}$	Diagonal matrix of graph eigenvalues λ_ℓ
$\boldsymbol{\Omega}$	Diagonal matrix of angular frequencies ω_k
$\mathscr{T}$	Localization operator
$\mathscr{D}_h$	Dictionary of atoms based on kernel h
D_h, D_h^*	Analysis and Synthesis operators
$\boldsymbol{\Sigma}$	Covariance matrix

Notation

In this dissertation we will use bold upper- and lowercase letters for linear operators (or matrices) $\boldsymbol{M}$ and column vectors $\boldsymbol{w}$, respectively. Furthermore, $\boldsymbol{x}$ will denote the vectorized version of $\boldsymbol{X}$. Complex conjugate, transpose and conjugate transpose are denoted as $\overline{\boldsymbol{X}}$, $\boldsymbol{X}^\intercal$ and $\boldsymbol{X}^*$, respectively. Depending on the context it will be clear when lowercase letters will denote scalar values and indices t, n or functions and kernels $g(\cdot)$, $h(\cdot)$. Similarly, uppercase letters can denote fixed constants A, B or random variables X, Y. For any symmetric positive definite matrix $\boldsymbol{M}$ with singular value decomposition $\boldsymbol{M} = \boldsymbol{U}\boldsymbol{\Lambda}\boldsymbol{U}^*$, the matrix function $f(\boldsymbol{M})$ is defined as $f(\boldsymbol{M}) = \boldsymbol{U} f(\boldsymbol{\Lambda})\boldsymbol{U}^*$, where the scalar function f has been applied to each diagonal entry of $\boldsymbol{\Lambda}$.

Abstract

The goal of cardiac electrophysiology is to obtain information about the mechanism, function, and performance of the electrical activities of the heart, the identification of deviation from normal pattern and the design of treatments. Offering a better insight into cardiac arrhythmias comprehension and management, signal processing can help the physician to enhance the treatment strategies, in particular in case of atrial fibrillation (AF), a very common atrial arrhythmia which is associated to significant morbidities, such as increased risk of mortality, heart failure, and thromboembolic events. Catheter ablation of AF is a therapeutic technique which uses radiofrequency energy to destroy atrial tissue involved in the arrhythmia sustenance, typically aiming at the electrical disconnection of the of the pulmonary veins triggers. However, recurrence rate is still very high, showing that the very complex and heterogeneous nature of AF still represents a challenging problem.

Leveraging the tools of non-stationary and statistical signal processing, the first part of our work has a twofold focus: firstly, we compare the performance of two different ablation technologies, based on contact force sensing or remote magnetic controlled, using signal-based criteria as surrogates for lesion assessment. Furthermore, we investigate the role of ablation parameters in lesion formation using the late-gadolinium enhanced magnetic resonance imaging. Secondly, we hypothesized that in human atria the frequency content of the bipolar signal is directly related to the local conduction velocity (CV), a key parameter characterizing the substrate abnormality and influencing atrial arrhythmias. Comparing the degree of spectral compression among signals recorded at different points of the endocardial surface in response to decreasing pacing rate, our experimental data demonstrate a significant correlation between CV and the corresponding spectral centroids.

However, complex spatio-temporal propagation pattern characterizing AF spurred the need for new signals acquisition and processing methods. Multi-electrode

catheters allow whole-chamber panoramic mapping of electrical activity but produce an amount of data which need to be preprocessed and analyzed to provide clinically relevant support to the physician. Graph signal processing has shown its potential on a variety of applications involving high-dimensional data on irregular domains and complex network. Nevertheless, though state-of-the-art graph-based methods have been successful for many tasks, so far they predominantly ignore the time-dimension of data.

To address this shortcoming, in the second part of this dissertation, we put forth a Time-Vertex Signal Processing Framework, as a particular case of the multi-dimensional graph signal processing. Linking together the time-domain signal processing techniques with the tools of GSP, the Time-Vertex Signal Processing facilitates the analysis of graph structured data which also evolve in time. We motivate our framework leveraging the notion of partial differential equations on graphs. We introduce joint operators, such as time-vertex localization and we present a novel approach to significantly improve the accuracy of fast joint filtering. We also illustrate how to build time-vertex dictionaries, providing conditions for efficient invertibility and examples of constructions.

The experimental results on a variety of datasets suggest that the proposed tools can bring significant benefits in various signal processing and learning tasks involving time-series on graphs. We close the gap between the two parts illustrating the application of graph and time-vertex signal processing to the challenging case of multi-channels intracardiac signals.

Keywords: Cardiac electrophysiology, Atrial fibrillation, Radiofrequency ablation, Pulmonary vein isolation, Statistical signal processing, Time-frequency analysis, Remote magnetic navigation, Contact sensing, Magnetic resonance imaging, Delayed-enhancement, Conduction velocity, Rotor, Graph, Graph signal processing, Multi-dimensional graph signal processing, Time-vertex signal processing, Joint stationarity, Partial differential equations.

Introduction

The history of electrophysiology, the study of electrical properties of biological cells and tissues, is long and fascinating. More than 200 years ago, Galvani discovered that the function of the nervous system is intrinsically linked to electrical activity [68], pushing the independent works of Matteucci [134] and Du Bois-Reymond [52], which can be considered the founders of modern electrophysiology. The first recording of bioelectrical signals can be traced back to around 150 years ago, with the first experiment attempting to record the electromagnetic field generated by the human body. In 1939 a fundamental step forward the comprehension of cell excitability is due to the Nobel Prize-winning work of Alan Hodgkin and Andrew Huxley "for their discoveries concerning the ionic mechanisms involved in excitation and inhibition in the peripheral and central portions of the nerve cell membrane" [88]. To them can be attributed the first intracellular recording of an action potential.

Generally speaking, the term biosignal denotes a great class of signals that can be recorded from the human body, whether electrical or non-electrical. The advent of the digital era significantly simplified the recording, processing, and transmission of biosignals. During the last decades, biosignals have been intensively analyzed to help uncover information which completely changed the way various diseases were diagnosed in the past. In cardiac, neurological, and neuromuscular applications, novel signal processing techniques have been developed for the interpretation of physiological measurements and the understanding of physiological systems [198].

The goal of cardiac electrophysiology is to obtain information about the mechanism, function, and performance of the electrical activities of the heart, the identification of deviation from normal pattern and the design of treatments. The human heart consists of 5 billion cardiomyocytes which allow the cardiac wavefront propagation via the gap junctions located on the intercalated disc. The normal heart rhythm, called sinus rhythm, is established by the sinoatrial node. The electrical

signal originates in the SA node and travels through the heart, causing the heart muscle to contract. The whole process repeats, on average, over 3 billion times in a lifetime. However, this incredible clockwork mechanism could be disrupted by abnormal heart rhythms or arrhythmias. Heart diseases are in fact the principal cause of mortality in the modern society. Among the different abnormal heart rhythms, atrial fibrillation (AF) is the most common sustained cardiac arrhythmia, occurring in up to 2% of the general population, with its prevalence increasing along with the age of the population. It is associated with significant morbidities, such as increased risk of mortality, heart failure, and thromboembolic events. Radiofrequency (RF) catheter ablation has been accepted as the effective therapy for this common arrhythmia, thanks to its low complication rates and high success rates in both paroxysmal and chronic AF. RF energy is used to eliminate the triggers of the arrhythmia and electrically isolate parts of the atrial tissue to prevent propagation of arrhythmogenic impulses.

The complex and heterogeneous nature of AF represents a challenging problem for physicians, biomedical engineers, and scientists, motivating the development of a number of methods for the analysis of the AF recordings much larger than those for any other cardiac arrhythmias. Allowing the simulation and analysis of the cardiac electrical activity, signal processing offers a better insight into cardiac arrhythmias comprehension and management. Above all, signal processing can help the physician to enhance the ablation strategies extracting features from the intracardiac signals that are fundamental to improve ablation outcome. Due to the complexity of AF mechanisms, standardized ablation strategy could achieve only limited success rate. Treatment of AF should be tailored to the individual patient in order to identify and eliminate the sources of arrhythmia. For this purpose, mapping of propagation pattern is extremely useful to recognize ectopic foci and re-entrant activities, but due to the high spatio-temporal variability, it requires an increase in the number of sites simultaneously recorded. Therefore, during the last two decades, electrophysiologists have been using multi-electrode basket catheters in the clinical practice to investigate in real-time the whole atrium. However, the difficulties in the interpretation of multi-channels biosignals have driven an increasing interest in the development of automated methods applicable in the clinical practice. In this context, the field of signal processing aims to provide decision support to the clinical operator in an uncomplicated and clinically relevant fashion.

In the modern era of big data, data mining and automation, the ever-increasing computational capabilities have contributed to the emerging of new data-oriented approaches to achieve practical solutions to problems in various disciplines. Many tasks in signal and image processing, machine learning and pattern recognition could now be solved even in case of high dimensional data or complex domains, and the area of health-care is not an exception to this. Among the numerous approaches which have emerged in the past years, graph-based methods for signal processing have shown promising results in the analysis of data exhibiting complex non-Euclidean properties or geometrically structured domains, such as those found in social, transportation, and biological networks, among others. This has been the driving force behind recent efforts in the signal processing field to extend harmonic analysis to high-dimensional datasets collected from a variety of fields, e.g., physics, engineering, genetics, and life science, which can be naturally modeled as graph signals, i.e., signals taking values on the nodes of weighted graphs.

Graph signal processing (GSP) generalizes classical signal processing to graph signals, merging algebraic and spectral graph theory with computational harmonic analysis. The introduction of the notion of frequency on graphs and the associated graph Fourier transform (GFT) was the fundamental breakthrough in the field, enabling data analysis in the graph frequency domain and leading to significant advancements in several signal processing problems. Thanks to its ability to deal with complex domains and irregular data, GSP seems an effective method to deal with the multi-channel signals recorded during AF. However, so far GSP research efforts have been focused on static signals, overlooking the inherently time-dependency of data. On the contrary, many of the systems of interest, particularly in the biomedical field, are inherently dynamic.

Motivated by the needs in this context, this dissertation is oriented in two directions: the first is the development of techniques, models, and criteria for the analysis of AF, using the concepts of non-stationary and statistical signal processing tailored for the field of cardiac electrophysiology. Secondly, we define the foundations of a new framework, denoted as Time-Vertex Signal Processing, that links together the time-domain signal processing techniques with the new tools of graph signal processing. We investigate the potentiality of the framework in numerous applications and datasets, including the challenging case of multi-channels intracardiac signals, finally closing the gap between the two parts. Although it is tempting to directly apply the techniques of graph signal processing and machine learning to cardiac

electrophysiology, it is important to never forget the physiological nature of the signals involved, which require a biological understanding for their interpretation.

Thesis outline and contributions

This thesis is separated into two parts which reflect the duality of the work. The first part is completely dedicated to the research in the field of cardiac electrophysiology, in particular, related to the analysis of atrial fibrillation, a widely diffused cardiac arrhythmia which affects millions of people in the world.

In **Chapter 1** we introduce the cardiac system, with a special emphasis on the point of view of the electrophysiology. We will present the cardiac electrophysiology from the cell model to the surface electrocardiogram, through the fundamental electrophysiological study. In the second part, we will present the pathophysiology of the atrial fibrillation, its classification and prevalence, and finally the most common theory behind its mechanism of initiation and sustenance.

Chapter 2 describes the most common procedure for the management and treatment of AF: the radiofrequency ablation. The main tools currently available to the clinicians are described, such as electroanatomical mapping, remote magnetic navigation and contact force sensing technology.

Chapter 3 presents the main signal processing techniques commonly used for the analysis of cardiac and intracardiac signals, especially those used throughout this work. Starting from time and frequency analysis, we will illustrate more advanced tools, such as time-frequency analysis, with examples in the domain of cardiac EP.

In **Chapter 4** we explore different strategies of RF ablation commonly adopted in the clinical practice. In Section 4.2, *we define electrocardiographic criteria to characterize the lesions produced during RF ablation and we use them to compare contact force guided ablation and remote-controlled magnetic navigation*. Moreover, we investigate the role of the ablation parameters, such as contact force, in the lesion creation. *We verified the relationship between these parameters and the scar revealed using the cardiac magnetic resonance with contrast enhancement* (Section 4.3).

Conversely, **Chapter 5** is dedicated to the analysis of the atrial substrate. The characterization of the atrial tissue is fundamental for a better understanding of

AF, in particular in case of persistent or long-lasting arrhythmia. In this regard, the conduction velocity is a key parameter for AF maintenance. *We propose the spectral centroid of the signals recorded by the intracardiac catheters as a surrogate parameter of conduction velocity and we demonstrate the correlation between the two variables in several settings and using different approaches*.

In the second part, we move our focus to the non-Euclidean world of the graphs. We will extend the definitions and tools of the GSP to the multidimensional case, using the notion of Cartesian product of graphs. Finally, we explore the possibilities of the time-varying graph representation, which enlarges the range of applications of classical GSP to new domains.

Chapter 6 provides a comprehensive introduction to graph signal processing (GSP) and the related graph spectral theory. We leverage the notion of GSP to build a *Multidimensional Graph Signal Processing Framework*, which allows us to analyze graph signals whose domain can be naturally described using graph product.

In **Chapter 7** we aim at elevating the notion of joint harmonic analysis to a full-fledged framework, referred to as the *Time-Vertex Signal Processing Framework*. *We illustrate how joint analysis emerges when analyzing the state evolution of simple Partial Differential Equations (PDEs) on graphs* (Section 7.4.1). We show the utility of joint filtering time-vertex signals and *we propose a fast filtering implementation, called Fast Fourier-Chebyshev (FFC) algorithm* (Section 7.5). After having defined a *joint localization operator*, we study redundant time-vertex dictionaries and we use them for signal analysis and synthesis, providing also the *proof of the time-vertex frame condition* guaranteeing that no information is lost. Finally, we complete the framework with the tools of statistical analysis *introducing the concept of joint stationarity*, which generalizes the classical definition of time and graph stationarity.

Chapter 8 provides experimental evidence for the *utility of joint harmonic analysis in a number of graph-temporal datasets that were up to now not fully exploited*, such as dynamic meshes, video and general dynamics over networks. The range of applications covers the classical signal processing problems of denoising, inpainting, and compression, but also extends to feature extraction for classification and source localization problems. Finally, we find an unexpected and powerful connection with the problems which arise in cardiac electrophysiology.

Part I

Cardiac Electrophysiology

Chapter 1

Cardiac Electrophysiology and Atrial Fibrillation

Cardiac electrophysiology (EP) is an interdisciplinary science, regarding not only biology and medicine but also physics and mathematics, as well as engineering. This is because the heart is not only a biological organ but also an electrical conductor and a mechanical pump. Unfortunately, the heart is not a perfect machine. The term *cardiac arrhythmia* denotes a group of conditions in which the heartbeat deviates from its physiological condition, becoming, depending on the characteristic of the arrhythmia, irregular, too fast, or too slow. Over the last century, a huge amount of studies regarding the nonlinear dynamics of both mechanical and electrical properties of the cardiac muscle have improved our knowledge about the phenomena involved in the heart activity and EP have gained widespread acceptance for the diagnosis and treatment of cardiac arrhythmias.

Atrial fibrillation (AF) is the most common sustained cardiac arrhythmia in clinical practice, occurring in up to 2% of the general population, a percentage that rises critically above 13% if we consider individuals aged above 80 years. It is associated with significant morbidities, such as increased risk of mortality, heart failure, and thromboembolic events. Multiple theories about the etiology of AF have been proposed due to its complexity. In this chapter, we will present the basis of cardiac EP and the basic concepts for electrophysiological studies and we will describe the mechanisms and pathophysiology of AF.

1.1 Morphological and Physiological Characteristics of the Heart

The human heart is a hollow muscular organ that lies in the thoracic cavity, between the lungs. It is enclosed and anchored by the pericardium, a double-walled sac of tough connective tissue that provides lubrication for heart's motion and allows heart expansion. The heart acts as the body's circulatory pump. By repeated, rhythmic contraction and relaxation, it ensures that every cell receives enough oxygen and nutrients to continue functioning normally.

The human heart is composed of four chambers: two superior atria and two inferior ventricles. Atria receive blood from veins and fill the ventricles. The ventricles are the discharging chambers that pump the blood into arteries. Functionally, the hearth can be divided into two sides, the left side that pumps blood through the systemic circuit and the right side that pumps blood through the pulmonary circuit.

Inferior vena cava and superior vena cava collect and direct venous blood into the right atrium. Through the tricuspid valve the blood reaches the right ventricle and from here it is pumped via the pulmonary artery into the lungs. In the pulmonary circulation, the deoxygenated blood is enriched with oxygen. It returns from the lungs through the pulmonary veins to the left atrium where it is pumped through the mitral valve into the left ventricle before leaving through the aortic valve to the aorta.

Structure and morphology of the tissue of chambers reflect the difference in function. Atria walls are relatively thinner since atrial contraction only helps to fill entirely the ventricles. Ventricles are the driving force of the blood circulation. In particular, the left ventricle has thicker walls than the right one, in order to provide a pressure wave sufficient to propel the blood throughout the entire body.

1.1.1 Electrophysiological genesis of the electrocardiogram

The cell that makes up the cardiac muscle are called cardiomyocytes. They share some characteristics with both skeletal and smooth muscles, but they have unique properties. The cardiomyocytes are of two types:

Myocardial contractile cells are the bulk of the cardiac muscle. They conduct the impulse and respond to the stimuli with a contraction.

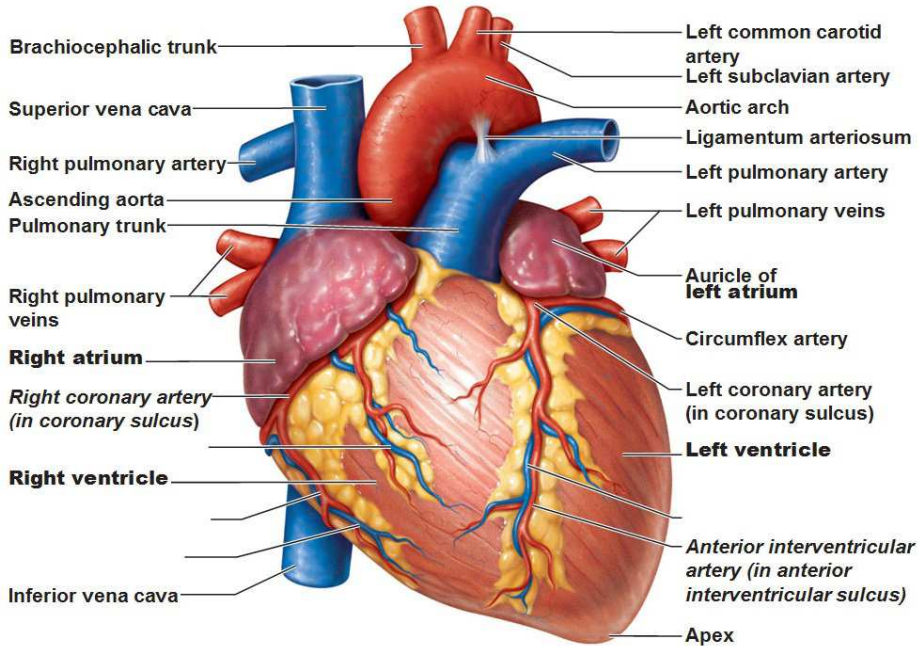

(a)

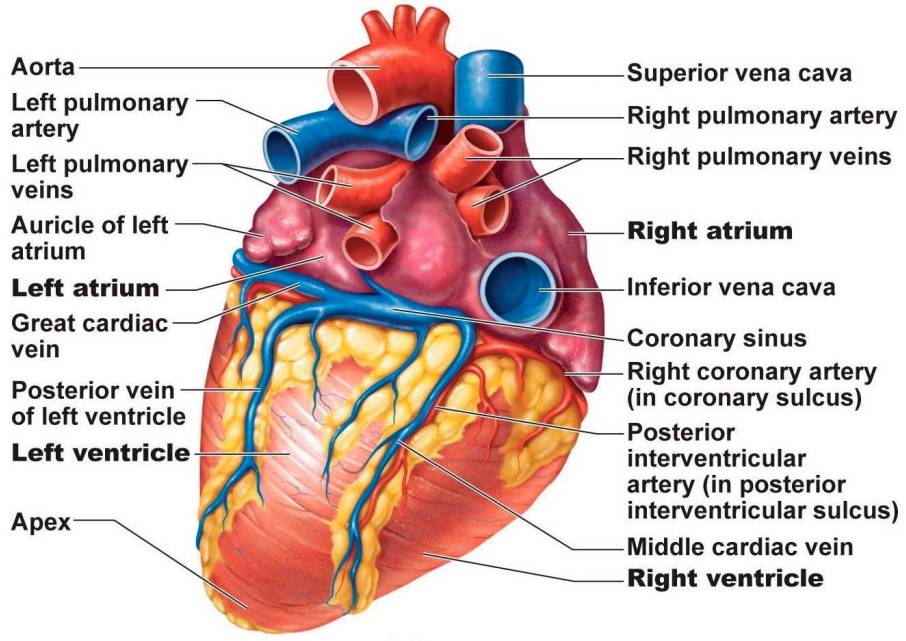

(b)

Figure 1.1 Heart anatomy, adapted from [130]: (a) Anterior view, (b) Posterior view

Myocardial conducting cells possess the ability to spontaneously generate and send out electrical impulses.

Cardiomyocytes are connected by cellular bridges, called gap junctions located on the intercalated disk. For this reason, the heart is a *functional syncytium*, which means that the electrical impulses, called *cardiac action potentials* (AP), propagate freely in every direction leading to a complete contraction of the cardiac muscle.

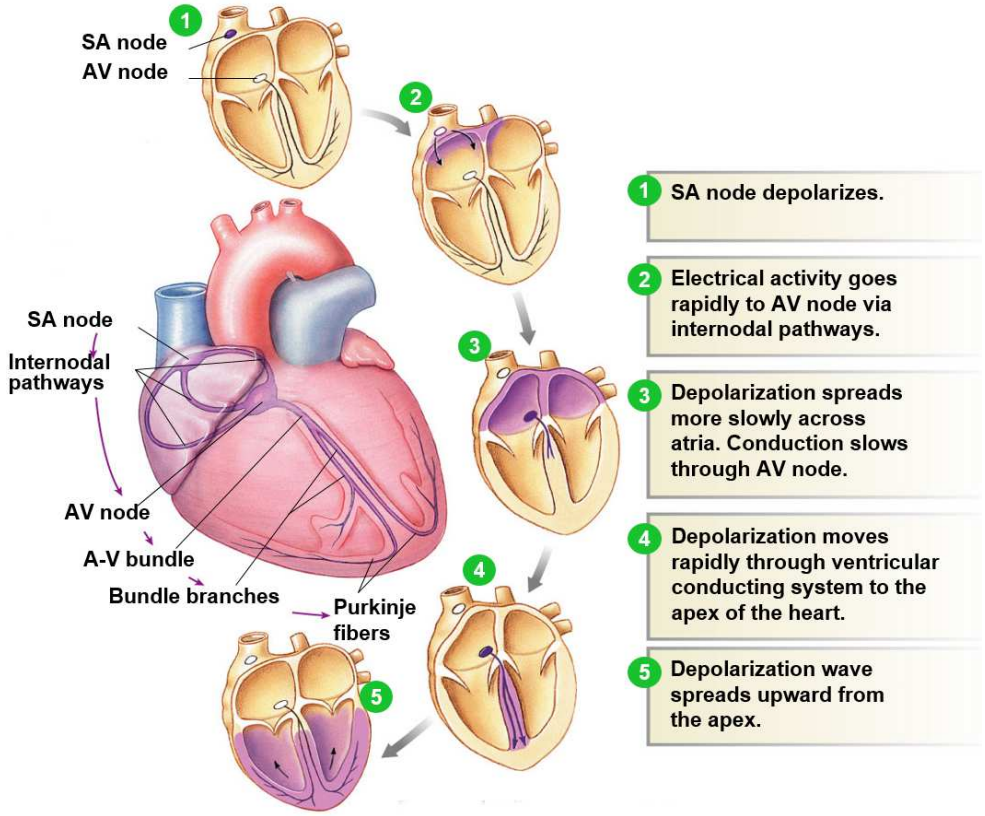

Figure 1.2 Heart conduction, adapted from [191].

Physiologically, the heart excitation starts at the *sinoatrial node* (SA node), which is the physiological, autonomous pacemaker. The impulse propagates through the atria and reaches the *atrioventricular node* (AV node), which delays the signal in order to optimize the filling of the ventricles. The distal part of the AV node, called *Bundle of His*, conducts the impulse along two pathways differently, activating separately the two ventricles through the Purkinje fibers. Spreading of the electrical activity produces the ventricular myocardium contraction (Fig. 1.2).

The action potential is the reaction of an excitable cell to a sufficiently strong external stimulus. It denotes a characteristic behavior of the membrane potential, i.e. the difference of potential between interior and exterior of each cardiac cell. Action potentials are generated by the movement of ions through the transmembrane ion channels in the cardiac cells. They are all-or-none signals, since either they occur fully or they do not occur at all. The ions involved in the AP dynamic are Na^+, K^+ and Ca^{++}. In Figure 1.3 we show the AP of a myocardial cell obtained by numerical simulations using the Courtemanche-Ramirez-Nattel model [40] for the contractile cells and the Dokos-Celler-Lovell model [51] for the pacemaker cells. The cardiac action potential can be divided into 4 phases:

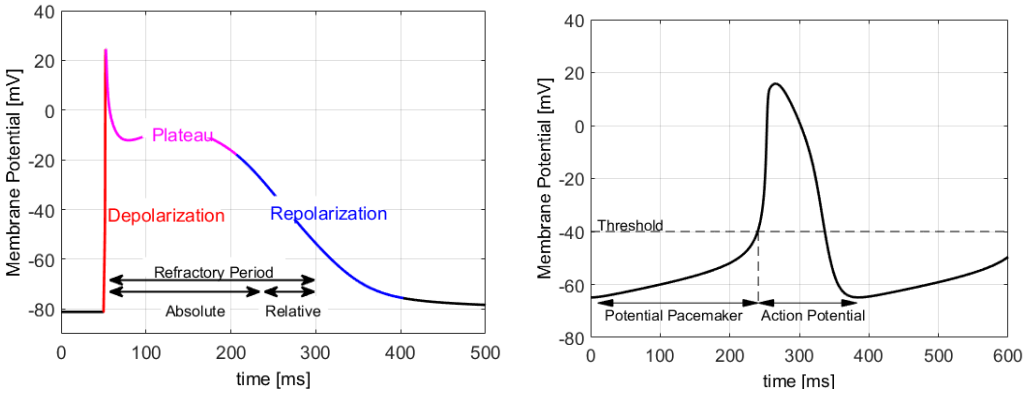

(a) Myocardial contractile cells (b) Myocardial conducting cells

Figure 1.3 Simulated action potentials of myocardial cells using Courtemanche-Ramirez-Nattel model (left) [40] and the Dokos-Celler-Lovell model (right) [51].

Resting Membrane Potential Considering a resting cardiac myocyte, assuming the outside of the cell at 0 mV, the potential measured inside the cell relative to the outside is about -85 to -95 mV. This *resting membrane potential* is determined by concentrations of positively and negatively charged ions across the cell membrane, the relative permeability of the cell membrane to these ions, and the ionic pumps that transport ions across the cell membrane. K^+ is the most important in determining the resting membrane potential. In the conducting cells it is an unstable phase. An inward current of Na^+ slowly depolarizes the membrane potential until it reaches a threshold (about -40 mV) causing the rapid depolarization.

Depolarization If the membrane potential reaches the threshold, either by external stimulation or automaticity, the sodium channels are opened and sodium flows

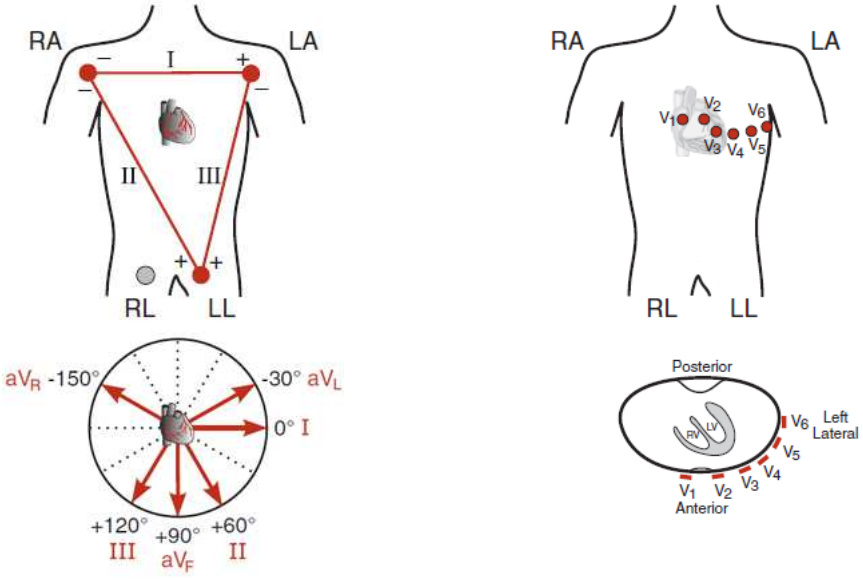

(a) Einthoven and Goldberger leads (b) Unipolar precordial Wilson leads

Figure 1.4 Standard ECG leads, adapted from [110].

into intracellular space causing a *rapid depolarization*. The number of sodium channels that the cell can open is related to the membrane potential. As a matter of fact, if the membrane potential is not at baseline, some of the Na^+ channels will be insensitive to the opening, causing a lower AP. This can be related to conduction delay, as well as the risk of arrhythmias.

Plateau Phase After the closure of the Na^+ channels, a *plateau phase* is due to the inward Ca^{++} current that causes a slow repolarization. During this phase, the cell is unexcitable until the transmembrane voltage reaches the threshold of $-20\,\text{mV}$. For this reason, it is called *absolute refractory period*.

Repolarization During the *relative refractory period* an inward potassium current leads to a complete repolarization. The cell is already excitable, but it will react with an AP of lower height and rising rate. Finally, the resting potential is reached again and the ion concentration is recovered.

The electrocardiogram (ECG) is a major instrument providing to the physician information about the rate and regularity of heartbeats as well as the size and position of the chambers, the presence of any damage to the heart, and the effect of drugs. An ECG is used to measure the cardiac electrical conduction system. Electrical impulses

propagate across the cardiac tissue and different potentials arise on the body's surface. Electrodes placed over the body pick up the potentials and translates them into a waveform. This configuration is called 12-lead ECG. It can be considered the projection of the spatial cardiac activity on the axis between the electrodes. For this reason, the depolarization wave can be described by a vector, termed *mean electrical vector*, whose components are measured by the leads. In particular, the displacement from the baseline is proportional to the amplitude of the electrical impulse, while the sign of the deflection is positive or negative if the impulse respectively approaches or leaves the positive electrode. Conventional leads positions are defined by Einthoven [56], Goldberger [71, 72], and Wilson [218, 217]. The Einthoven leads are bipolar leads that record the voltages between the right arm (RA), the left arm (LA), and the left leg (LL) (I, II, III, Fig. 1.4a). Using the same electrodes, Goldberger measured the voltage between one lead and the remaining two leads interconnected via a resistor (aVR, aVL, aVF, Fig. 1.4a). In addition to these 6 leads, Wilson defined another 6 electrode positions on the chest in close proximity to the heart, labeled from V1 to V6 (Fig. 1.4b). The reference electrode, called Wilson's central terminal, approximates the potential at infinity.

A physiological ECG consists of a succession of waves separated by segments without electrical activity. In a single cardiac cycle, the following components can be identified over the I lead (Fig. 1.5):

P wave : depolarization of the atria. The mean electrical vector is directed from the SA node towards the AV node.

PR segment : the impulse is delayed by the AV node, then propagates through the Bundle of His and the Purkinje fibers.

QRS complex : rapid depolarization of the ventricles. The amplitude of the deflection is very high since the ventricles are bigger than the atria.

ST segment : represents the period when the ventricles are depolarized.

T wave : repolarization of the ventricles.

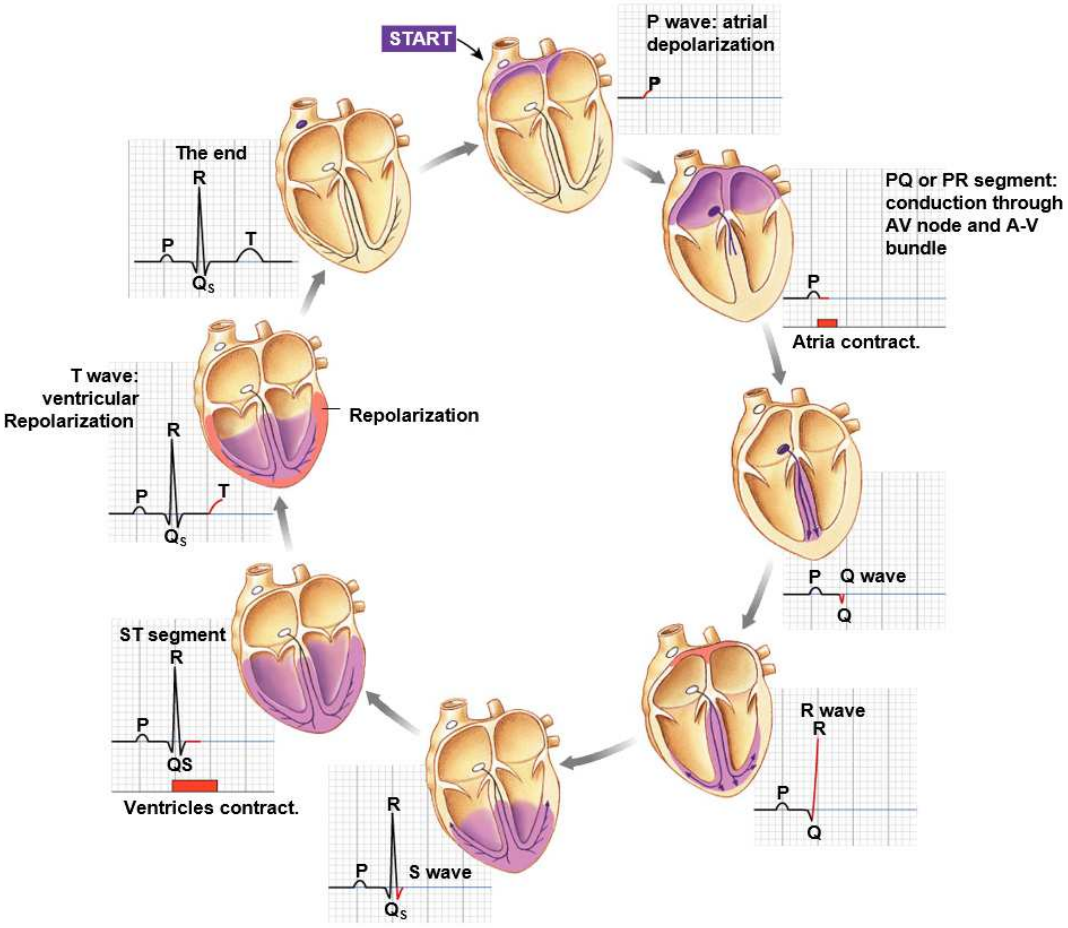

Figure 1.5 Cardiac cycle and physiological ECG, adapted from [191].

1.1.2 Electrophysiology study and intracardiac electrograms acquisition

Despite the 12-lead ECG utility, the electrophysiology study (EPS) is fundamental to the field of cardiac electrophysiology and cardiac arrhythmia management. A diagnostic electrophysiology study is an invasive, catheter-based procedure whose goal is to measure the electrical activity of the heart, evaluate the cardiac conduction pathways, investigate the nature of an arrhythmia and, if possible, free the patient from the burden of the arrhythmia by catheter ablation. An electrophysiology study can be performed in sinus rhythm, as well as during supraventricular or ventricular arrhythmias.

(a) Ablation catheter

(b) Circular mapping catheter

(c) Pentaray catheter

(d) Basket catheter

Figure 1.6 Examples of catheters typically used in clinical practice.

Cardiac catheters can be of many kinds and shapes, depending on their purpose (Fig. 1.6). Linear multipolar catheters are typically used for endocardiac monitoring and pacing, whereas the shaped catheters (e.g., circular, pentaray) are typically used for rapid mapping or for verifying pulmonary vein isolation. Among catheters for ablation, there are single point, multielectrode and balloon catheters, each one allowing a different ablation pattern. Electrodes are identified using numbers, except the first and last which are respectively called the proximal and distal with respect to the distance from the operator. Depending on the arrhythmia under investigation, catheters are positioned in one of the cardiac chambers and typically in the His bundle region and coronary sinus (CS). Intracardiac electrograms are in general more difficult to read, compared with surface ECG and the morphology of the signals vary due to tissue irregularities or unintentional movements of the catheter. Anyway, intracardiac ECG is indispensable for an EP study, since it reveals cardiac events that cannot be seen using only the 12-lead ECG, such as the depolarization of the fibers of the Bundle of His.

Coronary sinus has a central role in the EP study. Linear multipolar catheter inserted in the coronary sinus is the most used catheter for monitoring and measu-

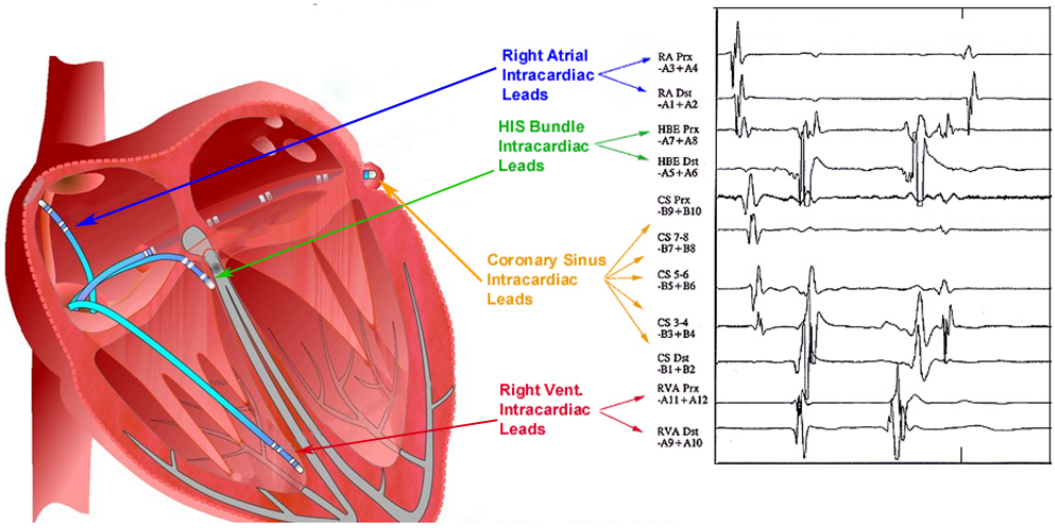

Figure 1.7 Illustration of an electrophysiological study. Depending on the arrhythmia under study, the intracardiac catheters are placed inside the cardiac chambers of interest. Each catheter is used to record the electrical activity in different points of the heart, providing useful information to the clinician for the diagnosis and eventually the treatment of the arrhythmia.

rement, since its position is stable inside the vessel, and it provides indispensable information for the diagnosis of arrhythmias. Moreover, since coronary sinus has its own muscle, it provides electrical connection between right and left atrium, which involves that CS channels set from proximal to distal allow a natural progression of signals, following the atrial activation sequence. For this reason, it is the location most commonly used for pacing.

1.2 Mechanisms and Pathophysiology of Atrial Fibrillation

Atrial fibrillation (AF) is a supraventricular arrhythmia commonly observed in the clinical practice, which is increasing in prevalence due to population aging. It is characterized by rapid and irregular activation or quivering of the atria due to a malfunction in the heart's electrical system and the meandering of abnormal electrical impulses. AF can lead to severe clinical consequences, including increased risk of heart failure, stroke or other heart-related complications and even death. Increased risk for the development of AF has been associated with factors such as

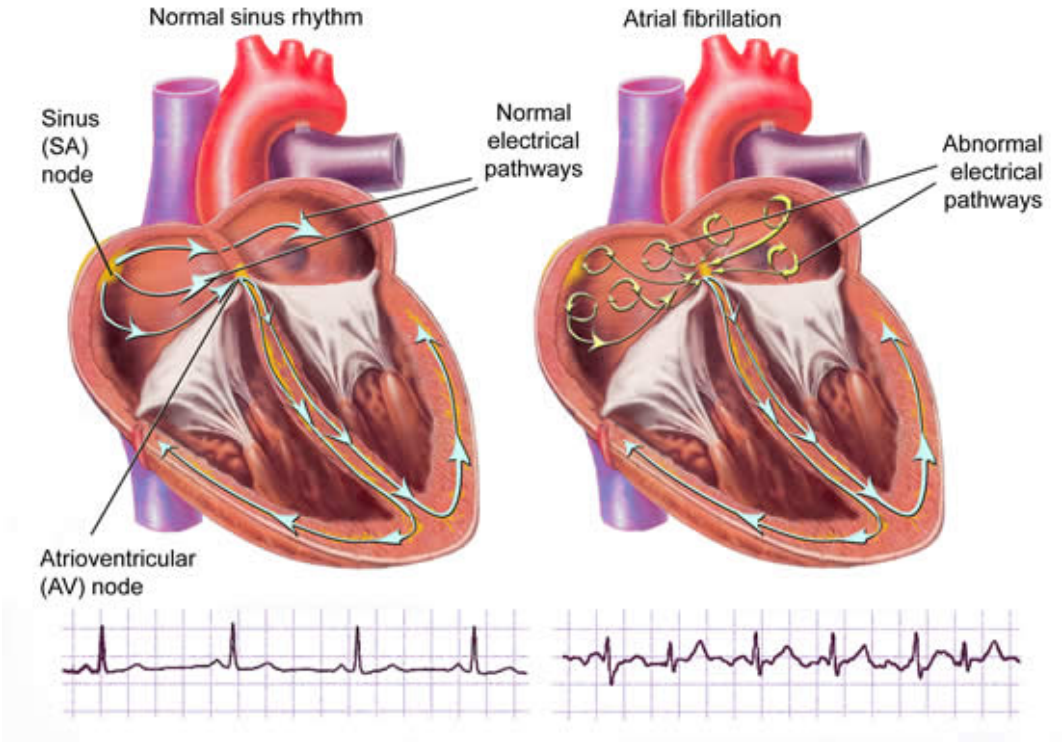

Figure 1.8 Cardiac model and electrocardiogram during normal sinus rhythm (left) and atrial fibrillation (right).

age, hypertension, and obesity. However, mechanisms behind AF are far from being completely understood.

Atrial fibrillation can be diagnosed by analysis of surface electrocardiogram. It is characterized by:

- absence of P waves
- irregular ventricular rate (irregular R-R interval)

Figure 1.8 shows the model typically adopted for the interpretation of AF, together with two examples of the surface ECGs recorded during regular sinus rhythm (left) and AF (right). The disappearance of P waves is due to chaotic activation of the atria and, for this reason, P waves are replaced by disorganized and continuous electrical activity. The small deflections in the electrocardiogram are usually denoted f waves, whose morphology, voltage and f-f interval are quite irregular and their frequency is very high. Due to disorganized electrical activity, if all of the impulses

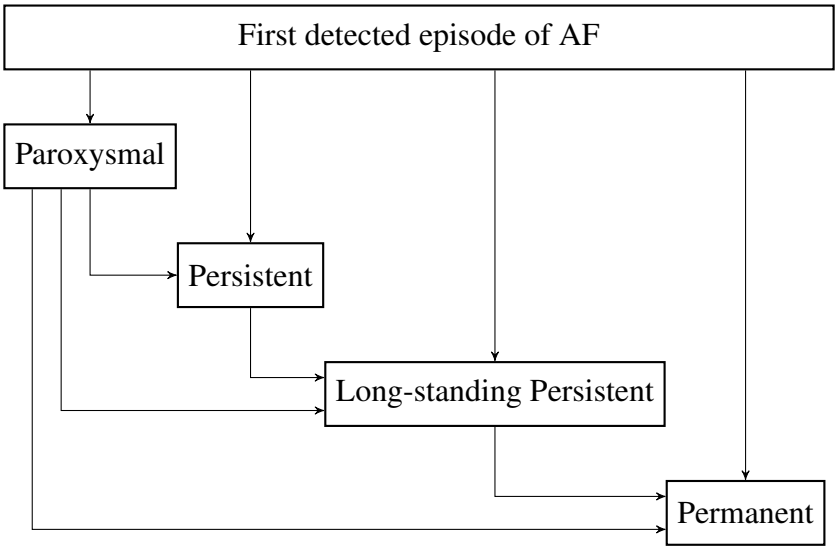

Figure 1.9 Atrial fibrillation classification, adapted from [30].

from the atria reached the ventricles there would be severe ventricular tachycardia. AV node performs a filter function, preventing the rapid activation of the ventricles. However, due to the chaotic atrial electrical activity and the variable AV conduction block, ventricle contractions are no more periodic. On the ECG, this results in an irregular R-R interval, which is the time difference between two consecutive ventricular activations.

1.2.1 Atrial fibrillation classification

AF is a progressive disease. It often begins with infrequent and short episodes which duration tends to become more frequent and longer, progressing to a chronic disease. For this reason, its classification is based on presentation and duration of episodes. According to the guideline for the management of patients with AF [96], the classification is the following:

Paroxysmal AF The episodes recur with variable frequency. It terminates spontaneously or with intervention within 7 days from the onset. After 48 h spontaneous termination probability is low, anticoagulation therapy should be considered.

Persistent AF Continuous episode lasts longer than 7 days or requires termination either with drugs or electrical cardioversion.

Long-standing persistent AF Arrhythmias is present from at least 1 year when is adopted a rhythm control therapy.

Permanent AF It represent a therapeutic attitude of patient and clinician rather than a pathophysiological condition. Patient and physician jointly decide to cease further attempt to restore and maintain the sinus rhythm.

1.2.2 General aspects and prevalence

According to recent statistics collected in the United States [70], approximately 3-5 million people in the US and 8.8 million people in Europe suffer from AF, but estimates indicate that, due to population aging, the number of patients with AF in Europe will be above 18 million by 2050 (Fig. 1.10). The prevalence of AF increases with age, from 0.5% at 40–50 years, to 5–15% at 80 years [86]. Even if it is not directly life-threatening, chronic episodes of AF often lead to severe complications. For example, patients with AF have a five-fold increased risk of stroke [103], a three-fold risk of heart failure [210], and rate of death is about double with respect to patients with normal sinus rhythm [15].

The onset of AF leads to a change in the trajectory of hospitalization, care utilization, and survival [164]. Since hospitalizations consistently represented the major cost driver, there is growing awareness of the economic burden of AF due to aging populations and constrained public finances. Cost of managing individual AF patients is very high; the estimates of the direct cost per patient-year ranged from $10100 to $14200 in the USA and from €450 to €3000 in Western Europe [219].

1.2.3 Atrial fibrillation mechanism

Pathophysiology of AF is very complex and not yet well understood. Structural heart disease is a common comorbidity of and a risk factor for AF, although various other factors have been shown to promote occurrence and maintenance of this disorder. Several structural and electrophysiological abnormalities have been shown to be involved in the pathophysiology of AF. They include atrial dilation, genetic predisposition, heterogeneous refractory periods of the atria, inflammation, abnormal electrical activity, and autonomic nervous system. It is well known that electrical cardioversion has a higher success rate to restore the sinus rhythm when AF duration

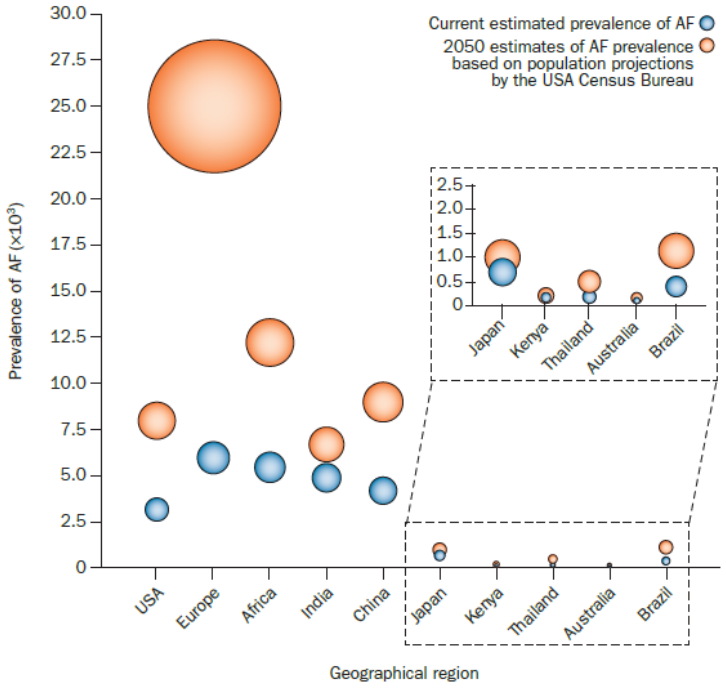

Figure 1.10 Global prevalence of AF in different regions and 2050 estimates, adapted from [168].

is less than 24 hours. This experimental evidence supports the hypothesis that "atrial fibrillation begets atrial fibrillation" [216], i.e., atrial fibrillation itself causes progressive changes to the atria, which promote the initiation, perpetuation, and progression of atrial fibrillation. This phenomenon is called *atrial remodelling*. Atrial remodeling abnormalities are of three kinds: structural, contractile, and electrical. They are related to each other creating a positive feedback-loop of remodeling during atrial fibrillation (Fig. 1.11).

Autonomic Remodelling

The autonomic nervous system plays an important role in the initiation and maintenance of AF. Bettoni et al. [18] show that fluctuations of the sympathetic and the parasympathetic tonus, measured by heart rate variability parameters, may occur before the onset of paroxysmal AF. In particular, the occurrence of paroxysmal AF is preceded by a primary increase in adrenergic tone followed by an abrupt shift toward vagal predominance. Such variations are observed in both patients with structural heart disease and those with normal hearts.

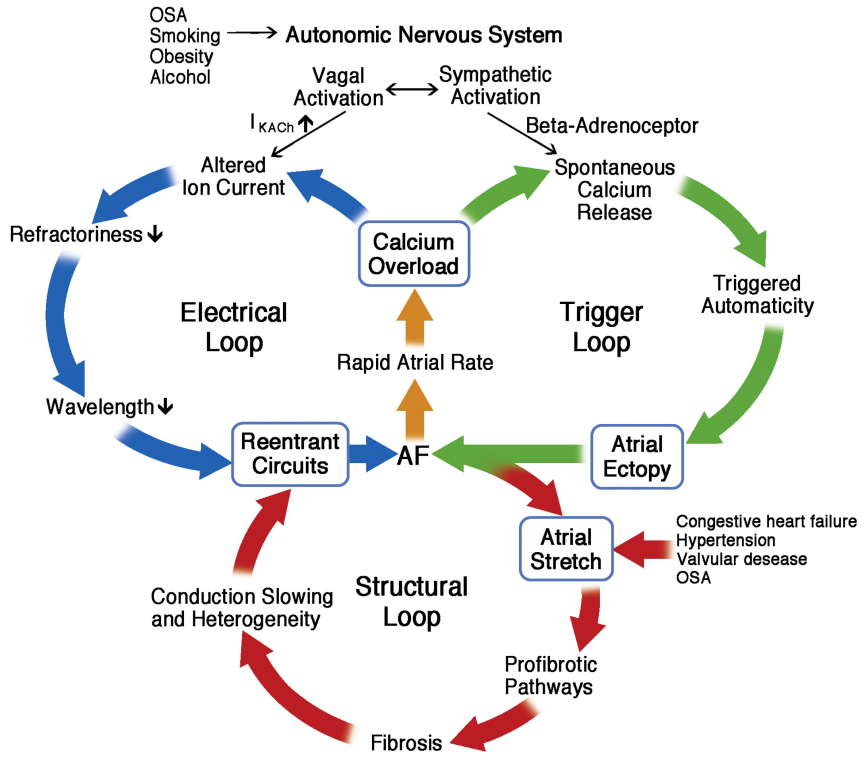

Figure 1.11 Mechanism of Atrial Fibrillation, adapted from [124].

Structural remodelling

Structural remodeling results in electrical dissociation between muscle bundles and local conduction heterogeneities. The most frequent pathologic change related to atrial fibrillation is the progressive fibrosis of the atria and loss of atrial muscle mass. Fibrosis and accumulation of extracellular matrix cause anisotropy of the atrial tissue, conduction block and perpetuation of AF. AF-induced structural remodeling is strongly related to contractile abnormalities, in particular to atria dilation, which causes loss of contractility and compliance. Stretch-related growth mechanisms lead to the activation of the renin-aldosterone angiotensin system, causing the fibrosis itself [145].

Electrophysiological remodeling process contributes to the increasing stability of the re-entry circuits. AF itself influences the expression of ionic channels of the cardiomyocytes and modifies, therefore, the electrical characteristics of these cells. Progressive Ca^{++} loading threatens cell viability, and the cells respond to minimize the impact of increased rate on intracellular Ca^{++} load. Since at each action potential Ca^{++} enters the cells through I_{Ca}, the high-rate stimulation leads to a substantial

increase of cellular Ca^{++} loading. In order to minimize this effect, the cells respond with a down-regulation of the L-type Ca^{++} with both short- and long-term defenses mechanism. However, because I_{Ca} is the major contributor to the AP plateau, the side-effects of Ca^{++} down-regulation are the reduction of the AP duration and the reduction of the refractory period, promoting re-entry circuits.

Electrical Remodelling

Multiple wavelets hypothesis The multiple wavelets hypothesis as the mechanism of re-entrant AF was first reported by Moe et al. [142], who proposed that wavefronts propagating through anisotropic atria may fractionate and separate in many self-perpetuating smaller wavelets. Based on this framework is the work of Alessie et al. [5], which developed the concept of *wavelength of re-entry*, defined as the product between refractory period and conduction velocity, i.e., the distance traveled by the electrical impulse in one refractory period. For this reason, the spatial and temporal distribution of the wavelets depends on the different electrical and anatomical characteristics of different part of the atria.

Until the end of the 1980s, Moe's hypothesis was considered the cause of atrial fibrillation, whose electrocardiographic diagnosis was justified by the fragmentation of the meandering wavelets. Even if recordings with multiple electrodes catheters supported this hypothesis, many other observations also evidence that an abnormal atrial substrate implicating atrial vulnerability should be considered in the pathogenesis of AF.

Focal trigger The focal trigger theory of AF initiation received a particular attention after the studies of Haissaguerre et al. [81]. The authors showed for the first time a focal source for AF originating from the pulmonary veins and reported successful ablation procedures of patients with paroxysmal AF. The pulmonary veins (PVs) were identified as the most frequent sources of abnormal electrical activity, but foci were also found in other cardiac structures such as the superior vena cava, ligament of Marshall, left posterior free wall, crista terminalis, and coronary sinus.

Focal triggers theory does not exclude the role of substrate modification in the pathophysiology of AF. In some patients with persistent AF, electrical isolation of PVs by catheter ablation may terminate the arrhythmia while in others AF may

persist after PVs disconnection, suggesting that in some patients sustained AF essentially depends on anatomical atrial substrate remodeling. These results drove the development of theories which assume the presence of different mechanisms acting in the same patient during AF.

Rotors Rotors are defined as the organizing sources, or drivers, of functional re-entrant activity in AF [208]. These structures are characterized by spiral waves that rotate in two or three dimensions around a pivot, called *phase singularity*, which is defined as the wave-break point where the excitation-recovery cycles meet and the activation phases change continuously from $-\pi$ to $+\pi$.

In 2012, Narayan et al. [147] showed that spatio-temporal maps derived from monophasic action potential catheters and 64-pole unipolar basket endocardial recordings of AF allow estimating propagation patterns consistent with rotors and focal impulses. The main hypothesis behind these studies is that, once eliminated the PV triggers, AF activity may be decomposed in deterministic and stochastic components: the organized, self-sustained and periodic rotors as drivers and a randomly distributed fragmentation of the resulting wavefronts leading to the formation of multiple wavelets. Wavelets may break up by collision with other wavelets or with the boundary of cardiac structures, or they may even generate new rotors, resulting into a fragmentation of wavefronts rotating with different frequencies, generating multiple wavelets which appear independent from each other. Moreover, phase singularities of fibrillatory rotors are predicted to precess, causing rotors meandering [224], increasing the variability and making difficult to distinguish between real drivers and temporary re-entrant activity.

Chapter 2

Radiofrequency Ablation of Atrial Fibrillation

Management of AF is focused on preventing circulatory instability using different strategies to control the heart rate and rhythm. These include antiarrhythmic drugs that slow down the rapid heart rate associated with AF, electrical cardioversion, catheter ablation of pathways that conduct abnormal electrical propagation, surgery maze procedure. Regardless of the antiarrhythmic strategy, anticoagulation therapy is always needed in order to prevent the formation of clots and reduce stroke risk factors. Pharmacologic therapy consists of anticoagulants, AV nodal blocking agents, and anti-arrhythmic drugs. Generally, anti-arrhythmic drugs are the first choice treatment, but often they are partially efficacious in maintaining sinus rhythm and result to have a substantial cardiac or extra-cardiac toxicity. However, the role of catheter ablation in the management of AF continues to evolve rapidly, with improvements in the efficacy and safety of the procedure.

Catheter ablation is a therapeutic technique which uses radiofrequency energy to destroy atrial tissue involved in the maintaining of the arrhythmia. The principal objective of atrial fibrillation ablation is the electrical disconnection of the pulmonary vein triggers from the atrial substrate. Ablation of atrial fibrillation is a complex and challenging procedure, characterized by a long learning curve. In less experienced laboratories, fluoroscopy time can be very high and, even more important, the risk of major complications, such as cardiac tamponade or atrioesophageal fistula, is not negligible. Improvement in technology and systematization of the technique help to

reduce these risks, shorten procedure time and minimize fluoroscopy time. On the other hand, operators are required to be familiar not only with traditional approaches, such as transseptal punctures and interpretation of complex intracardiac electrograms, but also with more and more sophisticated systems as the non-fluoroscopy 3D mapping system or remote magnetic navigation. The evaluation of the success rate of AF ablation is very controversial. Several methods have been proposed, including symptoms evaluation and Holter ECG monitoring. Long-term follow-up is the best way to assess the ablation outcome, but it can not be always performed.

2.1 Electroanatomical Mapping Systems

Electroanatomical mapping and navigation systems have greatly improved the ability of electrophysiologists to diagnose, treat and cure an ever-increasing variety of cardiac rhythm disorders [153]. They allow the visualization of the 3-dimensional position of electrophysiology catheters and the registration of electrical activity during sinus rhythm, as well as during arrhythmias, to create isopotential maps of the cardiac chambers and identify activation and propagation patterns. By sampling electrical and spatial information, the geometry of the mapped chamber based on the anatomy of the patient's own cardiac chamber is reconstructed in real-time and analyzed to assess the mechanism of arrhythmia and the appropriate site for ablation. The points sampled are connected through interpolation to create a triangle mesh and the faces of the mesh are colored to create electroanatomical map according to recorded values. The most common anatomical mapping systems used in the clinical setup are CARTO 3 and EnSite Precision electroanatomical cardiac mapping systems and the RhythmView Focal Impulse and Rotor Modulation (FIRM) mapping system.

2.1.1 CARTO 3 system

CARTO 3 navigation system (Biosense Webster, Inc., a Johnson & Johnson company, Diamond Bar, CA) is an electroanatomical mapping system which uses a magnetic field to accurately determine the location and orientation of the intracardiac catheters (Fig. 2.1). The main component of CARTO 3 localization system is a magnetic field emitter, called Locator Pad, placed below the patient table, approximately under the patient's chest. The generated magnetic field is coupled with a passive magnetic

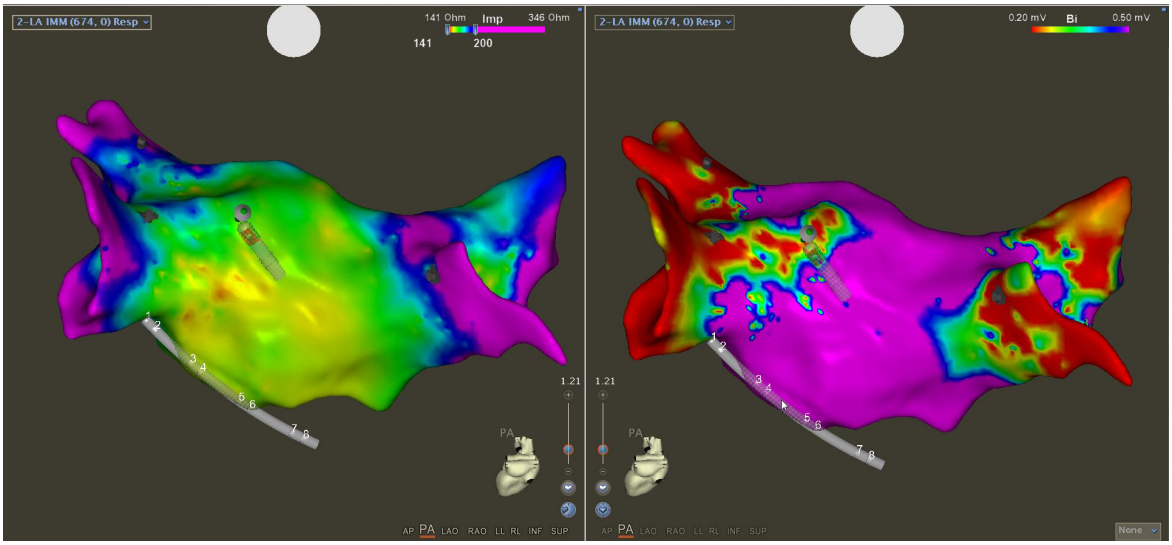

Figure 2.1 CARTO 3 electroanatomical mapping and navigation system

field sensor (copper wire coiled over a ferrite cylinder in a unique pattern) embedded in the catheter tip. Moreover, six reference patches are placed on the patient's body, enabling compensation for patient movements. The Locator Pad generates an ultra-low magnetic field in the range of 0.05 G to 0.2 G, which is sensed by the sensor in the catheter allowing the estimation of the distance from the coils. The location of the catheter is estimated using a GPS-like system, i.e., by intersecting the spheres of radii equal to the distance to the coils (Fig. 2.2a). The sensed magnetic field provides information about position and rotation of the catheter. Moreover, tracking of multiple mapping catheters is possible thanks to a hybrid system based on magnetic location technologies and current-based monitoring through the skin patches. The locator signal passing between each catheter electrode and the patch has a unique frequency allowing each catheter to be clearly distinguished, especially when they are close to each other.

VisiTag™ Module allows an intuitive visualization of parameters of lesion formation that can be used prospectively or retrospectively. According to operator preferences, tags appear on the electroanatomical map that accurately track, record and review catheter location and ablation data, allowing to objectively index ablation parameters to help facilitate consistency and continuity. A recent upgrade of the VisiTag module includes a new parameter, denoted *Ablation Index*, that takes into account the catheter-tissue contact force (see Section 2.2), the RF power and the

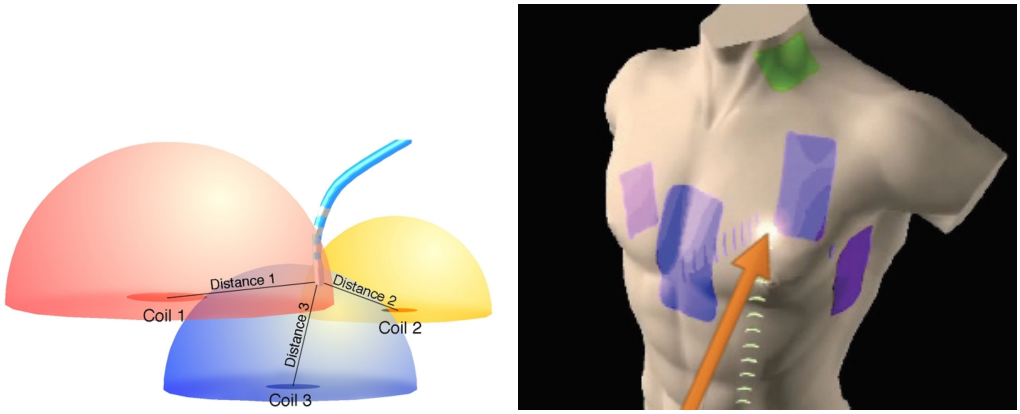

(a) CARTO 3 [91] (b) EnSite Precision

Figure 2.2 Catheter positioning systems

ablation time using the following formula [42]

$$\text{Ablation Index} = \left(k \int_0^t \text{CF}^a(\tau)\, \text{P}^b(\tau)\, \text{d}\tau \right)^c .$$

Ablation index is also dependent on the stability of the catheter during the power delivery, therefore it helps to achieve contiguous lesions and reproducible ablation strategy. Optimal values of Ablation Index have been proposed to deal with the regional variation of left atrial thickness [57].

Lastly, CARTO 3 has a *Fast Anatomical Mapping* feature which permits rapid creation of anatomical maps and simultaneously recording of localized electrical activity to enable more accurate electroanatomical representation. Especially using multipolar catheters such as LASSO® (Biosense Webster, Inc., Diamond Bar, CA), the mapping speed can further increase.

2.1.2 EnSite Precision system

The EnSite Precision™ Cardiac Mapping System (Abbott Electrophysiology, Menlo Park, California) is an impedance-based catheter navigation and mapping system (Fig. 2.3). Catheters localization is based on the capability of the catheters to measure the impedance field generated by three patient reference sensors placed on the patient's thorax. An 8 kHz signal is sent alternately through each pair of surface electrodes to create a voltage gradient along each axis, forming a transthoracic

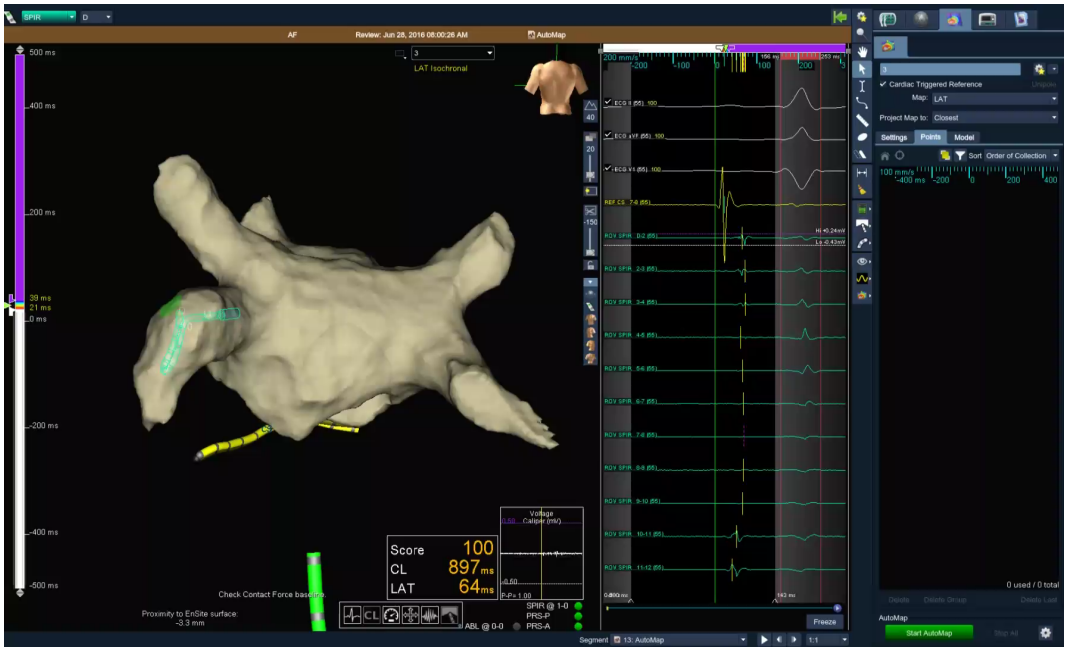

Figure 2.3 EnSite Precision electroanatomical mapping and navigation system

electrical field with the heart at its center (Fig. 2.2b). The mapping system has been updated with the Field Scaling Module, which includes a magnetic-based technology to correct impedance distortion and render a more precise and accurate geometry model when using sensor-enabled catheters.

The AutoMark Module is a lesion quality feature, allowing the operator to set the parameters for temperature, time, force, impedance drop, or power to identify a successful RF delivery. The system provides a different colored lesion marker depending on the selected parameters. Moreover, the AutoTrack Module allows the tracking of the catheter tip during RF delivery. EnSite Precision is equipped with the AutoMap Module together with the OneMap feature which allows to rapidly create high-density electroanatomical maps adopting automation strategies to increase resolution and avoid time-consuming evaluation of each data point. The operator can select inclusion or exclusion criteria to automatically reject points outside of the clinical morphology, such as catheter-induced ectopic beats.

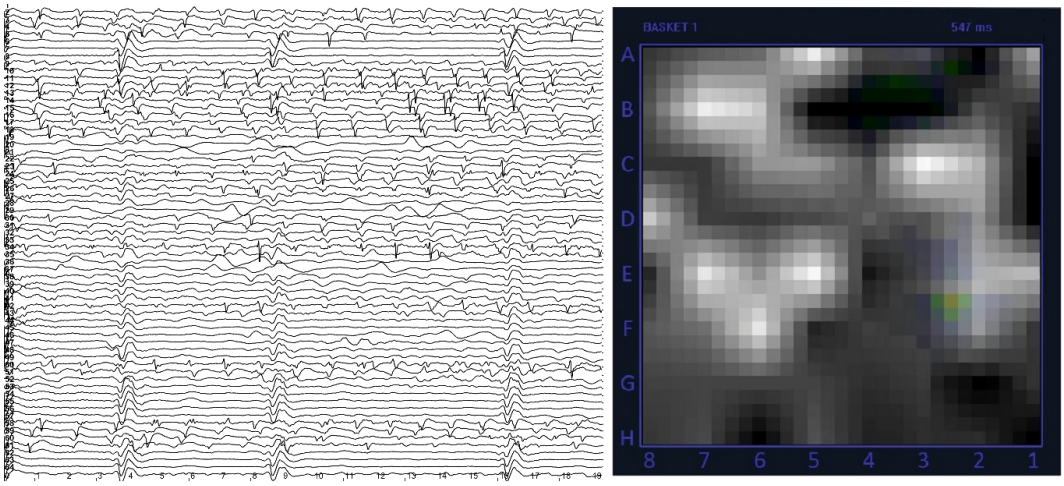

Figure 2.4 The RhythmView Focal Impulse Rotor Modulation mapping system. Left: signals recorded by the FIRMap catheter in the left atrium during AF. Right: the electrical activity is processed and visualized as activation map on an 8×8 square lattice, upsampled to help clinical interpretation.

2.1.3 RhythmView system

RhythmView (Abbott Electrophysiology, Menlo Park, California) Focal Impulse and Rotor Modulation is a system uniquely capable of mapping and visualizing electric rotors and focal impulses which sustain the irregular rhythms of AF. The mapping system comes with the FIRMap catheter, a basket catheter particularly designed to improve catheter-tissue contact. The FIRMap has a spherical wire basket with 64 evenly placed electrodes over the 8 splines that make up the basket. The basket expands, capturing the contours of the heart chambers and creating a panoramic map of the electrical heart activity. The RhythmView system and the FIRMap catheter work together with the Ensite Precision system which collects the information sent by the basket to create the 3D reconstruction of the heart and its electrophysiological activity.

The signals recorded during AF are exported in 1-minute epochs from the EP-WorkMate™ Claris™ recording system and imported into the RhythmView system. The algorithm selects the best 4-seconds in the recording, which are processed to create panoramic activation maps. Rotors are identified as peaks in the Rotational Activity Profiling (RAP) feature, which highlights rotational activity around a center using the isopotential movies and isochronal activation maps (Fig. 2.4). Focal beats in

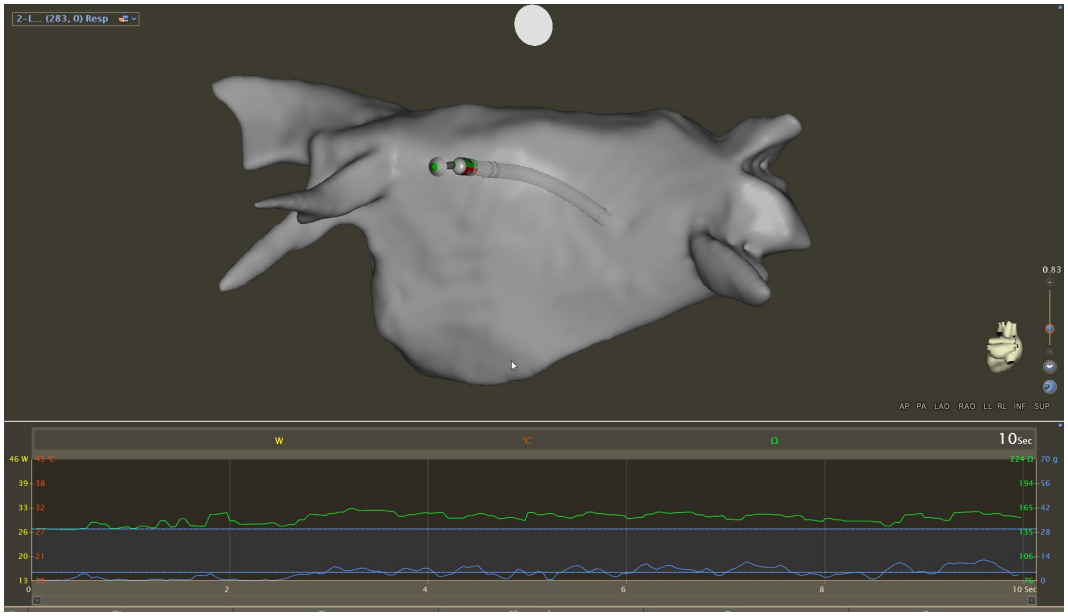

Figure 2.5 CARTO 3 Contact force data visualization

AF are identified at their point of origin from surrounding diastole from isopotential movies and isochronal maps.

By identifying specific areas of electrical rotational activity, studies have demonstrated a long-term success rate, even in patients who are normally difficult to treat with the traditional procedure.

2.2 Catheter-Tissue Contact Force Sensing

In order to achieve long-term success in treatment of atrial fibrillation, with permanent wide area isolation of the pulmonary veins, multiple individual focal lesions should be durable and transmural. Nontransmural lesion can lead to PV reconnection and recurrence of AF [157]. Catheter stability and good tissue contact are some of the variables that affect transmurality, and improved contact reduces dissipation of energy into the circulating blood pool resulting in better energy coupling to tissue. Up until the recent developments in RF catheters, catheter-tissue contact quality was measured indirectly by the operator through indirect methods such as fluoroscopic imaging of the catheter tip, tactile feedback from catheter manipulation, and changes in intracardiac electrograms and impedance, but these have been shown to

correlate poorly with tissue–electrode contact. Recently, several technologies have been developed to estimate real-time catheter-tissue contact by measuring the force applied to the tissue by the catheter to improve ablation lesion quality. ThermoCool® SmartTouch™ (ST) catheter (Biosense-Webster Inc., Baldwin Park, CA, USA) is one of the most advanced catheter developed by Biosense Webster. During the ablation procedures, the ST catheter enables measurement of the contact force and the direction of the catheter tip inside the heart. The catheter has a 3.5 mm externally irrigated tip electrode connected by a tiny precision spring to the shaft, allowing the tip to bend. The spring is surrounded by a magnetic signal emitter and three magnetic signal sensors, whose positions change according to the pressure applied to the catheter. Sensors positions are used to calculate the degree of deformation of this spring and a signal proportional to the micro-movements of the spring is transmitted via the magnetic emitter. The resolution of the measurement is less than 1 g in bench tests and the signal is sampled every 50 ms. The spring deformation is finally used to estimate catheter angle and contact force and visualize them in real-time on CARTO mapping system through numerical, graphical and vectorial representations (Fig. 2.5). Clinical experience with CF devices results in a faster procedure, shorter fluoroscopic time and less RF energy needed to perform PVI.

2.3 Remote Magnetic Navigation System

Besides the technical difficulty of ablation strategies, procedures can be very long and characterized by long exposure times to X-ray for both the patient and the operator. Multiple procedures per day can be very challenging for the operator, whose manual skills are put to the test during pulmonary vein isolation. As a matter of fact, in order to achieve complete vein isolation, long contiguous linear lesions are mandatory. Remote Magnetic Navigation technology aims to minimize the fluoroscopy time and the physical demands, to enhance catheter stability in order to increase procedural success, and, in particular, to help avoiding serious complications, therefore improving the safety of ablation procedures [156].

A robotic ablation starts the same way as a traditional catheter ablation. The operator inserts a catheter into the groin and guides the catheter to the right side of the heart. After making a puncture in the septum, the wall that separates the right and left sides of the heart, the physician controls the working tip through user-friendly

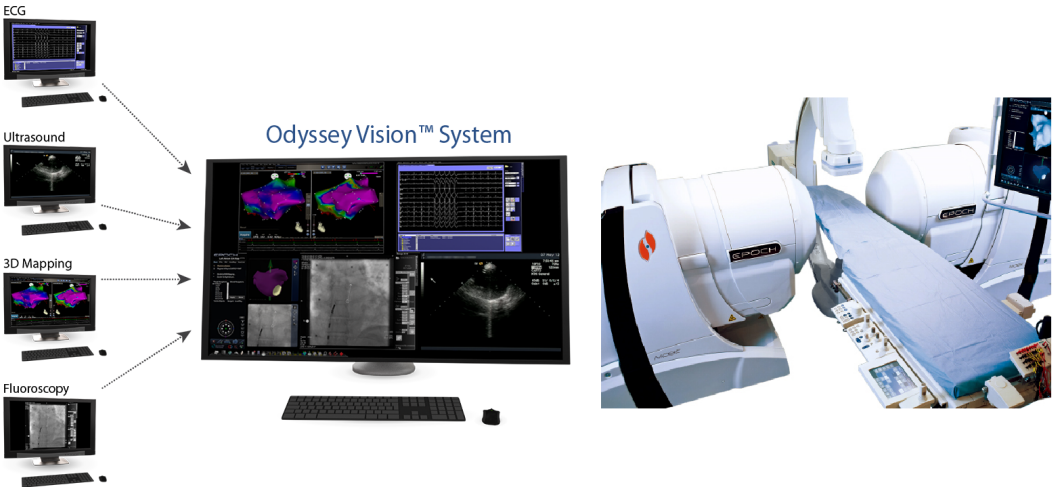

Figure 2.6 The Stereotaxis remote magnetic navigation system.

"point and click" and/or joystick-operated technology, which can be controlled either from beside the patient table, as in traditional procedures, or from a room adjacent.

2.3.1 Stereotaxis magnetic navigation system

Stereotaxis Niobe® Magnetic Navigation System (Stereotaxis, St. Louis, Mo, USA) is a remote navigation system, that works with the CARTO mapping system and ThermoCool® RMT ablation catheters (Biosense-Webster Inc., Baldwin Park, CA, USA). The patient's bed lies between two large permanent magnets, which track the movement in the catheter and send the information to the system, mounted on articulating or pivoting arms enclosed within a stationary housing (Fig. 2.6). These magnets generate magnetic navigation fields that are less than 10% of the strength of fields typically generated by the Magnetic Resonance Imaging (MRI) equipment and therefore require significantly less shielding. The catheter is driven through both mechanical and magnetic technologies, using a joystick which controls the mechanical catheter advancer and finely tunes the magnetic field allowing accurate catheter navigation. The components of the system are:

Niobe magnet system, which uses high-quality permanent magnets to navigate catheters through chambers of the heart with precision and safety

Vdrive automated catheter advancer, provides the clinician with greater responsiveness to remotely advances and retracts the catheter into the patient's heart, maintaining good stability of devices

Odyssey intuitive user interface which allows to control the magnetic field orientation, and it is able to aggregate and integrate a vast number of clinical lab information into one large screen and a single mouse and keyboard control.

Catheters are controlled directly at their working tip by the magnetic field and they are extremely soft and flexible. This inherently a-traumatic design is likely to greatly reduce the risk of perforation or damage to heart tissue or vessel walls.

2.4 Radiofrequency Ablation Procedure and Biophysics

Catheter ablation of atrial fibrillation is a closed chest procedure. The operator makes a small puncture in the groin, arm, or neck area and the catheters are inserted into the heart. The catheters typically used are an octapolar catheter in the coronary sinus and a deflectable ablation catheter whose tip is threaded through the septal wall, a tiny incision in the wall between the left and right atria, and is positioned to map the atrial chambers and ablate tissue around the pulmonary veins or at other sources of erratic electrical signals which cause the irregular heartbeat.

RF current is the most common energy source in catheter-based ablation, mainly because its effect on living tissues are well-understood, particularly under the point of view of safety. During the ablation procedure, an electric current in the range of 450-500 kHz is applied between the RF electrode and a reference electrode, the RF energy is transmitted to the tissue surface and converted into heat due to the tissue resistive heating effect. The heat propagates to the deeper layer of tissue by conduction, causing its death due to protein coagulation. A very large amount of studies have described in detail the biophysics of RF ablation, providing a comprehensive analysis of this technology and trying to define the best strategy to achieve complete and permanent elimination of arrhythmogenic substrate without producing collateral injury. Thereafter we summarize the main factors that affect RF ablation and its ability to deliver effective and transmural lesions.

In order to produce an irreversible thermal injury, a temperature rise above 50 °C is required, whereas lower tissue temperature results in reversible loss of cellular excitability. Moreover, a higher electrode-tissue interface temperature results in a larger lesion. Another strongly predictive parameter of lesion size is RF power, since increasing current flow through the tissue increases resistive heating and thereby lesion size, and due to the fact that power and current are proportional, higher power implies larger lesion.

In vivo, many factors (e.g., regional blood flow cooling effect) alter the heat transfer to tissue, making it less predictable. The unpredictability of temperature could results in impairment in the effectiveness of RF delivery. For example, coagulum can form at the electrode-tissue interface and a sudden rise in electrical impedance can occur, which limits energy delivery. When temperature exceed 100 °C, severe complications can arise for excessive temperature rise, such as steam pops leading to perforation and cardiac tamponade, happens An effective strategy against these events is catheter-tip cooling, which allows greater energy delivery keeping the temperature at electrode tip low enough to avoid complications; the price to pay is that temperature monitoring during irrigated catheter ablation is unreliable, since electrode and tissue temperature could be completely different.

Because of the variability of these factors in vivo, applied energy, power and current are poor indicators of the extent of lesion formation during RF ablation. Temperature-dependent impedance drop due to tissue heating is a useful surrogate of lesion formation, typically used in the clinical practice. However, whether cell death occurs due to tissue heating depends on both temperature and duration of energy delivery. Assuming stable catheter on the tissue surface, depending on the temperature, the duration time to achieve permanent electrical isolation ranges from few seconds to minutes. However, one of the greatest challenges is to keep the catheter stable during RF delivery due to patient movement, heart activity, blood flow and irregularity of tissue surface. Electroanatomical mapping system allows the physician to control catheter stability, and visualize electrode-tissue contact force. A simple but useful indicator of the average contact force and stability achieved during the entire RF delivery is the Force-Time Integral (FTI).

The 3-dimensional reconstruction of the left atrium is created with the electroanatomic mapping system (CARTO 3 or Ensite Precision). Other than the electroanatomical map, the operator adopts criteria based on fluoroscopy, impedance, and

electrical activity to recognize the PV ostium. In particular, entry of the veins is identified by an increase of the impedance to 140-150 Ω or disappearance of electrical activity. 8 mm tip-deflectable catheter or a 4 mm tip-irrigated catheter is used for mapping and ablation. Primarily, the ablation of atrial fibrillation consists of pulmonary vein isolation (PVI). The goal of the procedure is to eliminate the irregular heartbeat that typically originates from the four pulmonary veins, by electrical disconnecting them. RF is used to create contiguous focal lesions of scar tissue, called conduction blocks, which stop the erratic electrical signals propagation from the pulmonary veins through the heart. This method is most successful with paroxysmal atrial fibrillation [155]. The endpoint of a single RF delivery is voltage abatement of the local atrial electrogram by 90% or to < 0.05 mV. In some patients, if necessary, additional ablation lines are created along the left atrium (LA) roof, septum/anterior wall, or along the posterior mitral annulus. The ridge between the left superior PV (LSPV) and LA appendage can be identified by fragmented electrograms resulting from the collision of activity from the LA appendage and LSPV/LA.

In case of patients with recurrent nonparoxysmal AF who are refractory to other interventions or with a history of multiple unsuccessful ablations, it may be the case that AF is driven by spatially and temporally stable rotational drivers anchored on micro-anatomic tracks. FIRM-guided ablation is performed before conventional PVI ablation. The operator selects the basket catheter according to the LA diameter and places it in each atrium to record the unipolar signals during AF. Rotors and focal impulse are identified on the RhythmView system and localized on the 3D reconstruction visualized by the Ensite Precision mapping system. The electrophysiologist targets the rotor for ablation, unless judged to be a false positive upon visual inspection of the operator.

It is not so unusual to observe AF termination during the procedure. If this does not happen, electrical cardioversion is performed at the end of the procedure and, if there is an immediate recurrence of AF, contiguity and completeness of lesions is assessed.

Chapter 3

Digital Signal Processing for Cardiac and Endocavitarian Signals

The stochastic nature of physiological signals makes medicine one of the areas of most interest to the statistical analysis of the signals. In particular, thanks to the unique properties of the cardiac tissue and of the central and peripheral nervous system, cardiac electrophysiology and neuroscience offer the more interesting and important research environment for signal processing. The advance of hardware technology has allowed the development of devices that promote biomedical monitoring and assistance, as well as the real-time collection, management and processing of an ever-increasing amount of data. However, computational power is useless without the tools to exploit it combined with a deep understanding of the physiological phenomena. Together with the new fields of machine learning, data science and data mining, signal processing have been driving the development of techniques to extract and visualize useful information from raw data belonging to the biomedical field, to facilitate clinical decision making and to lead the physician to a more aware treatment of disease. In this chapter, we present some of the signal processing techniques along with their application to the branch of cardiac electrophysiology, with particular regard to those used throughout this work.

3.1 Fundamental Analysis of Electrophysiological Signals

3.1.1 Time domain

Physical signals, time series of economic or environmental data, and in general any waveform that changes in time can be characterized by quantities which summarize the information content of the signals and its behavior in the time domain. In the following we denote $\boldsymbol{x} = \{\boldsymbol{x}(t)\}_{t=1}^{T} \in \mathbb{R}^T$ a finite sequence of length T. Denoting $|\boldsymbol{x}(t)|^2$ the energy density, or instantaneous power, of the signal $\boldsymbol{x}$, its total energy $\|\boldsymbol{x}\|$ can be calculated as the time integral of the square of the signal amplitude. In the discrete time domain, we have

$$\|\boldsymbol{x}\|^2 = \sum_{t=1}^{T} |\boldsymbol{x}(t)|^2. \tag{3.1}$$

Particularly for non-stationary signals, mean time and duration are gross but useful indications of where the energy density of a signal is concentrated, and its distribution around the mean. Considering the usual definitions of average and variance, the mean time and duration can be computed as weighted mean and variance using the energy density as weights

$$\mu = \frac{\sum_{t=1}^{T} t|\boldsymbol{x}(t)|^2}{\sum_{t=1}^{T} |\boldsymbol{x}(t)|^2} \qquad \sigma^2 = \frac{\sum_{t=1}^{T} (t-\mu)^2|\boldsymbol{x}(t)|^2}{\sum_{t=1}^{T} |\boldsymbol{x}(t)|^2} \tag{3.2}$$

3.1.2 Frequency domain

Even if time domain representation is fundamental, in order to gain more understanding of physical signals, other representations should be considered. Mathematically, the signal is decomposed by projection over a complete set of functions. Besides time, the frequency domain is the most important signal representation since the frequency spectrum has a profound physical interpretation. The discrete Fourier transform of the discrete sequence $\boldsymbol{x}$ can be written as

$$\hat{\boldsymbol{x}}(k) = \frac{1}{\sqrt{T}} \sum_{t=1}^{T} \boldsymbol{x}(t) \mathrm{e}^{-\mathrm{j}\omega_k t} \qquad \text{with} \quad \omega_k = \frac{2\pi(k-1)}{T}, k = 1, 2, \ldots, T$$

and can be efficiently computed using the Fast Fourier Transform algorithm. As in the time domain, it is possible to define $|\dot{\boldsymbol{x}}(k)|^2$ as the energy density per unit frequency at frequency ω_k. Since total energy must be independent on representation, it holds

$$\|\boldsymbol{x}\|^2 = \sum_{t=1}^{T} |x(t)|^2 = \sum_{k=1}^{T} |\dot{\boldsymbol{x}}(k)|^2 = \|\dot{\boldsymbol{x}}\|^2 \tag{3.3}$$

which is Parseval's theorem. As in the time domain, the Fourier spectrum can be characterized by the average frequency $\dot{\mu}$ and the mean square bandwidth $\dot{\sigma}^2$

$$\dot{\mu} = \frac{\sum_{k=1}^{T} \omega_k |\dot{\boldsymbol{x}}(k)|^2}{\sum_{t=1}^{T} |\dot{\boldsymbol{x}}(k)|^2} \qquad \dot{\sigma}^2 = \frac{\sum_{k=1}^{T} (\omega_k - \dot{\mu}) |\dot{\boldsymbol{x}}(k)|^2}{\sum_{t=1}^{T} |\dot{x}(k)|^2} \tag{3.4}$$

3.2 Filtering of Cardiac Signals

Filtering is an essential step in the processing of intracardiac signals, which attempts to improve signal to noise ratio by minimizing artifacts, noise and other unwanted components such as muscle noise or baseline wander. A major concern is how the filtering influences the morphology of the ECG, in particular the QRS complex. Therefore distortion caused by the processing should be carefully quantified.

The most common filter is the power-line noise filter. Power-line interference is an unavoidable source of noise in the clinical environment, since it is produced internally by circuits within the system during operation. Different approaches have been implemented to suppress the interference, including notch filters and adaptive filters [129], Kalman filters [176], subtraction or blind source separation methods [122, 3].

Typically in EP recording systems, to remove unwanted information from the recorded electrograms, band pass filters are implemented as combination of high pass and low pass filters. Low frequency interferences in biomedical recordings, such as baseline wander, are generated by various sources, including respiration, body movements and variable catheter contact. These have frequencies generally less than 0.05 – 0.1 Hz. High pass filters can be designed to minimize low frequency changes in beat morphology which do not have cardiac origin. In particular concerning baseline wander removal, other strategies have been investigated, such as median filters or wavelet or spline decomposition [121]. The low pass filter with cutoff frequency

above the physiological range allows to remove high frequency environmental noise coming from outside the recording system.

Botteron preprocessing The Botteron preprocessing algorithm is used to emphasize the timing of the atrial activation and to enhance the periodicity or non-periodicity of the signal [24]. Such algorithm removes the detailed features of the signal morphology and transforms the electrogram into a sequence of pulses with simpler and more homogeneous shapes. The algorithm processes the signal with the following steps:

- Bandpass filtering at 40 - 250 Hz
- Computation of the absolute value
- Lowpass filtering at 20 Hz

The signal is transformed into a sequence of smooth monophasic pulses whose width is enlarged and whose amplitude is not directly related to the amplitude of the atrial beats.

Dominant Frequency Atrial activation rate can be estimated as the frequency containing maximum power in the frequency domain, often referred to as dominant frequency (DF). The DF analysis is based on the assumption that the electrogram signal can be approximated by a single sinusoidal signal with a frequency equal to the activation rate. This waveform is obtained through the Botteron preprocessing followed by the frequency spectrum estimation using the Welch's method for spectral density estimation [214]. The DF is defined as the frequency with the maximum power in the power spectrum. Several studies has shown that frequency mapping is able to identify localized sites of high-frequency activity during AF in humans. Ablation at these sites results in prolongation of the cycle length and termination of paroxysmal AF, indicating their role in the maintenance of AF [178, 173]. However, it has been shown that although DF analysis can be reliably used to measure local activation rate in ideal situations, several factors can contribute to the unpredictability of DF analysis related to recording techniques and signal properties. Moreover, the location of the dominant frequency is unstable, changing during the recording period.

3.3 Time-Frequency Representation

Time-frequency (TF) analysis aims at characterizing and describing signals whose frequency content evolves with time [37]. Joint time-frequency representation is a challenging problem whose complexity meant that several solutions were proposed over the decades. The motivation leading to TF representation are both mathematical and practical. Not only jointly representation offer a better understanding of the mathematical properties of signals, but, since real signals are often non-stationary, time-dependent variations can be appreciated with this method.

The most widely used TF transform is the *short-time Fourier transform*. It is used to extract the frequency content of a temporal signal at a given time, by first selecting a part of the signal using a window and then computing the discrete Fourier transform. More concretely, for a discrete signal $\boldsymbol{x}$ of length T, the circular discrete sampled STFT of $\boldsymbol{x}$ at the m-th (out of M) frequency band, and under window $\boldsymbol{h}$ is

$$\mathrm{STFT}\{\boldsymbol{x}\}(k,m) \stackrel{\Delta}{=} \sum_{t=1}^{T} \boldsymbol{x}(t)\,\overline{\boldsymbol{h}\,(t_k)}\,\mathrm{e}^{-2\pi \mathrm{j}\frac{(t-1)(m-1)}{M}},$$

where $t_k = \mod t - a(k-1)T + 1$, scalar a is the shift in time between two successive windows [167, equation 1], and $\mod tT$ finds the remainder after division by T, i.e., $\mod tT = t - T\lfloor \frac{t}{T} \rfloor$. Note that $k = 0, 1, \ldots, \lfloor \frac{T}{a} \rfloor - 1$ is the time band centered at ka and that $m = 1, \ldots, M$ is the frequency band index. For additional insights about this transform, we refer the reader to [76, 63].

The choice of the analysis window is a trade-off problem, since localization of signal components cannot be as good as we want in both time and frequency domain, due to the *uncertainty principle*. The degree of trade-off depends on the window, signal, and sampling frequency. Anyway, some windows, such as Hamming window, allow good compromise, offering reasonable localization in both time and frequency. The usual way to represent a TF distribution is the *spectrogram*. Spectrogram is usually represented as a graph with two geometric dimensions: the horizontal axis represents time, while the vertical axis is frequency; a third dimension indicating the amplitude of a particular frequency at a particular time is represented by the intensity or color of each point in the image.

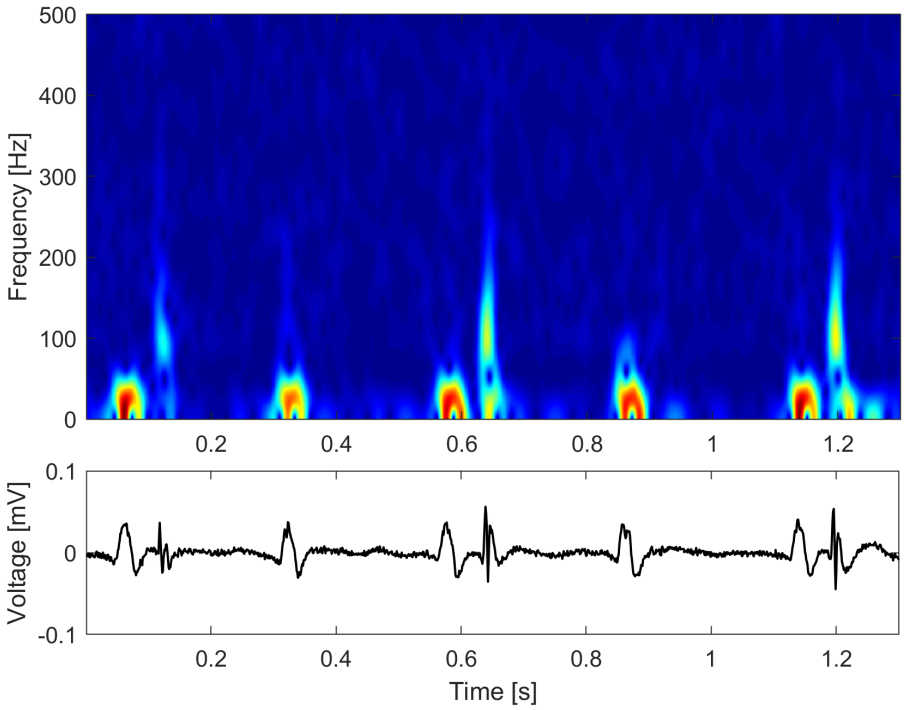

Figure 3.1 Example of time-frequency analysis of an intracardiac signal.

3.3.1 Time-frequency analysis of intracardiac signals

The main idea behind time-frequency analysis of cardiac signals is to build a new method for the study of cardiac phenomena. Over the last decades, thanks to the development of signal processing techniques for medical applications, frequency representation of cardiac signals has attracted the interest of the scientific community, in particular for the analysis of arrhythmias. TF domain, jointly with the other representations, offers new perspectives in the interpretation of intracardiac electrograms.

Time-frequency analysis of ECG has been used for classification [9], feature extraction [35], biometric purpose [149], but mainly for analysis of arrhythmias, in particular atrial fibrillation [201]. TF analysis allows the detection of changes in the AF frequency, which has been used for several purposes, such as refractoriness estimation [23], evaluation of antiarrhythmic drug effects [90], and the identification of high-frequency activity sites causing AF maintenance [178]. Moreover, TF spectrum reveals to be a useful instrument to characterize atrial fibrillation, determine single-impulse features, and potentially to provide a deeper understanding of the

underlying tissue [151]. For example, Figure 3.1 shows the spectrogram of the electrical activity recorded by a mapping catheter in the atrium. Two independent electrical cycles span the atrial wall with different periodicity. Time-frequency analysis shows the different spectra of the two potentials, suggesting that their electrophysiological characteristics, such as the propagation speed, are different.

3.3.2 Teager-Kaiser energy operator

Energy operator defined in (3.1) does not take into account the frequency of the signal. Kaiser in [99] defined a non-linear energy operator, termed *Teager-Kaiser Energy Operator*, as a real-time operator that regard both the amplitude and the frequency. This operator is derived by the equation of the discrete simple harmonic oscillator

$$x(n) = A\cos(\omega n + \varphi) \tag{3.5}$$

where A is the amplitude, $\omega = 2\pi f/f_s$ is the normalized frequency, f the frequency of $x(n)$, f_s the sampling frequency and φ the phase. Equation (3.5) has three unknowns: A, ω and φ. Considering the following system of equations

$$\begin{cases} x(n) & = A\cos(\omega n + \varphi) \\ x(n+1) & = A\cos(\omega(n+1) + \varphi) \\ x(n-1) & = A\cos(\omega(n-1) + \varphi), \end{cases}$$

its solution can be written as

$$x(n)^2 - x(n+1)x(n-1) = A^2\sin^2\omega \simeq A^2\omega^2$$

where the approximation holds if the value of ω is limited to $\omega < \pi/4$, i.e., $f/fs < 1/8$, with a relative error smaller than 11%.

Equation (3.5) is the solution of the second-order differential equation describing the dynamic of a mass-spring system

$$\frac{\mathrm{d}^2x}{\mathrm{d}t^2} + \frac{k}{m}x = 0.$$

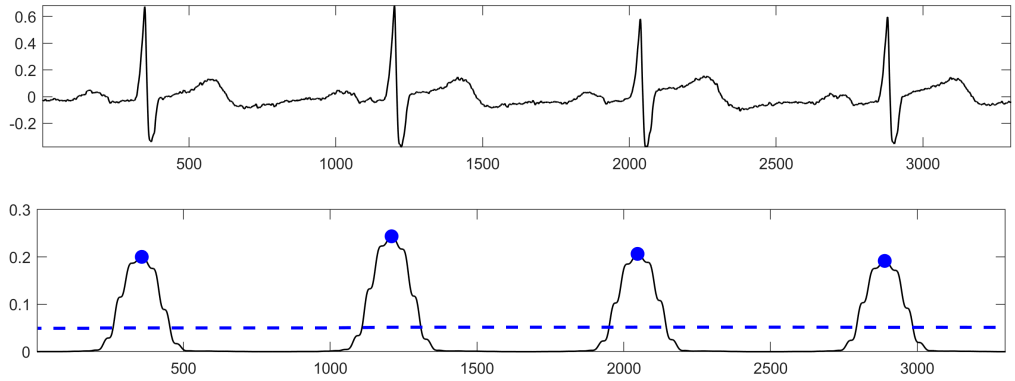

Figure 3.2 Pan-Tompkins algorithm. Above the original ECG raw signal recorded by lead I, below the transformed signal with detected QRS complexes (blue dots) and adaptive threshold (dashed blue).

The total energy of the system is the sum of the potential and the kinetic energies

$$E = \frac{1}{2}kx^2 + \frac{1}{2}m\frac{\mathrm{d}x}{\mathrm{d}t} = \frac{1}{2}m\omega^2A^2 \simeq \omega^2A^2$$

Thus, the energy of a simple oscillation is proportional to the square of the amplitude and the square of the frequency of the oscillation. Then, the non-linear energy operator is defined as

$$E_{TK}\{x\}(n) = x(n)^2 - x(n+1)\,x(n-1)$$

3.4 Signal Processing Algorithms for Cardiac Signals

3.4.1 Pan-Tompkins algorithm

The Pan-Tompkins algorithm has been developed in [152] to detect QRS complexes. It recognizes QRS complexes based on analysis of the slope, amplitude and width. Figure 3.3 shows the various processing steps involved in the algorithm. In order to isolate the portion of the wave where QRS energy is predominant and suppress other waves (P and T waves), the signal is filtered by a band-pass filter composed of cascaded high-pass and low-pass filters. Then a non-linear processing composed of differentiation and squaring is applied to the filtered signal to enhance QRS complex. Eventually, time averaging with window size depending on the sampling frequency

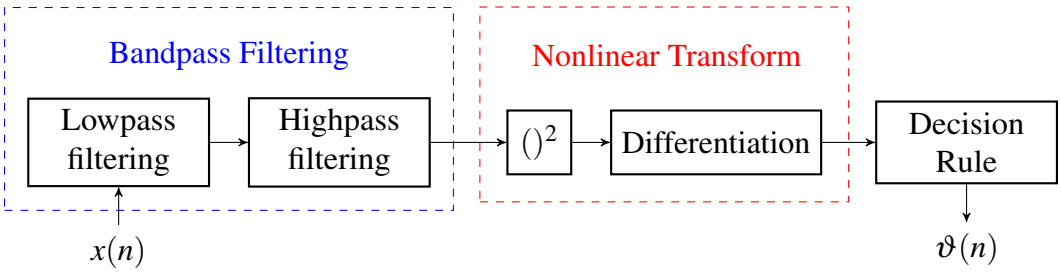

Figure 3.3 Block scheme of the Pan-Tompkins algorithm. The signal $x(n)$ is filtered using a cascade of lowpass and highpass filters, a nonlinear transformation enhances the QRS complex and finally, an adaptive decision rule returns the output $\vartheta(n)$.

is used to merge close peaks. Finally, the QRS peak is detected by applying an adaptive decision rule, typically an adaptive threshold, to test whether the QRS is present or not (Fig. 3.2). Detection of QRS is very useful also for the analysis of endocavitarian signals since it can be used to discriminate between near-field and far-field components. In particular, for the analysis of AF, it could be useful to eliminate the ventricular component of the signal.

3.4.2 Signal averaging

The most common way to deal with noise in the analysis of cardiac and intracardiac signals is using linear filtering. However, in many situations, we are interested also in the higher part of the frequency spectrum, because in many cases, low-amplitude high-frequency components hidden by noise contain useful information regarding the electrophysiological properties of the cardiac tissue. In order to overcome the limitations of linear filtering we should observe that cardiac signal is the realization of a periodic process, therefore we can exploit the periodicity, i.e., its statistical properties, to increase the signal to noise ratio (SNR) without compromising the frequency content.

For simplicity let us consider the surface ECG signal recorded by the lead I. The same analysis can be performed on the other surface signals, as well as on the intracardiac electrograms, assuming steady-state condition and that the catheter does not move during the recording. Assuming that our recording contains N potentials, in order to apply the averaging technique we need to split it into N windows, one for each potential. The position and the length of the windows can be determined

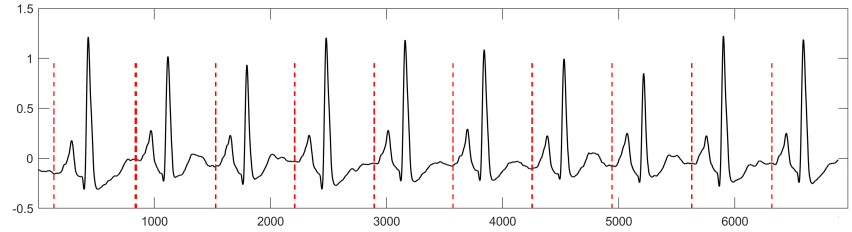

(a) ECG splitting according to QRS complex peaks and RR intervals

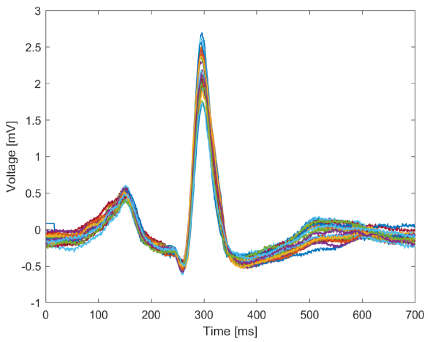

(b) Aligned ECG signals

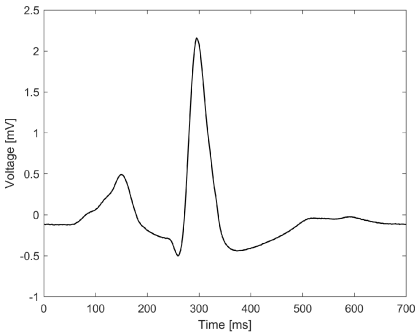

(c) Averaged ECG

Figure 3.4 Signal Averaged ECG. The signal is split into its periodic components, aligned according to the R wave position and averaged.

using the Pan-Tompkins algorithm: the windows will be centered on the QRS peaks identified by the algorithm and with adaptive length equal to the RR interval, i.e., time difference between two consecutive R waves (Fig. 3.4a). The obtained signals are zero padded to have the same length and aligned according to the R wave peak, as shown in Figure 3.4b. Finally, the averaged ECG is computed (Fig. 3.4c). Under non-restrictive assumptions, it can be proved that the SNR of the resulting signal is increased by a factor proportional to $\sqrt{N}$. Moreover, it contains the high frequency components of the original ECG which are in common, and are more likely to be related to the physiological electrical activity. A typical application of the signal averaging technique is the signal-averaged electrocardiography (SAECG). It is used to reveal small variations in the QRS complex, usually called “late potentials”, which are commonly related to ventricular tachyarrhythmias.

3.5 Statistical Analysis

Throughout this work we will almost constantly deal with data sampled from random variables with unknown distribution or realizations of random processes. Thereafter, the main tools and statistical tests used in this thesis are presented. We will particularly address the sample correlation coefficient and paired t-test, which have been widely used in Chapters 4 and 5 to validate the results.

Continuous variables are expressed as mean±std (standard deviation) if normally distributed, whereas median and range are used if the data were clearly skewed. Comparisons between two groups were made with Student's t tests and summarized with means and standard deviations for independent samples if normally distributed or, if not normally distributed, evaluated with the Mann-Whitney U test and summarized with medians and quartiles. Normality was assessed with the Kolmogorov-Smirnov test. Categorical variables were expressed as count and percentage and compared using the chi-squared test or Fisher's exact test. A probability value < 0.05 was considered statistically significant throughout.

Sample Correlation Coefficient The Pearson product-moment correlation coefficient is a statistic that measures the degree of linear correlation between two variables x and y and is defined as

$$\rho_{X,Y} = \frac{\operatorname{cov}(X,Y)}{\sigma_X \sigma_Y} = \frac{\mathbb{E}\left[(X-\mu_X)(Y-\mu_Y)\right]}{\sigma_X \sigma_Y}$$

where cov is the covariance, σ_X the standard deviation of X, μ_X is the mean of X, and $\mathbb{E}[\cdot]$ is the expectation. Considering a data pair, x and y, taken as random sample of the population X and Y, the correlation coefficient is called *sample correlation coefficient* and denoted with r. The sample correlation coefficient r of the data pairs $(\boldsymbol{x}, \boldsymbol{y})$, is

$$r = \frac{\sum_{n=1}^{N} (\boldsymbol{x}(n) - \bar{\boldsymbol{x}})(\boldsymbol{y}(n) - \bar{\boldsymbol{y}})}{\sqrt{\sum_{n=1}^{N} (\boldsymbol{x}(n) - \bar{\boldsymbol{x}})^2} \sqrt{\sum_{n=1}^{N} (\boldsymbol{y}(n) - \bar{\boldsymbol{y}})^2}}$$

where $\bar{\boldsymbol{x}}$ and $\bar{\boldsymbol{y}}$ denote the sample mean of the $\boldsymbol{x}$ and $\boldsymbol{y}$, respectively. When $r > 0$, the sample data pairs are positively correlated, whereas when $r < 0$, they are negatively correlated.

Statistical inference based on sample correlation coefficient aims to test the null hypothesis that the Pearson's correlation coefficient ρ between the two random variable X and Y, is equal to 0, based on the value of the sample correlation coefficient of the data pair $\boldsymbol{x}$ and $\boldsymbol{y}$. The significance of a sample correlation depends on the sample size and also on the value of r. Assuming that the samples, $\boldsymbol{x}$ and $\boldsymbol{y}$, are drawn from populations that follow a bivariate normal distribution, the sampling distribution of Pearson's correlation coefficient follows Student's t-distribution with degrees of freedom $n-2$. Specifically, if the underlying variables have a bivariate normal distribution, the variable

$$t = r\sqrt{\frac{n-2}{1-r^2}}$$

has a Student's t-distribution in the null case. Then, if the absolute value of t is greater than the $1-\alpha/2$ probability point of the CDF of Student's t-distribution, the null hypothesis can be rejected. This also holds approximately even if the observed values are non-normal, provided sample sizes are not very small. However, the sample correlation coefficient r is not robust, so its value can be misleading if outliers are present. In order to reveal spurious correlation due to outliers, inspection of the scatter plot between $\boldsymbol{x}$ and $\boldsymbol{y}$ is typically necessary.

Chapter 4

Ablation Strategy

Part of the work described in this chapter has been previously published in Grossi, S., Grassi, F., Galleani, L., Bianchi, F. and Conte, M. R., A comparison of contact force and remote magnetic navigation on lesion formation for the ablation of atrial fibrillation. Pacing Clin Electrophysiol.

4.1 Introduction

Circumferential PV antrum isolation technique through RF catheter ablation has been accepted as the effective therapy for patients with symptomatic AF, in particular in case of drug refractory paroxysmal AF. Despite acute procedural success, recurrence of atrial arrhythmia after pulmonary vein isolation (PVI) is still relatively common (from 20% to 55%) and it is frequently associated with electrical reconnection and consequent conduction recovery between the PVs and the left atrium. It is well understood that ineffective lesion formation may result in gaps in the isolation line, therefore formation of a durable permanent transmural scar is critical to block electrical conduction and prevent spontaneous PV ectopics from triggering AF.

In this chapter, we study the effect of different ablation techniques commonly used in the clinical practice of RF ablation of AF. In Section 4.2, we propose electrocardiographic criteria based on the attenuation, fragmentation and duration of the intracardiac signals for the characterization of the ablation sessions and compare contact force guided ablation and remote-controlled magnetic navigation. Afterwards, in Section 4.3, we investigate the issue of catheter-tissue CF and its

correlation with ablation outcome. We verify the relationship between CF and other ablation parameter with the scar revealed using the cardiac magnetic resonance with late gadolinium enhancement (LGE) which allows the detection and quantification of heart fibrotic tissue. Our analysis allows us to identify a force-time integral threshold which enables to deliver effective lesions.

4.1.1 Related work

Several studies have suggested that improving the quality of the lesions will offer better results and minimize the phenomenon of PV reconnection [165, 154, 117]. Poor catheter-tissue contact is believed to be a critical issue for low-RF energy transfer and suboptimal lesion formation [135, 172, 100], increasing the probability of producing an ineffective lesion. Conversely, high electrode-tissue CF may substantially increase the risk of steam pop and cardiac perforation. Therefore, optimization of electrode-tissue contact not only can produce more effective lesions, but also prevents complications due to excessive force. The use of a CF guide appears to be associated with a higher success rate in the ablation of AF [105], with an optimal range of CF for durable PV isolation between 10–30 g [172, 171, 223, 104]. Moreover, the variability of the catheter contact throughout the cardiac cycle plays a role in the efficacy of lesion production. Constant or intermittent contact produces larger or smaller lesions, respectively, despite constant RF power and identical peak contact forces [183]. Remote magnetic navigation has been proposed as a method to overcome the problem of catheter stability [19].

Electrocardiographic-based lesion assessment

Because the real-time evaluation of pointwise lesion formation in the myocardium is not possible in clinical practice, intracardiac signal amplitude decrease and impedance drop during ablation are used as surrogate parameters to estimate the lesion dimensions [29, 177, 85]. Lesion dimension and quality are both crucial in determining the effect of ablation lesions. Small lesions tend to be more homogeneous, whereas large lesions have a more inhomogeneous aspect. This difference may theoretically be responsible for slow-anisotropic conduction and pro-arrhythmia [2]. Lesion quality can also not be directly evaluated and must instead be estimated by surrogate parameters such as post-ablation signal fragmentation and duration [97, 199].

Magnetic Resonance Imaging for RF scar evaluation

Over the last years, it has been proved that late gadolinium enhancement (LGE) cardiac magnetic resonance (CMR) imaging is able to identify RF-induced myocardial scar. Moreover, the correlation between LGE burden after the ablation and successful clinical outcome has been demonstrated. Therefore, delayed-enhancement CMR (DE-CMR) is considered a reliable tool to identify gaps in previous PVI and to guide re-ablation procedures. Previous studies have also investigated the optimal parameters needed to achieve transmurality, using quantitative DE-CMR analysis. However, lesion formation depends also on other parameters including the power delivered, temperature of the catheter tip, duration of RF delivery, and catheter stability.

4.2 Contact Force and Remote Magnetic Navigation: Acute Outcome Comparison

In this section we will compare CF- and robotic magnetic-guided PVI in patients with paroxysmal AF in terms of lesion formation during AF ablation (acute success) and sinus rhythm maintenance one year after the procedure using electrically-based surrogate parameters commonly recorded during the clinical practice.

4.2.1 Population characteristic

Between March 2014 and March 2016, based on a prospective non-randomized protocol, 44 patients with drug refractory paroxysmal AF underwent a circumferential PVI procedure. Patients gave written consent to participate in the study and were randomly divided into two groups: 22 patients were included in group 1 and underwent an ablation with the CF-guided irrigated Thermocool SmartTouch (ST) catheter, and 22 patients were assigned to group 2 and ablated with the magnetic irrigated Remote Magnetic Thermocool RMT catheter, guided by the Niobe Remote Magnetic Navigation system. Patients had no contraindications for magnetic navigation such an implantable cardioverter defibrillator, pacemakers or vascular clips. Patients were treated with effective oral anticoagulation therapy for at least 4 weeks before the procedure, and the absence of LA thrombus was confirmed by transesophageal echocardiography performed within 24 hours before the procedure.

Antiarrhythmic drugs and digoxin were discontinued for at least 5 half-lives. No patients were taking amiodarone. Table 4.1 summarizes the baseline characteristics of the patients enrolled in the study.

Table 4.1 Patient Characteristics

Parameters	**SmartTouch (22)**	**RMT (22)**	**p value**
Male	18 (82)	10 (45)	0.01
Age (years)	60±9	62±12	0.42
BMI	27.1±5.1	25±6.8	28
Atrial volume (ml)	99±22	103±24	0.78
Ejection fraction (%)	57±7	57±9	0.82
AF age (years)	5.5±4.9	4.1±3.5	0.30
Hypertension	14 (64)	14 (64)	1
Ischemic CM	1 (4)	3 (14)	0.30
Valvular CM	3 (14)	0 (0)	0.07
Dilated CM	1 (4)	0 (0)	0.30
Diabetes Mellitus	3 (13.6)	5 (23)	0.43
NYHA I	13 (60)	15 (68)	0.53
NYHA II	9 (41)	7 (32)	0.53
CHA_2DS_2-VASc	1.4±1.2	1.9±1.4	0.10

Values are presented as n (%) or mean±SD

4.2.2 Ablation procedure

Oral anticoagulation was not discontinued, and the procedure was performed under heparin infusion with an ACT $\geq$ 300 s. Cardiac catheters were introduced into the heart using 8 F sheaths in femoral veins. We used an octapolar catheter in the coronary sinus as reference. After a single transseptal puncture, the ablation catheter was directly introduced from the RA into the LA. If AF was present, sinus rhythm restoration was obtained by electrical cardioversion; subsequently, 3D anatomical mapping of the left atrium and pulmonary veins was performed with the CARTO 3 mapping system with resolution in the range of 14–16. PV ostia were defined by criteria based on fluoroscopy, impedance, and electrical activity. A 500-kHz ablation unit was used for ablation (Stockert EP shuttle, Biosense-Webster Inc., Baldwin Park, CA, USA). RF power settings were 35 W throughout the procedure; irrigation

flow was 30 ml/min during RF ablation, with a temperature limit of 43 °C; and every RF delivery was limited to 30 s at one location (without movement of the catheter). Ablation lesions were deployed on a point-by-point basis along a continuous line around PVs at a distance of at least 5 mm from the true ostium with the target of 30 s of RF application with a CF ranging between 10 and 30 g. The operator aimed to reduce, as much as possible, the distance between contiguous ablation points. Ablation data in terms of power, time, temperature and CF were obtained through CARTO VisiTag and were continuously recorded and visible to the investigator during the entire procedure. Catheter macro-movement was detected via fluoroscopy or CARTO 3, whereas micro-movement was defined as a paradoxical increase in electrogram amplitude post-RF ablation compared to pre-RF ablation. After PVI, a LASSO circular catheter was introduced into the LA and effective isolation was checked for each vein. Additional RF pulses were subsequently delivered to complete PV isolation if required.

Pulmonary veins isolation

Complete PV isolation was considered the final endpoint of the ablation procedure and was achieved in all patients by encircling the PV ostia and subsequent refinement guided by a LASSO catheter. Additional RF delivery was required to complete the PV isolation after encircling in 13 of the left superior pulmonary veins, 9 of the left inferior pulmonary veins, 9 of the right superior pulmonary veins and 14 of the right inferior pulmonary veins in both groups. There were no statistically significant differences in the PVI rate between the two groups after encircling or in the number of additional RF pulses required to complete PVI (Table 4.2).

Table 4.2 LASSO-guided PVI summary. For each vein, the number of patients in each group who required additional ablation after circular encircling and the median of the additional RF pulses delivered is shown. Statistical significance was not reached in any of the PV.

Pulmonary	**LASSO-guided PVI**			**Additional RF**		
Vein	SmartTouch	RMT	p value	SmartTouch	RMT	p value
LSPV	6 (27)	7 (31)	0.28	4±3	7±4	0.09
LIPV	4 (18)	5 (22)	0.24	9±2	8±4	0.42
RSPV	5 (22)	4 (18)	0.11	5±3	7±2	0.11
RIPV	8 (36)	6 (27)	0.35	6±3	5±1	0.57

Values are presented as n (%) or median±interquartile range

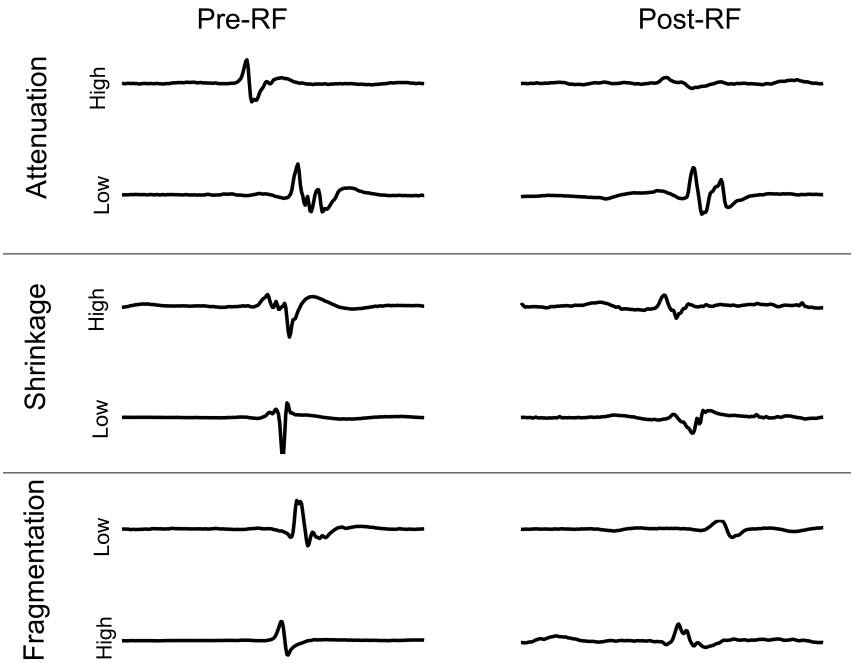

Figure 4.1 Example of signals before and after single-point RF ablation for signal-based lesion assessment criteria. For each criterion, an example of a high and low value is shown.

4.2.3 Lesion assessment criteria

Four different criteria were used to characterize the lesions in terms of dimension and quality; in particular, energy attenuation and impedance drop were used to assess lesion dimension, whereas signal fragmentation and shrinkage were used as surrogates of lesion quality. Figure 4.1 summarizes the signal-based parameters used for lesion assessment.

Lesion dimension surrogates

Signal energy attenuation Due to high variability in the peak-peak amplitude of the EGMs, the energy of the atrial signal was estimated as the sum in time over the squared amplitude of the bipolar and unipolar voltage recorded by the catheter tip. Energies of the local signals recorded before and after RF ablation were compared, and relative attenuation was measured.

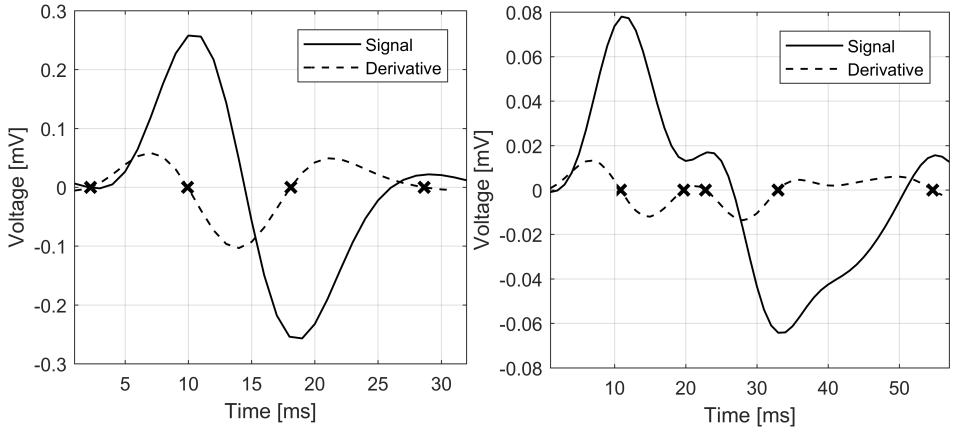

Figure 4.2 Example of fragmentation estimation before (left) and after (right) single-point RF ablation. Each plot shows the endocavitarian signal (solid line) and its derivative (dashed). Small crosses identify the zero-crossing of the derivative, corresponding to the changes of slope of the signal. Local increases or decreases in the number of deflections represent more or less fractionated waveform propagating under the catheter tip, respectively. The fragmentation index is obtained as the difference of numbers of zero-crossing.

Impedance drop The impedance values were measured between the ablation catheter tip and the ground using a 50 kHz current that was sampled at 10 Hz. Impedance values recorded before and after ablation for each RF pulse were compared, and the difference was measured.

Lesion quality surrogates

Signal fragmentation We measured the number of deflections of the signal before and after the RF delivery. To estimate the deflection of the signal, we computed the first derivative in the time of the pulse and we counted the number of zero-crossings, which can be interpreted as a change in the trajectory of propagation. Therefore, we denote the difference between the zero-crosses of the first derivative before and after the RF delivery as the fragmentation index. Figure 4.2 shows an example of fragmentation estimation of the pulses recorded before and after the RF delivery.

Signal shrinkage The shrinkage of the pulse was assessed, and its duration before and after RF ablation was compared. Every pulse was visually inspected by the operator to verify the correctness of the duration measured by the algorithm. In case of a questionable measurement, it was manually corrected or, if impossible, rejected.

Shrinkage was obtained as the relative variation of the duration of the pulse and is shown as percentages, with 0% indicating the same duration after RF ablation.

4.2.4 Results

A total of 2832 RF lesions were released in the group of patients (median 64.5 per patient, range 24-106); 283 RF lesions met the inclusion criteria (median 6 per patient, range 2-15). For each pair of signals recorded before and after RF pulse application, amplitude reduction, impedance drop, shrinkage and fragmentation were measured and relative variations were estimated by algorithms performing the same analysis on both groups. The mean force applied with an ST catheter was 15.9 $\pm$ 3.66 g. Table 4.3 shows a summary of the procedure parameters and the results of the analysis.

Table 4.3 Procedure and results summary

	SmartTouch	**RMT**	**p value**
Global Parameters			
RF Lesions	66 (29, 89)	61.5 (24, 106)	0.55
RF Time (min)	32.6 (16.2, 53.9)	26.2 (13.8, 53.9)	0.69
Mean CF (g)	15.91±3.66	-	-
Sinus Rhythm Maintenance at 1 year	77.2%	77.2%	
Analyzed Lesions			
RF Lesions	5 (2,12)	7 (2,15)	0.12
RF Time (s)	30 (25.91, 34.75)	29.4 (25.12, 34.61)	0.092
Bipolar Attenuation (%)	83.4±18.5	74.3±22.0	<0.001
Unipolar Attenuation (%)	73.7±14.3	67.6±18.8	0.007
Impedance Drop (Ω)	10.3±7.7	6.3±5.4	<0.001
Shrinkage (%)	-25.4±29.5	0.2±21.4	<0.001
Fragmentation	0.44±1.40	-0.12±1.0	0.007
Mean CF (g)	14.31±6.72	-	-

Values are presented as n (%), mean±SD or median (min, max)

Lesion dimension surrogates

Classically, the attenuation of the EGM has been used to evaluate the efficacy of a singular ablation. Unipolar and bipolar atrial EGM attenuation has been found to be associated with the transmurality of ablative lesions [69]. However, the extent to which signal attenuation must be pursued to obtain a transmural lesion had not been clear. Although in clinical studies a reduction in EGM amplitude $\geq$80% has often been considered an optimal target to achieve transmurality [169], other data show efficacy at lower levels of signal reduction, typically of approximately 60% [177]. Morphology changes in sinus rhythm EGMs occur together with voltage reduction in the case of bipolar signals as a consequence of local changes in activation and alterations in myocardial properties [150, 27]. Therefore, RF-related morphologic variation of the bipolar signal may impact peak-to-peak voltage reduction, which cannot be considered a reliable sign of a transmural lesion. To minimize the effect of signal morphology modification and exclude artefacts and noise, time-frequency analysis was used to identify and measure the variation in time and the global attenuation after RF delivery of the atrial signal. Figure 4 shows the lesion dimension surrogate parameter outcomes for the two catheters: signal attenuation is represented as a percentage between 0% (unaltered) and 100%, whereas the impedance is the real value measured by the catheter tip expressed in Ohm. The mean signal attenuation percentages obtained using ST and RMT were 77$\pm$18% and 64$\pm$24%, respectively ($p<0.001$), demonstrating the increased effectiveness of the ST in terms of the transmurality of lesion formation. Regarding the other lesion dimension surrogate, the mean impedance drop after ablation was 10.9$\pm$7.6 Ω and 8.7$\pm$5.5 Ω, respectively ($p<0.01$), for the ST and RMT catheter. These results suggest the increased effectiveness of the ST catheter in RF lesion formation in terms of dimension and transmurality.

However, as shown in Figure 4.3, it was impossible to assess a linear relationship between CF and signal amplitude reduction in the ST group, whereas impedance drop correlates weakly with CF ($p<0.01$). In a previous study, CF was shown to be a sensitive and specific parameter for the identification of transmurality based on EGM abatement [118]. Conversely, another group found that the amplitude of the EGM has a more variable response to ablation than impedance drop, and it may not be as useful as a surrogate for lesion formation, particularly in cases with a single point ablation [205]. Moreover, it has been determined that a higher mean CF is associated

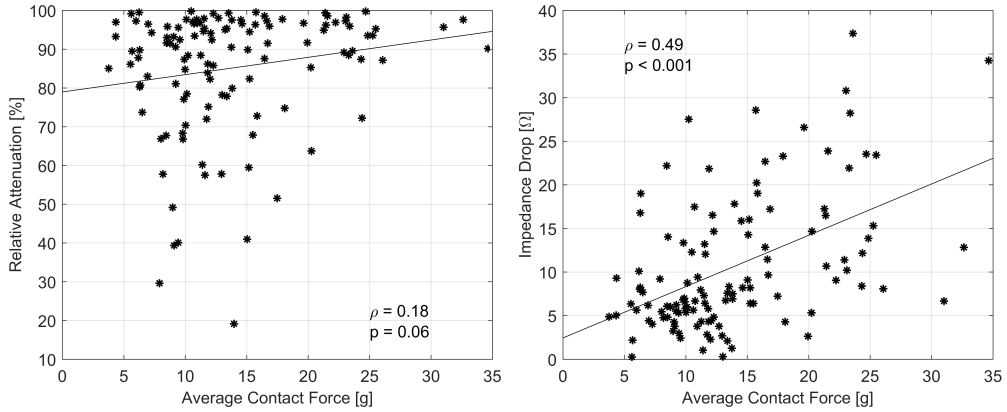

Figure 4.3 Correlation between average contact force and surrogate parameters related to lesion dimension. For each RF delivery, contact force is averaged and compared with the relative signal energy attenuation (left) and with impedance drop (right). Plots show very low correlation between energy reduction and CF, whereas impedance drop exhibits higher correlation with average CF.

with an increased CF variation over time, which can limit the positive effect of the higher force [206]. This behaviour is consistent with the lack of evidence of a linear correlation between AF ablation results and CF, whereas specific ranges of values correlate better with clinical results [172]. A clinical expression of plateauing exists in lesion formation; further increase in CF beyond a critical level does not coincide with better contact with the tissue.

Lesion quality surrogates

In contrast to what was observed regarding lesion dimension, the RMT approach performed better than ST in terms of lesion homogeneity, achieving higher signal shrinkage (0.2$\pm$21.4% and -25.4$\pm$29.5% $p<0.001$, respectively) and lower fragmentation indexes (-0.12$\pm$1 and 0.44$\pm$1.4, $p<0.001$, respectively). Post-ablation atrial potentials were shorter in duration and less fragmented in RMN-treated patients. Several studies have investigated the characteristic intracardiac signal, in terms of fractionation and width, in areas displaying diffuse or patchy fibrosis [106, 95]. According to the results, the fibrotic substrate induces a reduction of conduction velocity, i.e. an increase EGM width, independently on the fibrosis pattern. Analysis of electrogram fractionation showed that patchy fibrosis caused fractionation of the signal whereas diffuse fibrosis produced normally shaped with no effect on fragmentation. Clinical studies suggest that areas featured by long-lasting and fragmented

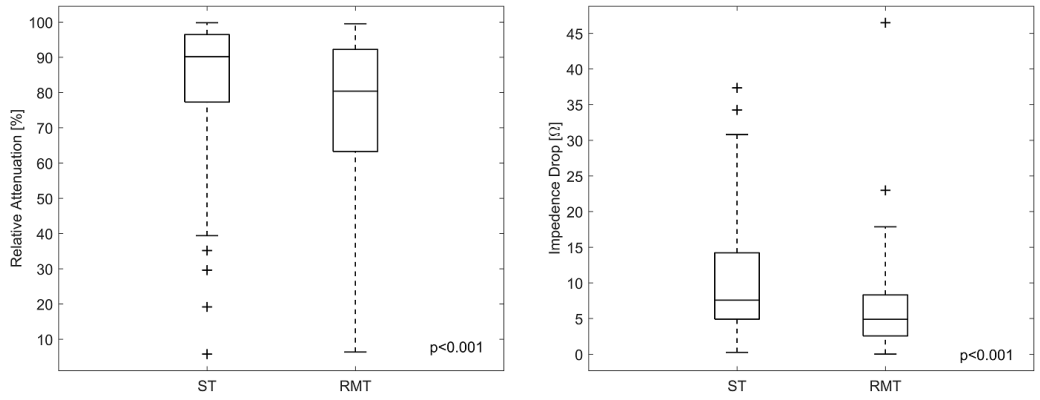

Figure 4.4 Comparison between RMT and ST using the amplitude reduction (left) and the impedance drop (right) as surrogates of RF lesion dimension. Relative attenuation is represented via percentage between 0% (unaltered) and 100%. Box plots show the median as the central mark, the edges of the box are the 25th and 75th percentiles, the whiskers extend to the most extreme values, and crosses are outliers.

post-ablation potentials may represent slow conduction pathways of the re-entrant circuit responsible for the pro-arrhythmic side effect of left atrial ablation [80, 102]. Several studies have also investigated the relationship between the fragmentation and duration of the atrial signal and the level of tissue fibrosis, which definitely affects the conduction properties of the signal [45]. The highly stable RMT catheter appears to be able to concentrate the RF energy delivery to a restricted area of tissue, producing a denser, albeit slightly smaller, scar that is less susceptible to pro-arrhythmia effects. Both the dimension and quality of the lesions were evaluated by two parameters: the consistent variation in voltage and impedance for lesion dimension and fragmentation and shrinkage for lesion quality represent a further validation of the study results.

Clinical follow-up at 1 year

The results of a clinical follow-up at 1 year were not better in the group of patients treated with an ST catheter compared to those treated with RMN. In fact, the percentage of patients who were free from AF was the same in the two groups (77.2% in both groups). Even if the number of patients is not sufficient to validate the comparison in terms of clinical efficacy, our results are consistent with a large observational study by Weiss et al. [213] in which comparative analysis of CF guided manual irrigated tip versus RMN catheters showed that the long-term outcomes are

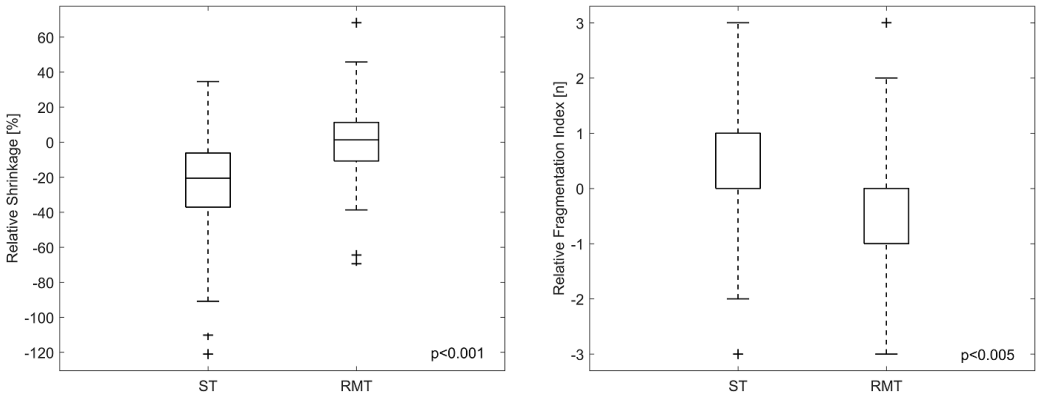

Figure 4.5 Comparison of lesion quality between RMT and ST. Relative shrinkage (left) is represented as percentages (0% unaltered, the higher the better). Relative fragmentation (right) is represented as pure numbers (0 unaltered, the lower the better). Box plots show the median as the central mark, the edges of the box are the 25th and 75th percentiles, the whiskers extend to the most extreme values, and crosses are outliers.

similar at 1 and 3 years. One explanation may be that signal attenuation higher than 60% was achieved by both approaches, a value that appears to be the critical threshold for transmural lesion formation. In a previous study, lesion characteristics and catheter behaviour were compared using an instrumented three-dimensional cardiac contact model in a dynamic beating-heart phantom with avian tissue substrate. The mean stability (deviation from an initial contact point) measured with a conventional catheter and the RMT catheter was 2.06 mm and 1.06 mm ($p<0.05$), respectively, at the same applied force. The results showed that RMN with CF equal to 10 g creates lesions with sizes equivalent to those related to the conventional catheter application of 40 g of force due to the superior intrinsic stability of the RMN [116]. Moreover, it has been shown that a stiffer sheath and catheter as well as a less compliant myocardial region, correspond to a higher CF variability for a given CF due to a higher sensitivity of the catheter tip with respect to the cardiac and respiration motion. The RMN catheter is equipped with a flexible stem with elastic properties capable of damping cardiac and thoracic movements, reducing the negative effect on tissue-catheter contact. The higher quality of the lesion probably enables the RMT catheter to compensate for the smaller dimension of the lesion compared to those produced by the ST catheter and may have contributed to the equality in terms of sinus rhythm maintenance in the two arms of the study. It should be noted that we analysed the signals from the first circular ablation session only. We did not analyse signals from the second lasso-guided ablation session because it was

necessary to apply RF pulses near sites where previous lesions had already been created. Nonetheless, the follow-up results are respondent to the signal analysis; in the second session, complete PVI was achieved in all patients without significant differences in the number of RF pulses between the two groups.

4.3 Relationship between Late-Gadolinium Enhanced Magnetic Resonance Imaging and Scar Formation

During RF ablation, the capability of producing an effective lesion depends not only on catheter-tissue CF but also on other parameters including the power delivered, temperature of the catheter tip, duration of RF delivery, and catheter stability. In this section we analyze the relationship between these parameters, with particular regard to the force-time integral (FTI), and the produced scar, assessed using magnetic resonance imaging with enhancing contrast. To collect the data we use CARTO VisiTag system, which allow the automatic filtering of the ablation information according to operator-selected thresholds.

4.3.1 Population characteristic

Between January 2016 and February 2017, based on a prospective non-randomized protocol, n = 10 patients (1 woman, 10%) with drug refractory paroxysmal AF underwent a circumferential PVI procedure. Patients gave written consent to participate in the study and underwent an ablation with the CF-guided irrigated Thermocool SmartTouch catheter (ST). Patients were treated with effective oral anticoagulation therapy for at least 4 weeks before the procedure, and the absence of left atrial thrombus was confirmed by transesophageal echocardiography performed within 24 hours before the procedure. Antiarrhythmic drugs and digoxin were discontinued for at least 5 half-lives. No patients were taking amiodarone. For each patient, pre-procedural and post-procedural DE-CMR scans were performed and analysed. Data analysis was performed on a total of 592 VisiTags (median 63 per patient, IQR 54-68). Table 4.4 summarizes the baseline characteristics of the patients enrolled in the study.

Table 4.4 Patient characteristics enrolled in LGE-CMR study

Parameters	**Patients (n=10)**
Male	9 (90)
Age (years)	50.8±9.5
BMI	26.2±2.8
Atrial volume (ml)	25.8±4
Ejection fraction (%)	60±5
Paroxysmal AF	10 (100)
AF age (years)	2.9±3.9
Hyperthyroidism	1 (10)
Coronary artery disease	1 (10)
CHA_2DS_2-VASc	
0	9 (90)
1	1 (10)
>1	0 (0)
Fluoroscopy time (min)	1.9±0.58
DAP ($\mu Gy\,m^2$)	33.9±21.2
Time of pre-procedural MRI (days)	10.5 (7.75, 34)
Time of post-procedural MRI (days)	126 (109, 154)

Values are presented as n (%), mean±SD or median (IQR 25% - 75%)

4.3.2 Cardiac magnetic resonance imaging

All patients underwent MRI study according to a standard protocol [7, 196]. MRI was performed according to standard protocols, using a 1.5 Tesla scanner (Philips Ingenia, Best, The Netherlands) and a 32-element cardiac phased-array coil and cardiac package. LGE-MR was performed 20 minutes after injection of 0.2 mmol/kg of gadolinium contrast agent (gadobutrol, Gadovist, Bayer Schering, Berlin, Germany) using a 3D inversion-recovery Turbo Field echo sequence with fat saturation, acquired on a four chambers view plane and a single breath hold in expiration. ECG gating was used and all images were acquired during the diastolic phase. Imaging parameters included: FOV 300mm, voxel size $1.5 \times 1.5 \times 3$ mm, 3 mm slice thickness, TR/TE 4 ms/1.28 ms, flip angle 10°. The optimal inversion time was set to null left ventricle myocardium with a look locker sequence (range: 240-330 ms). Typical scan time for the DE-MRI study was 5 to 9 minutes, depending on the subject's respiration and heart rate. Similar MR sequences were used for images acquired before ablation and between 3-6 months after the ablation.

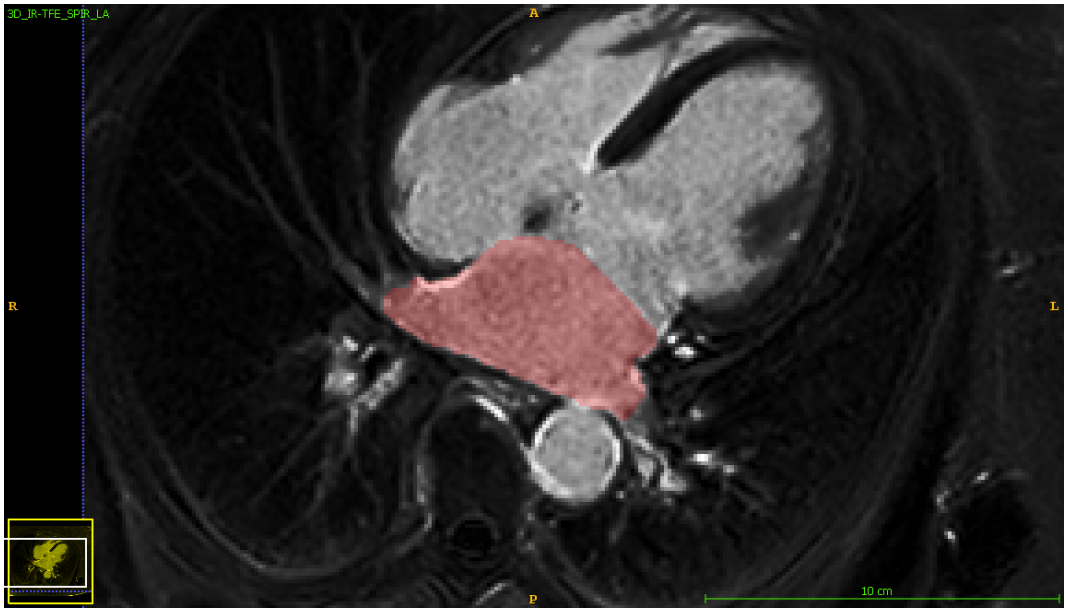

Figure 4.6 Axial plane of the high-resolution delay-enhancement cardiac magnetic resonance at the atrial level. LA is manually segmented in each slide and 3D shell is reconstructed for each level. Pixel intensity map is projected on the shell.

4.3.3 Image processing and late-gadolinium enhancement analysis

Three-dimensional visualization and segmentation of the CMR scans were performed with ITK-SNAP 3.6 [221]. Full LA volume and antral region of PVs were manually segmented in the axial orientation by an experienced operator blinded to the ablation procedures and clinical outcome. Three-dimensional shell was automatically reconstructed from the segmentation (Fig. 4.6). For measurement of LA enhancement, we used the image intensity ratio (IIR), defined as the mean pixel intensity of each sector divided by the mean pixel intensity of the entire LA blood pool [108, 50]. Pixel signal intensity maps obtained from DE-CMR were projected on the shell [112] and colour coded using an analysis software written in MATLAB (The Mathworks Inc, Natick, Mass). The extent of the fibrosis was quantified using a threshold-based algorithm [114, 166] where the threshold was set according to the mean pixel value in the region of interest (ROI), plus 1.5 standard deviations.

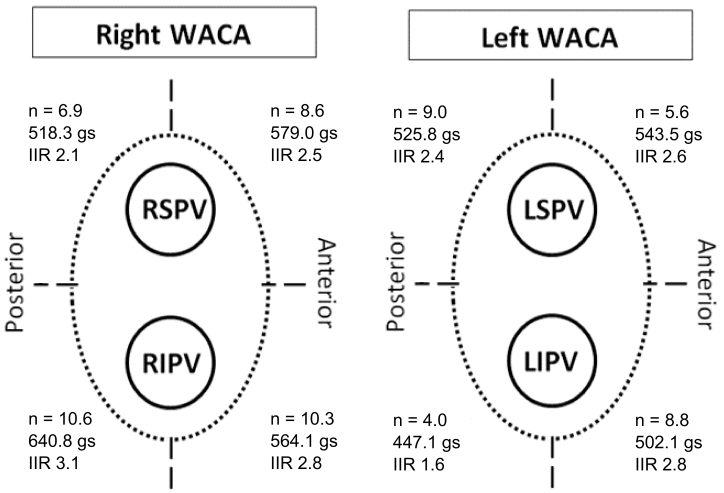

Figure 4.7 Segmentation of the left and right pair of pulmonary veins during ablation: anterior superior, anterior inferior, posterior inferior, posterior superior. For each ablation site, average number of lesions, FTI and IIR are shown.

4.3.4 Ablation procedure

The ablation protocol adopted in the study is similar to the one described in Section 4.2. In the following, we will recall it for the convenience of the reader, highlighting the main differences. Cardiac catheters were introduced into the heart using 8 F sheaths in femoral veins. We used an octapolar catheter in the CS as reference. After a single transseptal puncture, the ablation catheter was directly introduced from the RA into the LA to map the cardiac chamber. The pre-ablation tomographic imaging was merged with the CARTO 3 electroanatomical map using the CARTO-Merge system. Having available the high-fidelity anatomical information not only helps the physician to rapidly identify the anatomy and location of the PV and other anatomical structures, but also improves the safety and efficacy of the procedure. RF power was set to 35 W throughout the procedure, irrigation flow was 30 ml/min during ablation, with a temperature limit of 43 °C. Ablation lesions were deployed on a point-by-point basis along a continuous line around PVs at a distance of at least 5 mm from the true ostium with the target of 60 s of RF application and CF ranging between 10 and 30 g. The operator aimed at reducing, as much as possible, the distance between contiguous ablation points. For each patient, the ablation line around each pair of PV was divided in 4 sections. Ablation data in terms of power, time, temperature and CF were obtained through CARTO VisiTag and were continuously

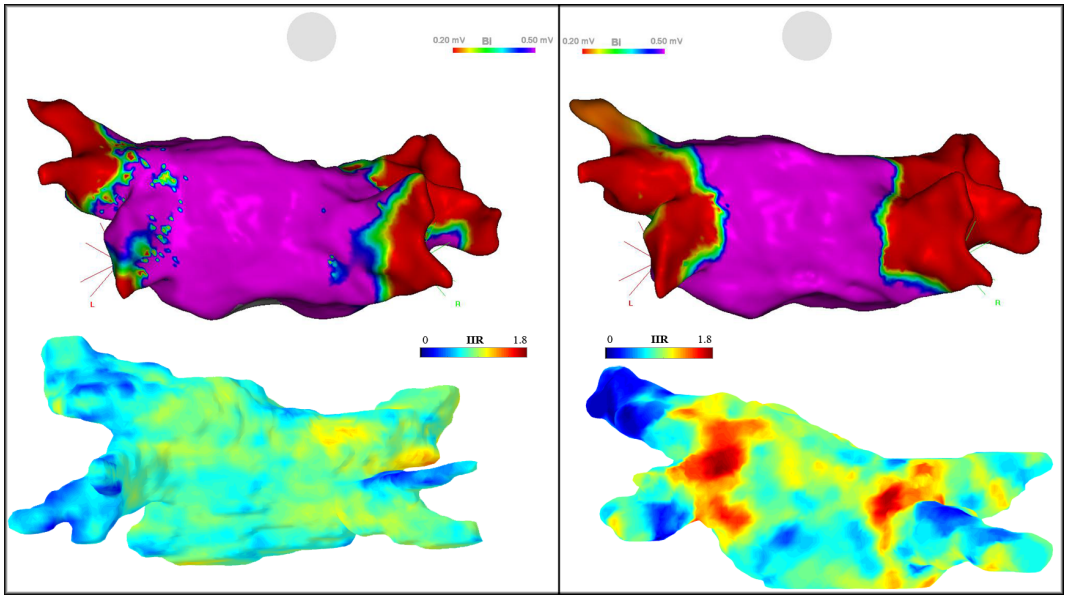

Figure 4.8 Comparison between voltage maps (above) and reconstructed MRI shells (below). Preprocedural MRI (left) and postprocedural MRI (right) are performed at most few days before and at least 3 months after the ablation procedure, respectively. Correspondent voltage maps are estimated at the beginning and at the end of the procedure.

recorded and visible to the investigator during the entire procedure. VisiTags appear only if stability, duration and CF thresholds are satisfied. Figure 4.7 shows the PV segmentation and summarizes the ablation data for each segment for all patients.

4.3.5 Pre-existent scar analysis and voltage map

Analysis of pre-ablation DE-CMR scans was needed to denote areas of pre-existent scar, potentially leading to misleading interpretation of the results. Pre- and post-CMR reconstructed 3D shells were registered using the Iterative Closest Point (ICP) algorithm [17] which computes the optimal affine transform for registering two surfaces represented as clouds of points. All the pre/post pairs of segments were compared by an algorithm to compute the increasing of LGE burden and visually inspected to exclude the one with pre-existent scar. Additionally, we visually compare the extent of scars before and after the ablation and the voltage maps obtained at the beginning and at the end of the procedure, respectively.

Median time between pre-procedural scans and ablation is 10.5 days (range 7.75-34 days). PV ostium are segmented according to procedure protocol and analysed.

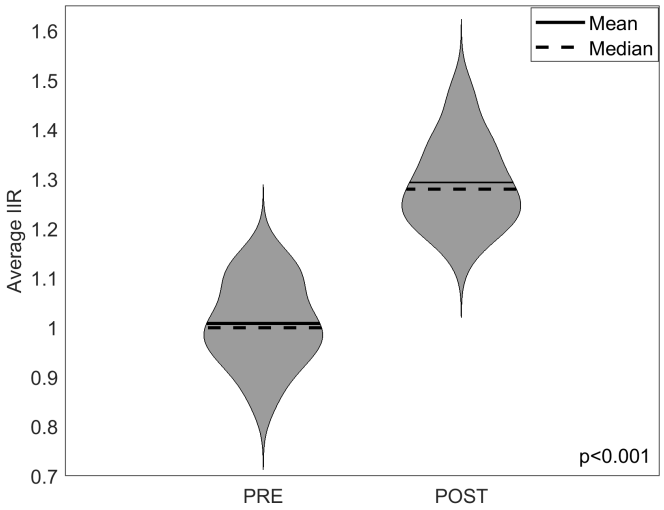

Figure 4.9 LGE burden before and after ablation procedure. The distribution of average IIR per vein increases significantly in the post-ablation MRI.

Pre-existent scars were found in 3 out 80 segments (3.75%). Figure 4.8 shows a representative example of comparison between electroanatomical maps and color-coded DE-CMR shells pre- and post-ablation. In many cases it was possible to associate high IIR zones with low or fragmented voltage areas on the map [148]. Moreover, the figure shows that average IIR in the LA significantly increased after ablation in comparison with baseline. Figure 4.9 illustrates the statistical summary of the LGE burden around the PV ostium pre- and post-procedure. IIR intensity averaged over all patients increases from 1 ± 0.08 to 1.27 ± 0.11 (p<0.001) after the ablation.

4.3.6 Post-procedural scar level and RF parameters analysis

During the procedure, VisiTags were labelled with unique numbers and, depending on their location, manually assigned to the correspondent section, chosen among the anterior/posterior pair of the four PV. For each section, RF delivery parameters are extracted from the corresponding group of VisiTags and averaged. We firstly investigated the correlation between FTI and impedance drop for each vein segment. Figure 4.10 shows that the two variables are strongly correlated, with correlation coefficient $\rho = 0.59$ ($p < 0.001$). This preliminary results suggest that, by combining contact force and duration information, FTI can be used to predict the effectiveness of RF delivery in lesion formation. To further verify our hypothesis, we will look for

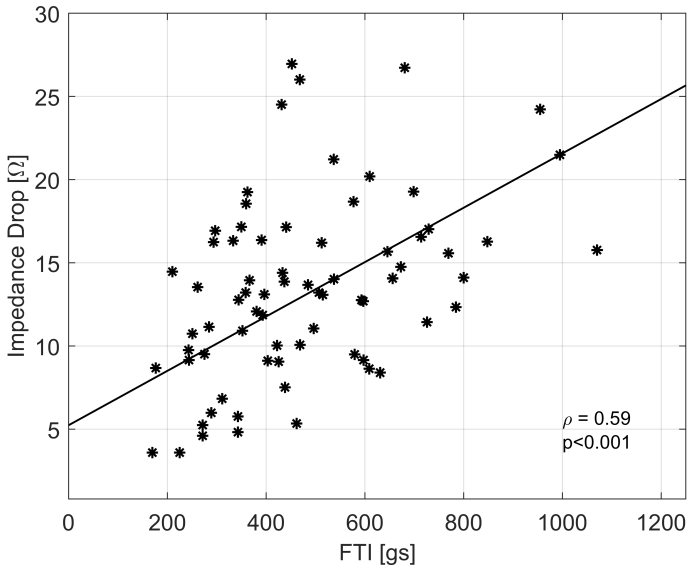

Figure 4.10 Correlation between FTI and impedance drop for each ablation site.

a relationship between high values of FTI and scar presence using LGE-CMR. All post-procedural CMR imaging were performed at least 3 months after the ablation procedure (median 126 days, IQR 109-154.5). We partition the PV ostium on the DE-CMR reconstructed shell in eight equivalent sections. We estimate the scar level by averaging the values of IIR per section and by discretizing it according to the 25%, 50% and 75% percentiles. We obtain four intervals, numbered from 1 to 4, corresponding to increasing lesion levels. Segments for which IIR was below the threshold were assigned to scar level 0.

Table 4.5 Patients-averaged PVI summary.

Pulmonary Vein		**FTI**	**Impedance Drop**	**Number of VisiTag**	**IIR**
RSPV	Anterior	535.72±311.89	14.07±5.66	8.4±3.8	2.5±1.2
	Posterior	505.4±206.07	9.44±4.16	7±3.4	2.2±1.3
RIPV	Anterior	537.83± 266.8	12.25±3.75	11± 5	2.5±1.4
	Posterior	608.28±250.76	15.99±6.88	10.2±4.4	2.7± 1
LSPV	Anterior	566.71±256.02	14.01±3.46	5.3± 1	3±1.3
	Posterior	537.03±193.98	17.26±6.21	9.2±2.7	2.6±1.1
LIPV	Anterior	502.06±351.76	15.89±9.71	8.8±5	2.6±1.4
	Posterior	398± 333.7	12.54±9.04	4.9±4.7	2.1±1.3
p value		0.21	0.17	0.37	0.94

Values are presented as mean±SD.

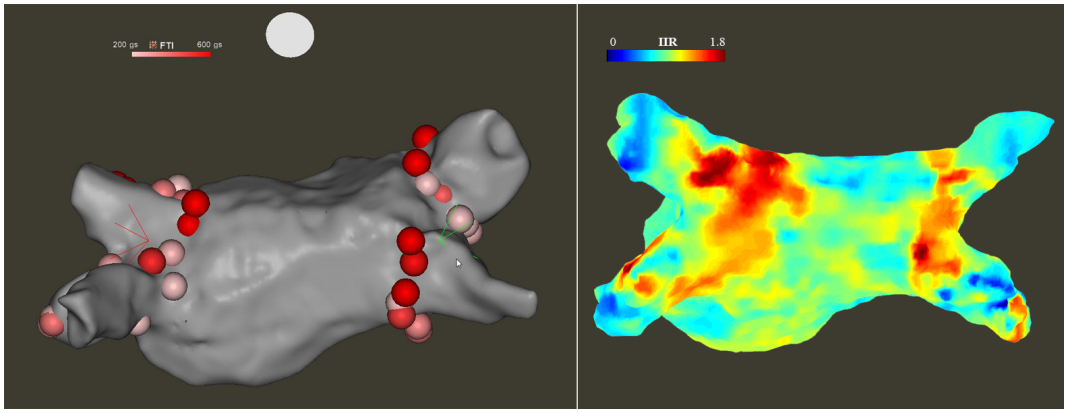

Figure 4.11 Correlation between lesions location and IIR. 3D electroanatomical map (left) shows the position of the VisiTag with associated FTI values. The left atrial shell (right) is derived from CMR scans and IIR values are projected on the nearest pixel. The positions of VisiTag with higher FTI correspond to zones with higher IIR.

Values belonging to the same segment are averaged among the patients to validate the data excluding deterministic bias in the PV ablation. Statistical analysis of the PVI summary for all the patients in Table 4.5 shows that there are not statistically significant differences between the PV segments in terms of FTI, impedance drop, number of VisiTags and IIR. In Figure 4.11, an example of electroanatomical map with VisiTag for a patient shows the PVI encircling on the left and DE-CMR reconstructed shell with color-coded IIR on the right. Similarly, in most of the cases it was possible to visually correlate the PV segments associated to VisiTags having higher FTI with areas characterized by high values of IIR.

The left plot in Figure 4.12 demonstrates the correlation between FTI and the scar level for each segment of the PV. It shows that it is possible to identify a threshold value at 400 gs under which the effectiveness of the RF delivery is very low, since the vast majority of lesions are in the first two groups. Conversely, FTI values above 600 gs guarantees the creation of a lesion that is still present after at least 3 months from the ablation procedure.

During this study, we had the possibility to conduct the same analysis using as predicting variable of scar formation the Ablation Index parameter, recently included in the CARTO VisiTag module. As explained in Section 2.1.1, Ablation Index gathers information regarding catheter-tissue CF, RF power and ablation time, and provides a single number to the operator. Together with CARTO VisiTag stability filter, Ablation Index aims at being as predicting as possible regarding the effectiveness

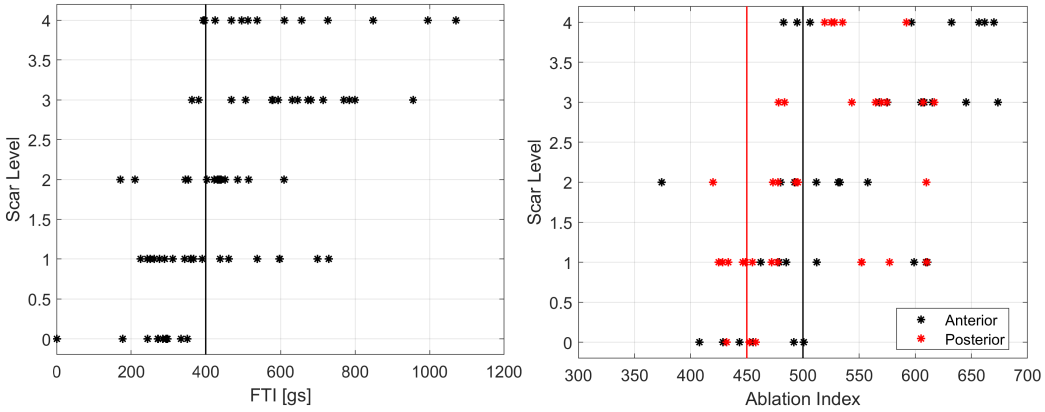

Figure 4.12 Correlation between average FTI (left), Ablation Index (right) and quantized scar level per ablation site. Level 0 corresponds to areas with IIR below the threshold differentiating healthy tissue from scar. IIR values above the threshold are grouped in four levels using 25%, 50% and 75% percentile. A level of 3 or 4 denotes the presence of scar, whereas a value below 2 corresponds to very low IIR. It is possible to identify approximately the value FTI = 400 gs as threshold for scar formation, whereas 450 and 500 are the Ablation Index threshold for scar formation on posterior (red) and anterior wall (black), respectively.

of RF delivery. Since the operator was blind to Ablation Index value during the procedure, we can consider this part of the study retrospective. Our goal was to verify if our results are in agreement with the Ablation Index values suggested in literature. Figure 4.12 shows on the right the chart relating the scar level with the Ablation Index, indicating with different colors whether the point was on the posterior (red) or anterior (black) wall. Similarly to the FTI case, the results show that it is possible to identify the Ablation Index thresholds for the posterior and anterior at 450 and 500, respectively, which are similar to those proposed in the literature.

Chapter 5

Substrate Analysis

Part of the work described in this chapter has been previously published in Grossi, S., Grassi, F., Galleani, L., Bianchi, F., Sibona Masi, A. and Conte, M. R. (2016), Atrial Conduction Velocity Correlates with Frequency Content of Bipolar Signal. Pacing and Clinical Electrophysiology, 39: 814–821.

5.1 Introduction

Conduction velocity (CV) is a fundamental substrate parameter influencing atrial arrhythmias. In diseased atria, tissue fibrosis, abnormal membrane excitability and cell coupling reduce conduction wavelength thus favoring reentrant circuits through reduction of CV [4, 192, 111, 64]. The knowledge of CV distribution on the atrial surface would be critically useful for the construction of velocity related substrate maps [120].

Experimental and modelling studies have investigated the determinants of conduction velocity, by looking at the changes of the action potential in different conditions. Among several mechanisms, experimental evidences show that CV depends on the heart rate and typically it decreases at higher rates. In this chapter we hypothesize that in human atria the frequency content of the bipolar signal, recorded from the endocardial surface, is related to CV and its spectral compression during decreasing pacing cycle length (PCL) stimulation could serve as a marker of anisotropic distribution of CV. We demonstrate the correlation between the spectral centroid and the CV in several settings and using different approaches.

5.1.1 Related work

Although anisotropy in conduction velocity is a key substrate abnormality feature, CV measurements in humans are difficult [84] and no direct CV measurement has been performed so far with the available electroanatomical mapping systems, with the exception of the time consuming calculation from the local activation time [46, 113, 182, 65]. Several methods have been investigated for the CV estimation, ranging from signal voltage [94], to wavefront modelling [174, 212]. For a complete review of techniques for automated local activation time annotation and conduction velocity estimation we refer the reader to [31].

Conduction velocity and frequency in human muscle fibers

In human muscle fibers, CV and frequency content of the surface electromyogram (EMG) signal are directly related. Over the past years, several studies aimed at characterizing the conduction velocity in human muscle fibers, leading to a deeper understanding of the mechanism involved in the propagation of the electrical impulse along the conductive cells of the skeletal muscles [98, 59, 140]. It is well documented that muscle fiber conduction velocity reflects the modifications of the properties of the neuromuscular system as a consequence of pathology [49, 48], fatigue [138] or pain [58]. The analysis of the surface electromyogram revealed that a strict correlation seems to exist between conduction velocity and changes in the EMG amplitude and power spectral density [202, 55, 6, 119]. Therefore, monitoring changes in the frequency spectrum of the surface EMG has become a popular method to estimate muscle fatigue during various types of muscle contraction. Different estimators have been developed, such has median frequency [87], spectral compression [128] or spectral multidip approach [60], but independently from the used estimator, almost all studies report that in the skeletal muscle, such as brachioradialis biceps or abductor pollicis brevis muscle [10], when the CV increases also the reference frequency of the signal increases, and the spectral compression grows [21].

5.2 Study protocol and methods

5.2.1 Rate-dependent conduction velocity restitution

Increased heart-rate, for example during intense physical activity, affects relative durations of systole and diastole to ensure correct filling of the chambers and consequent efficient blood pumping. At cellular level, if an action potential starts too early after the preceding, not all ionic processes will completely recover to their resting states, therefore transmembrane current will be reduced and APD will be shorter. Moreover, when a sequence of pulses propagates along the tissue, the propagation speed and the action potential duration of each pulse mutually depend on one or several previous inter-beat intervals. This dependence is called restitution, and the rate-dependent changes in CV are called *CV restitution*. The AP duration and CV restitution curves are important determinants of conduction properties since they can be considered a first approximation of changes that occur in ionic currents in cardiac cells. The steepness of the restitution curves can affect the stability of a re-entry pattern [64, 220]. During in-vivo experiments effective refractory periods are difficult to determine, therefore CV restitution is also expressed as the relation between CV and preceding pacing cycle length [211].

5.2.2 Population characteristics and procedure protocol

The study can be organized in three steps. At each step we search for the correlation between the CV and the characteristic of the frequency spectrum of the intracardiac signal in a different and increasingly complex domain, from the tubular shaped CS, to the atrial wall, and finally to the whole atrial chamber. For the first step, fifteen patients affected by supraventricular arrhythmias without overt structural heart disease were submitted to standard EPS and ablation of the index arrhythmia performed in a single session in the fasting, unsedated state and after discontinuation of all antiarrhythmic drugs for at least five half-lives. Written informed consent for EPS and ablation was obtained from each patient. Two quadripolar catheters were inserted via the femoral vein at the right ventricular apex and in proximity of His bundle. An octapolar deflectable catheter was inserted into the coronary sinus. Patients in whom isoproterenol infusion was necessary for the arrhythmia induction were not enrolled in the study. After clinical arrhythmia had been properly diagnosed

and definitively cured by ablation, velocity measures were performed. In the second step, we looked for the CV-frequency correlation in one patient with paroxysmal AF, using the LASSO catheter, taking advantage of its circular shape. After performing PVI and assessing electrical isolation with the LASSO, the catheter was placed on the posterior atrial wall to perform the measurements. In the last step, we conduct our study in one patients enrolled for RF ablation of AF using the RhythmView system and the FIRMap basket catheter. CV protocol was applied before starting the ablation, to avoid conduction impairment due to the RF-induced scars in the areas marked as rotors.

The EGMs were recorded at sampling frequency of 1000 Hz and with voltage range 2 mV and exported with BARD® LABSYSTEM™ PRO EP Recording System (C.R. Bard, Inc., a Boston Scientific company, Lowell, MA). During the acquisition, intracardiac signals were filtered using a combination of low pass and high pass filters with cut-off frequency respectively of 30 Hz and 250 Hz and an adaptive notch filter for the power line interference cancellation. Measurement protocol was based on incremental pacing (Biotronik UHS 3000, stimulus amplitude twice the threshold, 1 ms pulse width) that was always performed from the CS catheter, possibly from both the catheter extremities. The initial PCL of 600 ms was stepwise decreased to 500, 400, 300, and 250 ms. Pacing was performed only if 1:1 capture in sinus rhythm was always present.

5.2.3 Signal analysis

High voltage spikes on the stimulation dipole were considered as the starting time instants for pulse extraction. Due to the pacing pulse strength, the pacing far-field was also detected by the other dipoles of the catheter few milliseconds after the onset of the pacing pulse. Since these spikes could impair the correct wavefront detection, the first 10 milliseconds of the signal were removed from the analysis. In order to reject signals not captured or corrupted by artifacts, a mean pulse was first calculated averaging all the available pulses. Each pulse in the sequence was then compared with the mean pulse and rejected if its sample correlation coefficient was below a given threshold.

The Botteron preprocessing algorithm was used to emphasize the timing of the atrial activation and to enhance the periodicity or non-periodicity of the signal. The

Teager-Kaiser energy operator was used to estimate the energy of the intracardiac signal. The output produced by the TK operator was filtered with a Gaussian low-pass filter with cut-off frequency of 25 Hz, which is compatible with the physiological frequency range of 0-20 Hz. The Gaussian filter smooths out effectively the abrupt variations of the TK output.

5.3 Linear Octapolar Catheter in the Coronary Sinus

In this section, we assess the existence of a strict correlation between CV measured in human atria and the frequency content of the local bipolar signal. The activation times of the signals recorded by an octapolar catheter positioned in the CS were used to measure CV during incremental pacing. CS was chosen because of anatomical features enabling catheter stability and the presence of atrial signal.

5.3.1 Conduction velocity and spectral centroid estimation

Estimation of the CV was performed as the ratio between the distance Δs travelled by the propagating pulse and the propagation time Δt. The electrodes have size 1 mm (besides the first one of size 2 mm) and they are separated by steps of 2 and 10 mm, therefore the total distance is Δs=47 mm. The high-voltage peaks were identified on the pacing channel and the recorded pulse was extracted using a window of length between 90 and 120 ms starting immediately after the pacing pulse. Then, the propagation time Δt was estimated by using the Botteron preprocessing algorithm and the TK operator. The Botteron preprocessing algorithm was used to make the energy profile more robust with respect to variations of the signal morphology. Then, the activation time was obtained as the barycenter of the filtered TK energy of the signal. The barycenter in time of the pulse is estimated as the mean time of the signal, computing the weighted average with respect to time using the absolute value of the TK energy as weight. Finally, the propagation time Δt was determined as the difference between the stimulus time and the activation time.

Frequency analysis of the bipolar signals recorded by the detection dipole of the CS catheter was performed. Data were windowed using a Hamming window centered on the activation times. The spectral centroid (SpC) of the pulse was calculated as the barycenter of the frequency spectrum of the signal. The barycenter

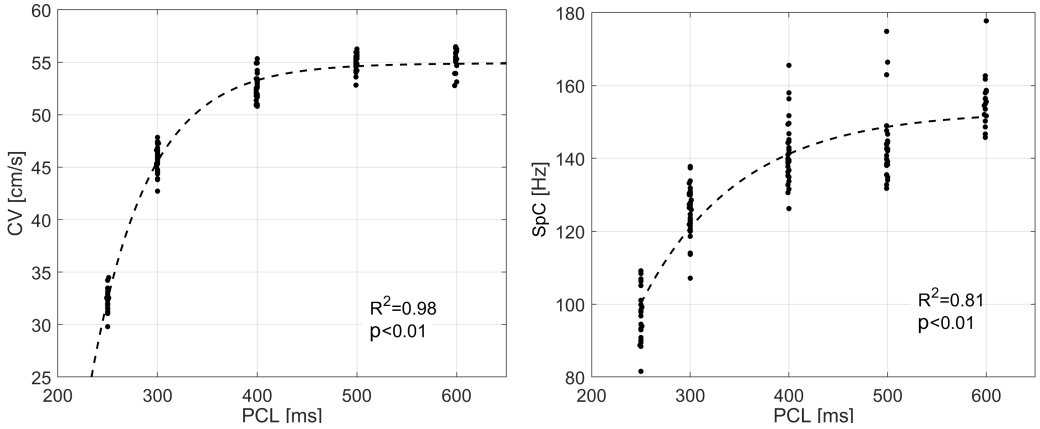

Figure 5.1 Restitution curves in patient 12: CV restitution (left) and SpC restitution (right). CV and SpC measurements (dots) and fitted curves (dashed) shows the expected physiological behavior of myocardial conductive fibers.

in frequency, also called spectral centroid, is computed as the weighted mean of the frequency with the corresponding magnitudes of the spectrum distribution as the weights.

5.3.2 Electrical restitution at different heart rates

We were able to obtain the typical restitution curves with the inverse relationship between CV and PCL predicted by the physiological model of myocardial fibers. Two sequences of paired CV and SpC measurements, associated to the direction of propagation, were obtained for each patient, by pacing from CS dipole 1-2 and 7-8, respectively. CV and SpC were processed by a moving average to attenuate the oscillations due to the recording noise and were plotted as a function of PCL in order to obtain restitution curves. CV and SpC restitution curves were estimated for every patient (single restitution curve) and from the data of the whole group of patients (average restitution curve) to investigate the adherence of restitution to the expected physiological behavior. To assure steady-state condition, 23 ± 10 beats per bin were recorded for every PCL. Each inter-beat interval was calculated as the time difference with respect to the previous event. To quantify rate-dependent changes, data were binned with the pacing intervals approximately at the center of the bin. Five bins separated at 230, 270, 350, 450, 550, and 650 ms were obtained. The results were statistically analyzed by calculating, for every bin, the mean CV, the mean SpC, and the standard error of the mean.

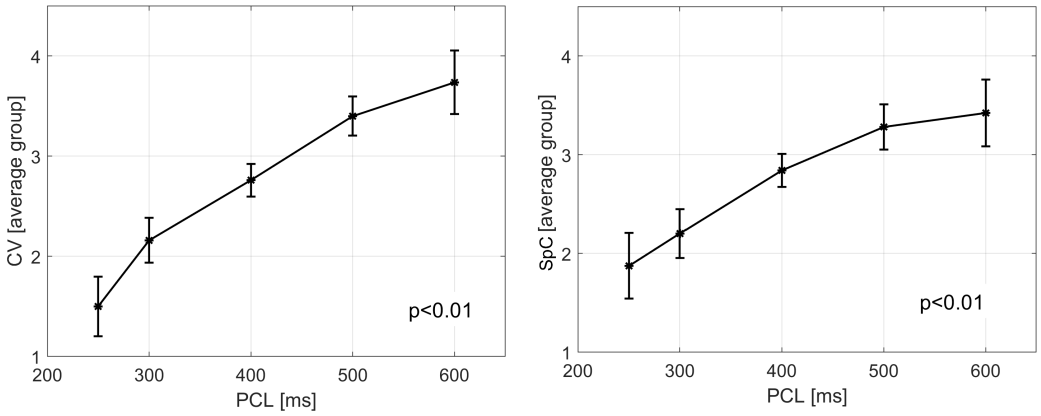

Figure 5.2 Average restitution curves: CV restitution (left) and SpC restitution (right). CV and SpC groups of all patients corresponding to the same PCL are averaged. Average groups (dots) are shown and trend (solid) is emphasized. Bars represent the standard error of the mean of each group.

CV typical restitution curves were paralleled by SpC restitution curves. Figure 5.1 shows an example of CV restitution for patient 12. In this case, CV was 55 cm/s for a PCL of 600 ms, and 32 cm/s for a PCL of 250 ms. Similar decrease was found also in the SpC behavior. The inverse relationship between CV/SpC and PCL was confirmed by average curves (Fig. 5.2), obtained using the quintiles grouped values of the whole population: CV/SpC decreases as PCL decreases, with a constant slope curve between 600 and 300 ms. Between 300 and 250 ms, the restitution reduction is greater as in the case of the single restitution curve. The average curves are flatter than the single curves due to the linearization effect of the quintiles velocity grouping method.

5.3.3 Correlation between velocity and frequency

A highly significant correlation between CV and SpC was observed in every single patient. Table 5.1 summarizes the patients characteristic and provide a statistical summary of the results: the average correlation coefficient is very high for both directions of propagations, with a p-value denoting statistical significance ($p<0.001$). It is possible to notice that the correlation was slightly lower in the case of pacing site CS 1-2. This is probably due to the non-physiological travelling path of the wavefront forced by the pacing site. The correlation was confirmed for the group

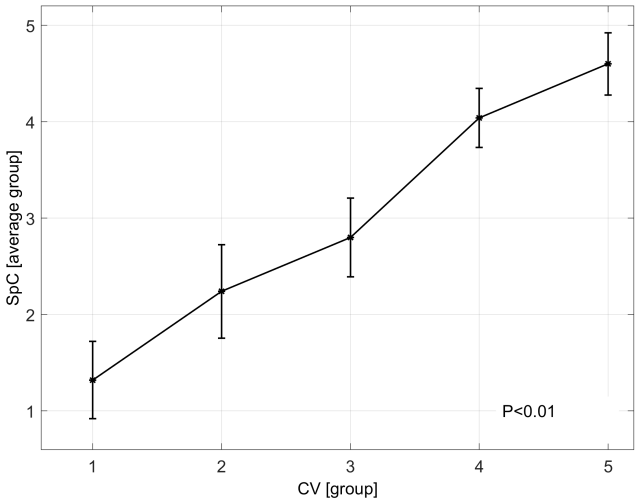

Figure 5.3 Correlation diagram between different groups of CV and SpC. The SpC indexes of all the patients corresponding to the same CV indexes are averaged. Average groups (dots) are shown and trend (solid) is emphasized. Bars represent the standard error of the mean of each group.

analysis, as shown in Fig. 5.3. CV and SpC were expressed in quintiles to overcome the variability of the inter-patients absolute values.

Table 5.1 Patients characteristic and results summary

Parameter	**Patients (n=15)**	**p-value**
Male	8 (53)	
Age (years)	48.4 ± 19.7	
Diagnosis		
AVRNT	7 (47)	
WPW	8 (53)	
Correlation CV-SpC		
CS 1-2	0.75 ± 0.25	< 0.001
CS 1-8	0.88 ± 0.1	< 0.001

Values are presented as n (%) or mean±SD

AVRNT: Atrioventricular Nodal Reentrant Tachycardia

WPW: Wolff–Parkinson–White syndrome

As a consequence of their strict correlation SpC can be used as a marker of local CV. Figure 5.4 (left) compares the frequency distributions of the bipolar signals obtained by pacing with PCL of 600 ms and 250 ms. The plot shows a vertical

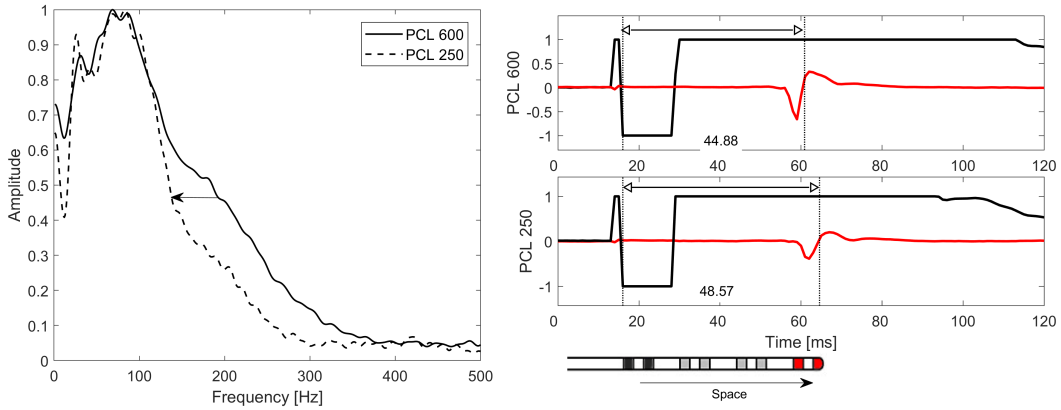

Figure 5.4 Intra-atrial activation delay at different PCL and spectral compression of captured bipolar signals. (left) Frequency distributions of the captured signals (grey curves in panel B) at PCL 600 ms (solid) and PCL 250 ms (dashed) with normalized amplitudes. The arrow shows the reduction of the barycenter of the spectra, which are 133 Hz for PCL 600 ms, and 115 Hz for PCL 250 ms. Bipolar signals recorded at CS 7-8 and CS 1-2 (right). The black signal is the stimulus paced by the black dipole. The grey curve is the signal captured by the grey dipole. The arrow indicates the direction of propagation and the space traveled by the pulse. Delays are evaluated as the difference between activation times. Propagation times are 48.57 cm/s at PCL of 600 ms, and 44.88 cm/s at PCL of 250 ms.

line corresponding to the barycenter of the frequency distribution. It is evident that increasing the pacing frequency by 60% results in a spectral compression of about 15%. This happens because smaller PCL implies smaller CV, and, consequently, a smoother signal, as it can be seen by comparing the two plots on the right in Fig. 5.4 corresponding to the two cases. Since the frequency content of a smoother signal is more concentrated in the lower part of the frequency axis, we observe a bandwidth reduction for the case PCL 250 ms.

5.4 Circular Decapolar Catheter on the Left Atrial Wall

LASSO catheters comprise a ring of 10–20 electrodes, which is often variable in diameter, typically 15–25 mm, so they allow lower density recording of spatiotemporal information. Multipolar circular catheters are typically used during pulmonary vein isolation procedures in order to verify complete isolation. Their shape is intended to

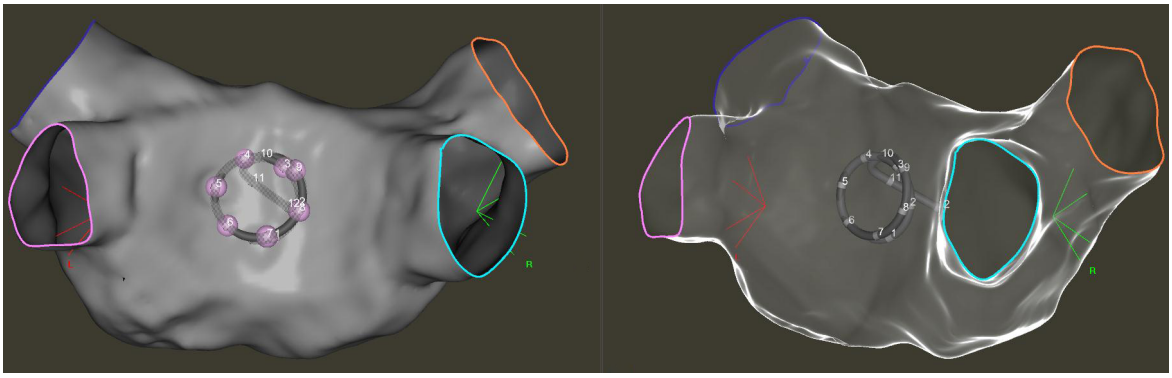

Figure 5.5 3D reconstruction of the left atrium obtained with CARTO 3 showing the position of the decapolar catheter during the recording.

help accurately mapping the pulmonary anatomy and identify the sleeves of myocardium that extend into the pulmonary veins, which are the pathways of aberrant electrical conduction.

In this section we extend the previous result obtained in the coronary sinus to the atrial wall, taking advantage of the shape of the LASSO catheter. During the EPS, the linear octapolar catheter was placed in the coronary sinus for pacing and CS 3-4 dipole was set as pacing site. LASSO decapolar catheter was positioned on the atrium wall. Figure 5.5 shows the 3D reconstruction of the left atrium obtained with CARTO 3 showing the circular catheter during the recording.

5.4.1 Propagation parameter estimation

A method to analyze the complete activation pattern comprising the whole set of catheter electrodes is presented in [212]. It is based on the assumption that the activation pattern $t(n)$ of a plane excitation wavefront that travels across a circular catheter can be described by a sinusoidal curve. The activation sequence is modelled as a cosine function

$$t_i = t_c - A\cos(\varphi_i - \varphi_0) = t_c - A\cos(\gamma(i-1) - \varphi_0) \qquad i = 1.5, 2.5, \ldots \qquad (5.1)$$

where i denotes the virtual electrode standing for the catheter dipoles, t_c represents the center activation time, φ_i is the angle at which the virtual electrode i is placed, and φ_0 describes the angle at which the earliest activation occurs. Assuming that $\varphi_{1.5} = 0°$, φ can be expressed as $\varphi(n) = \gamma(n-1)$, where the parameter γ describes

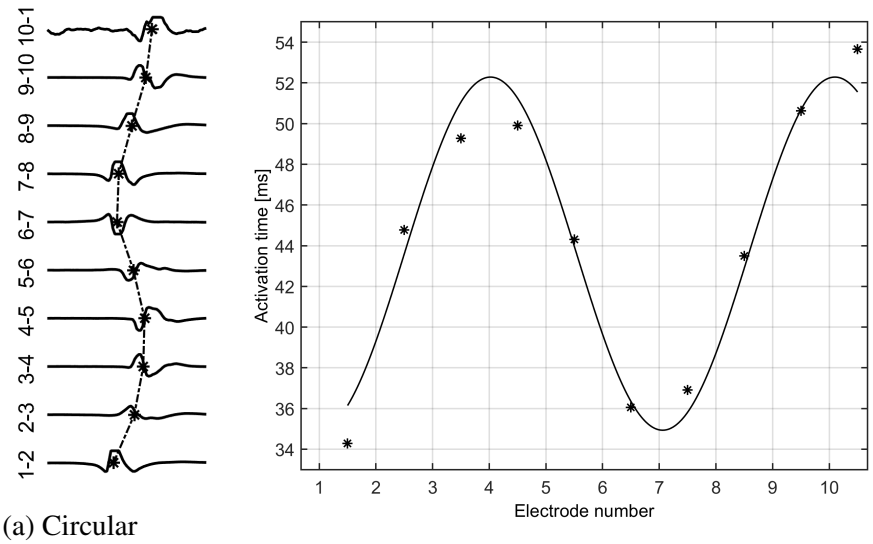

(a) Circular catheter signals

(b) Cosine fit of activation time

Figure 5.6 Analysis of signals during stimulation from CS 3-4 catheter.

the angle offset between two neighbour electrodes. Figure 5.6a shows an example of LASSO activation during pacing, validating the assumptions of the model.

The three unknowns t_c, A and φ_0 are estimated for each activation sequence through nonlinear least squares algorithm. The initial values and boundaries are derived from the parameters and mapped positions of the catheters. The incidence angle φ_0 represents the wave direction, while the CV is calculated from the catheter radius r and the cosine amplitude A as $\text{CV} = r/A$. The result of the fitting for one pulse is depicted in Figure 5.6b.

5.4.2 Wavefront feature extraction

The LASSO catheter records simultaneously 10 bipolar signals, therefore for each pulse we estimate the spectral centroid as in the case of the linear catheter, whereas the conduction velocity has the same value for the whole catheter, because it is evaluated using the cosine model (5.1). Since the radius of the LASSO catheter can be manually adjusted by the operator during the procedure, we need to estimate it during the stimulation. For example, Figure 5.5 shows the case in which the catheter is folded on itself. The catheter radius can be obtained once again exploiting the particular shape of the catheter and the knowledge of the electrodes positions in the space. We exported the coordinates of the electrodes from the CARTO 3 mapping

Table 5.2 Sample correlation coefficient between CV and spectral centroid for each sequence recorded with circular catheter.

Electrodes	$\rho_{CV,SpC}$	**p-value**
LASSO 1-2	0.472	<0.001
LASSO 2-3	0.722	<0.001
LASSO 3-4	0.691	<0.001
LASSO 4-5	0.820	<0.001
LASSO 5-6	0.764	<0.001
LASSO 6-7	0.659	<0.001
LASSO 7-8	0.296	<0.001
LASSO 8-9	0.660	<0.001
LASSO 9-10	0.687	<0.001
LASSO 10-1	0.707	<0.001

system and we fit a circle based on those coordinates. The estimated radius can be used to estimate the CV.

After obtaining the sequences of CV, we can correlate them with the estimated SpCs for each channel. The statistical analysis in Table 5.2 shows that the correlation coefficients are positive with a statistically significant p-value for all the electrodes of the catheter. Together with CV estimates, circular catheters and cosine fit model enables estimation of the angle of arrival of the wavefront, as well as the offset angle between the dipoles on the catheter. In our case the whole circle is constituted by 6 dipoles and $380^\circ/6 = 63.3^\circ$ and from the fit we obtained $\gamma = 60.6 \pm 0.78^\circ$. Assuming $\varphi_{1.5} = 0^\circ$, the direction of arrival of the wavefront φ_0 can be obtained from the fit, giving $\varphi_0 = -0.7751 \pm 8.3015^\circ$. By looking at the catheter position, since the first electrode of the LASSO catheter approximately faces the pacing dipole of the CS catheter, a slightly negative result is acceptable. Another noticeable feature is the high dispersion around the mean value. This can be justified considering that the impulse has to propagate along a nonphysiological path, across different fibers oriented along different directions. As a consequence, the wavefront propagation may change during the stimulation, impairing also the correlation between CV and SpC.

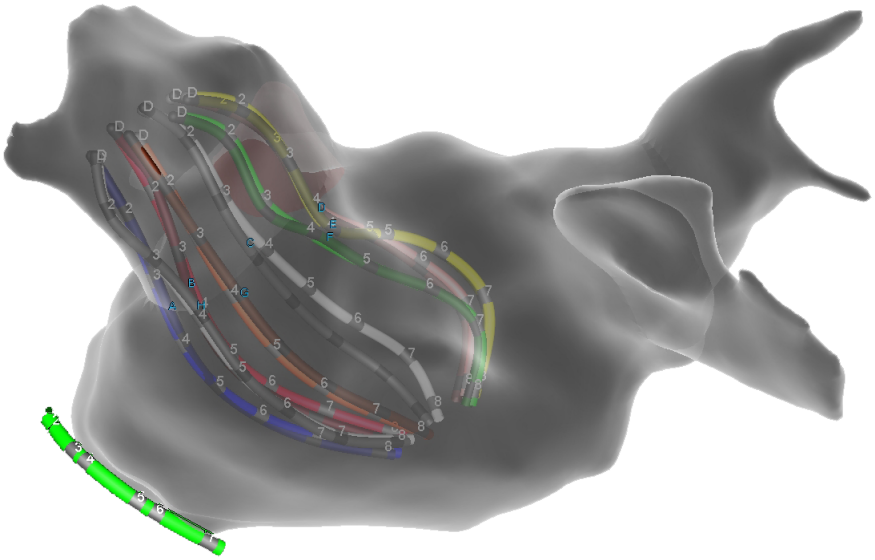

Figure 5.7 3D reconstruction of the left atrium obtained with Ensite Precision, showing the positions of the basket catheter and the CS catheter.

5.5 Basket 64-Polar Catheter in the Left Atrium

In this section we try to extend the previous results to the more complex case of signals recorded by the basket catheter placed in the left atrium, validating therefore our model for the generic case of signal recorded in the left atrium, and not only in the CS or the atrial wall. By proving that the spectral centroid of the intracardiac signal recorded in a generic atrial location and the local CV at the same location are strongly correlated would enable the physicians to estimate panoramic CV maps using multi-electrode catheters. By pacing at different PCL, we could obtain insightful maps of the CV variability at different heart rates by mean of the SpC, without directly computing the CV in the whole atrium. We straightforwardly apply the method of the linear octapolar setting in the CS with some minor modifications. As before, the stimuli were delivered from the electrode 3-4 of octapolar catheter placed in the CS, whereas the tissue physiological response was recorded by the electrode of the basket catheter in the left atrium (Fig. 5.7). Due to the distance between the electrodes of the catheter, we decided to use the unipolar instead of the bipolar signals. Traditionally, LAT of unipolar pulses is obtained by taking the point of maximum negative slope of the signal. CV is again obtained by dividing the distance between the pacing electrode and each recording electrode of the basket by the related conduction delay.

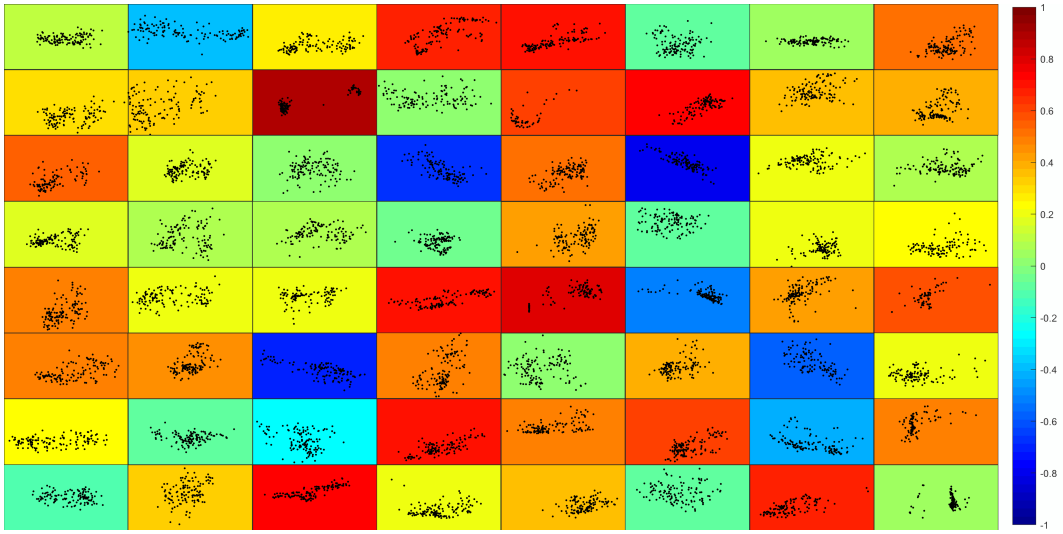

Figure 5.8 Correlation between CV and SpC for every electrode of the basket catheter. Average correlation is 0.22.

However, it has to be notice that, particularly in this case, the calculation of CV by means of the space-time ratio could be an excessive simplification. The wavefront propagates across the tissue, travelling from the CS to the atria and reaching the electrodes, therefore its CV is affected by the whole travelled path, whereas the SpC is supposed to be a local substrate parameter.

The proposed analysis justifies the poor results shown in Figure 5.8. The 8×8 matrix of scatter plots illustrates for each electrode the CV and SpC of the sequence of pulse recorded by that electrode. Each scatter plot has a background color that is a function of the correlation between CV and SpC depicted in the plot itself. The colorbar on the right shows the map between the correlation interval $[-1,1]$ to the colormap from blue to red. The average correlation coefficient for the whole dataset is 0.22 ($p < 0.001$). It is possible to notice that the two variables are in few cases strongly positively correlated, whereas most of the times the correlation is from 0.5 to 0. Unfortunately, in some cases the correlation appear to be negative. From preliminary analysis it seems that very low or negative correlation can be associated with strong signal interference, or low SNR.

Obviously, it is difficult to draw conclusions from one single experiment. However, the results suggest that the correlation under investigation has been found in the simple case of signals recorded in the CS and on the atrium wall, but unfortunately the case of generic multi-electrode recording is far from being completely understood.

The problem addressed is very difficult, due to the extremely variable conditions under which it has been analyzed, in particular during in-vivo procedures. Cardiac fibres are very complicatedly disposed, signal can propagate along multiple different paths and each of them has different conduction properties and activation time, since the number of myocytes per unit physical length can change. Furthermore, the attenuation caused by the muscles is practically unpredictable and not reproducible and changes cycle after cycle, both from one channel to another both in the same channel from one pulse to the successive, making very difficult a reliable analysis of the conduction velocity and the frequency of the signal.

A critical difference with respect to the first setting, where the patients were affected by supraventricular arrhythmia without structural heart disease, is that in this case the pathological condition of the atrial tissue of patients suffering from AF could most probably interfere with the CV measurements of our experiment, impairing the CV restitution mechanism and prejudice our results. Finally, due to the distance between the electrodes of the basket catheter, here we have decided to use the unipolar signals, differently from the previous experiments. Unipolar signals are much more difficult to analyze with respect to bipolar, due to presence of noise and artifacts, but have the major advantage to be orientation-independent. Moreover, in order to be sure that the model that relates CV and SpC is still valid, it may be necessary to repeat the previous experiments using also unipolar signals. In Chapter 8 we will prove that graphs are a useful tool to represent and model the multi-electrode catheters and we will show how to use Graph Signal Processing to gain better insight into the analysis of multipolar intracardiac signals.

Part II

Graph Signal Processing

Chapter 6

Harmonic Analysis on Graphs

Whether examining consensus and rumor spreading over social networks [43, 1, 77], transportation networks [143] and related epidemic spreading [158], neuronal activation patterns [89] or time-evolving functional network in the brain [193], as well as other datasets collected from a variety of fields, such as physics, engineering, and life-science, much of the high-dimensional data exhibit complex non-Euclidean properties.

An emerging way to deal with these issues is to use a graph to capture the structure underlying the data. This has been the driving force behind recent efforts in the signal processing field to extend harmonic analysis to graph signals, i.e., signals supported on the vertices of irregular graphs [186, 179]. In the field of graph signal processing, the introduction of the graph Fourier transform has enabled us to perform harmonic analysis taking into account the structure of the data, and has led to improvements for tasks such as clustering [12], semi-supervised learning [13, 195], low-rank extraction [185, 184], spectral estimation [162, 131], non-stationary analysis [83, 38] and, in general, geometric learning problems [25]. In this chapter, we present the main notions, tools and algorithms of GSP, which will be successively leverage to extend it to multidimensional and time-varying domains.

6.1 Graph Nomenclature

A graph is defined by the tuple $G = (\mathscr{V}, \mathscr{E}, W)$ where $\mathscr{V}$ is the set of vertices indexed by $1, ..., |\mathscr{V}| = N$, and $\mathscr{E} \subseteq \mathscr{V} \times \mathscr{V}$ is the set of edges connecting pair of nodes.

We denote $e = (n,m)$ the edge connecting the node v_n and v_m. Usually, the edge connects two nodes if a certain relation can be determined between them. This relation can be quantified by a weight function $W\colon \mathscr{V} \times \mathscr{V} \to \mathbb{R}$ which reflects to what extent two nodes are related to each other. In case of simple binary graphs the weights function is defined as $W(v_n, v_m) = 1$ if the edge $e(n,m)$ exists, 0 otherwise. More complex weight functions allow us to define finer graph structure. Typically the weight function is represented using the weight matrix $\boldsymbol{W} \in \mathbb{R}^{N\times N}$, where $\boldsymbol{W}(n,m) = W(v_n, v_m)$ is the weight associated to the edge connecting the nodes indexed by n and m. If no edge exists between nodes n and m, the weight is set to 0.

In general throughout this work we will consider connected, weighted undirected graphs, unless otherwise specified. Therefore, $(n,m) \in \mathscr{E}$ implies $(m,n) \in \mathscr{E}$ and the weight matrix is symmetric. Moreover, we assume $\boldsymbol{W}$ to be non-negative and with zero diagonal. Given a node $v_n \in \mathscr{V}$, its degree $d(v_n) = \boldsymbol{d}(n)$ is defined as the sum of the weights of the connected edges, i.e.,

$$\boldsymbol{d}(n) = \sum_{m=1}^{N} \boldsymbol{W}(n,m),$$

or, in matrix notation, $\boldsymbol{d} = \boldsymbol{W}\mathbf{1}$. The degree measures the connectivity of each node of the network.

A graph signal is defined as the map $x\colon \mathscr{V} \to \mathbb{R}$ assigning one value to each vertex. It is convenient to represent the graph signal x as a vector $\boldsymbol{x} \in \mathbb{R}^N$, where the n$^{\text{th}}$ component is the signal value at the n^{th} vertex, i.e., $x(v_n) = \boldsymbol{x}(n)$. The scalar product of two graph signals $\boldsymbol{x}$ and $\boldsymbol{y}$ is defined as

$$\langle \boldsymbol{x}, \boldsymbol{y} \rangle_{\mathbb{R}^{|\mathscr{V}|}} = \sum_{n=1}^{N} \boldsymbol{x}(n)\boldsymbol{y}^*(n) = \boldsymbol{y}^*\boldsymbol{x}.$$

We can also define an edge signal as the map $\vec{x}\colon \mathscr{E} \to \mathbb{R}$ assigning one value to each edge. An edge signal can be represented as a vector $\vec{\boldsymbol{x}} \in \mathbb{R}^{|\mathscr{E}|}$ or a matrix $\vec{\boldsymbol{X}} \in \mathbb{R}^{N\times N}$ with the same sparsity pattern of the adjacency matrix $\boldsymbol{W}$. The edge signal $\vec{\boldsymbol{x}}$ can be interpreted as the discrete analogous of the tangent vector field on the graph G. As before, the inner product of two edge signals $\vec{\boldsymbol{x}}$ and $\vec{\boldsymbol{y}}$ is defined as

$$\langle \vec{\boldsymbol{x}}, \vec{\boldsymbol{y}} \rangle_{\mathbb{R}^{|\mathscr{E}|}} = \sum_{n=1}^{N} \vec{\boldsymbol{x}}(n)\vec{\boldsymbol{y}}^*(n) = \vec{\boldsymbol{y}}^*\vec{\boldsymbol{x}}.$$

6.1.1 Discrete calculus on graphs

As in the classical case, it is possible to define differential operator acting on scalar or vector functions on the graph [123]. Given a graph signal $\boldsymbol{x} \in \mathbb{R}^N$, the edge derivative with respect to edge $e = (n,m)$ at vertex n is given by

$$\left.\frac{\partial \boldsymbol{x}}{\partial e}\right|_n = \sqrt{\boldsymbol{W}(n,m)}\left[\boldsymbol{x}(n) - \boldsymbol{x}(m)\right]. \tag{6.1}$$

Therefore, the graph gradient of $\boldsymbol{x}$ at vertex n is the linear map $\nabla\colon \mathbb{R}^{|\mathscr{V}|} \to \mathbb{R}^{|\mathscr{E}|}$ defined as

$$\nabla_G \boldsymbol{x}|_n = \left\{ \left.\frac{\partial \boldsymbol{x}}{\partial e}\right|_n \right\}_{e\in\mathscr{E}}. \tag{6.2}$$

The divergence of an edge signal div_G is defined as the adjoint of the gradient operator on graphs, therefore $\mathrm{div}_G = \nabla_G^*$. Given a graph signal $x \in \mathbb{R}^{|\mathscr{V}|}$ and an edge signal $\boldsymbol{y} \in \mathbb{R}^{|\mathscr{E}|}$, the operators satisfy

$$\langle \nabla_G \boldsymbol{x}, \boldsymbol{y}\rangle_{\mathbb{R}^{|\mathscr{E}|}} = \langle \boldsymbol{x}, \nabla_G^* \boldsymbol{y}\rangle_{\mathbb{R}^{|\mathscr{V}|}}.$$

Using the discrete calculus results, it is possible to derive the expression of the combinatorial Laplacian operator $\boldsymbol{L}_G\colon \mathbb{R}^N \to \mathbb{R}^N$ defined as

$$\boldsymbol{L}_G = \nabla_G^* \nabla_G = \boldsymbol{D} - \boldsymbol{W} \tag{6.3}$$

where $\boldsymbol{D}$ is the diagonal degree matrix, $\boldsymbol{D}(n,n) = \boldsymbol{d}(n)$. The combinatorial Laplacian matrix is a symmetric, positive semidefinite matrix and can be interpreted as the finite difference approximation of the continuous Laplacian operator [195] or the Laplace-Beltrami operator for Riemannian manifolds [28].

Other definitions of graph Laplacian are widely used, for example the normalized Laplacian

$$\boldsymbol{L}'_G = \boldsymbol{D}^{-\frac{1}{2}} \boldsymbol{L}_G \boldsymbol{D}^{-\frac{1}{2}} = \boldsymbol{I} - \boldsymbol{D}^{-\frac{1}{2}} \boldsymbol{W} \boldsymbol{D}^{-\frac{1}{2}}$$

or the random walk Laplacian

$$\boldsymbol{L}_G^{\mathrm{rw}} = \boldsymbol{D}^{-1} \boldsymbol{L}_G$$

The choice of the Laplacian is highly dependent on the application and there is no general rule to tell which one should be used in any given situation.

6.2 Spectral Graph Theory

The spectral graph theory has been leveraged as a tool to define frequency spectra and expansion bases for graph Fourier transforms. Being the graph Laplacian $\boldsymbol{L}_G$ a real symmetric positive semi-definite matrix, from the spectral theorem, it has a complete set of orthonormal eigenvectors $U = \{\boldsymbol{u}_\ell\}_{\ell=1}^N$ with associated real nonnegative eigenvalues $\Lambda = \{\lambda_\ell\}_{\ell=1}^N$ and can be written as:

$$\boldsymbol{L}_G = \boldsymbol{U}\boldsymbol{\Lambda}\boldsymbol{U}^*$$

As in the classical case, it is possible to define the graph Fourier transform (GFT) $\tilde{\boldsymbol{x}}$ of the graph signal $\boldsymbol{x} \in \mathbb{R}^N$ on the vertices of G as the expansion of $\boldsymbol{x}$ in terms of the eigenvectors of the graph Laplacian [83, 186, 188]:

$$\tilde{\boldsymbol{x}}(\lambda_\ell) = \sum_{i=1}^{N} \boldsymbol{x}(i)\boldsymbol{u}(i)_\ell^* \tag{6.4}$$

that can be conveniently written in matrix notation as

$$\tilde{\boldsymbol{x}} = \boldsymbol{U}^*\boldsymbol{x}$$

6.2.1 Graph filters

The graph Fourier transform allows us to extend the filtering operations to the graph domain. Similarly to the classical domain, filtering a graph signal can be interpreted as the amplification and attenuation of the frequency component obtained through the Fourier transform. Due to the lack of the shift-invariance property, it is necessary to define a generalized convolution theorem, which states that a point-wise multiplication in the spectral domain is still a valid convolution in the dual domain, i.e., the vertex domain in the case of the graph.

In general, it is possible to define a continuous function $g\colon \mathbb{R}_+ \to \mathbb{R}$ and to evaluate it at the graph eigenvalues to obtain the coefficients of the filter. Therefore, considering a graph signal $\boldsymbol{x}$ and the filter transfer function $g(\cdot)$, the filtered signal $\boldsymbol{y}$ can be written in the graph spectral domain as

$$\tilde{\boldsymbol{y}}(\lambda_\ell) = g(\lambda_\ell)\tilde{\boldsymbol{x}}(\lambda_\ell)$$

or conveniently in matrix form $\tilde{\boldsymbol{y}} = g(\boldsymbol{\Lambda})\tilde{\boldsymbol{x}}$, where $g(\boldsymbol{\Lambda}) = \text{diag}([g(\lambda_1), g(\lambda_2), \ldots, g(\lambda_N]))$. In the vertex domain we have

$$\boldsymbol{y}(n) = \sum_{\ell=1}^{N} g(\lambda_\ell)\tilde{\boldsymbol{x}}(\lambda_\ell)\boldsymbol{u}_\ell(n)$$

and in matrix form $\boldsymbol{y} = g(\boldsymbol{L}_G)\boldsymbol{x}$, where $g(\boldsymbol{L}_G) = \boldsymbol{U}g(\boldsymbol{\Lambda})\boldsymbol{U}^*$.

Fast filtering of graph signals using Chebyshev polynomials

In many real-world applications, the graph has thousands or even more nodes (e.g., social networks, knowledge networks [141]). This poses considerable limitations to harmonic analysis on these huge graphs, since performing the GFT requires the diagonalization of the graph Laplacian, which has complexity $\mathscr{O}(N^3)$ and memory requirement $\mathscr{O}(N^2)$. Hence, the graph Fourier transform, and consequently filtering on graph, is only feasible in case of graphs with only a few thousand vertices. To be able to tackle problems of larger size, more efficient methods have been proposed in the literature. Among the several possibilities [163], we will discuss a method based on Chebyshev polynomials approximation [132], which allows to perform filtering of graph signals with complexity to $\mathscr{O}(|\mathscr{E}|)$. For a more detailed discussion we refer the reader to [83].

To overcome the unfeasibility of solving the eigendecomposition of $\boldsymbol{L}_G$, we need to perform the filtering operation in the vertex domain, i.e., $\boldsymbol{y} = g(\boldsymbol{L}_G)\boldsymbol{x}$ with $g(\boldsymbol{L}_G) = \boldsymbol{U}g(\boldsymbol{\Lambda})\boldsymbol{U}^*$. If we restrict the filter to be a polynomial function of order M of the eigenvalues λ, we have $g(\lambda) = p_0 + p_1\lambda + \cdots + p_M\lambda$. Thus, in the vertex domain $g(\boldsymbol{L}_G)$ can be written as a polynomial of the Laplacian matrix $\boldsymbol{L}_G$

$$\boldsymbol{y} = g(\boldsymbol{L}_G)\boldsymbol{x} = (p_0\boldsymbol{I} + p_1\boldsymbol{L}_G + \cdots + p_M\boldsymbol{L}_G)\boldsymbol{x}. \tag{6.5}$$

Pursuing the idea of filtering the graph signal $\boldsymbol{x}$ by mean of polynomials of the Laplacian matrix, we are interested in approximation techniques based on polynomials that can also be efficiently evaluated. For $x \in [-1, 1]$, the Chebyshev polynomials of

the first kind are defined by the recurrence relation

$$\begin{cases} T_0 = 1 \\ T_1 = x \\ T_{n+1} = 2xT_n - T_{n-1} \end{cases} \tag{6.6}$$

These polynomials admit a closed form solution $T_m(x) = \cos(m \arccos(x))$ which shows that $T_m(x) \in [-1,1]$ for $x \in [-1,1]$. The Chebyshev polynomials form an orthogonal basis for $L^2\left([-1,1], \frac{\mathrm{d}x}{\sqrt{1-x^2}}\right)$, therefore, every function $g(x)$ in that Hilbert space admits a convergent Chebyshev series

$$g(x) = \frac{1}{2}c_0 + \sum_{m=1}^{+\infty} c_m T_m(x),$$

with coefficients

$$c_m = \frac{2}{\pi}\int_0^{\pi} \cos(m\vartheta) g(\cos(m\vartheta))\,\mathrm{d}\vartheta.$$

Therefore, to approximate the filter $g(\lambda)$ with $\lambda \in [0, \lambda_{\max}]$ we apply the transformation $x' = a(x-1)$ with $a = \lambda_{\max}/2$. Hence, we can write the Chebyshev recurrence relation as function of the Laplacian matrix as

$$\widetilde{T}_{n+1}\boldsymbol{x} = \frac{2}{a}(\boldsymbol{L}_G - \boldsymbol{I})\widetilde{T}_n(\boldsymbol{L}_G)\boldsymbol{x} - \widetilde{T}_{n-1}(\boldsymbol{L}_G)\boldsymbol{x}. \tag{6.7}$$

Finally, the filtering operation can be implemented as

$$\boldsymbol{y} = g(\boldsymbol{L}_G)\boldsymbol{x} = \frac{1}{2}c_0\boldsymbol{I}\boldsymbol{x} + \sum_{m=1}^{+\infty} c_m \widetilde{T}_m(\boldsymbol{L}_G)\boldsymbol{x} \tag{6.8}$$

Obviously, we are interested in the case of truncated sum up to the M-th term. Taking advantage of the recursive nature of the algorithm, its computational cost scales linearly with the number of edges $\mathscr{O}(M|\mathscr{E}|)$. In most of the cases the Laplacian is a sparse matrix, thus $|\mathscr{E}| \ll N^2$, which implies a much lower computational cost with respect to the eigendecomposition of the Laplacian matrix. Moreover, apart from storing the Laplacian, the additional memory consumed by this algorithm is only $4N$. In the next chapter, we will leverage this technique to perform filtering of graph signals that also evolve in time.

6.2.2 Graph filter banks and frames

Good signal representations are important in almost any machine learning or signal processing problems. For example, in the classic case, the wavelet and the short time Fourier transforms respectively enable time-scale and time-frequency analysis of the signal. These transforms, as many others, are based on collection of filters, that can be denoted as g_k. The filters can be designed to emphasize desired signal characteristics, resulting in substantial improvements of semi-supervised and unsupervised learning, or to incorporate in a problem prior assumption on the data, such as smoothness or sparseness in the transformed domain.

As in the classical case, the atoms of the representations are built by applying a transform (e.g. scaling or modulation) to a mother function and shifting the resulting functions. In the graph domain, the mother function will be replaced by a graph kernel and the shifting by an operator suitable to graphs.

Graph localization operator

The concept of localization on the graph stems from the *translation* defined in the time domain. The translation operator can be written as

$$\mathscr{T}_\tau^T h(t) = \mathscr{T}_0^T h(t-\tau), \quad t,\tau = 1,\ldots,T \text{ and } t > \tau. \tag{6.9}$$

Let us assume that the discrete periodic time domain of finite length T can be represented as a cycle graph with T vertices. Thus, $\mathscr{T}_0^T h = \boldsymbol{U}_T \boldsymbol{h}$ is the inverse Fourier transform of $\boldsymbol{h}$ and $\boldsymbol{U}_T$ is the orthonormal Fourier basis. Hence, for a cyclic graph, this operator computes the inverse Fourier transform of the frequency response h, and translates it to vertex $t-\tau$. We can verify this by using the fact that the complex exponential Fourier basis forms the eigenvector set of all cyclic graphs [200], implies that

$$\begin{aligned}\mathscr{T}_\tau^T h(t) &= \frac{1}{T}\sum_{k=1}^{T} h(\omega_k)\mathrm{e}^{-\omega_k\tau}\,\mathrm{e}^{\omega_k t} \\ &= \frac{1}{T}\sum_{k=1}^{T} h(\omega_k)\,\mathrm{e}^{\omega_k(t-\tau)} = \mathscr{T}_0^T h(t-\tau).\end{aligned} \tag{6.10}$$

In the case of irregular graphs, due to the lack of the shift invariance property of the graphs, the concept of translation is replaced by localization. It differs from classical translation because the shape of the localized filter adapts to the graph and varies as a function of its topology. For a general graph G, the value at the vertex v_n of a filter with frequency response h localized onto vertex v_m is

$$\mathscr{T}_m^G h(n) \stackrel{\Delta}{=} h(\boldsymbol{L}_G)\,\boldsymbol{\delta}_m(n) = \sum_{\ell=1}^{N} h(\lambda_\ell)\,\boldsymbol{u}_\ell^*(m)\,\boldsymbol{u}_\ell(n), \tag{6.11}$$

where $\boldsymbol{\delta}_m$ is a Kronecker delta centered at vertex v_m. For a sufficiently regular function h, this operation localizes the filter around m [188, Theorem 1 and Corollary 2]. Additional insights about the localization operator can be found in [162, 188, 83, 161].

Graph dictionaries and frames

A graph filter bank is a collection of graph kernels $\{g_z(\lambda)\}_{z\in\mathscr{Z}}$ that are used to filter and separate the graph signal $\boldsymbol{x}$ in different components, each one having a different spectrum depending on the shape of $g_z(\lambda)$. The filters are obtained as a composition of the transformation function $s_z(\cdot)$ parametrized by $z \in \mathscr{Z} \subset \mathbb{R}$ and the graph mother kernel $g(\lambda)$

$$g_z(\lambda) = g(s_z(\lambda)). \tag{6.12}$$

The atoms of the dictionary $\mathscr{D}_g$ are obtained localizing the transformed kernel on the vertices of the graph

$$\mathscr{D}_g = \left\{ \mathscr{T}_m^G g_z \right\} \qquad \text{for } m \in \mathscr{V},\ z \in \mathscr{Z} \subset \mathbb{R} \tag{6.13}$$

The operators which allow us to compute the coefficients of the signal $\boldsymbol{x}$ with respect to the dictionary $\mathscr{D}_g$ and vice versa are the *analysis* and *synthesis* operators, respectively. Specifically, the analysis operator D_g consists in applying the filters of the dictionary to the graph signal

$$\boldsymbol{c} = \{\boldsymbol{c}_z\}_{z\in\mathscr{Z}} = D_g\{\boldsymbol{x}\} = \{g_z(\boldsymbol{L})\boldsymbol{x}\}_{z\in\mathscr{Z}}\,. \tag{6.14}$$

The synthesis operator D_g^* is defined as the adjoint of the analysis operator, i.e.,

$$\boldsymbol{y} = D_g^*\{\boldsymbol{c}\} = \sum_z g(\boldsymbol{L})\boldsymbol{c}_z \tag{6.15}$$

and it constructs a graph signal $\boldsymbol{y}$ starting from the coefficients $\boldsymbol{c}$. For a generic dictionary $\mathscr{D}_g$ there are no guarantees regarding the invertibility of the transform, i.e., $\boldsymbol{y} = D_g^* D_g\{\boldsymbol{x}\} \neq \boldsymbol{x}$. In several applications in signal processing one is interested not only in processing data in another convenient representation, but also to recover the original signal from its alternative representation. Redundant invertible dictionaries are referred to as *frames* [34, 115]. In order to guarantee that $\boldsymbol{c} = D_g\{\boldsymbol{x}\}$ is a valid representation for $\boldsymbol{x}$, i.e., no information is lost in the transformation, we need to prove that the dictionary $\mathscr{D}_g$ is a frame [190, Lemma 1], [83, Theorem 5.6].

Definition 1 (**Graph frame**). *Given the filter bank $\{g_z(\lambda)\}_{z\in\mathscr{Z}}$, the graph dictionary $\mathscr{D}_g$ is a frame if, given the constants*

$$A = \min_\ell \sum_z |g_z(\lambda_\ell)|^2, \qquad B = \max_\ell \sum_z |g_z(\lambda_\ell)|^2.$$

called lower and upper frame bounds, it holds

$$A\|\boldsymbol{x}\|_2^2 \leq \|D_g\{\boldsymbol{x}\}\|_2^2 \leq B\|\boldsymbol{x}\|_2^2$$

with

$$0 < A \leq B < \infty \tag{6.16}$$

for every graph signal $\boldsymbol{x} \in \mathbb{R}^N$. Moreover, if $A = B$ the frame is said to be tight.

The frame condition in Definition 1 ensures that the sum of all filters is non-zero everywhere in the spectral domain, assuring that no components in the frequency spectrum is lost during analysis and reconstruction. Different tilings of the vertex-frequency domain are possible depending on the filters used to build the filter bank, such as spectral graph wavelets [83], spectrum-adapted wavelets and vertex-frequency frames [190], or learned parametric dictionaries [204].

6.3 Multidimensional Graph Signal Processing

Due to the advancement of data acquisition technologies, nowadays it is easy to generate massive tensor data in a variety of research and application fields, for example for multiview videos, hyperspectral imaging, multi-sensor radar detection, biomedical signals analysis (e.g., tomographic imaging, multichannel electroencephalography [20]). Unfortunately, dealing with this huge amount of data is not as simple as producing them. As we pointed out at the beginning of the chapter, in an incredible variety of applications, graphs are powerful mathematical representation useful to describe the data domains. In case of multidimensional signals (tensors), a general framework providing the tools to analyze and process such signals is needed. In this context, the idea of multidimensional graph signal processing can be traced back to the study [180] aiming at processing multi-modal signals with different graphs associated with each of their modalities. We denote Multidimensional GSP (MGSP) the framework comprising techniques and methods for the analysis of multidimensional signals on graphs. In this section we will extend the tools of the GSP, as harmonic analysis, filtering and localization to multidimensional graph signals. This will provide a generalized framework, which includes the fundamental case of time-varying graph signals that we will present in detail in Chapter 7.

6.3.1 Multidimensional graph representation

The idea behind MGSP is to use graph products, such as the graph Cartesian product, to model each dimension of the domain by each factor graph. In the following we will limit our analysis to the case of 2-dimensional domains, but all our results can be easily generalized to the n-dimensional case.

Definition 2 (Graph Cartesian product). *Let us consider two graphs $G_1(\mathscr{V}_1, \mathscr{E}_1, \boldsymbol{W}_1)$ and $G_2(\mathscr{V}_2, \mathscr{E}_2, \boldsymbol{W}_2)$. The Cartesian product $G_\times = G_1 \times G_2$ is a graph such that the vertex set is the Cartesian product $\mathscr{V}_\times = \mathscr{V}_1 \times \mathscr{V}_2$ and the edges are set according to the following rules: any two vertices (n_1, n_2) and (m_1, m_2) are adjacent in $G_\times$ if and only if either*

- $n_1 = m_1$ *and* $(n_2, m_2) \in \mathscr{E}_2$
- $n_2 = m_2$ *and* $(n_1, m_1) \in \mathscr{E}_1$.

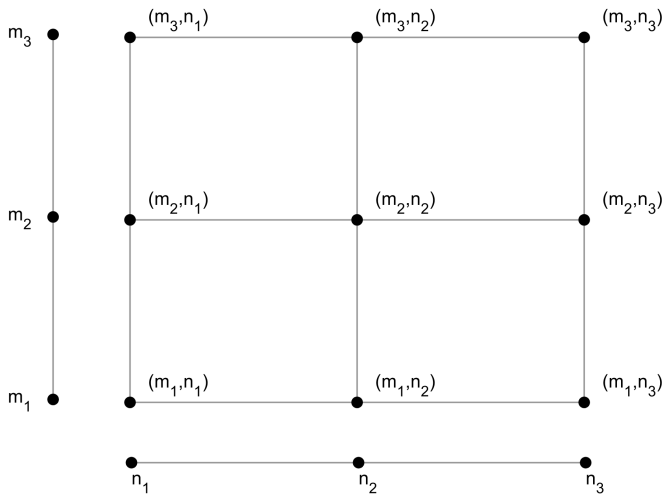

Figure 6.1 Example of graph Cartesian product. The Cartesian product of two path graphs gives a 2D grid.

The adjacency matrix of the Cartesian product graph $G_\times$ is given by the matrix Cartesian product:

$$\boldsymbol{W}_\times = \boldsymbol{W}_1 \times \boldsymbol{W}_2 = \boldsymbol{W}_1 \otimes \boldsymbol{I}_2 + \boldsymbol{I}_1 \otimes \boldsymbol{W}_2$$

Lemma 1. *Assuming $\boldsymbol{L}_1 = \boldsymbol{D}_1 - \boldsymbol{W}_1$ and $\boldsymbol{L}_2 = \boldsymbol{D}_2 - \boldsymbol{W}_2$, the degree matrix $\boldsymbol{D}_\times$ of the graph $G_\times = G_1 \times G_2$ which satisfies definition 2 is given as*

$$\boldsymbol{D}_\times = \boldsymbol{D}_1 \otimes \boldsymbol{I}_2 + \boldsymbol{I}_1 \otimes \boldsymbol{D}_2 = \boldsymbol{D}_1 \times \boldsymbol{D}_2$$

The combinatorial Laplacian of $G_\times$ is

$$\boldsymbol{L}_\times = \boldsymbol{L}_1 \otimes \boldsymbol{I}_2 + \boldsymbol{I}_1 \otimes \boldsymbol{L}_2 = \boldsymbol{L}_1 \times \boldsymbol{L}_2$$

The eigenvectors matrix of $G_\times$ can be computed as

$$\boldsymbol{U}_\times = \boldsymbol{U}_1 \otimes \boldsymbol{U}_2.$$

where $\boldsymbol{U}_1$ and $\boldsymbol{U}_2$ diagonalizes the Laplacians $\boldsymbol{L}_1$ and $\boldsymbol{L}_2$ with eigenvalues $\boldsymbol{\Lambda}_1$ and $\boldsymbol{\Lambda}_2$, respectively. The matrix $\boldsymbol{U}_\times$ diagonalize the Laplacian $\boldsymbol{L}_\times$ with eigenvalues

equal to the sum of all the pairs $(\lambda_{1,\ell_1}, \lambda_{2,\ell_2})$*, i.e.,*

$$\boldsymbol{L}_\times = \boldsymbol{U}_\times(\boldsymbol{\Lambda}_1 \times \boldsymbol{\Lambda}_2)\boldsymbol{U}_\times^* = \boldsymbol{U}_\times \boldsymbol{\Lambda}_\times \boldsymbol{U}_\times^*$$

Proof. For the proof please refer to Appendix A.1. □

Figure 6.1 shows a very simple example of graph Cartesian product between two path graphs G_1 and G_2. The resulting graph $G_\times = G_1 \times G_2$, is a 2-dimensional grid graph, where each vertex can be identified as a couple (v_n, v_m).

The natural extension of the concept of graph signal to the 2-dimensional graph domain is the 2-dimensional graph signal, which is defined as the map $X : \mathscr{V}_1 \times \mathscr{V}_2 \to \mathbb{R}$ and can be represented as a matrix $\boldsymbol{X} \in \mathbb{R}^{N_1 \times N_2}$, where $X(n_1, n_2)$ is the value of the signal on the node denoted $(n_1, n_2) \in \mathscr{V}_\times$.

6.3.2 Multidimensional graph Fourier transform

Let us suppose that the multidimensional graph domain can be written an $G_\times = G_1 \times G_2$. The Laplacian matrices of the separated domains can be decomposed as

$$\boldsymbol{L}_1 = \boldsymbol{U}_1 \boldsymbol{\Lambda}_1 \boldsymbol{U}_1^*$$
$$\boldsymbol{L}_2 = \boldsymbol{U}_2 \boldsymbol{\Lambda}_2 \boldsymbol{U}_2^*$$

and the corresponding GFTs of the graph signals $\boldsymbol{x}_1 \in \mathbb{R}^{N_1}$ and $\boldsymbol{x}_2 \in \mathbb{R}^{N_2}$ are $\tilde{\boldsymbol{x}}_1 = \boldsymbol{U}_1^* \boldsymbol{x}_1$ and $\tilde{\boldsymbol{x}}_2 = \boldsymbol{U}_2^* \boldsymbol{x}_2$. The 2-dimensional graph Fourier transform (GFT_2) of the 2D graph signal $\boldsymbol{X}$ with respect to the graph $G_\times$ is defined as

$$\widetilde{\boldsymbol{X}}(\ell_1, \ell_2) = \mathrm{GFT}_2\{\boldsymbol{X}\} = \sum_{n=1}^{N_1} \sum_{m=1}^{N_2} \boldsymbol{X}(n,m) \boldsymbol{u}_{1,\ell_1}^*(n) \boldsymbol{u}_{2,\ell_2}^*(m)$$

which can be written conveniently in matrix notation as

$$\mathrm{GFT}_2\{\boldsymbol{X}\} = \boldsymbol{U}_1^* \boldsymbol{X} \overline{\boldsymbol{U}}_2 \tag{6.17}$$

6.3.3 Multidimensional graph filters and filter banks

In the following we will revisit step by step the concept of graph filter and graph dictionary defined in Section 6.2.1 and Section 6.2.2 in the context of multidimensional graph signal processing. Once again, we will limit our analysis to the 2-dimensional case, but all the definitions can be extended to n-dimensions straightforwardly.

Multidimensional graph filters

The 2D graph filter $g\colon \mathbb{R}_+ \times \mathbb{R}_+ \to \mathbb{R}$ is defined as the map from the Cartesian product between the set of eigenvalues (λ_1, λ_2) to the real domain. Similarly to the 1-dimensional case, the filter can be defined as a 2D continuous function evaluated for $(\lambda_{1,\ell_1}, \lambda_{2,\ell_2})$. Considering the 2D graph signal $\boldsymbol{X}$ and the filter transfer function $g(\cdot,\cdot)$, the output of a 2D graph filter $\boldsymbol{Y}$ can be written in the graph spectral domain as

$$\boldsymbol{Y} = g(\boldsymbol{L}_1, \boldsymbol{L}_2)\, \boldsymbol{X} = \boldsymbol{U}_\times\, g(\boldsymbol{\Lambda}_1, \boldsymbol{\Lambda}_2) \boldsymbol{U}_\times^*\, \boldsymbol{X},$$

where $g(\boldsymbol{\Lambda}_1, \boldsymbol{\Lambda}_2)$ is a diagonal $N_1N_2 \times N_1N_2$ matrix defined as

$$g(\boldsymbol{\Lambda}_1, \boldsymbol{\Lambda}_2) = \text{diag vec} \left(\begin{bmatrix} g(\lambda_{1,1}, \lambda_{2,1}) & \cdots & g(\lambda_{1,1}, \lambda_{2,N_2}) \\ \vdots & \ddots & \vdots \\ g(\lambda_{1,N_1}, \lambda_{2,1}) & \cdots & g(\lambda_{1,N_1}, \lambda_{2,N_2}) \end{bmatrix} \right)$$

and the diag vec$(\boldsymbol{A})$ operator creates a matrix with diagonal elements of the vectorized form of $\boldsymbol{A}$.

Multidimensional graph localization operator

Let us consider the localization operators for the two separate graphs $\mathscr{T}^{G_1}$ and $\mathscr{T}^{G_2}$. The 2-dimensional kernel $g(\lambda_1, \lambda_2)$ can be localized independently on the graphs G_1 and G_2 through

$$\mathscr{T}_{m_1}^{G_1} g(n_1, \lambda_2) = \sum_{\ell_1=1}^{N_1} g(\lambda_{1,\ell_1}, \lambda_2) \boldsymbol{u}_{1,\ell_1}(n_1) \boldsymbol{u}_{1,\ell_1}(n_1)^* \qquad \text{for } \lambda_2 = \lambda_{2,1}, \lambda_{2,2}, \ldots, \lambda_{2,N_2},$$

and

$$\mathscr{T}_{m_2}^{G_2} g(\lambda_1, n_2) = \sum_{\ell_2=1}^{N_2} g(\lambda_1, \lambda_{2,\ell_2}) \boldsymbol{u}_{2,\ell_2}(n_2) \boldsymbol{u}_{2,\ell_2}(n_2)^* \qquad \text{for } \lambda_1 = \lambda_{1,1}, \lambda_{1,2}, \ldots, \lambda_{1,N_1}.$$

The 2-dimensional localization operator is defined as

$$\mathscr{T}_{m_1,m_2}^{G_\times} g(n_1, n_2) = \sum_{\substack{\ell_1=1 \\ \ell_2=1}}^{N_1,N_2} g(\lambda_{1,\ell_1}, \lambda_{2,\ell_2}) \boldsymbol{u}_{1,\ell_1}(n_1) \boldsymbol{u}_{1,\ell_1}^*(n_1) \boldsymbol{u}_{2,\ell_2}(n_2) \boldsymbol{u}_{2,\ell_2}^*(n_2).$$

It is straightforward to prove that

$$\mathscr{T}_{m_1,m_2}^{G_\times} g = \mathscr{T}_{m_1}^{G_1} \mathscr{T}_{m_2}^{G_2} g. \tag{6.18}$$

Multidimensional graph dictionary and frame

Having defined all the needed building blocks, we can finally denote *2D graph filter bank* a collection of $\{g_z\}_{z \in \mathscr{Z}}$ joint filters. Applying the set of filters to the signal provides a new representation, that can be interpreted as the projection of the signal on a set of localized atoms defined by the filter bank [36].

The linear analysis operator D_g associated to the 2D filter bank $\{g_z\}_{z \in \mathscr{Z}}$ that provides the coefficient $\{\boldsymbol{C}_z\}_{z \in \mathscr{Z}}$ in the new representation is given by

$$\boldsymbol{C}_z(m_1, m_2) = D_g\{\boldsymbol{X}\}(m_1, m_2, z) = \langle \boldsymbol{X}, \mathscr{T}_{m_1,m_2}^{G_\times} g_z \rangle,$$

and the synthesis operator

$$\boldsymbol{Y}(n_1, n_2) = D_h^*\{\boldsymbol{C}\}(n,t) = \sum_z \langle \boldsymbol{C}_z, \mathscr{T}_{n_1,n_2}^{G_\times} g_z \rangle.$$

The discussion Section 6.2.2 related to the frame theory can be extended straightforwardly to the multidimensional case. As previously notice, in general $\boldsymbol{X} \neq \boldsymbol{Y}$, therefore if we want to recover the original signal $\boldsymbol{X}$ from its representation $D_g\{\boldsymbol{X}\} = \boldsymbol{C}$ we need to prove that the 2D graph dictionary $\mathscr{D}_g$ is a frame.

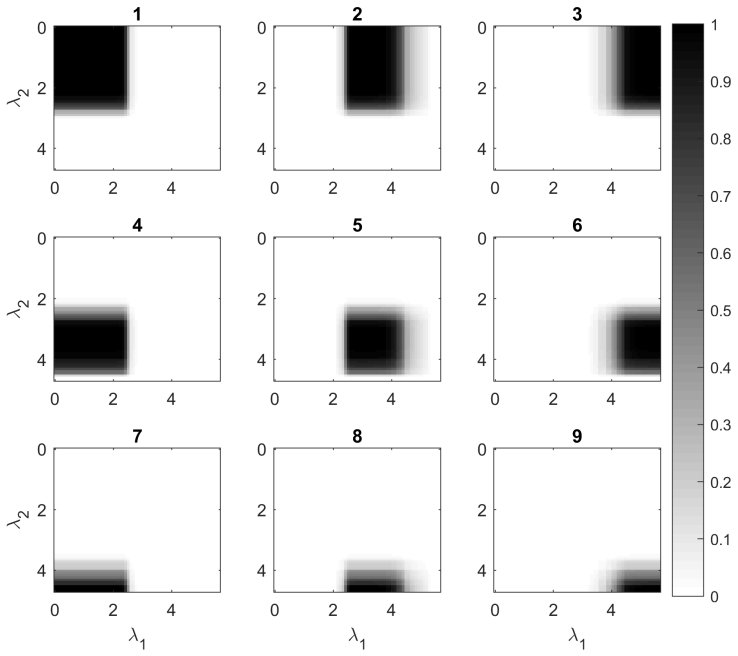

Figure 6.2 Example of 2-dimensional Meyer graph filter banks composed by 9 graph 2D filters. The frequency response of each filter is visualized as a continuous function of the eigenvalues λ_1 and λ_2.

Theorem 1 (2 dimensional graph frame). *Given the 2D graph filter bank* $\{g_z(\lambda)\}_{z\in\mathscr{Z}}$, *the graph dictionary* $\mathscr{D}_g$ *is a frame if, given the constants*

$$A = \min_{\ell_1,\ell_2} \sum_z |g_z(\lambda_{1,\ell_1}, \lambda_{2,\ell_2})|^2, \qquad B = \max_{\ell_1,\ell_2} \sum_z |g_z(\lambda_{1,\ell_1}, \lambda_{2,\ell_2})|^2.$$

called lower and upper frame bounds, it holds

$$A\|\boldsymbol{X}\|_F^2 \leq \|D_g\{\boldsymbol{X}\}\|_F^2 \leq B\|\boldsymbol{X}\|_F^2$$

with

$$0 < A \leq B < \infty \tag{6.19}$$

for every graph signal $\boldsymbol{X} \in \mathbb{R}^{N_1\times N_2}$. *Moreover, if* $A = B$ *the frame is said to be tight.*

Proof. For the proof we defer the reader to Theorem 2 with proof in Appendix B.3, which proves the frame bound condition in the particular case of G_2 being a ring graph representing the time domain. □

Illustration: 2D Meyer filter bank In Figure 6.2 we illustrate an example of 2-dimensional graph filter bank, obtained using the Meyer mother kernel and a set of parameter for the transformation function which gives 9 filters. Notice that the filters span the entire 2D frequency domain, which here is depicted as continuous for simplicity reasons, therefore the filter bank is not only a separable filter bank, but it is also a frame. Moreover, since the sum overall the spectrum is constant, the coefficients A and B satisfy the frame bound 1 with the equality, hence the frame is tight.

Chapter 7

Time-Vertex Harmonic Analysis

Part of the work described in this chapter has been previously published in F. Grassi, A. Loukas, N. Perraudin and B. Ricaud, "A Time-Vertex Signal Processing Framework: Scalable Processing and Meaningful Representations for Time-Series on Graphs," in IEEE Transactions on Signal Processing, vol. 66, no. 3, pp. 817-829, Feb.1, 2018.

7.1 Introduction

Though state-of-the-art graph-based methods have been successful for many tasks, so far they predominantly ignore the time-dimension of data, for example by treating successive signals independently or performing a global average [89, 162, 101]. On the contrary, many of the systems to which GSP is applied to are inherently dynamic. Consider for instance a road network, and suppose that we want to infer traffic conditions given flow information over a subset of highways and streets. Approaches that do not take into account the temporal evolution of traffic will be unable to provide insights about transient phenomena, such as rush hour traffic, bottlenecks caused by blockage, and stop waves in case of traffic data. Similarly, if we want to estimate the weather conditions on a geographical region given temperature measurements from a small set of weather stations, ignoring the seasonal variations of weather will bias our prediction (Fig. 7.1). Moreover, when the weather dynamics are slow and predictable, taking into account the time dimension, e.g., by imposing a smoothness prior, can yield accuracy improvements in the reconstruction effort.

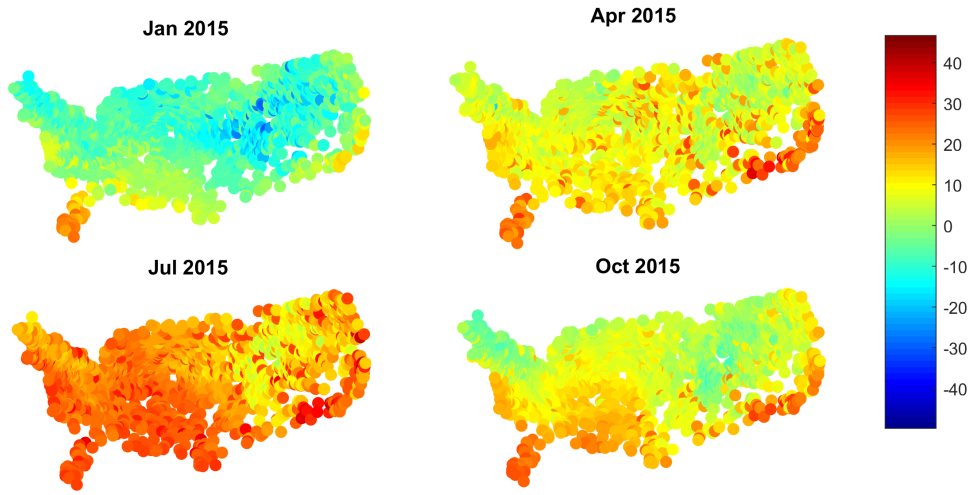

Figure 7.1 Four snapshots of average temperature from the Daily Global Historical Climatology Network (GHCN-DAILY) recorded by the NOAA National Climatic Data Center [137].

Recently, several ideas are beginning to emerge related to the analysis of time-varying graph signals, such as Joint time-vertex Fourier transform (JFT) [126] and the joint time-vertex filters [92] and filter banks [74]. While these constitute notable contributions, we argue that the potential of joint harmonic analysis is yet unexplored, both in terms of its foundations, algorithms, and applications.

7.1.1 Related work

The time-vertex framework is intimately linked with the stochastic analysis of multivariate signals and, therefore, with graphical models (e.g., [41] and references therein). The main difference between graphical models and GSP lies in the assumption about the relation between the signal and graph [222]. Graphical models adopt a purely Bayesian setting, where edges denote conditional dependencies between variables. As such, the graph usually is a proxy for the covariance and is learned from the data. On the other hand, GSP assumes that the graph is given and its relation to the signal can be understood through harmonic analysis.

Collaboration between the graph theory and signal processing communities has led to new tools to process and analyze time-varying graphs and signals on a graph, such as multilayer graphs and tensor products of graphs [109, 16, 44, 194]. The notion of joint time-vertex harmonic analysis was further realized in [126] by one

of the authors of this work. Therein, the joint Fourier analysis is presented and its properties analyzed in detail, together with examples of joint filters. In this work, we leverage these concepts proposing a framework in which the joint Fourier transform is just one of the building blocks.

Visualization and filtering of time-varying graph signals

The idea of analyzing the behavior of graph filters with time-varying signals first appeared in [127], showing that they could be analyzed by applying jointly a GFT and a Z-transform and as such they possess a joint frequency response. Since then, we have seen a number of works dealing with time-varying signals on graphs. Authors in [207] propose a method that relies on graph wavelet theory and product graphs to visualize time-varying data defined on the vertices of a graph in order to identify spatial and/or temporal variations. A step towards the graphical model has been carried out by the authors in [136]. In this work, the authors assume data time dependencies to be modeled by an auto-regressive (AR) process and they propose several algorithms to estimate the network structure capturing the spatio-temporal dependencies and the coefficients of the AR process expressed as graph polynomial filters. In order to deal with the high computational complexity of the eigendecomposition, different filtering approximation algorithms have been proposed, mainly based on polynomials: centralized and distributed joint filter 2D Chebychev polynomials [126], separable rational implementations [92], and autoregressive models [93].

7.2 Joint Time-Vertex Fourier Transform

The joint time-vertex domain consist of a graph $G = (\mathscr{V}, \mathscr{E}, W)$ and the finite discrete time domain, typically periodic. Notice that also the time domain can be represented as a cycle graph with length T. We suppose that the signal on a graph is sampled at T successive regular intervals of unit length. That is, if we denote by $\boldsymbol{x}_t \in \mathbb{R}^N$ the graph signal at instant t, the time-varying graph signal corresponds to the matrix $\boldsymbol{X} = [\boldsymbol{x}_1, \boldsymbol{x}_2, \ldots, \boldsymbol{x}_T] \in \mathbb{R}^{N \times T}$. Equivalently, $\boldsymbol{X}^\intercal = \left[\boldsymbol{x}^1, \boldsymbol{x}^2, \ldots, \boldsymbol{x}^N\right]^\intercal$ holds N temporal signals $\boldsymbol{x}^n \in \mathbb{R}^T$, one for each vertex v_n. Furthermore, we refer to both $\boldsymbol{X}$ and its vectorized form $\boldsymbol{x} = \mathrm{vec}(\boldsymbol{X}) \in \mathbb{R}^{NT}$ as "time-vertex signal".

The main idea of harmonic analysis is to decompose a signal into oscillating modes thanks to the Fourier transform. For instance, one analyses oscillations along the temporal axis by applying the Discrete Fourier Transform (DFT) independently to each row of $\boldsymbol{X}$

$$\mathrm{DFT}\{\boldsymbol{X}\} = \boldsymbol{X}\overline{U}_T, \tag{7.1}$$

where $\boldsymbol{U}_T$ is the normalized DFT matrix defined as

$$\boldsymbol{U}_T^*(t,k) = \frac{\mathrm{e}^{-\mathrm{j}\omega_k t}}{\sqrt{T}}, \quad \text{with} \quad \omega_k = \frac{2\pi(k-1)}{T}, \tag{7.2}$$

with $t,k = 1,2,\ldots,T$. Similarly, the GFT allows us to analyze oscillations of the time-vertex signal $\boldsymbol{X}$ along the graph edges. As each column of $\boldsymbol{X}$ represents a time instant, the GFT of $\boldsymbol{X}$ for all t reads

$$\mathrm{GFT}\{\boldsymbol{X}\} = \widetilde{\boldsymbol{X}} = \boldsymbol{U}_G^*\boldsymbol{X}, \tag{7.3}$$

where $\boldsymbol{U}_G$ is again obtained by the eigendecomposition $\boldsymbol{L}_G = \boldsymbol{U}_G\boldsymbol{\Lambda}_G\boldsymbol{U}_G^*$ of the graph Laplacian.

Harmonic time-vertex analysis amounts to analyzing oscillations *jointly* along both the time and the vertex dimensions. Hence, assuming a non-varying graph in time, the *joint time-vertex Fourier transform*, or JFT for short, is obtained by applying the GFT on the graph dimension and the DFT along the time dimension [126]

$$\widehat{\boldsymbol{X}}(\ell,k) = \frac{1}{\sqrt{T}} \sum_{n=1}^{N} \sum_{t=1}^{T} \boldsymbol{X}(n,t)\boldsymbol{u}_\ell^*(n)\mathrm{e}^{-\mathrm{j}\omega_k t}.$$

The above expression can be conveniently rewritten in matrix form as

$$\widehat{\boldsymbol{X}} = \mathrm{JFT}\{\boldsymbol{X}\} = \boldsymbol{U}_G^*\boldsymbol{X}\overline{\boldsymbol{U}}_T. \tag{7.4}$$

Expressed in vector form, the transform becomes

$$\hat{\boldsymbol{x}} = \mathrm{JFT}\{\boldsymbol{x}\} = \boldsymbol{U}_J^*\boldsymbol{x}, \tag{7.5}$$

where $\boldsymbol{U}_J = \boldsymbol{U}_T \otimes \boldsymbol{U}_G$ is the Kronecker product of the basis. The relation between Eq. (7.4) and Eq. (7.5) is obtained through the property of the Kronecker product $(\boldsymbol{M}_1 \otimes \boldsymbol{M}_2)\,\boldsymbol{x} = \boldsymbol{M}_2\boldsymbol{X}\boldsymbol{M}_1^\intercal$.

Properties of JFT.

Property 1. *JFT is an invertible transform. The inverse JFT in matrix and vector form are, respectively,* $\text{JFT}^{-1}\{\widehat{\boldsymbol{X}}\} = \boldsymbol{U}_G \boldsymbol{X} \boldsymbol{U}_T^\intercal$ *and* $\text{JFT}^{-1}\{\hat{\boldsymbol{x}}\} = \boldsymbol{U}_J \boldsymbol{x}$.

Property 2. *The Parseval relation holds:*

$$\sum_{n,t=1}^{N,T} |\boldsymbol{X}(n,t)|^2 = \sum_{\ell,k=1}^{N,T} |\widehat{\boldsymbol{X}}(\ell,k)|^2. \tag{7.6}$$

Property 3. *The transform is independent of the order GFT and DFT are applied to the time-vertex signal*

$$\text{JFT}\{\boldsymbol{X}\} = \text{GFT}\{\text{DFT}\{\boldsymbol{X}\}\} = \text{DFT}\{\text{GFT}\{\boldsymbol{X}\}\}.$$

Property 4. *The subspace of zero graph and temporal frequency is spanned by the constant time-vertex signal* $\mathbf{1}\mathbf{1}^*$*, with* $\mathbf{1}$ *being the all-ones vector.*

7.3 Joint Time-Vertex Calculus

In the following, we briefly present the main time-vertex differential operators. These will help us (a) to perform calculus on finite, discrete time and space, and (b) to characterize the properties of the signals, such as smoothness, while taking into account the intrinsic structure of the data domain.

Time and vertex domains. Before introducing the time-vertex operators, we will define the standard operators in the time and graph domains applied to a time-vertex signal. Given a time-vertex signal $\boldsymbol{x} \in \mathbb{R}^N$, the first order time difference operator is defined as

$$\boldsymbol{X} \nabla_T|_t = \boldsymbol{x}_t - \boldsymbol{x}_{t-1},$$

taken here with periodic boundary conditions. Hence, the symmetric time Laplacian matrix $\boldsymbol{L}_T = \nabla_T^* \nabla_T$ is the discrete second order derivative in time with reversed sign

$$\boldsymbol{X} \boldsymbol{L}_T|_t = -\boldsymbol{x}_{t+1} + 2\boldsymbol{x}_t - \boldsymbol{x}_{t-1} \tag{7.7}$$

with $\boldsymbol{x}_{T+1} = \boldsymbol{x}_1$. As a circulant matrix, it has eigendecomposition $\boldsymbol{L}_T = \boldsymbol{U}_T \boldsymbol{\Lambda}_T \boldsymbol{U}_T^*$, where

$$\boldsymbol{\Lambda}_T(k,k) = 2\left(1 - \cos\left(\omega_k\right)\right). \tag{7.8}$$

The edge derivative with respect to edge $e = (n,m)$ at vertex n of the time-vertex signal $\boldsymbol{X}$ is given by

$$\left.\frac{\partial \boldsymbol{X}}{\partial e}\right|_n = \sqrt{\boldsymbol{W}(n,m)}\,[\boldsymbol{x}^n - \boldsymbol{x}^m]\,. \tag{7.9}$$

and, as before, $\boldsymbol{L}_G = \nabla_G^* \nabla_G$, where ∇_G^* is the divergence operator of the graph.

Joint domain. We define the joint gradient of a time-vertex signal $\boldsymbol{X}$ by concatenation of the time and graph gradients:

$$\nabla_J \boldsymbol{x} = \mathrm{vec}\left(\begin{bmatrix} \boldsymbol{X}\nabla_T^{\mathsf{T}} \\ \nabla_G \boldsymbol{X} \end{bmatrix}\right). \tag{7.10}$$

Therefore ∇_J can be rewritten as

$$\nabla_J = \begin{bmatrix} \nabla_T \otimes \boldsymbol{I}_G \\ \boldsymbol{I}_T \otimes \nabla_G \end{bmatrix}. \tag{7.11}$$

The Laplacian is classically defined to equal the divergence of the gradient, and also in this case the joint Laplacian is $\boldsymbol{L}_J = \nabla_J^* \nabla_J$. Expanding the expression while exploiting the mixed-product property of the Kronecker product, we find

$$\begin{aligned}
\boldsymbol{L}_J &= (\nabla_T \otimes \boldsymbol{I}_G)^*(\nabla_T \otimes \boldsymbol{I}_G) + (\boldsymbol{I}_T \otimes \nabla_G)^*(\boldsymbol{I}_T \otimes \nabla_G) \\
&= (\nabla_T^* \otimes \boldsymbol{I}_G)(\nabla_T \otimes \boldsymbol{I}_G) + (\boldsymbol{I}_T \otimes \nabla_G^*)(\boldsymbol{I}_T \otimes \nabla_G) \\
&= (\nabla_T^* \nabla_T) \otimes \boldsymbol{I}_G + \boldsymbol{I}_T \otimes (\nabla_G^* \nabla_G) \\
&= \boldsymbol{L}_T \otimes \boldsymbol{I}_G + \boldsymbol{I}_T \otimes \boldsymbol{L}_G = \boldsymbol{L}_T \times \boldsymbol{L}_G,
\end{aligned}$$

and therefore $\boldsymbol{L}_J$ is also equivalent to the Cartesian product between the time and graph Laplacians, proving that time-vertex domain can be interpreted as a particular case of multidimensional graph domain defined in Section 6.3. The joint Laplacian operator $\boldsymbol{L}_J$ applied to the time-vertex signal $\boldsymbol{x}$ is

$$\boldsymbol{L}_J \boldsymbol{x} = (\boldsymbol{L}_T \times \boldsymbol{L}_G)\,\boldsymbol{x} = \mathrm{vec}(\boldsymbol{L}_G \boldsymbol{X} + \boldsymbol{X}\boldsymbol{L}_T)\,.$$

The result of the Cartesian product is a multilayer graph, referred to as the *joint graph* J, where the original graph G is copied at each time step $t = 1, 2, \ldots, T$. Additionally, each node at layer t is connected to itself at layer $t-1$ and $t+1$ with periodic

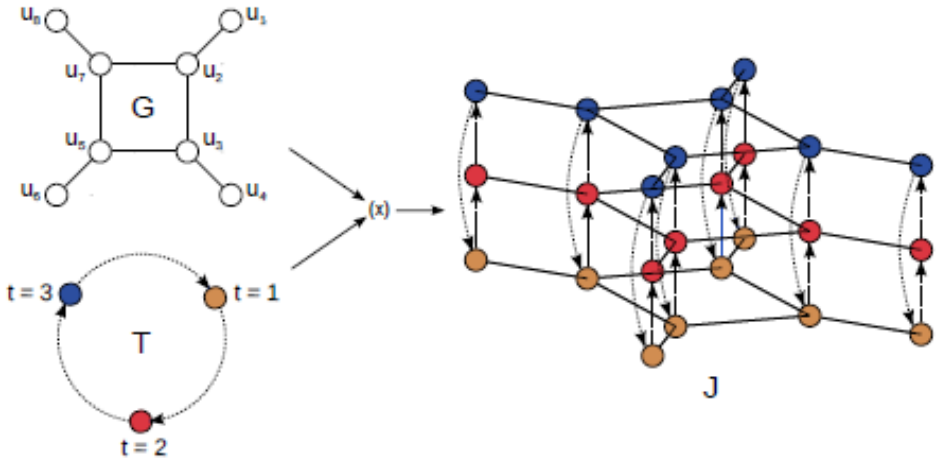

Figure 7.2 The joint graph J is the graph resulting from the Cartesian product of the input graph G and the discrete time domain classically represented as the cycle graph of length T.

boundary conditions. Figure 7.2, which was borrowed from [126], shows an example of joint graph construction as Cartesian product between a graph G and the time domain represented as a cycle graph with length T.

It is useful to remind that, in the case of multidimensional graph domain, the Kronecker product of the two eigenvectors basis $\boldsymbol{U}_T$ and $\boldsymbol{U}_G$ diagonalize the joint Laplacian with eigenvalues equal to the sum of all the pairs (ω_k, λ_ℓ):

$$\begin{aligned}\boldsymbol{L}_J &= \boldsymbol{L}_T \otimes \boldsymbol{I}_G + \boldsymbol{I}_T \otimes \boldsymbol{L}_G \\ &= (\boldsymbol{U}_T \boldsymbol{\Lambda}_T \boldsymbol{U}_T^*) \otimes \boldsymbol{I}_G + \boldsymbol{I}_T \otimes (\boldsymbol{U}_G \boldsymbol{\Lambda}_G \boldsymbol{U}_G^*) \\ &= (\boldsymbol{U}_T \otimes \boldsymbol{U}_G)(\boldsymbol{\Lambda}_T \times \boldsymbol{\Lambda}_G)(\boldsymbol{U}_T \otimes \boldsymbol{U}_G)^* = \boldsymbol{U}_J \boldsymbol{\Lambda}_J \boldsymbol{U}_J^*\end{aligned}$$

where we have used the mixed-product property of the Kronecker product. Please notice that here we consider the Cartesian product for its amenable spectral properties, but in general other graph products could be considered, such as the Kronecker product $J = G \otimes G_T$ or the strong product $J = G \boxtimes G_T = G \times G_T + G \otimes G_T$ [180], capable of modelling more complex time-spatial relations. However, one should be aware that this increase in complexity comes with a price to pay: the eigendecomposition of the combinatorial joint Laplacian cannot be simply derived from the eigenvectors of the separate domains.

Measures of joint variation. The gradient and its various norms are often used as regularizers in regression because they capture the variation of the signal over a domain of interest. The ℓ_2-norm of the joint gradient measures the total variation of the signal across edges and consecutive steps. Observe that

$$\begin{aligned}\|\nabla_J \boldsymbol{x}\|_2^2 &= \boldsymbol{x}^\intercal \boldsymbol{L}_J \boldsymbol{x} = \|\nabla_G \boldsymbol{X}\|_F^2 + \|\boldsymbol{X}\nabla_T\|_F^2 \\ &= \mathrm{tr}(\boldsymbol{X}^\intercal \boldsymbol{L}_G \boldsymbol{X}) + \mathrm{tr}(\boldsymbol{X}\boldsymbol{L}_T\boldsymbol{X}^\intercal)\end{aligned} \tag{7.12}$$

meaning that $\|\nabla_J \boldsymbol{x}\|_2^2$ is separable over the two domains.

Analogously, the ℓ_1-norm of the joint gradient can be written as the sum of the ℓ_1-norms

$$\|\nabla_J \boldsymbol{x}\|_1 = \|\mathrm{vec}(\nabla_G \boldsymbol{X})\|_1 + \|\mathrm{vec}(\boldsymbol{X}\nabla_T)\|_1, \tag{7.13}$$

which is often referred to as the Total Variation (TV) norm. In general, it is possible to define a mixed norm $\mathrm{N}_{p,q}(\cdot)$

$$\mathrm{N}_{p,q}(\boldsymbol{x}) \triangleq w_G \|\mathrm{vec}(\nabla_G \boldsymbol{X})\|_p^p + w_T \|\mathrm{vec}(\boldsymbol{X}\nabla_T)\|_q^q \tag{7.14}$$

where the p-norm and the q-norm are computed independently on the two domains and w_G, w_T are non-negative weights. Such norms are often useful when the signal vary differently (e.g., smooth or piece-wise) across the two domains, as we will show in Section 8.3.2.

7.4 Dynamics over Graphs

This section motivates the JFT further by showing that it can be used to characterize two linear PDEs evolving over the graph by kernels defined in the joint frequency domain, and also to provide insight on standard non-linear PDEs used in epidemic modeling. Our interest in PDEs analysis is related to their capability of encoding information about the structure of the underlying domain, whether continuous or discrete [197, 39]. Moreover, PDEs are not only simple but powerful models of many phenomena observed in reality, but also a motivation for the Fourier transform [66, 146].

7.4.1 Linear dynamics on graphs

We are interested in linear PDEs whose solution at each time step can be expressed as a linear operator applied to the initial condition. In particular, we consider the heat diffusion and the wave equations defined in the discrete setting. We denote as $\boldsymbol{x}_1$ the initial condition of the PDEs, or equivalently in the joint spectral domain $\boldsymbol{Z}(\ell,k) = \widetilde{\boldsymbol{x}_1}(\ell)\,\boldsymbol{U}_T^*(k,1)$.

Heat equation

The discrete heat diffusion equation

$$\boldsymbol{x}_t - \boldsymbol{x}_{t-1} = -s\boldsymbol{L}_G\boldsymbol{x}_t$$

is, arguably, one of the simplest dynamics described by differential equations. The parameter s represents thermal diffusivity and is interpreted as a scale parameter for multiscale dynamic graph wavelet analysis [38] and graph scale-space theory [125]. It is well understood that

$$\boldsymbol{x}_t = (\boldsymbol{I} - s\boldsymbol{L}_G)^{t-1}\boldsymbol{x}_1.$$

Evaluating both the GFT and DFT, one also finds that the solution also has distinct structure in the joint spectral domain

$$\widehat{\boldsymbol{X}}(\ell,k) = \frac{1}{\sqrt{T}}\frac{a(\lambda_\ell,\omega_k)^T - 1}{a(\lambda_\ell,\omega_k) - 1}\boldsymbol{Z}(\ell,k) \tag{7.15}$$

where $a(\lambda_\ell,\omega_k) = (1 - s\lambda_\ell)\,\mathrm{e}^{-\mathrm{j}\omega_k}$. The detailed proof can be found in Appendix B.1. The JFT of a heat diffusion process therefore exhibits a smooth non-separable low-pass form.

Wave equation

More interesting dynamics can be modeled by the discrete second order differential equation

$$\boldsymbol{X}\boldsymbol{L}_T = s\boldsymbol{L}_G\boldsymbol{X}$$

which represents a discrete wave propagating on a graph with speed $s > 0$. Figure 7.3 shows two waves propagating on a regular 2D lattice and on an irregular sensor

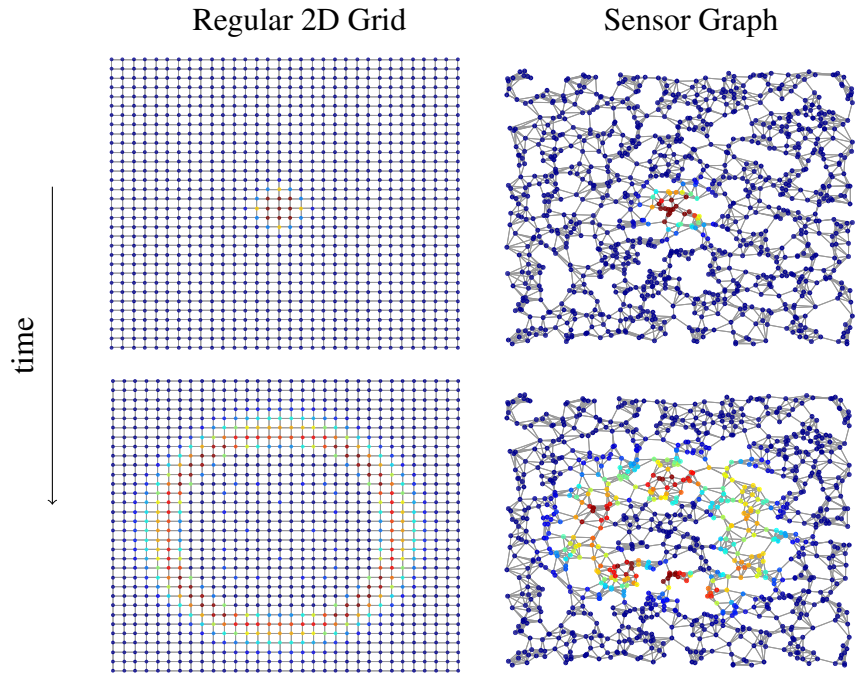

Figure 7.3 Solution to the wave equation on a regular 2D grid and on a sensor graph at different points in time. The propagating behavior is evident even in the case of irregular domain.

graph. In Appendix B.2, we show that the solution in the joint spectral domain can be written as

$$\widehat{\boldsymbol{X}}(\ell,k) = \widehat{K}_s(\lambda_\ell,\omega_k)\boldsymbol{Z}(\ell,k) \tag{7.16}$$

where

$$\widehat{K}_s(\lambda_\ell,\omega_k) = \sum_t \cos(t\vartheta_\ell)\mathrm{e}^{-\mathrm{j}\omega_k t}$$

and $\vartheta_\ell = \arccos(1-\frac{s\lambda_\ell}{2})$. To guarantee stability $s < 4/\lambda_{max}$. We remark that this result is in agreement with the stability analysis of numerical solver for the discrete wave equation presented in [54]. The distinctive pattern of a wave in the joint spectral domain, shown in Fig. 7.4 (bottom right), is sparser and more structured that the original (top left), GFT (top right), and DFT (bottom left) representations.

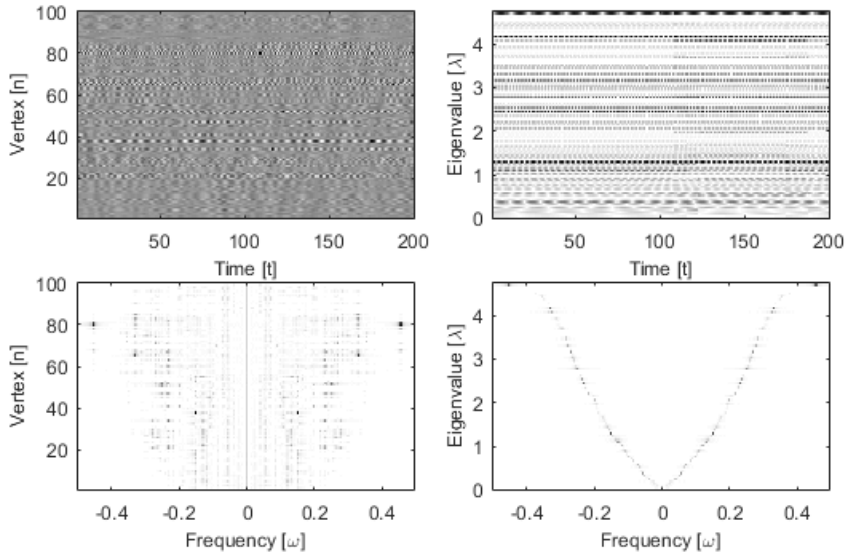

Figure 7.4 Frequency analysis of multiple waves propagating on a random sensor graph. The signals on each node of the graph evolve according to a PDE, but their time-vertex representation (top left) does not highlight any relation between the two domains. Similarly, GFT (top right) and DFT (bottom left) are not able to show the underlying structure. It is evident that JFT (bottom right) succeeds in representing the signal in the most meaningful way, revealing its regular pattern.

7.4.2 Complex dynamics over networks: the illustrative example of epidemic models

We next give an example of how the JFT provides insights on the evolution of a non-linear, discrete, and non-deterministic model for the spread of an infectious disease. In particular, we focus on the dynamics corresponding to different compartmental models commonly used in epidemiology [107]. We simulated the epidemics spreading over $N = 695$ cities of Europe according to two different models: the Susceptible-Exposed-Infected-Recovered (SEIR) model and the SEIRS model, where the immunity of recovered individuals is only temporary. The models are parametrized by the contagion probability of infection, the infectious, latent and immunity periods. Each node of the graph represents a city with a fixed population of individuals. Moreover, inter-city connections are modeled using two graphs, a terrestrial location-based graph and the graph of airline connections between the major city in Europe.

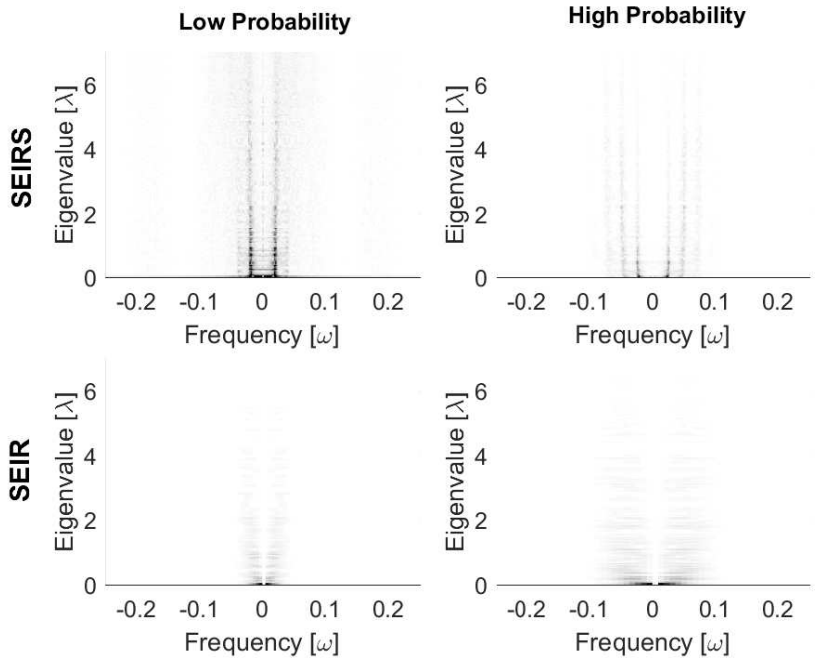

Figure 7.5 JFT of the signal representing the number of infected for different realization of epidemic spreads, using different models and contagion probability. The transform allows us to distinguish between the different parameters of the model.

Figure 7.5 shows the JFT of the simulated epidemic breakouts for the two different models. Each image shows the JFT of the signal describing the evolution of the number of infected over the graph. The transform is shown in the (ω, λ) plane, with a gray-scale color coded representation, where darker gray means higher energy. Observe that for the SEIRS model (top) the spectrum is characterized by regularly spaced lines along the angular frequency axis, occurring because every individual can be infected again after the temporary immunity period ceases. The spacing between the lines is due to both the immunity and latent periods. The SEIR model on the contrary exhibits a more diffusive behaviour, without evident periodicity. For each one of the models, we also simulated scenarios with high and low probabilities of contagion. It is seen that the high probability case is characterized by more energy in the higher part of the spectrum, due to a more impulsive behaviour of the epidemic breakout. It is interesting to note that the joint spectral representation allows us to differentiate between the different models and their parameters.

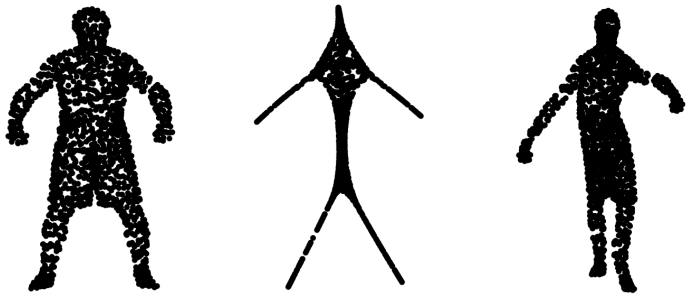

Figure 7.6 The effect of joint filters is easily visualized for the case of a dynamic mesh of a dancer. By filtering the original mesh (left) using a joint low-pass separable filter one approximates the time-varying skeleton of the dancer (center). Using a non-separable wave filter, the fluidity of the dancer's motion is emphasized (right).

7.5 Joint Time-Vertex Filters

In the following section we will recall the definition of multidimensional filter already given in Section 6.3.3, specifying this definition in the context of the time-vertex signal processing. A joint filter $h(\boldsymbol{L}_G, \boldsymbol{L}_T)$ is a function defined in the joint two-dimensional spectral domain $h : \mathbb{R}_+ \times \mathbb{R} \mapsto \mathbb{C}$ and is evaluated at the graph eigenvalues λ and the angular frequencies ω. Similarly to both the classical and the graph case, the generalized filtering operator is applied by means of the convolution theorem, i.e., point-wise multiplication in the spectral domain. The output of a joint filter is

$$h(\boldsymbol{L}_G, \boldsymbol{L}_T)\,\boldsymbol{x} = \boldsymbol{U}_J\, h(\boldsymbol{\Lambda}_G, \boldsymbol{\Omega})\, \boldsymbol{U}_J^* \boldsymbol{x}, \tag{7.17}$$

where $h(\boldsymbol{\Lambda}_G, \boldsymbol{\Omega})$ is a diagonal $NT \times NT$ matrix defined as

$$h(\boldsymbol{\Lambda}_G, \boldsymbol{\Omega}) = \text{diag vec}\left(\begin{bmatrix} h(\lambda_1, \omega_1) & \cdots & h(\lambda_1, \omega_T) \\ \vdots & \ddots & \vdots \\ h(\lambda_N, \omega_1) & \cdots & h(\lambda_N, \omega_T) \end{bmatrix}\right)$$

and the diag vec$(\boldsymbol{A})$ operator creates a matrix whose diagonal elements are the vectorized form of $\boldsymbol{A}$.

Illustration: dynamic mesh filtering. Figure 7.6 shows an example of joint filtering of a mesh representing a dancer[1]. The time-vertex signal $\boldsymbol{X} \in \mathbb{R}^{N \times T \times 3}$, with $N = 1502$ and $T = 573$, describes the time-varying coordinates of each vertex of the mesh. We design (a) a joint separable lowpass filter that attenuates high frequency components in both graph and time domains, and (b) a wave filter whose frequency response is described in Eq. (7.16). In the first case, we obtain the approximate skeleton of the mesh with rigid movements, whereas the wave filter produces a fluid (wavy) dancer, enhancing the frequency components in a nonlinear fashion. We remark that this effect can only be obtained using non-separable filters.

Separable vs. non-separable filters. A notable family of joint filters are those that have *separable* response

$$h(\lambda, \omega) = h_1(\lambda)\, h_2(\omega). \tag{7.18}$$

These filters have a straightforward interpretation: the frequency response of each filter affects only the domain where it is defined

$$h(\boldsymbol{L}_G, \boldsymbol{L}_T)\boldsymbol{x} = \mathrm{vec}(h_1(\boldsymbol{L}_G)\boldsymbol{X} h_2(\boldsymbol{L}_T))\,. \tag{7.19}$$

Moreover, since they can be designed independently at the two domains, joint filters can be obtained by combining graph and temporal filters [92]. However, due to their simple form, separable filters cannot model the dynamics of PDEs (e.g., waves or heat diffusion), where there is an interplay between the temporal and graph frequency domains. For this reason, in the following we find an efficient joint filter implementation for separable as well as non-separable filtering objectives.

7.5.1 Fast joint filtering

Due to the high complexity of eigendecomposition, as discussed in Section 6.2.1, graph filters are almost always implemented using fast polynomial [189] and rational [93] approximations. In the context of time-vertex analysis, the importance of fast joint filtering is emphasized by the increase of the problem's dimensions. Recognizing this need, researchers have recently proposed distributed joint filter 2D Chebychev polynomial [126] and separable rational [92] implementations, ap-

[1] http://research.microsoft.com/en-us/um/redmond/events/geometrycompression/data/default.html

propriate for arbitrary and separable joint response functions, respectively. In the following, we improve upon state of the art by enhancing the filtering approximation at a similar (up to logarithmic factors) complexity.

The Fast Fourier Chebyshev (FFC) algorithm. The basic idea of our algorithm is to exploit the small complexity of FFT and perform graph filtering in the time-frequency domain. Concretely, to filter $\boldsymbol{X}$ with response $h(\lambda,\omega)$, we do the following:

1. Compute the FFT of every row of $\boldsymbol{X}$, at a total complexity of $\mathscr{O}(NT\log T)$.
2. For each ω_k, approximate $h(\lambda,\omega_k)$ with a Chebyshev polynomial of order M_G and use the fast graph Chebyshev recursion [83] to filter the corresponding angular frequency component of $\boldsymbol{X}$. The complexity of this step is $\mathscr{O}(M_G T|\mathscr{E}|)$.
3. Use the inverse FFT to obtain the filtered time-vertex signal, with complexity $\mathscr{O}(NT\log T)$.

Our scheme can approximate both separable and non-separable joint filters using $\mathscr{O}(T|\mathscr{E}|M_G + NT\log T)$ operations, which up to a logarithmic factor is a linear complexity to the number of edges $|\mathscr{E}|$, nodes N, timesteps T, and filter order M_G. Moreover, it can be performed distributedly since both the FFT and the graph Chebychev recursion necessitate only local or few hop information.

Numerical comparison. To evaluate the approximation properties of the above scheme, we show in Figure 7.7 numerical experiments for an ideal separable lowpass filter and a non-separable wave filter on a time-vertex graph with size $N = 5000$, $T = 3000$. In detail, the approximated filtering functions (low pass and wave) are, respectively,

$$h_{\mathrm{LP}}(\lambda_\ell,\omega_k) = \frac{\mathrm{e}^{-(\lambda_\ell-\lambda_{\mathrm{cf}})}}{1+\mathrm{e}^{-(\lambda_\ell-\lambda_{\mathrm{cf}})}}\frac{\mathrm{e}^{-(|\omega_k|-\omega_{\mathrm{cf}})}}{1+\mathrm{e}^{-(|\omega_k|-\omega_{\mathrm{cf}})}} \tag{7.20}$$

$$h_{\mathrm{wave}}(\lambda_\ell,\omega_k) = \mathrm{e}^{-|\pi|\omega_k|-\arccos(1-\lambda_\ell/(2\lambda_{\max})|^2}. \tag{7.21}$$

For each case, we compare our algorithm with the state-of-the-art, i.e., Chebyshev2D approximation [126] and the ARMA2D approach [92], while choosing M_G and M_T as graph and temporal polynomial orders, respectively (here $M_G = M_T$).

As shown in Figure 7.7, FFC results in a significant improvement in accuracy for the same order and the difference is particularly prominent in the non-separable case (ARMA2D cannot be used here). We remark however that, to interpret these results correctly, one has to consider the complexity of each method:

method	complexity	applicability
FFC	$\mathcal{O}(T\|\mathscr{E}\|M_G + NT\log T)$	all
Cheby2D [126]	$\mathcal{O}(T\|\mathscr{E}\|M_T + NTM_TM_G)$	all
ARMA2D [92]	$\mathcal{O}(T\|\mathscr{E}\|M_G + T\|\mathscr{E}\|M_T)$	separable

Therefore, for the same order, the three different methods feature slightly different complexities, implying that a direct comparison of accuracy is very difficult. Figure 7.7, which compares error as a function of the order, does not reveal that the three different methods actually have different computation times for the same order. Nevertheless, in our experiments for all orders larger than 2, the asymptotic complexity of FFC is the smallest (since here $M_G = M_T$, $\log T < M_TM_G$, and $\log T < |\mathscr{E}|M_T/N$). We also note that, in practice one often needs $M_T \gg \log T$ to achieve a good approximation, in which case FFC is the fastest.

7.6 Joint Time-Vertex Dictionaries and Frames

So far, we have looked at time-vertex signals through the lenses of the canonical joint Fourier bases. However, in some cases it is beneficial to also consider alternative representations, as we have shown in Section 6.2.2 and Section 6.3.3 related to the context of GSP. The purpose of this section is to show how one can define analogous representations for time-vertex signals. These can be used for instance to generate features given as an input to a classifier (see Section 8.4.1) or to regularize an optimization problem such as (8.5).

Following the same approach of the graph domain, in order to build the atoms of the dictionary, we will define a kernel to which we will apply the transformation

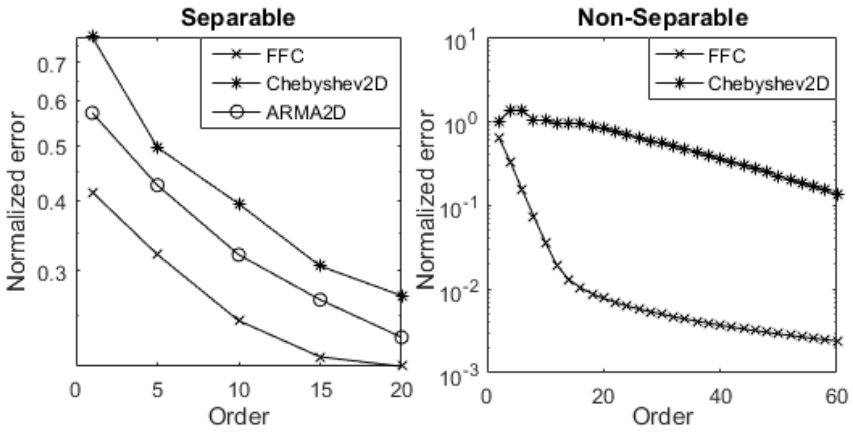

Figure 7.7 Fast joint filtering comparison using different algorithms to approximate the ideal joint lowpass filter (left) and a non-separable wave filter (right) approximated in Eq (7.20) and Eq (7.21), respectively. The proposed method (FFC) outperforms the others, in particular for non-separable filters.

function. The difference is that the kernel is defined in the time-vertex frequency domain and the localization performed using the joint time-vertex localization operator. The spectral time-vertex wavelet and the short time-vertex Fourier transforms follow as consequences of our framework.

7.6.1 Joint time-vertex localization

The ability to localize a kernel over a particular time and vertex is a key ingredient of our dictionary construction. In the following, we define the *joint time-vertex localization operator*, a generalization of the graph localization defined in Eq. (6.11) and time translation (Eq. (6.9), as the filtering with a two-dimensional Kronecker delta

$$\mathscr{T}^{J}_{m,\tau} h \stackrel{\Delta}{=} \mathrm{mat}(h(\boldsymbol{L}_J)\,(\boldsymbol{\delta}_m \otimes \boldsymbol{\delta}_\tau)) \tag{7.22}$$

$$\stackrel{\Delta}{=} h(\boldsymbol{L}_G, \boldsymbol{L}_T)\,(\boldsymbol{\delta}_m \otimes \boldsymbol{\delta}_\tau)\,. \tag{7.23}$$

where $\mathrm{mat}(\mathrm{vec}(\boldsymbol{X})) = \boldsymbol{X}$ is the matricization operator. It turns out that the joint time-vertex localization operator has the advantages of both the graph localization

and the traditional translation operator. Indeed, we observe the following relations

$$\begin{aligned}\mathscr{T}^J_{m,\tau} h(n,t) &= \frac{1}{T} \sum_{\substack{\ell=1 \\ k=1}}^{N,T} h(\lambda_\ell, \omega_k) \bar{\boldsymbol{u}}_\ell(m) \mathrm{e}^{-\mathrm{j}\omega_k \tau} \boldsymbol{u}_\ell(n) \mathrm{e}^{\mathrm{j}\omega_k t} \\ &= \frac{1}{T} \sum_{k=1}^{T} \left(\sum_{\ell=1}^{N} h(\lambda_\ell, \omega_k) \bar{\boldsymbol{u}}_\ell(m) \boldsymbol{u}_\ell(n) \right) \mathrm{e}^{\mathrm{j}\omega_k (t-\tau)} \end{aligned} \tag{7.24}$$

From (7.24), it follows that joint localization consists of three steps: (a) localizing independently all kernels $h(\cdot, \omega_k)$, (b) computing the inverse DFT along the other dimension, and (c) translating the result. Joint localization is thus equivalent to independent application of a graph localization and a translation. Note that the steps (a) and (b) can be considered as localizing the signal along the time dimension.

When the filter is separable, i.e. $h(\lambda, \omega) = h_G(\lambda) h_T(\omega)$, the joint localization is simply

$$h(\boldsymbol{L}_G, \boldsymbol{L}_T) \, (\boldsymbol{\delta}_\tau \otimes \boldsymbol{\delta}_m) = \mathrm{vec}(h_G(\boldsymbol{L}_G)(\boldsymbol{\delta}_\tau \otimes \boldsymbol{\delta}_m^\mathsf{T}) h_T(\boldsymbol{L}_T)) \,, \tag{7.25}$$

showing that the filter can be localized independently in time and in the vertex domain.

7.6.2 Joint time-vertex dictionaries

We proceed to present our dictionary construction for time-vertex signals. We start with a mother time-vertex kernel $h(\lambda, \omega)$ and a transformation $s_{z_\lambda, z_\omega}(\cdot, \cdot)$ parametrized by some values $[z_\lambda, z_\omega]$ belonging to the finite 2D set $\mathscr{Z}_\lambda \times \mathscr{Z}_\omega \subset \mathbb{R}^2$ and controlling the kernel's shape along the vertex and time domains. The transformed kernel is then obtained by composition

$$h_{z_\lambda, z_\omega}(\lambda, \omega) = h(s_{z_\lambda, z_\omega}(\lambda, \omega)). \tag{7.26}$$

We build our dictionary by transforming $h(\lambda, \omega)$ with all $z_\lambda, z_\omega \in \mathscr{Z}_\lambda \times \mathscr{Z}_\omega$, (possibly) normalizing, and jointly localizing the resulting kernels $h_{z_\lambda, z_\omega}(\lambda, \omega)$ at each node m and time τ. Concretely, the dictionary is

$$\begin{aligned}\mathscr{D}_h = \{ \mathscr{T}^J_{m,\tau} h_{z_\lambda, z_\omega} \} \quad &\text{for} \quad m \in \mathscr{V}, \ \tau = 1, 2, \ldots, T, \\ &\text{and } [z_\lambda, z_\omega] \in \{ \mathscr{Z}_\lambda \times \mathscr{Z}_\omega \}. \end{aligned} \tag{7.27}$$

When $\mathscr{D}_h$ is overly redundant, one may choose to consider only a subset of values for m and τ.

We next consider two interesting examples of the proposed dictionary construction that are generalizations of the short-time Fourier and wavelet transforms [34, 76]:

Short Time-Vertex Fourier Transform (STVFT). Set $s_{z_\lambda,z_\omega}(\cdot,\cdot)$ to a shift in the spectral domain

$$s_{z_\lambda,z_\omega}(\lambda,\omega) = [\lambda - z_\lambda, \omega - z_\omega]. \tag{7.28}$$

This transform can be considered as a modulation. Nevertheless, we note that it does not correspond to a multiplication by an eigenvector as in [187, 188]. Our construction is more related to [190, Section 3]. Then, given a separable mother kernel $h(\lambda,\omega) = h_G(\lambda)h_T(\omega)$ and a finite 2D set $\mathscr{Z}_\lambda \times \mathscr{Z}_\omega \subset \mathbb{R}^2$, the STVFT of signal $\boldsymbol{X}$ is defined as

$$\begin{aligned}\mathrm{STVFT}\{\boldsymbol{X}\}(m,\tau,z_\lambda,z_\omega) &\triangleq \langle \boldsymbol{X}, \mathscr{T}^J_{m,\tau} h(\lambda - z_\lambda, \omega - z_\omega)\rangle \\ &= \frac{1}{\sqrt{T}} \sum_{\ell,k} h(\lambda_\ell - z_\lambda, \omega_k - z_\omega)\widehat{\boldsymbol{X}}(\ell,k)\boldsymbol{u}_\ell(m)\mathrm{e}^{\mathrm{j}\omega_k\tau}.\end{aligned}$$

Provided that $h(\lambda,\omega)$ is localized around $[0,0]$, the amplitude of the coefficient (n,t,z_λ,z_ω) indicates the presence of the spectral mode $[z_\lambda,z_\omega]$ at vertex m and time τ. Moreover, since the mother kernel is separable, the design in the two domains can be performed independently:

For the graph domain, we suggest to select the values of z_λ to be equally spaced in $[0,\lambda_{\max}]$ [190, Section 3]. The spacing should be selected such that $\sum_{z_\lambda\in\mathscr{Z}_\lambda} h_G^2(\lambda_\ell - z_\lambda) \approx c$ for every λ_ℓ, ensuring good conditioning of the associated frame (see [83, Theorem 5.6]). Because of the graph irregularity, in most of the cases, we need to keep all possible values for m, i.e., $m = 1,2,\ldots,N$.

For the time domain, we recover a traditional STFT, with the difference that $h_T(\omega)$ is defined in the spectral domain. Nevertheless, for convenience, the window can still be designed in the time domain. As a rule of thumb $|\mathscr{Z}_\omega| = l_{h_T}$, where l_{h_T} is the support of h_T in the time domain[2], and the values of τ should be sampled regularly with a spacing $\frac{l_{h_T}}{R}$, where R is the desired redundancy. The choice of the

[2]In practice, the kernel is chosen to have a compact support in the time-domain.

window is highly linked to the addressed problem. Nevertheless, there are some general rules that are usually considered. Because of the Heisenberg uncertainty principle, there is a trade-off between localization in time and frequency. As a result, one should choose first the desired precision in one of the two domains. Then, a window shape can be selected that minimizes the uncertainty in order to maximize the simultaneous precision in both domains (i.e., it should be similar to a Gaussian function). Eventually, the sampling parameters have to be chosen. Usually in order to avoid unnecessary computations, the length of the support of the windows is used as the number of frequency channels. Then, the shift in time is selected to achieve a desired redundancy or to ensure some properties such as tightness. For a more complete treatment we refer the reader to [34].

Spectral Time-Vertex Wavelet Transform (STVWT). Following the idea developed in [83], we set $s_{z_\lambda,z_\omega}(\cdot,\cdot)$ to a generalized graph dilation (or scaling), i.e., a multiplication in the spectral domain

$$s_{z_\lambda,z_\omega}(\lambda,\omega) = [z_\lambda\,\lambda, z_\omega\,\omega]. \tag{7.29}$$

Then, given a kernel $h(\lambda,\omega)$ the STVWT of $\boldsymbol{X}$ reads

$$\begin{aligned}\mathrm{STVWT}\{\boldsymbol{X}\}(m,\tau,z_\lambda,z_\omega) &\triangleq \langle \boldsymbol{X}, \mathscr{T}^J_{m,\tau} h(z_\lambda\,\lambda, z_\omega\,\omega)\rangle \\ &= \frac{1}{\sqrt{T}}\sum_{\ell,k} h(z_\lambda\,\lambda, z_\omega\,\omega)\widehat{\boldsymbol{X}}(\ell,k)\boldsymbol{u}_\ell(m)\mathrm{e}^{\mathrm{j}\omega_k\tau},\end{aligned}$$

where z_λ, z_ω are the scale parameters for the vertex and the time dimensions. A usual requirement for $h(\lambda,\omega)$ is that it has a zero DC component, i.e., $h(0,0)=0$. Contrarily to the STVFT, the mother kernel here may not be separable, as illustrated in Section 8.4.2.

The choice of the discretization lattice $[m,\tau,z_\lambda,z_\omega]$ is thus more involved and case dependent: we suggest that m and τ take all possible N and T values respectively, while z_λ and z_ω are carefully selected depending on the application. This choice is justified by the computational complexity detailed in the following.

Illustration: dynamic mesh manipulation. Figure 7.8 shows an example of manipulation of a dynamic mesh representing a walking dog using a joint dictionary. We design the filter bank using a separable tight Meyer mother kernel, with 4 filters

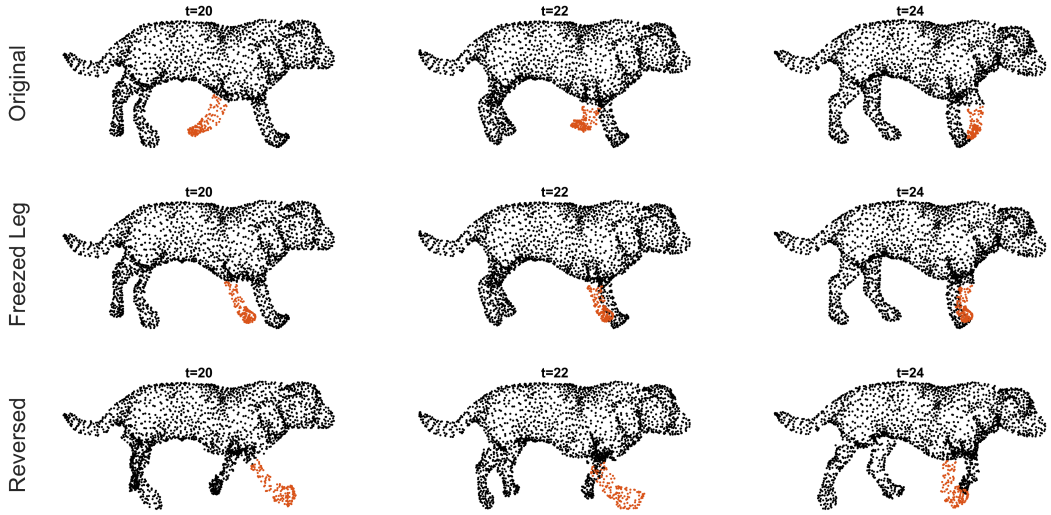

Figure 7.8 Manipulation of dog dynamic mesh using a joint dictionary based on the Meyer filter bank. The columns show the meshes at three different time steps to illustrate the changes in the time domain. The first row displays the original mesh, whereas the second and third show the correspondent manipulated meshes. In the second row, we set to zero the coefficients of the medium-high frequency localized on the paw of the dog (red dots), resulting in the absence of movement without affecting the general quality. Conversely, in the third we change the signs of the coefficients localized on the four legs, inverting the alternating leading leg.

in the graphs domain and 4 in the time domain. As in the previous example, the time-vertex signal $\boldsymbol{X} \in \mathbb{R}^{N \times T \times 3}$, with $N = 2502$ and $T = 59$, describes the time-varying coordinates of each vertex of the mesh. The three columns in the figure show the mesh at three different time steps, for $t = 20, 22, 24$, to illustrate the changes in the time domain. The first row displays the original mesh, whereas the second and third show the manipulated meshes at the same time instant. The meshes in the second row are obtained using the dictionary analysis operator and putting to zero all the coefficients localized on the paw of the dog, with the exception of those corresponding to the scaling function. In the time-vertex domain this corresponds to freeze the movements of the paw without affecting the general quality. Finally, the last triplet of meshes shows the dog with inverted leading leg alternation, obtained changing the signs of the coefficients in the medium-high frequency band in the joint spectral domain, localized on the four legs of the dog.

7.6.3 Joint time-vertex frames

To make the proposed dictionaries and associated signal representations usable in practice, we next provide answers to three key questions: (a) How can we compute the representations efficiently (i.e., performing analysis and synthesis)? (b) How can we guarantee that the associated transforms are well-conditioned such that they can be successfully inverted? (c) How to efficiently invert them, recovering the original signal? The second point is particularly important since a well conditioned transform allows for more robust representations, for instance when the dictionary is used to solve a synthesis or analysis regression problem with a sparse regularizer.

Efficient analysis and synthesis.

The dictionary atoms can be seen as a filter bank $\{h_z(\lambda,\omega)\}_{z\in\mathscr{Z}_\lambda\times\mathscr{Z}_\omega}$, in which case the operators going from the signal to the representation domain and back are, once again, the analysis operator

$$D_h\{\boldsymbol{X}\}(m,\tau,z) = \langle \boldsymbol{X}, \mathscr{T}^J_{m,\tau} h_z\rangle = \boldsymbol{C}_z(m,\tau),$$

and the synthesis operator

$$D^*_h\{\boldsymbol{C}\}(n,t) = \sum_z \langle \boldsymbol{C}_z, \mathscr{T}^J_{n,t} h_z\rangle = \boldsymbol{Y}(n,t).$$

Notice that in general $\boldsymbol{X}\neq\boldsymbol{Y}$, and equality holds only when the filter-bank is a unitary tight frame.

Instead of computing the dictionary explicitly (an operation that is costly both in memory and in computations), one may acquire the analysis coefficients for all m,τ by joint filtering $\boldsymbol{X}$ with kernel h_{z_λ,z_ω} taking advantage of the relation $\boldsymbol{C}_z = \mathrm{mat}(h_z(\boldsymbol{L}_G,\boldsymbol{L}_T)\boldsymbol{x})$. Similarly synthesis can be performed by summing filtering operations. Using our FFC filtering algorithm presented in Section 7.5.1, the total analysis complexity is thus $\mathscr{O}(|\mathscr{Z}_\lambda\times\mathscr{Z}_\omega|(T|\mathscr{E}|M_G+NT\log T))$, where typically $M_G\approx 50$.

The drawback of this technique is that it does not allow us to take advantage of sub-sampling the lattice $[n,t]$, especially in the non-separable case. Indeed, a filtering operation will always provide all coefficients regardless of the desired lattice. While

addressing this computational problem is beyond the scope of this contribution, we note that we can still efficiently perform a sub-sampled STVFT by first filtering only in the graph domain and second computing a traditional STFT.

Conditioning and frame bounds.

The following theorem generalizes the classic [34] results regarding the frame bounds, providing a condition for a joint time-vertex dictionary to be a frame, as presented in the case of graphs in Definition 1.

Theorem 2. *Let* $\{h_z(\lambda,\omega)\}_{z\in\mathscr{Z}_\lambda\times\mathscr{Z}_\omega}$ *be the kernels of a time-vertex dictionary* $\mathscr{D}_h$*, and set*

$$A = \min_{\ell,k} \sum_z |h_z(\lambda_\ell,\omega_k)|^2,$$
$$B = \max_{\ell,k} \sum_z |h_z(\lambda_\ell,\omega_k)|^2.$$

If $0 < A \leq B < \infty$*, then* D_h *is a frame in the sense:*

$$A\|\boldsymbol{X}\|_F^2 \leq \|D_h\{\boldsymbol{X}\}\|_F^2 \leq B\|\boldsymbol{X}\|_F^2 \tag{7.30}$$

for any time-vertex signal $\boldsymbol{X} \in \mathbb{R}^{N\times T}$*.*

Proof. For the proof please refer to Appendix B.3. □

As in the case of GSP, the frame bound theorem asserts that, if $A > 0$, no information is lost when the analysis operator is applied to a time-vertex signal, thus the transform is invertible. Furthermore, the ratio A/B of the frame bounds is related to the condition number of the frame operator $S_h\{\boldsymbol{X}\} = D_h^*\{D_h\{\boldsymbol{X}\}\}$, hence it is decisive for efficient reconstruction when we want to recover the signal from its representation solving an optimization problem [83, Section 7].

Efficient inversion.

To recover the signal $\boldsymbol{X}$ from the coefficients $\boldsymbol{C}$, a solution is to use the pseudo-inverse, i.e. $\boldsymbol{X} = D_h^{\dagger}\{\boldsymbol{C}\}$ or to solve the following convex problem

$$\arg\min_{\boldsymbol{X}} \|D_h\{\boldsymbol{X}\} - \boldsymbol{C}\|_2^2.$$

Problematically, these are computationally intractable for large values of N and T. We will instead design a dual set of kernels that allows us to invert the transform by a single synthesis operation. To this end, we search for a set of filters $\tilde{h}$ such that $D_{\tilde{h}}^{*}\{D_h\{\boldsymbol{X}\}\} = \boldsymbol{X}$. It is not difficult to see that this equality is satisfied when

$$\sum_{z_\lambda, z_\omega} \tilde{h}_{z_\lambda, z_\omega}(\lambda_\ell, \omega_k)\, \overline{h_{z_\lambda, z_\omega}}(\lambda_\ell, \omega_k) = 1, \quad \forall\, \lambda_\ell, \omega_k. \tag{7.31}$$

Although redundant joint time-vertex frames admit an infinite number of dual kernel sets satisfying (7.31), the typical choice is to use the *canonical dual*, defined as

$$\tilde{h}_{z_\lambda, z_\omega}(\lambda_\ell, \omega_k) = \left(\sum_{z'_\lambda, z'_\omega} h^2_{z'_\lambda, z'_\omega}(\lambda_\ell, \omega_k) \right)^{-1} h_{z_\lambda, z_\omega}(\lambda_\ell, \omega_k). \tag{7.32}$$

In fact, this corresponds to the pseudo-inverse of D_h, i.e., $D_h^{\dagger} = D_{\tilde{h}}^{*}$, while also having a low computational complexity.

To summarize, given an invertible time-vertex transform D_h and coefficients $\boldsymbol{C}$, the inverse transform of D_h associated with the set of kernels $\{h_{z_\lambda, z_\omega}\}_{[z_\lambda, z_\omega] \in \mathscr{Z}}$ is

$$\boldsymbol{X} = D_{\tilde{h}}^{*}\{\boldsymbol{C}\} = \sum_{z_\lambda, z_\omega} \tilde{h}_{z_\lambda, z_\omega}(\boldsymbol{L}_G, \boldsymbol{L}_T)\boldsymbol{C}_{z_\lambda, z_\omega}, \tag{7.33}$$

where $\tilde{h}$ is defined in (7.32).

7.7 Joint Time-Vertex Stationarity

In the context of statistical signal processing, we can interpret the time-vertex signal $\boldsymbol{X}$ as a discrete multivariate stochastic process with finite number of time-steps T that is indexed by vertex v_i and time t. We refer to such processes as *joint time-*

vertex processes, or *joint* processes. Our objective is to provide a definition of stationarity that captures statistical invariance of the first two moments of a joint process $\boldsymbol{x} = \text{vec}(\boldsymbol{X}) \sim \mathscr{D}(\mathbb{E}[\boldsymbol{x}], \boldsymbol{\Sigma})$, which are the mean $\mathbb{E}[\boldsymbol{x}]$ and the covariance $\boldsymbol{\Sigma}_{\boldsymbol{x}}$, and, at the same time, expresses its statistical properties with respect to the graph and temporal structure.

Without any assumption, the covariance of the process $\boldsymbol{x}$ can be written as the matrix

$$\boldsymbol{\Sigma} = \begin{bmatrix} \boldsymbol{\Sigma}(1,1) & \boldsymbol{\Sigma}(1,2) & \cdots & \boldsymbol{\Sigma}(1,T) \\ \boldsymbol{\Sigma}(2,1) & \boldsymbol{\Sigma}(2,2) & & \\ \vdots & & \ddots & \\ \boldsymbol{\Sigma}(T,1) & & & \boldsymbol{\Sigma}(T,T) \end{bmatrix}. \tag{7.34}$$

Let us review the established definitions of stationarity over time and vertex domains, respectively. We will see that enforcing the structure on the covariance matrix relative to time and vertex stationarity will lead us to a necessary and sufficient condition for joint stationarity.

Definition 3 (Time stationarity)**.** *A joint process $\boldsymbol{X} = [\boldsymbol{x}^1, \boldsymbol{x}^2, \ldots, \boldsymbol{x}^N]$ is Time Wide-Sense Stationary (TWSS), if and only if the following two properties hold:*

1. *The expected value is constant over the time domain*

$$\mathbb{E}[\boldsymbol{x}^n] = c\mathbf{1}_T \qquad n = 1, \ldots, N.$$

2. *For all t_1 and t_2, the second moment $\boldsymbol{\Sigma}(t_1, t_2)$ satisfies*

$$\boldsymbol{\Sigma}(t_1, t_2) = \boldsymbol{\Sigma}(t_1 - t_2 + 1, 1) = \boldsymbol{\Gamma}(\tau) \qquad \tau = t_2 - t_1$$

The Time Power Spectral Density (TPSD) is defined as

$$\widehat{\boldsymbol{\Gamma}}_k = \sum_{\tau=1}^{T} \boldsymbol{\Gamma}_\tau \mathrm{e}^{-\mathrm{j}\omega_k \tau} \tag{7.35}$$

Therefore, assuming time stationarity is equivalent to asserting that the statistics of the first moment is independent of time and the second moment can be written as

a block circulant matrix

$$\boldsymbol{\Sigma} = \begin{bmatrix} \boldsymbol{\Gamma}(1) & \boldsymbol{\Gamma}(T) & \cdots & \boldsymbol{\Gamma}(2) \\ \boldsymbol{\Gamma}(2) & \boldsymbol{\Gamma}(1) & & \\ \vdots & & \ddots & \\ \boldsymbol{\Gamma}(T) & & & \boldsymbol{\Gamma}(1) \end{bmatrix}. \tag{7.36}$$

We also observe that the TPSD is the Fourier transform of the autocorrelation in time $\boldsymbol{\Gamma}$, agreeing with the Wiener-Khintchine Theorem [215]. To summarize, TPSD encodes the statistics of the signal in the spectral domain. This consideration allows us to generalize the concept of stationarity to graph signals. Please refer to the work of Perraudin and Vandergheynst [162] for a more detailed study. We express a variation of their definition in the following.

Definition 4 (Vertex stationarity)**.** *A joint process $\boldsymbol{X} = [\boldsymbol{x}_1 \boldsymbol{x}_2 \dots \boldsymbol{x}_T]$ is called Vertex Wide-Sense (or second order) Stationary (VWSS), if and only if the following two properties hold:*

1. *The expected value is in the null space of the graph Laplacian*

$$\boldsymbol{L}_G \mathbb{E}[\boldsymbol{x}_t] = \boldsymbol{0}_N.$$

2. *For all t_1 and t_2, there exists a graph kernel $\gamma_{t_1,t_2}(\boldsymbol{L}_G)$, such that*

$$\boldsymbol{\Sigma}(t_1,t_2) = \gamma_{t_1,t_2}(\boldsymbol{L}_G) \tag{7.37}$$

The kernel γ_{t_1,t_2} is the autocorrelation function of signal $\boldsymbol{x}_t$ in the graph Fourier domain and is also referred to as Vertex Power Spectral Density (VPSD).

Considering that the null space of $\boldsymbol{L}_T$ in both the normalized and the combinatorial case is the span of the constant eigenvector $\boldsymbol{1}_T$, the first condition of the above definition is analogous to the corresponding condition of the time stationarity definition. It follows from the definition above that the covariance matrix of a VWSS

process is a block matrix where each block is a linear graph filter, i.e.,

$$\boldsymbol{\Sigma} = \begin{bmatrix} \gamma_{1,1}(\boldsymbol{L}_G) & \gamma_{1,2}(\boldsymbol{L}_G) & \cdots & \gamma_{1,T}(\boldsymbol{L}_G) \\ \gamma_{2,1}(\boldsymbol{L}_G) & \gamma_{2,2}(\boldsymbol{L}_G) & & \\ \vdots & & \ddots & \\ \gamma_{T,1}(T) & & & \gamma_{T,T}(\boldsymbol{L}_G) \end{bmatrix}.$$

This second condition is in fact equivalent to a generalization of the Wiener-Khintchine theorem and implies that $\boldsymbol{\Sigma}_{\boldsymbol{x}_t}$ is jointly diagonalizable with $\boldsymbol{L}_G$, whereas for a TWSS process the covariance is Toeplitz and thus also diagonalizable with the DFT matrix $\boldsymbol{U}_T$.

We now unify the TWSS and VWSS definitions in order to leverage both the time and vertex domain statistics.

Definition 5 (Joint stationarity)**.** *A process $\boldsymbol{X}$ is called Jointly (or time-vertex) Wide-Sense Stationary (JWSS), if and only if $\boldsymbol{x} = vec(\boldsymbol{X})$ satisfies the following properties:*

1. *The expected value is in the null space of the joint Laplacian*

$$\boldsymbol{L}_J \mathbb{E}[\boldsymbol{x}] = \boldsymbol{0}_{NT}.$$

2. *There exists a joint filter $h(\boldsymbol{L}_G, \boldsymbol{L}_T)$, such that*

$$\boldsymbol{\Sigma} = h(\boldsymbol{L}_G, \boldsymbol{L}_T) \tag{7.38}$$

The kernel $h(\cdot,\cdot)$ is a non-negative real function referred to as joint power spectral density (JPSD).

With the usual choice of $\boldsymbol{L}_G$ being the combinatorial graph Laplacian, the definition above is in fact equivalent to say that the mean of the process $\mathbb{E}[\boldsymbol{x}]$ is constant. Moreover, the covariance matrix $\boldsymbol{\Sigma}$ of a JWSS process is jointly diagonalizable with the joint Laplacian $\boldsymbol{L}_J$, hence it can be considered a generalization of the Wiener-Khintchine theorem.

Finally, the following theorem asserts that joint stationarity is equivalent to stationarity in both domains.

Theorem 3. *If a joint process $\boldsymbol{X}$ is JWSS, then it is both TWSS and VWSS.*

Proof. For the proof please refer to Appendix B.4. □

Property 1 (White *i.i.d.* noise)**.** *White i.i.d. noise $\boldsymbol{w} \in \mathbb{R}^{NT}$ is JWSS for any graph. Indeed, the first moment $\mathbb{E}[\boldsymbol{w}]$ is constant for any time and vertex. Moreover, due to being an identity matrix, the covariance of $\boldsymbol{w}$ is diagonalized by the joint Fourier basis of any graph $\boldsymbol{\Sigma}_{\boldsymbol{w}} = \boldsymbol{I} = \boldsymbol{U}_J \boldsymbol{I} \boldsymbol{U}_J^*$. This last equation tells us that the JPSD is constant, which implies that similar to the classical case, white noise contains all joint (time-vertex) frequencies.*

An interesting property of JWSS processes is that stationarity is preserved through a filtering operation.

Theorem 4. *When a joint filter $f(\boldsymbol{L}_G, \boldsymbol{L}_T)$ is applied to a JWSS process $\boldsymbol{X}$, the result $\boldsymbol{Y}$ remains JWSS with mean $f(0,0)\,\mathbb{E}[\boldsymbol{X}]$ and JPSD that satisfies*

$$h_{\boldsymbol{y}}(\lambda, \omega) = f^2(\lambda, \omega)\, h_{\boldsymbol{x}}(\lambda, \omega). \tag{7.39}$$

Proof. For the proof please refer to Appendix B.4. □

Theorem 4 provides a simple way to artificially produce JWSS signals with a prescribed PSD f^2 by simply filtering white noise with the joint filter $f(\boldsymbol{L}_G, \boldsymbol{L}_T)$. The resulting signal will be stationary with PSD f^2 and this holds for white noise abiding to any distribution (not only Gaussian). Whenever it is clear from the context, in the following we simply refer to the TPSD, VPSD, and JPSD as PSD.

7.7.1 Joint power spectral density estimation

As the JPSD is central in our method, we need a reliable way to compute it. Since we take into account the correlation both in the time and in the vertex domain, the actual size of the covariance matrix $\boldsymbol{\Sigma}$ is $NT \times NT$. In many cases, this matrix is not computable nor can be even stored. Additionally, using classical covariance estimation methods, the number of samples necessary for obtaining a reasonable

estimation accuracy can be prohibitive. The number of samples needed for obtaining a good sample covariance matrix of an n-dimensional process is generally not known, but for distributions with finite second moment it has been shown to be $O(n\log n)$ by Rudelson [175, 209]. In our case, this theorem implies that we need $O(NT\log(NT))$ signals, of NT variables each, to obtain a good estimate of the statistics of a joint process.

To circumvent this issue, we leverage the time-vertex structure of the data. The basic idea behind our approach stems from two established methods used to estimate the TPSD of a temporal signal, namely Bartlett's and Welch's methods. In Bartlett's method [11], the signal is first cut into equally sized segments without overlap. Then, the Fourier transform of each segment is computed. Finally, the PSD is obtained by averaging over segments the squared amplitude of the Fourier coefficients. Welch's method [214] is a generalization that works with overlapping segments. We can see the TPSD estimation of both methods as the averaging over time of the squared coefficients of the Short Time Fourier Transform (STFT), already discussed in Section 3.3. Based on the idea that the Bartlett method is an average of STFT coefficients, we propose to use the GFT of the STFT as a tool to estimate the joint PSD. Consider a time window $\boldsymbol{g}$ and a time-vertex signal $\boldsymbol{X}$. We first define the coefficients' tensor as

$$\begin{aligned}\boldsymbol{C}_{n,k,m} &\triangleq \sum_{i=1}^{N} [\boldsymbol{U}_G]_{i,n}\,\mathrm{STFT}\{\boldsymbol{x}^i\}(k,m)\\ &= \sum_{i=1}^{N} [\boldsymbol{U}_G]_{i,n} \sum_{t=1}^{T} \boldsymbol{X}_{i,t}\,\overline{\boldsymbol{g}(t_k)}\, e^{-2\pi j \frac{(t-1)(m-1)}{M}}.\end{aligned}$$

A usual parameter for M is the support size of $\boldsymbol{g}$. Then, for half-overlapping windows, we set a to $M/2$. For any discrete vertex frequency λ_n and time frequency $\omega_m = 2\pi m/M$, our JPSD estimator is

$$\tilde{h}(\lambda_n,\omega_m) \triangleq \frac{a}{T\|\boldsymbol{g}\|_2^2} \sum_{k=0}^{\lfloor T/a \rfloor - 1} \boldsymbol{C}_{n,k,m}^2 \tag{7.40}$$

In order to get an estimate of h at $\omega \neq \omega_m$, we interpolate between the known points. Alternatively, with sufficient computational power, one may set $M = T$. Though

alternative choices are possible, we suggest using the iterated sine window

$$g(t) = \sin\left(0.5\pi\cos\left(\pi t/M\right)^2\right)\chi_{[-M/2,M/2]}(t),$$

where $\chi_{[-M/2,M/2]}(t) = 1$ if $t \in [-M/2, M/2]$ and 0 otherwise, as it turns the STFT into a tight operator for $M = 2a$.

7.7.2 Recovery of JWSS process

We can leverage our definition of stationarity to generalize the optimization framework of [162], useful for denoising, interpolating, and more generally deconvolving stationary processes. Concretely, suppose that our measurements $\boldsymbol{y}$ are generated by a linear model

$$\boldsymbol{y} = \boldsymbol{A}\boldsymbol{x} + \boldsymbol{w}, \tag{7.41}$$

where, as in the rest of this document, $\boldsymbol{x}$ and $\boldsymbol{y}$ are the vectorized version of $\boldsymbol{X}, \boldsymbol{Y}$. Further, suppose that the JPSD of $\boldsymbol{x}$ is $h_{\boldsymbol{X}}$, whereas the noise $\boldsymbol{w}$ is zero mean, has JPSD $h_{\boldsymbol{W}}$ and may follow any distribution. Matrix $\boldsymbol{A}$ is a general linear operator, not assumed to be jointly diagonalizable with $\boldsymbol{L}_J$. We propose to recover $\boldsymbol{x}$ as the solution of the Wiener optimization problem

$$\dot{\boldsymbol{x}} = \arg\min_{\boldsymbol{x}} \|\boldsymbol{A}\boldsymbol{x} - \boldsymbol{y}\|_2^2 + \|f(\boldsymbol{L}_J)(\boldsymbol{x} - \mathbb{E}[\boldsymbol{x}])\|_2^2, \tag{7.42}$$

where $f(\lambda, \omega)$ are the joint Fourier penalization weights, defined as

$$f(\lambda,\omega) \triangleq \left|\sqrt{\frac{h_{\boldsymbol{W}}(\lambda,\omega)}{h_{\boldsymbol{X}}(\lambda,\omega)}}\right| = \frac{1}{\sqrt{\mathrm{SNR}(\lambda,\omega)}}. \tag{7.43}$$

In the noise-less case, one alternatively solves the problem

$$\dot{\mathbf{x}} = \arg\min_{\boldsymbol{x}} \|h_{\boldsymbol{X}}^{-\frac{1}{2}}(\boldsymbol{L}_J)\,\boldsymbol{x}\|_2^2, \quad \text{subject to} \quad \boldsymbol{A}\boldsymbol{x} = \boldsymbol{y}. \tag{7.44}$$

Intuitively, the weight $f(\lambda, \omega)$ heavily penalizes frequencies associated with low SNR and vice-versa. Formally, we can show that:

- If $\boldsymbol{X}$ is a Gaussian process, then the solution of Problem (7.42) coincides with a MAP estimator.

- If $\boldsymbol{A}$ is a masking operator, then the solution of Problem (7.42) coincides with the minimum mean square error linear estimator.
- If $\boldsymbol{A} = a(\boldsymbol{L}_J)$ is a joint filter, then the solution of Problem (7.42) is a joint Wiener filter [126].

The proofs are generalizations of Theorems 3, 4 and 5 of [162].

Comparison to the MAP estimator. There are three main advantages of the Wiener optimization framework over a Gaussian MAP estimator based on an empirical covariance matrix estimate. Firstly, assuming stationarity allows for a more robust estimate of the covariance matrix. This is crucial in this problem since we typically expect the number of variables $N \times T$ to be large and an empirical estimate of the covariance matrix to be expensive. Secondly, storing the covariance might not be possible as it consists of $O((NT)^2)$ elements. On the contrary, the JPSD $h_{\boldsymbol{X}}$ has only NT elements. Finally, thanks to proximal splitting methods, we can derive an algorithm for solving Problem (7.42) which requires only the application of $\boldsymbol{A}$ and spectral graph filtering. On the contrary the classical Gaussian MAP estimator requires the inverse of a large part of the covariance matrix.

Chapter 8

Applications of Time-Vertex Analysis: Signal Processing, Machine Learning and Cardiac Electrophysiology

Part of the work described in this chapter has been previously published in F. Grassi, A. Loukas, N. Perraudin and B. Ricaud, "A Time-Vertex Signal Processing Framework: Scalable Processing and Meaningful Representations for Time-Series on Graphs," in IEEE Transactions on Signal Processing, vol. 66, no. 3, pp. 817-829, Feb.1, 2018.

8.1 Introduction

The suitability of the time-vertex framework for several classes of problems is illustrated on a wide variety of datasets: (a) dynamic meshes representing a walking dog and a dancing man, (b) the Caltrans Performance Measurement System (PeMS) traffic dataset depicting high resolution daily vehicle flow of 10 consecutive days in the highways of Sacramento measured every 5 minutes, (c) simulated SEIR- or SEIRS-type epidemics over Europe, (d) the Kuala Lumpur City Centre (KLCC) time-lapse video and (e) earthquake waveforms recorded by seismic stations geographically distributed in New Zealand, connected to the GeoNet Network, (f) the hourly weather observations collected in the region of Brest (France), (g) the

intracardiac signals recorded using a 64-electrode basket catheter placed in patients affected by AF.

The application shown in this chapter should be regarded as illustrative examples aiming at showing the usefulness of the framework to a number of scenarios. Results suggest that joint analysis of time-vertex signals can bring forth benefits in signal denoising and recovery, learning and source localization problems. We remark that these preliminary results require more extensive and exhaustive investigations, analysis and comparison with the state-of-the-art techniques. We acknowledge that there are different techniques that are very efficient for each problem under consideration, as denoising of meshes, or inpainting of video, but our goal is to show the versatility and potentiality of the time-vertex framework.

All the experiments presented in this chapter were done using the GSPBOX [160], the UNLocBoX [159] and the LTFAT [167]. Code reproducing the experiments is available at https://lts2.epfl.ch/reproducible-research/a-time-vertex-signal-processing-framework/.

8.2 Compactness of representation

A key motivation behind the joint harmonic analysis is the capability of encoding time-varying graph-dependent signal evolution in a compact way. Our first step will therefore be to examine the energy compaction of the JFT transform in four datasets: two meshes representing a dancer ($N = 1502$ points in $\mathbb{R}^3$ and $T = 570$ timesteps) and a dog walking ($N = 2502$ points in $\mathbb{R}^3$ and $T = 52$ timesteps), the PeMS traffic flow dataset ($N = 710$ stations measuring traffic over $T = 2880$ intervals of 5-minute length each) and the number of infected individuals in an SEIRS epidemic (see Section 7.4.2 for description). Transforms with good energy compaction are desirable because they summarize the data well and can be used to construct efficient regularizers for regression problems.

To measure energy compactness, we compute the DFT, GFT and JFT for each dataset, we replace the spectrum coefficients with magnitudes smaller than the p-th percentile with zeros and perform the corresponding inverse transform on the resulting coefficients. Denoting by $\boldsymbol{X}$ the original signal and $\boldsymbol{X}_p$ the compressed one, the compression error is for each p given by $\|\boldsymbol{X}_p - \boldsymbol{X}\|_F / \|\boldsymbol{X}\|_F$. As shown in

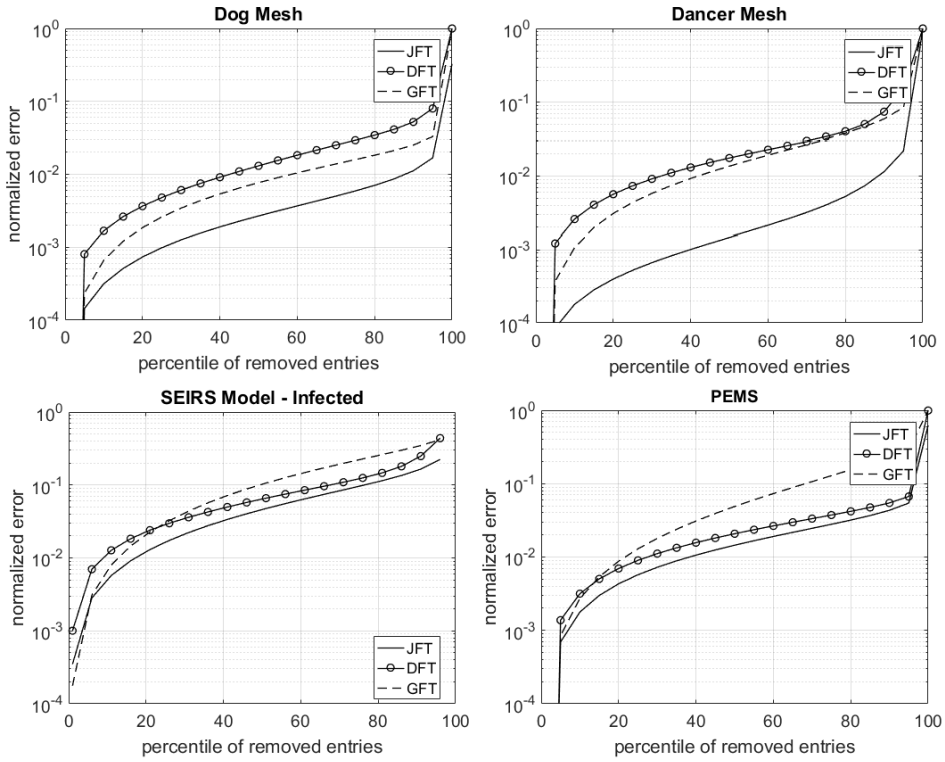

Figure 8.1 Compactness of the transforms for different datasets: dog and dancer meshes (above) number of infected over Europe according to SEIRS model (below left) and traffic flow measured by the PeMS (below right). Normalized error is computed reconstructing the signal after thresholding the values of the transforms below the p-th percentile.

Figure 8.1, JFT exhibits better energy compaction properties in all the datasets, and especially for the meshes where the graph captures well the signal structure.

8.3 Regression problems with joint variation priors

We next examine the utility of joint variation priors for regression problems in two example applications.

8.3.1 Denoising of dynamic meshes

Whenever a smoothness prior can be assumed, the joint Tikhonov regularization can be used to denoise a time-varying graph signal. The prior can be easily expressed in the time-vertex domain thanks to Eq. (7.12). Joint denoising is then performed by

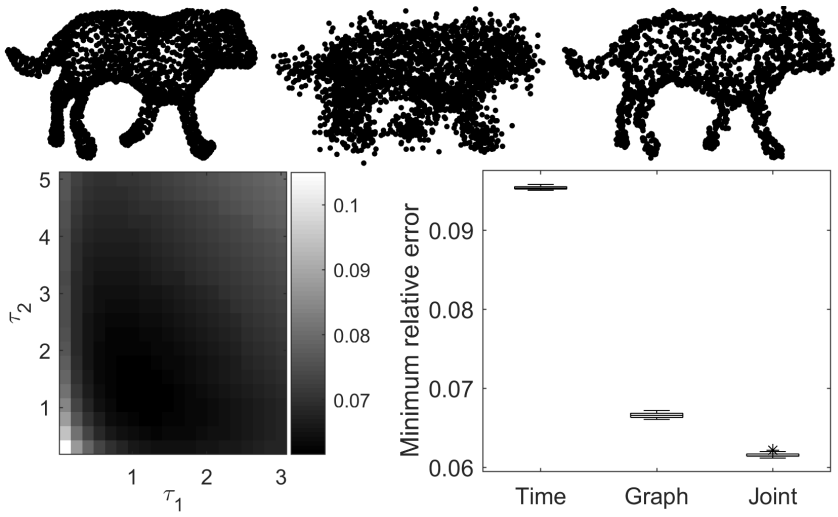

Figure 8.2 Joint variation priors are useful in denoising the coordinates of dynamic meshes. The original mesh (left) was corrupted with random Gaussian noise (center, normalized error 0.2); shown here for one realization of the noise. After the denoising, the error decreases to 0.06 (right). The normalized error as a function of parameters τ_1 and τ_2 is shown in a heat-map (below left) average over 20 realizations. The boxplot (below right) shows the minimum achievable error for a time ($\tau = 0$), graph ($\tau_2 = 0$) and joint variation prior.

solving the following optimization problem

$$\arg\min_{\boldsymbol{X}} \|\boldsymbol{X} - \boldsymbol{Y}\|_F^2 + \tau_1 \|\nabla_G \boldsymbol{X}\|_F^2 + \tau_2 \|\boldsymbol{X} \nabla_T\|_F^2, \tag{8.1}$$

where the regularization terms require the solution to be smooth in both graph and time domains. This problem has a closed form solution in our framework, which is a joint non-separable lowpass filter

$$h_{\mathrm{TIK}}(\lambda_\ell, \omega_k) = \frac{1}{1 + \tau_1 \lambda_\ell + 2\tau_2 (1 - \cos(2\pi\omega_k))}. \tag{8.2}$$

In order to investigate its performance, we consider the vertices of a mesh of size $2502 \times 59 \times 3$ representing a walking dog, we add Gaussian noise to the coordinates, we build a k nearest neighbor graph based on the distances between the time average of the coordinates and finally we solve the problem (8.1) for each coordinate dimension. We averaged the results over 20 realizations of the noise.

The meshes in Figure 8.2 represent, from left to right, the original, the noisy and the recovered one, for one realization of the noise. Remarkably, the normalized error drops from 0.20 to 0.06, respectively before and after denoising, making the

dog distinguishable again. As a side effect, the dog appears to be thinner, due to the graph regularization. The heat-map in the left corner of the figure shows the role of the regularization parameters. We found (using exhaustive search) that the lowest error is achieved when $\tau_1 = 0.71$ and $\tau_2 = 1.78$. We compare the performance of the joint Tikhonov regularization with respect to time- and graph-only for the best parameter combinations of all methods. The boxplot on the right shows the minimum achievable error statistics in the three cases over the 20 realizations. It is easy to see that the graph plays a major role in the denoising, since it encodes the structural information of the mesh. Nevertheless, the joint approach performs the best, i.e., 0.062 ± 0.0002, taking advantage of the smoothness in both domains, while graph and time methods achieve 0.067 ± 0.0003 and 0.095 ± 0.0002, respectively.

8.3.2 Inpainting of time-lapse video

We consider the problem of time-vertex signal recovery from noisy, corrupted, and incomplete measurements. Depending on the characteristics of the signal, the prior $\mathrm{N}_{p,q}(\boldsymbol{x})$ with different values of p and q and different weights can be used. A typical signal recovery problem in signal processing is the image inpainting, i.e., trying to replace corrupted or lost part of the image. Since patch-graphs allow non-local image processing [26], our goal is to extend graph-based non-local processing to video inpainting and recovery. However, since our framework is constrained to static graphs, we focus on the particular case of time-lapse videos, whose structure stays majorly invariant throughout the video. To this end, we corrupted a time-lapse video that shows the skyline of the Kuala Lumpur City Centre, whose statistical properties were amenable from a graph perspective, being the skyline static with time-varying colors. The video has size $160 \times 214 \times 3 \times 604$ (height $\times$ width $\times$ colors $\times$ frames). We removed 20% of the pixels and 20% of the frames from the original KLCC video, achieving a normalized error of 0.61. The inpainting is performed solving the optimization problem for each color using as regularizer $\mathrm{N}_{1,2}(\boldsymbol{x})$:

$$\arg\min_{\boldsymbol{X}} \|\boldsymbol{M} \circ \boldsymbol{X} - \boldsymbol{Y}\|_F^2 + \gamma_1 \|\nabla_G \boldsymbol{X}\|_1 + \gamma_2 \|\boldsymbol{X} \nabla_T\|_F^2, \tag{8.3}$$

where $\boldsymbol{M}$ is the mask of the missing entries. The patch graph G is constructed from the video averaged in time. The rationale is that the l_1 norm over the graph will restore the missing pixels, being each frame approximately piece-wise constant,

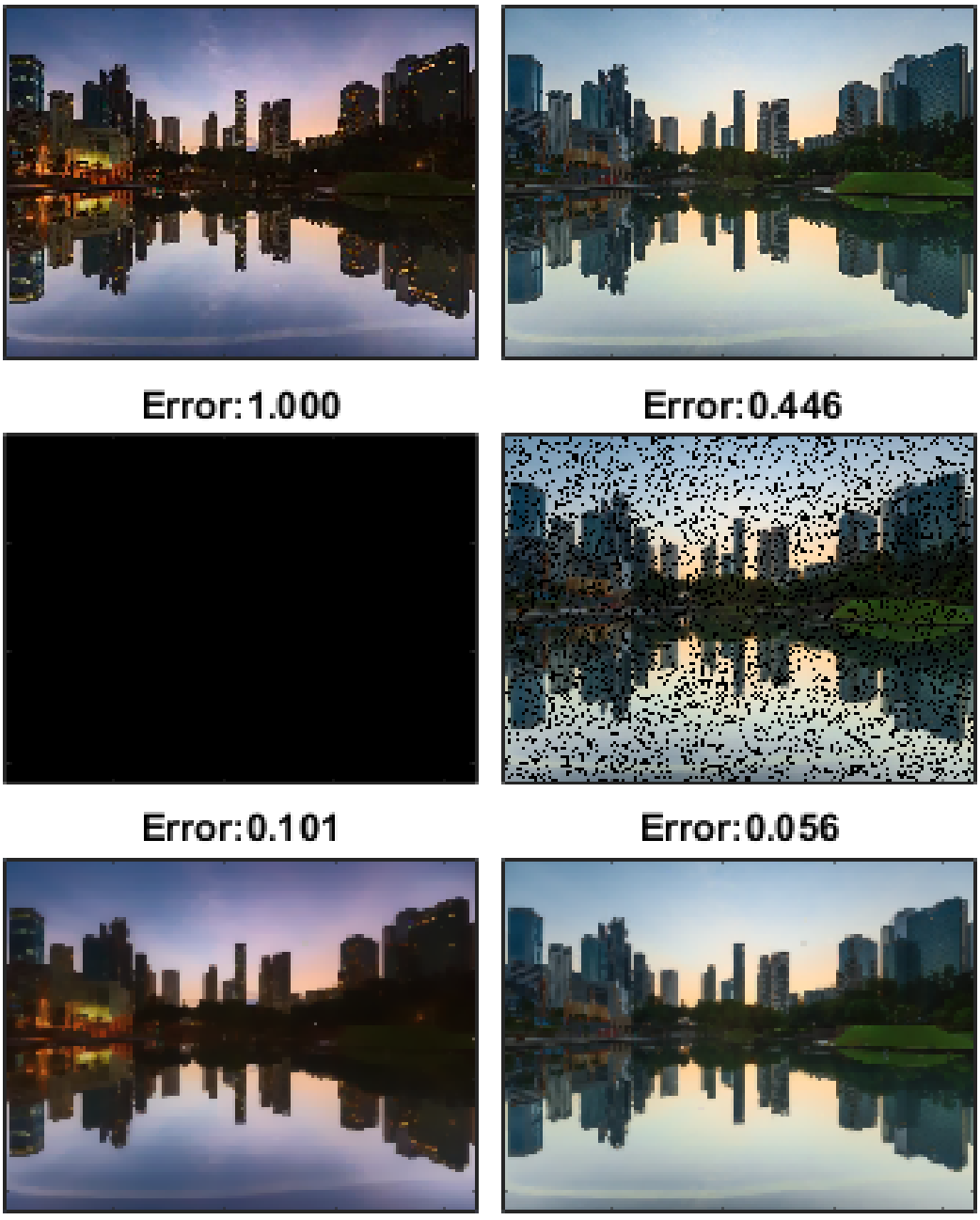

Figure 8.3 Visual inspection of video inpainting results. We show two frames extracted from the video (top), their corrupted counterparts (middle left frame is missing entirely, whereas middle right frame has missing pixels), and the reconstructions using our method with an $N_{1,2}$ regularizer (bottom).

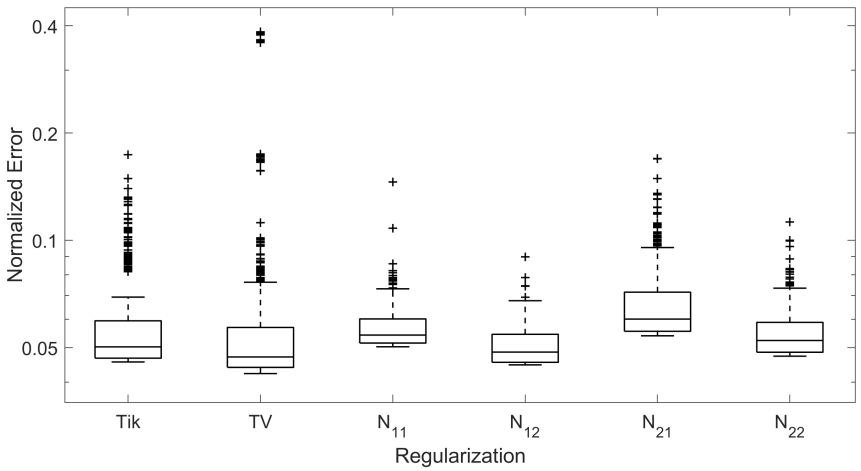

Figure 8.4 Comparison of video inpainting performances between Tikhonov, TV and Joint regularizations. Each box represents a statistical summary of the error evaluated for each frame of the whole video. Although TV achieves the best recovery for some frames, in case of occluded frames the error is very large. Joint regularization $\mathrm{N}_{1,2}(\boldsymbol{x})$ trades the lowest error achievable with a better average recovery.

whereas the l_2 norm in time recovers the smooth changes of the colors from dawn until dusk.

Table 8.1 Video inpainting normalized errors

Regularizer	Pixels	Frames	Total
Tikhonov	0.051	0.100	0.059
TV	**0.048**	0.122	0.060
$\mathrm{N}_{1,1}(\boldsymbol{x})$	0.056	0.059	0.057
$\mathrm{N}_{1,2}(\boldsymbol{x})$	0.050	**0.055**	**0.051**
$\mathrm{N}_{2,1}(\boldsymbol{x})$	0.061	0.103	0.068
$\mathrm{N}_{2,2}(\boldsymbol{x})$	0.053	0.066	0.055

Figure 8.3 shows two frames of the video, their corrupted counterparts and the result of the recovery, along with the respective normalized errors. The recovered video has a normalized error of 0.049, illustrating that the joint inpainting is able to restore the global quality of the video even in case of considerable missing information.

We compare the recovery performance with all the joint regularizers $\mathrm{N}_{p,q}(\boldsymbol{x})$ for $p,q = \{1,2\}$, and with two baseline algorithms, based on 3D-Tikhonov and isotropic

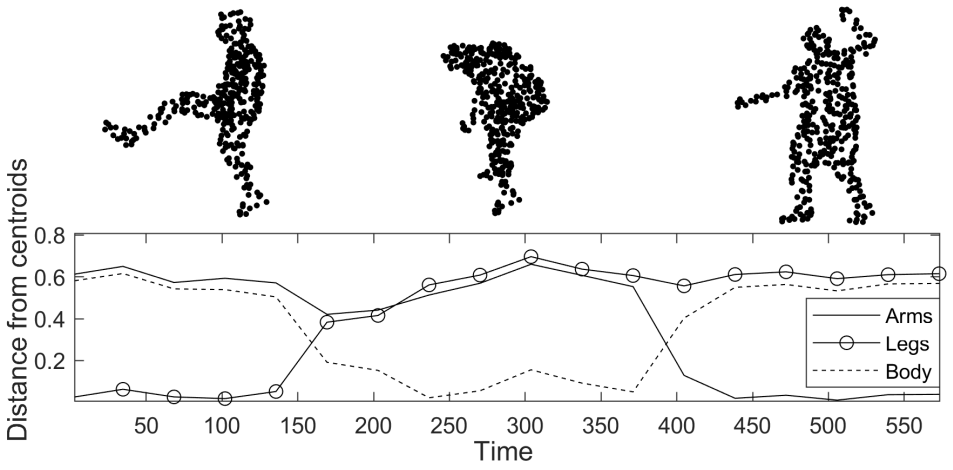

Figure 8.5 Clustering of the dancer mesh (no noise): the plot (below) shows the distance of the points stemming from the STVFT representation of three frames (above) of the time-varying mesh closest to the clusters centroids. Each frame shows a different phase of the dance.

3D-TV regularizations [32]. The last two correspond to using a grid graph with equal weights on the edges. Table 8.1 reports the normalized errors averaged over the pixels-only, frames-only and the whole video. The better performance achieved by the joint regularizer $\mathrm{N}_{1,2}(\boldsymbol{x})$ is due to its capability to restore missing frames, while missing pixels recovery performances are almost the same. Figure 8.4 illustrates a summary statistics of the errors computed over each frame. Although TV performs the best in the median, in case of occluded frames the error is much larger with respect to the joint recovery, leading to a higher average error.

8.4 Overcomplete representations

We examine the utility of STVFT and STVWT, respectively, as a feature extractor for dynamic mesh clustering and as a dictionary used to uncover the wave-like structure and epicenter of a seismic event.

8.4.1 Clustering dynamic meshes using STVFT

We consider the motion classification of a dynamic mesh representing the dancer, corrupted with additive sparse noise with density 0.1 with normally distributed

entries and SNR of -20 dB and -10 dB. Our objective is to determine the phase of the dance (*moving arms*, *stretching legs* and *bending body*) at each frames by performing spectral clustering on some representations of the windowed signal. To obtain the ground-truth, we labeled each frame by hand and verified that, when the noiseless signal (i.e., the actual trajectory of the points in time over each window) was used to define the features, one obtains a classification accuracy of 0.926.

Since we want to localize spatial-structured phenomena in time, our approach will be to use a STVFT to derive the representation. To capture the geometry of the problem, we used a nearest neighbour graph constructed based on the coordinates of the mesh vertices averaged in time; this graph was fixed for the whole sequence. As explained in Section 7.6.2, the STVFT is separable, meaning that we can handle the vertex and the time dimensions separately. In the time domain we use a rectangular window with support equal to 50 samples in time and spacing such that the overlap is 60%. For the vertex dimension, we use the Itersine kernel (defined in the GSP-BOX [160]) that we uniformly translate at 5 different positions in the graph spectral domain.

The STVFT provides features associated to a time instant that we can directly use to classify the dance (see Figure 8.5 for a visual illustration of the clustering results). Other transforms such as GFT, DFT, and JFT do not have this property. Hence, in order to compare with these other transforms, we use the same rectangular windows (width 50, overlap 20 samples) to extract 27 time sequences from the signal. We then used the transformed data associated with each sequence as a point to be clustered. Figure 8.6 illustrates the clustering accuracy statistics over 20 realizations of sparse noise for features constructed based on the magnitude of five representations: the windowed sequences, as well as their GFT, DFT, JFT, and STVFT representations. Observe how the presence of sparse noise severely hampers classification when the raw signal is used, with the average accuracy dropping from 0.926 for the clean signals to 0.469 and 0.74 for -20 dB and -10 dB, respectively. We can also see that the two representations leading to the highest median accuracy are the JFT and STVFT, suggesting the utility of joint harmonic representations. Nevertheless, the STVFT provides more robust estimates with an average accuracy of 0.869 rather than 0.792 for the JFT at -20 dB.

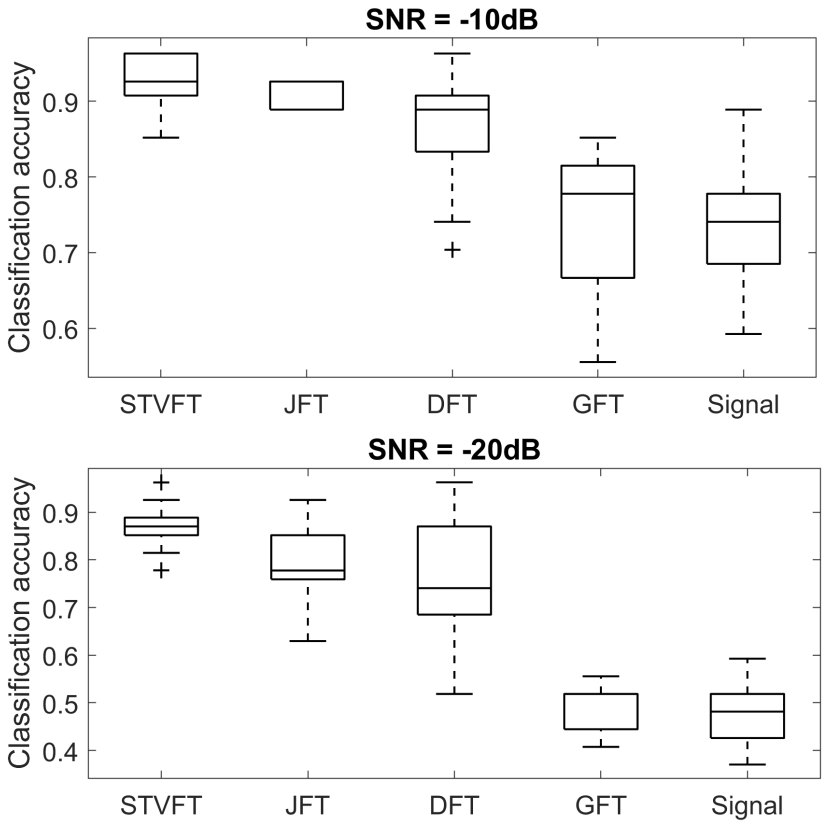

Figure 8.6 Comparison of clustering accuracy using different transforms in case of sparse Gaussian noise for SNR -20 dB and -10 dB. Each box shows a summary statistics of the accuracy computed over 20 different realizations of the noise. Results show that SVTFT achieves the highest accuracy in average.

8.4.2 Seismic epicenter estimation with STVWT

We analyze seismic events recorded by the GeoNet[1] sensor network whose epicenters were chosen to be randomly distributed in different areas of New Zealand. Each waveform consists of 300 seconds sampled at 100 Hz, starting few seconds before the seismic event. The graph is created using the coordinates of the available stations for each event and connecting the closest stations. We will use the STVWT with mother kernel based on the wave PDE, which allows us to decompose the signal as a sum of PDE solutions [74]. As a first approximation, when the waves propagate in a continuous domain or a regular lattice, seismic waveforms can be modeled as oscillating damped waves [67]. Our premise is thus that we can approximate the seismic waveforms using a small set of damped waves propagating on the graph

[1] http://www.geonet.org.nz/quakes

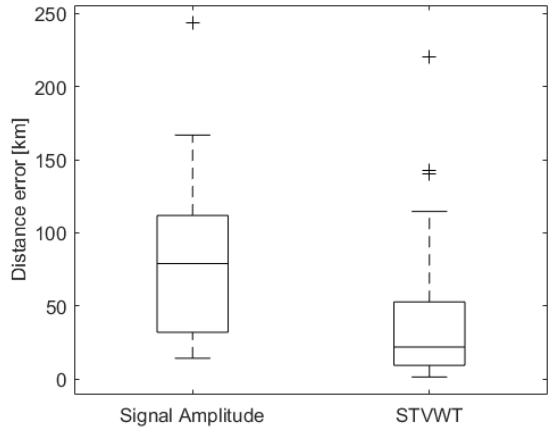

Figure 8.7 Comparison of seismic epicenter localization performances between amplitude-based approach and STVWT. The bar graph shows that the second outperforms the first, suggesting that the damped wave model assumption significantly improves the source estimation performance.

connecting the seismic stations. Thus, we expect the damped wave mother kernel

$$h(\lambda_\ell, \omega_k) = \frac{1}{\sqrt{T}} \frac{e^{\beta + j\omega_k} + \lambda_\ell/2 - 1}{2(\cosh(\beta + j\omega_k) + \lambda_\ell/2 - 1)} \tag{8.4}$$

to be a good approximation of the seismic waves recorded by the sensors, with the damping factor β chosen to fit the damping present in the seismic signals. To construct the STVWT, we select 10 equally spaced values in $[0,2]$ for z_λ and set $z_\omega = 1$. To estimate the epicenter of the earthquake we solve

$$\arg\min_{\boldsymbol{C}} \|D_h^*\{\boldsymbol{C}\} - \boldsymbol{X}\|_2^2 + \gamma\|\boldsymbol{C}\|_1, \tag{8.5}$$

where γ is the regularization parameter controlling the trade-off between the fidelity term (selected using exhaustive search) and the sparseness assumption and D_h^* is the synthesis operator associated with STVWT.

The solution provides important pieces of information. Firstly, using the synthesis operator we can obtain a denoised version of the original process. Secondly, the non-zero coefficients of $\boldsymbol{C}$, describe the origins and amplitudes of the different components. Therefore, for each node we take the maximum value over time and scales and we use the result as weights to average the graph coordinates to obtain the epicenter. Being a weighted average of different coordinates, the estimated source

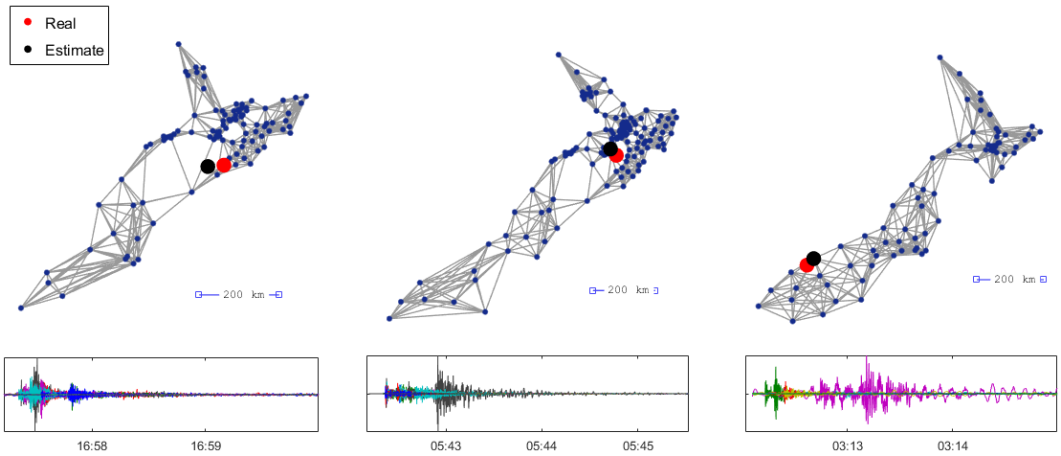

Figure 8.8 Results for 3 different seismic events in New Zealand. Top: the graph is created using the coordinates of the available stations for each event and connecting the closest stations. The stars and the circles are the true and estimated sources of the seismic wave respectively. Bottom: Signal recorded by the sensors over time for each event.

will not correspond to a vertex of the graph in general. We compare the performance of STVWT with the estimate obtained using only the signal amplitude: for each earthquake we average the coordinates of the stations using as weights the energy of the signals. Figure 8.7 shows the comparison over 40 different seismic events randomly distributed over New Zealand between the two methods. STVWT based on the damped wave kernel achieves an average error of 48.5 km, providing an almost twofold improvement over the baseline, whose average performance is 88.3 km. Figure 8.8 illustrates the estimate for 3 different seismic events and the respective seismic waveforms. These results show that the proposed method significantly improves the source estimation performance.

8.5 Joint stationarity

We apply the joint stationarity methods to a weather dataset depicting the temperature of 32 weather stations, over a span of 31 days. Our experiment aims at showing that 1) joint stationarity is a useful model, even in datasets which may violate the strict conditions of our definition, and 2) that time-vertex stationarity can yield a significant increase in denoising and recovery accuracy, as compared to time- or vertex-based methods, on a real dataset.

The French national meteorological service has published in open access a dataset[2] with hourly weather observations collected during the Month of January 2014 in the region of Brest (France). The graph is built from the coordinates of the weather stations by connecting all the neighbors in a given radius with a weight function $[\boldsymbol{W}_G]_{i_1,i_2} = \exp(-k\,d(i_1,i_2)^2)$, where $d(i_1,i_2)$ is the Euclidean distance between the stations i_1 and i_2. Parameter k is adjusted to obtain an average degree around 3 (k, however, is not a sensitive parameter). As sole pre-processing, we remove the mean (over time and stations) of the temperature. This is equivalent to removing the first moment.

The dataset, which consisted of a total of $T = 744$ timesteps, was split into two parts of size ρT and $(1-\rho)T$, respectively. We use the first part of the dataset to estimate the PSD and the second to quantify the joint filter performance. We compare our joint method to the state-of-the-art Wiener filters for the disjoint time/vertex domains, which are known to outperform non-statistics based methods, such as graph/time Tikhonov and graph/time TV. To highlight the benefit of the joint approach, in the disjoint cases we use the entire dataset to estimate the PSD (for $\rho = 1$ the same data are used for both training and testing).

8.5.1 Denoising

For this experiment, we add Gaussian random noise to the data and remove the noise using the Wiener filter ($\boldsymbol{A} = \boldsymbol{I}$ in problem (7.42)). The result is displayed in Figure 8.9a. Joint stationarity outperforms time or vertex stationarity especially when the noise level is high. Indeed, joint stationarity allows the estimator to average over more samples. In order to obtain a good denoising, we need a good JPSD estimation. The effect of the dataset size can be observed through the parameter ρ, with larger ρ resulting in higher accuracy. Especially for large input SNR, the joint approach becomes particularly meaningful as it outperforms other approaches, even when a very small portion of the data is used for JPSD estimation.

[2] https://donneespubliques.meteofrance.fr/donnees_libres/Hackathon/RADOMEH.tar.gz

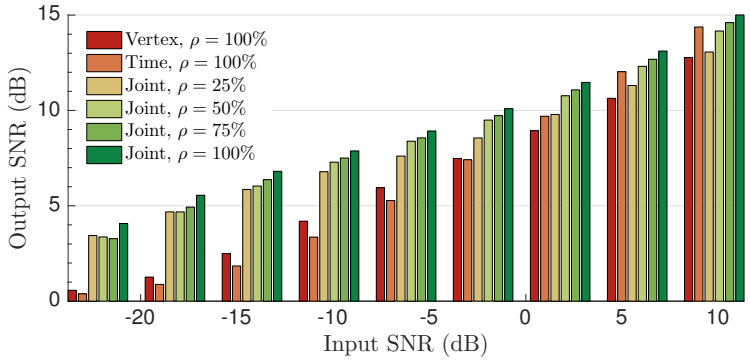

(a) Denoising

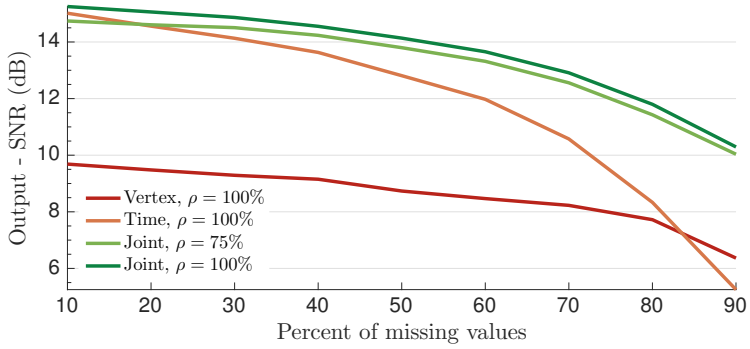

(b) Recovery

Figure 8.9 Experiments on Molene temperatures. The joint approach becomes especially meaningful when the available data are very noisy or are few. The recovery performance is slightly improved when a larger percentage ρ of data are available for training.

8.5.2 Recovery

We also consider a recovery problem, where a given percentage of entries of matrix $\boldsymbol{X}$ is missing. Figure 8.9b depicts the recovery error obtained using problem (7.44). Again, we observe a significant improvement over competing methods. This improvement is achieved because the joint approach leverages the correlation both in the time and in the vertex domain: each random variable in a TWSS or VWSS process is dependent on only $T-1$ or $N-1$ other random variables, respectively (rather than $NT-1$ as in the joint case), implying a higher recovery variance.

8.6 Spatio-temporal harmonic analysis of multipolar signals

Historically, an EPS is mainly based on the ability of an expert electrophysiologist to interpret the intracardiac signals and then diagnosis the arrhythmia affecting the patient (Section 1.1.2). Despite the great utility of the multi-electrode catheters during the cardiac mapping phase of a typical ablation procedure, the potential of such tools has not yet been exploited completely. Moreover, in many cases the signals are too many even to be visualized on the screen of the recording system. For these reasons, new techniques able to convey the huge amount of information to the physician in a useful fashion are needed.

During RF ablation of AF, multi-electrode catheters are particularly useful to get a better insight on the chaotic electrical activation of the atria. For example, the RhythmView system described in Section 2.1.3 takes advantage of the panoramic view offered by the basket FIRMap to identify rotor drivers of AF. Due to their recent application in the clinical practice, several studies have started to appear in the literature regarding the analysis of multipolar signals. An interesting methodology for the analysis of signals recorded from multi-electrode baskets can be found in a recent series of papers [133, 82, 47]. In the attempt of overcoming bipolar EGMs polarity and shape dependence on catheter orientation, omnipolar recording are defined using multiple unipolar electrodes arranged in cliques and can be used to accurately determine cardiac activation sources and wavefront trajectory speed at a single location.

Due to their ability to model spatio-temporal dynamics, graphs have been successfully employed to describe functional and structural brain connectivity [89, 193, 75]. Similarly, thanks to the recent availability of multi-electrode recordings, EP researchers are trying to define heart functional connectivity. In the work of Tao et al. [203], the authors hypothesize that catheter ablation of persistent AF is associated with improvement in both local and global connectivity within the heart communication networks [8]. To test this hypothesis, multi-electrode recordings before and after the rotors ablation using the RhythmView system and FIRMap catheter were analyzed using notions derived from information and graph theory. In this section we propose a new graph-based model to describe multi-electrode catheters, particularly suitable for basket catheters, together with some preliminary results. We present the follo-

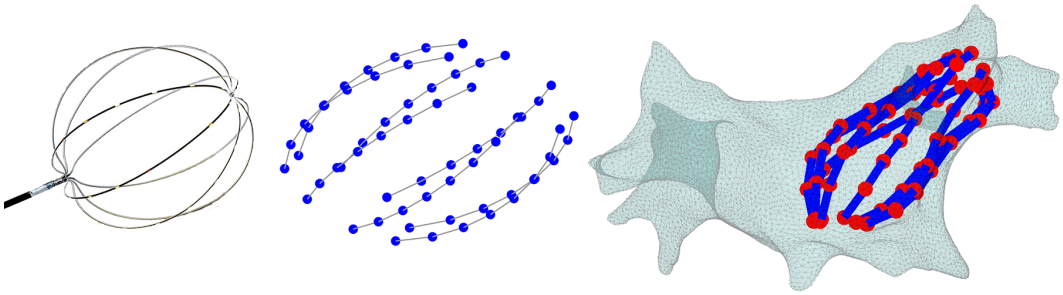

Figure 8.10 Example of graph model of the multi-electrode basket catheter. Each node in the graph represents one unipolar electrode. Edges can model the splines of the catheter (center), or can be estimated from the distance between electrodes or the electrical activity. On the right, the catheter, modeled as a graph, is displayed inside the electroanatomical map.

wing work without claiming to be complete, on the contrary our contribution is only a first step towards the application of the GSP to the very complex and challenging field of cardiac electrophysiology.

8.6.1 Graph modelling of multi-electrode catheters

The intracardiac 64-pole basket catheters can be easily modelled as a graph G with $N = 64$ nodes, one for each electrode. Several approaches can be used to determine the graph connectivity, ranging from the physical connection between the electrodes, i.e., the splines, as in Figure 8.10, to the distance between the electrodes (Fig. 8.12a), to more complex cases in which we want to model heart functional connectivity using surrogates, such as signals correlation, time delay, or mutual information [203].

Once having defined the graph, we can use the time-vertex domain to represent the multi-electrode unipolar recordings as time-vertex signals $\boldsymbol{X}$ on the graph G. Figure 8.11 shows an example of time-varying GFT for a multi-electrode recording in the left atrium during CS stimulation. The signal recorded from one electrode during one cardiac activation is shown below. The GFT is represented on the time-eigenvalues plane, showing the evolution of the graph signal spectrum in time. Interestingly, the GFT of the atrial component has much higher energy in the high frequency spectrum with respect to the ventricular activation, facilitating the identification of the far-field components which is common to all the electrodes. From this example, it is clear that the graph allows us to visualize easily spatio-temporal data and extract useful information.

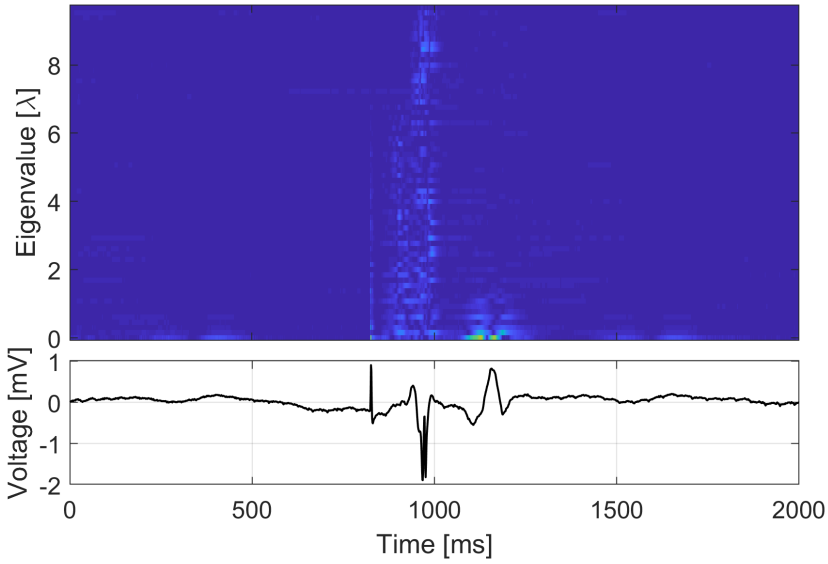

Figure 8.11 GFT of the time-vertex signal recorded by a basket catheter placed in the left atrium during CS stimulation. In the panel above the GFT is represented on the time-eigenvalues plane, showing the evolution of the graph signal spectrum in time. Below, the example of intracardiac signal recorded from one electrode during one cardiac activation. Interestingly, the GFT of the atrial component has much higher energy in the high frequency spectrum with respect to the ventricular activation.

In both surface and intramuscular electromyography (EMG), it is relatively simple to increase the number of electrodes used in the recording setting, hence, not only unipolar and bipolar, but also more advanced schemes are used for electromyographic recordings [61, 62]. For example, double differential recordings are typically used to enhance the capability to discriminate the action potentials of separate motor units [22]. Differently from EMG, where the electrodes can be manually placed on the skin according to a preferred pattern, regular differential schemes are not suitable for intracardiac recordings. Therefore, we need new methods to build intracardiac multipolar signals, which could overcome the classical limitation of the unipolar and bipolar recordings. We argue that graph operators can be used to define new techniques to determine myocardial activation, which are simple to compute, but, more important, easily understood by an electrophysiology expert. Considering the time-vertex signal $\boldsymbol{X}$ the matrix of the filtered unipolar recordings, a reasonable choice is to use the normalized graph Laplacian $\boldsymbol{L}'_G$ applied to $\boldsymbol{X}$ to build the graph-based multipolar signals. Interestingly, it is possible to interpret the time-vertex signal $\boldsymbol{Y} = \boldsymbol{L}'_G\boldsymbol{X}$ as the collection of multiple differential recordings, where the number of electrodes used in the difference depends on the graph connectivity (Fig. 8.12). Clas-

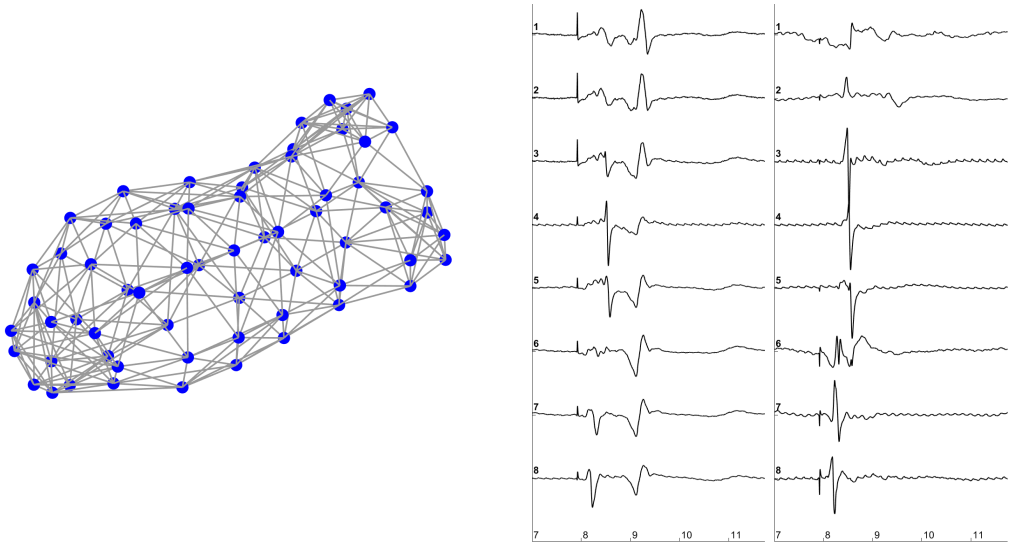

(a) Graph of the electrode coordinates.

(b) Filtered unipolar signals (left) and graph-based multipolar signals (right).

Figure 8.12 Graph-based construction of multipolar signals using k-nn graph obtained from the electrodes coordinates. In the right pair of plots, the first eight out of 64 unipolar and multipolar signals are shown.

sically, differential sensors are used to enhance the components of the signals that originates immediately below the electrodes, eliminating the far-field components which are in common to all the electrodes in the multipole. Actually, the Laplacian operator applied to a graph signal performs exactly the same operation, removing the spatial low-pass components and preserving the high-frequency oscillations which characterize each node of the graph (Fig. 8.12b).

Multipolar signals and conduction velocity

In Section 5.5 we investigated the relationship between the conduction velocity in the left atrium and the spectral centroid of the local intracardiac signals recorded by the basket catheter. Unfortunately, the results were not as good as the one obtained in simpler settings, as in the coronary sinus or the atrial wall. Among the several difficulties encountered during the analysis, we hypothesized that the use of unipolar signals may have lowered the correlation between the two variables. However, in many cases it is not obvious which electrodes to use to form the dipole, due to the distance between the electrodes and the irregular shape taken by the basket in the atrium. Therefore, the bipolar configuration seems unsuitable to our purpose. For

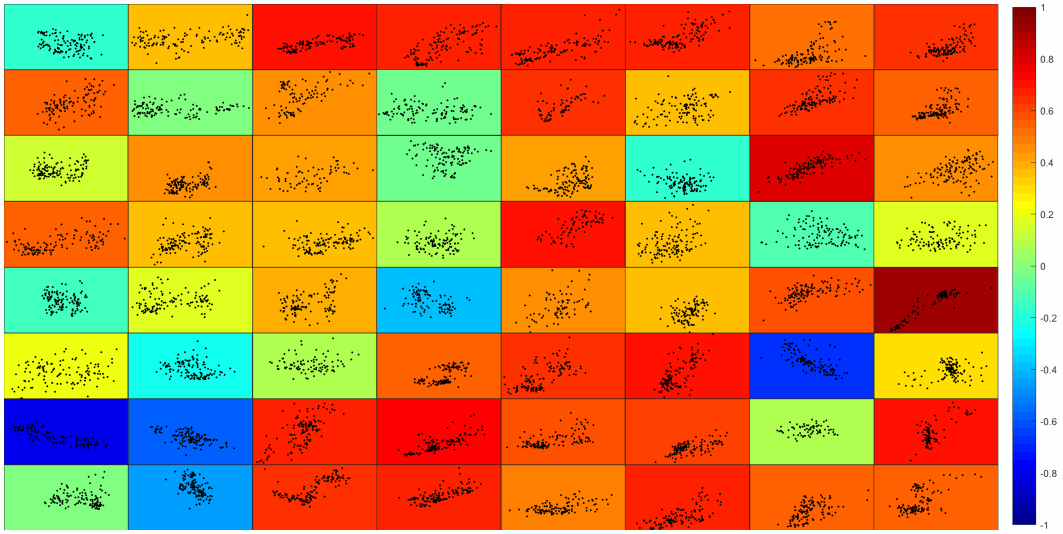

Figure 8.13 Correlation between CV and SpC for every electrode of the basket catheter using graph-based multipolar signals. Average correlation is 0.33.

these reasons, we used multipolar signals in the attempt to improve the results of Section 5.5. Figure 8.13 shows the matrix of scatter plots corresponding to Figure 5.8, where we have used multipolar signals to compute the SpC. Comparing the two figures, it is evident that graph-based multipolar recordings lead to higher correlation for many electrodes, with an average correlation of 0.33 for the whole basket. The improvement can probably be attributed to the spatial high-pass nature of the multi-differential configuration, which attenuates irrelevant or unwanted components.

8.6.2 Atrial fibrillation rotor drivers analysis and visualization

Re-entrant electrical activity during AF is one of the most promising theory explaining the mechanism of the arrhythmia. Unfortunately, until now, the only system capable of analyzing multichannel recordings, identify re-entry patterns and provide to the physician an estimate of the rotor singularity point is the RhythmView system. As described in Section 2.1.3, the 64 estimated LATs are projected on an 8×8 matrix, linearly interpolated and displayed on a regular lattice. This is clearly an oversimplification of the real atrial activation, where not only the anatomy of the chamber is not taken into account, but even the shape of the catheter and the distances between the electrodes are overlooked.

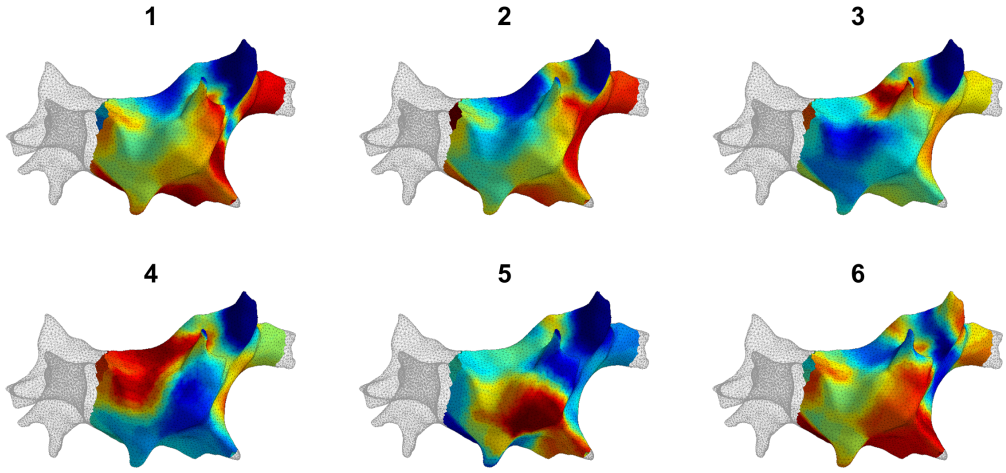

Figure 8.14 Rotational electrical activity recorded during AF using 64-polar basket catheter.

The knowledge of the electrode coordinates would allow to model the basket as a graph, obtaining more accurate reconstruction of the activation map, without neglecting the actual electrode distribution with respect to the atrium, developing graph-based approach to adapt the linear interpolation to the non-linear anatomy of the mapped chamber and accurately identify the driver rotors. Finally, data visualization plays a major role in the clinical practice. In many cases the rotors are difficult to visualize on the regular lattice and finding their location on the electroanatomical map is a non-trivial task. Performing the algorithm directly on the graph and projecting the result on the cardiac mesh would simplify the work of the physician. Figure 8.14 shows the activation map estimated by the RhythmView system, projected on the anatomical mesh reconstructed using the NavX mapping system. The sequence of plots show the presence of a re-entrant electrical activity rotating around a pivot placed on the anterior wall. Obviously, the rotor is much more interpretable directly on the anatomical mesh.

Conclusions

In this dissertation we addressed the issues and the shortcomings encountered in two fields which are apparently very different, cardiac electrophysiology and graph signal processing. Working in parallel on these problems, we discovered that they have in common the inherent complexity of the underlying domains.

In cardiac electrophysiology, our main research activity was focused on the analysis of intracardiac signals recorded during atrial fibrillation (AF), a very common supraventricular arrhythmia characterized by rapid and irregular activation of the atria. AF is a very complex arrhythmia and its mechanisms are still not completely understood. Despite the numerous advances over the past decade, catheter ablation of AF continues to be a challenge, with still unsatisfactory recurrence rate, motivating the research for improved modalities. Analysis of intracardiac signals recorded during AF could provide deeper understanding of atrial electrical conduction, wavefront propagation, re-entrant and ectopic focal activity, in order to develop more effective treatments.

Our contribution in this direction consists in the development of statistical and non-stationary signal processing techniques targeting the two main issues of AF: (a) the permanent electrical isolation of arrhythmogenic sources (such as pulmonary veins) and (b) the characterization of the atrial substrate. To address the first, we developed signal-based criteria as surrogates for lesion assessment that are simple and immediate to evaluate, therefore they can be used in the clinical practice and also automatically evaluated by ad-hoc algorithms even during the procedure. We used these criteria to compare the two different approaches for the ablation of paroxysmal AF, the contact force enabled SmartTouch catheter and the remote magnetic controlled RMT catheter, characterized by complementary performance. We also investigated the role of biophysical ablation parameters in the process of scar formation using MRI with scar-enhancing contrast.

Atrial substrate characterization is a challenging task which would allow to precisely describe the mechanism of AF for each single patient, tailoring the ablation strategy to his particular condition. Conduction velocity (CV) is a fundamental substrate parameter influencing atrial arrhythmias. Typically, CV maps are difficult to estimate and require time-consuming calculations using local activation time maps. We exploit the well-known mechanism of the CV restitution to demonstrate that a significant correlation exists between the CV and the spectral compression of intracardiac signals recorded in the coronary sinus and on the atrial wall.

The ambitious goal of our work was to put the foundation for a signal processing framework which is able to deal with irregular domains and complex data evolving in time with dynamical models that can also be inferred from physiological systems.

Thanks to the general mathematical nature of graphs, capable of capturing the underlying structure of data collected from a variety of fields, such as transportation, chemistry, and social science, graph signal processing (GSP) has experienced an amazing growth in the last years, and it is hence the perfect candidate to build the basis of our framework. However, several shortcomings in GSP have to be addressed. Firstly, the inherently complexity and irregularity of the graph domain makes difficult to match the intuition from the classical Euclidean setting. Even more critically, so far GSP techniques neglected the inherently time-dependency of data. On the contrary, in the biomedical field, time domain is essential and physiological systems are often modelled as highly dynamical systems.

Therefore, we proposed the Time-Vertex Signal Processing (TVSP) framework, which leverages both the time-domain and graph signal processing techniques to analyze graph structured data evolving in time. Being interested in signals recorded from the real world, the data-driven approach is not enough. We motivate the harmonic time-vertex analysis as an analysis tool for the state evolution of simple Partial Differential Equations on graphs, and we illustrated how joint frequency analysis can be meaningful for the study of nonlinear and stochastic processes evolving on graphs. To elevate time-vertex signal processing to a full-fledged framework we introduced several joint operators, such as time-vertex localization, filter-banks and frame. We also present a novel approach, denoted Fast Fourier-Chebyshev algorithm, which significantly improves the accuracy of fast joint filtering. Finally, our experimental results on a variety of datasets suggest that the proposed

tools can bring forth significant benefits in various signal processing and learning tasks involving time-series on graphs.

Not only the two directions travelled throughout this thesis share the fascinating intrinsic complexity of the underlying domain, but working on multi-channels intracardiac signals gave us also the possibility to preliminary explore their intersection, applying the tools of GSP and TVSP to intracardiac signals recorded by multi-electrode basket catheters. We illustrated their utility in different clinical applications, opening the possibilities to further developments.

Future directions

Although Graph Signal Processing can no longer be considered an emerging field after an astonishing number of contributions by an incredibly active scientific community, working in such recent and expanding research topic means that the ideas to be explored are definitely too much compared to the time available during a PhD. In a similar way, cardiac electrophysiology is still far from having explained the mechanisms of AF, and we hope that our contributions could be small steps towards this goal. Nevertheless, during these years, numerous theories have emerged that it would certainly be worth investigating. For this reason, we propose here some future directions that can be investigated in the future.

Functional imaging for ablation strategy improvement

With the advance of MRI technology, the ever-increasing resolution achievable in dynamical CMR enables the physician not only to diagnose more complex pathological structural heart conditions but also to identify arrhythmogenic lesion gaps with higher precision. Moreover, other diagnostic imaging techniques, such as positron emission tomography (PET), are emerging as alternative ways to detect unhealthy cardiac tissue overcoming the main limitations of MRI. We encourage a more extensive use of LGE-MRI in the clinical practice to assess the major flaws of the current ablation approach. We foresee a prospective study aiming at analyze the role of the new parametric indices, e.g., ablation index, in assessing scar formation, in particular during ablation of AF.

Simultaneous use of mapping methods for substrate characterization

As we have extensively discussed, the complexity of atrial fibrillation is principally due to its ability to cause alterations of the tissue which provide a substrate for maintenance. Therefore, substrate characterization is a fundamental task in order to develop more efficient ablation strategies. Our contribution in this direction is a first step towards the definition of new methods to estimate atrial conduction velocity which are fast and simple to use in the clinical practice. However, not only more data are needed to validate these results, but also more accurate models, for example based on graphs, should be used in complex cases, e.g., when using basket catheters. Moreover, other approaches are possible, which are alternative or complementary to the intracardiac one. ECG imaging (ECGI) is a panoramic mapping technique based on the recording of a high number of surface ECG signals (~ 250) which are projected on a high-resolution 3D model of the heart obtained by noncontrast thoracic computer tomography scans [79]. The cardiac surface potentials and unipolar electrograms are reconstructed by the system using mathematical reconstruction algorithms and investigated taking also into account the real cardiac anatomy. Several reports have demonstrated the utility of noninvasive panoramic mapping of AF in identification of active sources, ectopic foci and stable and unstable rotor drivers [53]. Therefore, panoramic activation and conduction velocity maps can be easily determined and correlated with the location of the re-entrant activity. In our opinion, the simultaneous use of different mapping methods, such as intracardiac multi-electrode diagnostic catheters, non-invasive ECGI and the epicardial mapping may help to get more insight into the most complex AF mechanisms, unveiling phenomena as transmural re-entrant activity and arrhythmogenic alteration of the substrate, which are determinant in the arrhythmia sustenance and progression.

Discrete calculus on graphs: The Case of the Missing Curl

One of the most fascinating aspects about graph signal processing is its ambiguous relationship with the classical Euclidean domain. While exploring the concepts and the tools belonging to the domain of harmonic analysis, it is very easy to stumble upon unexpected similarities (e.g., the eigenfunctions of the Laplacian define the canonical basis of the Fourier transform), as well as confounding differences, as

the lack of translation invariance. In particular, in the field of discrete calculus, the analogy between the classical notions of gradient and divergence with those defined on graphs is really intriguing and opens up to further studies regarding dynamics over networks. However, it was impossible not to notice the absence of another fundamental operator widely used in this context: *the curl*. To the best of our knowledge, an explicitly use of the notion of curl in GSP appears only in the paper by Ravazzi et al. [170], where, nevertheless, the graph is only used to compute the gradient for 2D images, whereas the curl is still defined in the Euclidean domain. In graph theory, several authors have provided different definitions of curl of networks. Worthy of note are the definitions of curl as operator on triple of adjacent edges (triangles) [73] and as the result of the Helmoltz decomposition of a vector field (flow) on the graph [78]. An interesting result regarding the curl operator on weighted networks, which is close to the GSP domain, is presented in the work by Bendito et al. [14]. Their discrete vector calculus theory on graphs is based on the concept of *tangent spaces of graphs*. A tangent space is the vector space defined at each vertex v_n of the graph as a linear combination of the edges incident at v_n. As a consequence, the definitions of gradient, divergence and curl arise naturally in their work. We believe that an analysis of their work in the light of GSP is needed to unveil its potentiality in this domain.

Advection as Laplacian for directed graphs

Throughout this thesis we have assumed that the natural way to describe complex non-Euclidean domain is using undirected graphs. However, in numerous applications, it could be useful to consider directed edges to model directional flow of information. An alternative approach to GSP, described in a series of papers (e.g., [179–181]) proposes the eigendecomposition of the adjacency matrix $\boldsymbol{W}$ or the more general shift matrix $\boldsymbol{S}$, instead of the Laplacian matrix $\boldsymbol{L}$, as Fourier basis, highlighting as major strength the generality of their approach. However, leaving aside the technical difficulties arising from the eigendecomposition of a general matrix (it is well-known that the Jordan's form cannot be explicitly computed due to its numerically instability [144]), it is our opinion that the only way a valid Fourier transform could emerge is from the eigendecomposition of the symmetric semi-definite positive Laplacian matrix, or its variants. Nevertheless, we believe that a "frequency" transform for directed graph, which could be complementary to the

GFT defined in Eq. (6.4), may arise from the analysis of the *advection equation on graphs* [33]. The advection equation is a PDE that governs the motion of a conserved scalar field as it is advected by a known velocity vector field. We observe that a *graph advection operator* could be defined as the divergence of the outer flow operator $\boldsymbol{F}_o \in \mathbb{R}^{E \times N} = \min\{\nabla_G(e,n), 0\}$, i.e.,

$$\boldsymbol{A} = \nabla_G^* \boldsymbol{F}_o = \boldsymbol{D}_o - \boldsymbol{W}^\intercal \tag{8.6}$$

where $\boldsymbol{D}_o$ is the outer degree matrix. Even if not symmetric, this operator has amenable spectral properties and, more importantly, in the vertex domain can be easily understood using the advection PDE.

Bibliography

[1] Adamic, L. A. and Glance, N. (2005). The political blogosphere and the 2004 U.S. election. In *Proceedings of the 3rd international workshop on Link discovery*, pages 36–43. ACM.

[2] Akca, F., Hubay, M., Zima, E., Széplaki, G., Végh, E. M., Skopál, J., Lendvai, Z., Theuns, D., Merkely, B., and Szili-Torok, T. (2014). High-Volume Lesions Using a New Second-Generation Open Irrigation Radiofrequency Catheter Are Associated with the Development of Inhomogeneous Lesions. *Pacing and Clinical Electrophysiology*, 37(7):864–873.

[3] Akwei-Sekyere, S. (2015). Powerline noise elimination in biomedical signals via blind source separation and wavelet analysis. *PeerJ*, 3:e1086.

[4] Allessie, M. A., Bonke, F. I., and Schopman, F. J. (1977). Circus movement in rabbit atrial muscle as a mechanism of tachycardia. III. The "leading circle" concept: a new model of circus movement in cardiac tissue without the involvement of an anatomical obstacle. *Circulation research*, 41(1):9–18.

[5] Allessie, M. A., Lammers, W. J. E. P., Bonke, F. I. M., and Hollen, J. (1985). Experimental evaluation of Moe's multiple wavelet hypothesis of atrial fibrillation. In Zipes, D. P. and Jalife, J., editors, *Cardiac Electrophysiology and Arrhythmias*, pages 265–276. Grune {&} Stratton.

[6] Arendt-Nielsen, L., Mills, K. R., and Forster, A. (1989). Changes in muscle fiber conduction velocity, mean power frequency, and mean EMG voltage during prolonged submaximal contractions. *Muscle & Nerve*, 12(6):493–497.

[7] Arujuna, A., Karim, R., Caulfield, D., Knowles, B., Rhode, K., Schaeffter, T., Kato, B., Rinaldi, C. A., Cooklin, M., Razavi, R., O-Neill, M. D., and Gill, J. S. (2012). Acute pulmonary vein isolation is achieved by a combination of reversible and irreversible atrial injury after catheter ablation. *Circulation: Arrhythmia and Electrophysiology*, 5(4):691–700.

[8] Ashikaga, H., Aguilar-Rodriguez, J., Gorsky, S., Lusczek, E., Marquitti, F. M. D., Thompson, B., Wu, D., and Garland, J. (2015). Modelling the heart as a communication system. *Journal of The Royal Society Interface*, 12(105):20141201–20141201.

[9] Aviña-Cervantes, J. G., Torres-Cisneros, M., Saavedra Martínez, J. E., and Pinales, J. (2006). Frequency, time-frequency and wavelet analysis of ECG signal. In *Electronics and Photonics, 2006. MEP 2006. Multiconference on*, pages 257–261.

[10] Barandun, M., von Tscharner, V., Meuli-Simmen, C., Bowen, V., and Valderrabano, V. (2007). Frequency and conduction velocity analysis of the abductor pollicis brevis muscle during early fatigue. *Journal of Electromyography and Kinesiology*, 19(1):65–74.

[11] Bartlett, M. S. (1950). Periodogram analysis and continuous spectra. *Biometrika*, 37(1/2):1–16.

[12] Belkin, M. and Niyogi, P. (2001a). Laplacian Eigenmaps and Spectral Techniques for Embedding and Clustering. In *Nips*, volume 14, pages 585–591.

[13] Belkin, M. and Niyogi, P. (2001b). Semi-supervised learning on Riemannian manifolds. *Machine learning*, 56(1-3):209–239.

[14] Bendito, E., Carmona, A., Encinas, A., and Gesto, J. (2008). The curl of a weighted network. *Applicable Analysis and Discrete Mathematics*, 2(2):241–254.

[15] Benjamin, E. J., Wolf, P. A., D'Agostino, R. B., Silbershatz, H., Kannel, W. B., and Levy, D. (1998). Impact of Atrial Fibrillation on the Risk of Death : The Framingham Heart Study. *Circulation*, 98(10):946–952.

[16] Benzi, K., Ricaud, B., and Vandergheynst, P. (2016). Principal Patterns on Graphs: Discovering Coherent Structures in Datasets. *IEEE Transactions on Signal and Information Processing over Networks*, 2(2):160–173.

[17] Besl, P. and McKay, N. D. (1992). A method for registration of 3-D shapes. *IEEE Transactions on Pattern Analysis and Machine Intelligence*, 14(2):239–256.

[18] Bettoni, M. and Zimmermann, M. (2002). Autonomic tone variations before the onset of paroxysmal atrial fibrillation. *Circulation*, 105(23):2753–2759.

[19] Bhaskaran, A., Barry, M. A. T., Al Raisi, S. I., Chik, W., Nguyen, D. T., Pouliopoulos, J., Nalliah, C., Hendricks, R., Thomas, S., McEwan, A. L., Kovoor, P., and Thiagalingam, A. (2015). Magnetic guidance versus manual control: comparison of radiofrequency lesion dimensions and evaluation of the effect of heart wall motion in a myocardial phantom. *Journal of interventional cardiac electrophysiology : an international journal of arrhythmias and pacing*, 44(1):1–8.

[20] Bianchi, A. M., Baselli, G., Babiloni, F., and Rizzo, G. (2015). Multidimensional Processes: In Italy, biomedical signal and image processing embraces a multiparametric, multimodal, multiscale paradigm. *IEEE Pulse*, 6(4):44–49.

[21] Bigland-Ritchie, B., Donovan, E. F., and Roussos, C. S. (1981). Conduction velocity and EMG power spectrum changes in fatigue of sustained maximal efforts. *Journal of Applied Physiology*, 51(5):1300–1305.

[22] Blok, J. H., van Dijk, J. P., Drost, G., Zwarts, M. J., and Stegeman, D. F. (2002). A high-density multichannel surface electromyography system for the characterization of single motor units. *Review of Scientific Instruments*, 73(4):1887–1897.

[23] Bollmann, A., Husser, D., Mainardi, L., Lombardi, F., Langley, P., Murray, A., Rieta, J. J., Millet, J., Olsson, S. B., Stridh, M., and Sornmo, L. (2006). Analysis of surface electrocardiograms in atrial fibrillation: techniques, research, and clinical applications. *Europace : European pacing, arrhythmias, and cardiac electrophysiology : journal of the working groups on cardiac pacing, arrhythmias, and cardiac cellular electrophysiology of the European Society of Cardiology*, 8(11):911–926.

[24] Botteron, G. and Smith, J. (1995). A technique for measurement of the extent of spatial organization of atrial activation during atrial fibrillation in the intact human heart. *Biomedical Engineering, IEEE Transactions on*, 42(6):579–586.

[25] Bronstein, M. M., Bruna, J., LeCun, Y., Szlam, A., and Vandergheynst, P. (2017). Geometric Deep Learning: Going beyond Euclidean data. *IEEE Signal Processing Magazine*, 34(4):18–42.

[26] Buades, A., Coll, B., and Morel, J. M. (2005). A non-local algorithm for image denoising. In *Proceedings of the IEEE Computer Society Conference on Computer Vision and Pattern Recognition*, volume 2, pages 60–65.

[27] Bun, S.-S., Ayari, A., Latcu, D. G., Errahmouni, A., and Saoudi, N. (2017). Radiofrequency catheter ablation of atrial fibrillation: Electrical modification suggesting transmurality is faster achieved with remote magnetic catheter in comparison with contact force use. *Journal of Cardiovascular Electrophysiology*.

[28] Burago, D., Ivanov, S., and Kurylev, Y. (2013). A graph discretization of the Laplace-Beltrami operator. *Journal of Spectral Theory*, 4(4):675–714.

[29] Calkins, H., Kuck, K.-H., Cappato, R., Brugada, J., Camm, A. J., Chen, S.-A., Crijns, H. J. G., Damiano Jr, R. J., Davies, D. W., DiMarco, J., Edgerton, J. R., Ellenbogen, K., Ezekowitz, M. D., Haines, D. E., Haïssaguerre, M., Hindricks, G., Iesaka, Y., Jackman, W. M., Jalife, J., Jais, P., Kalman, J., Keane, D., Kim, Y.-H., Kirchhof, P., Klein, G., Kottkamp, H., Kumagai, K., Lindsay, B. D., Mansour, M., Marchlinski, F. E., McCarthy, P. M., Mont, J. L., Morady, F., Nademanee, K., Nakagawa, H., Natale, A., Nattel, S., Packer, D. L., Pappone, C., Prystowsky, E., Raviele, A., Reddy, V., Ruskin, J. N., Shemin, R. J., Tsao, H.-M., and Wilber, D. (2012). 2012 HRS/EHRA/ECAS Expert Consensus Statement on Catheter and Surgical Ablation of Atrial Fibrillation: recommendations for patient selection, procedural techniques, patient management and follow-up, definitions, endpoints, and research trial design. *Europace : European pacing, arrhythmias, and cardiac electrophysiology : journal of the working groups on cardiac pacing, arrhythmias, and cardiac cellular electrophysiology of the European Society of Cardiology*, 14(4):528–606.

[30] Camm, A. J., Kirchhof, P., Lip, G. Y. H., Schotten, U., Savelieva, I., Ernst, S., Van Gelder, I. C., Al-Attar, N., Hindricks, G., Prendergast, B., Heidbuchel, H., Alfieri, O., Angelini, A., Atar, D., Colonna, P., De Caterina, R., De Sutter, J., Goette, A., Gorenek, B., Heldal, M., Hohloser, S. H., Kolh, P., Le Heuzey, J.-Y., Ponikowski, P., Rutten, F. H., Vahanian, A., Auricchio, A., Bax, J., Ceconi, C., Dean, V., Filippatos, G., Funck-Brentano, C., Hobbs, R., Kearney, P., McDonagh, T., Popescu, B. A., Reiner, Z., Sechtem, U., Sirnes, P. A., Tendera, M., Vardas, P. E., Widimsky, P., Vardas, P. E., Agladze, V., Aliot, E., Balabanski, T., Blomstrom-Lundqvist, C., Capucci, A., Crijns, H. J. G., Dahlof, B., Folliguet, T., Glikson, M., Goethals, M., Gulba, D. C., Ho, S. Y., Klautz, R. J. M., Kose, S., McMurray, J., Perrone Filardi, P., Raatikainen, P., Salvador, M. J., Schalij, M. J., Shpektor, A., Sousa, J., Stepinska, J., Uuetoa, H., Zamorano, J. L., and Zupan, I. (2010). Guidelines for the management of atrial fibrillation: The Task Force for the Management of Atrial Fibrillation of the European Society of Cardiology (ESC). *European Heart Journal*, 31(19):2369–2429.

[31] Cantwell, C., Roney, C., Ng, F., Siggers, J., Sherwin, S., and Peters, N. (2015). Techniques for automated local activation time annotation and conduction velocity estimation in cardiac mapping. *Computers in Biology and Medicine*, 65:229–242.

[32] Chan, S. H., Khoshabeh, R., Gibson, K. B., Gill, P. E., and Nguyen, T. Q. (2011). An augmented Lagrangian method for total variation video restoration. *IEEE Trans Image Process*, 20(11):3097–3111.

[33] Chapman, A. and Mesbahi, M. (2011). Advection on graphs. In *50th IEEE Conference on Decision and Control and European Control Conference*, pages 1461–1466, Orlando, FL, USA.

[34] Christensen, O. (2016). *An introduction to frames and Riesz bases (Second Edition)*. Birkhäuser.

[35] Christov, I., Gómez-Herrero, G., Krasteva, V., Jekova, I., Gotchev, A., and Egiazarian, K. (2006). Comparative study of morphological and time-frequency ECG descriptors for heartbeat classification. *Medical Engineering and Physics*, 28(9):876–887.

[36] Chung, F. R. K. (1997). *Spectral Graph Theory*. Vol. 92 of the {CBMS} Regional Conference Series in Mathematics, {American Mathematical Society}.

[37] Cohen, L. (1994). *Time-Frequency Analysis*. Prentice Hall, Upper Saddle River, NJ, USA.

[38] Coifman, R. R. and Maggioni, M. (2006). Diffusion Wavelets. *Applied and Computational Harmonic Analysis*, 21(1):53–94.

[39] Courant, R., Friedrichs, K., and Lewy, H. (1967). On the Partial Difference Equations of Mathematical Physics. *IBM Journal of Research and Development*, 11(2):215–234.

[40] Courtemanche, M., Ramirez, R. J., and Nattel, S. (1998). Ionic mechanisms underlying human atrial action potential properties : insights from a mathematical model Ionic mechanisms underlying human atrial action potential properties : insights from a mathematical model. *American Journal of Physiology - Heart and Circulatory Physiology*, 275(1):1522–1539.

[41] Dahlhaus, R. and Eichler, M. (2003). Causality and graphical models in time series analysis. *Highly Structured Stochastic Systems*, pages 115–137.

[42] Das, M., Loveday, J. J., Wynn, G. J., Gomes, S., Saeed, Y., Bonnett, L. J., Waktare, J. E., Todd, D. M., Hall, M. C., Snowdon, R. L., Modi, S., and Gupta, D. (2017). Ablation index, a novel marker of ablation lesion quality: Prediction of pulmonary vein reconnection at repeat electrophysiology study and regional differences in target values. *Europace*, 19(5):775–783.

[43] De Domenico, M., Lima, A., Mougel, P., and Musolesi, M. (2013a). The Anatomy of a Scientific Rumor. *Scientific Reports*, 3(1):2980.

[44] De Domenico, M., Solé-Ribalta, A., Cozzo, E., Kivelä, M., Moreno, Y., Porter, M. A., Gómez, S., and Arenas, A. (2013b). Mathematical Formulation of Multilayer Networks. *Physical Review X*, 3(4):041022.

[45] de Jong, S., van Veen, T. A. B., van Rijen, H. V. M., and de Bakker, J. M. T. (2011). Fibrosis and Cardiac Arrhythmias. *Journal of Cardiovascular Pharmacology*, 57(6):630–638.

[46] De Ponti, R., Ho, S. Y., Salerno-Uriarte, J. A., Tritto, M., and Spadacini, G. (2002). Electroanatomic Analysis of Sinus Impulse Propagation in Normal Human Atria. *Journal of Cardiovascular Electrophysiology*, 13(1):1–10.

[47] Deno, D. C., Balachandran, R., Morgan, D., Ahmad, F., Masse, S., and Nanthakumar, K. (2017). Orientation-Independent Catheter-Based Characterization of Myocardial Activation. *IEEE Transactions on Biomedical Engineering*, 64(5):1067–1177.

[48] der Hoeven, J. H., Links, T. P., Zwarts, M. J., and Van Weerden, T. W. (1994). Muscle fiber conduction velocity in the diagnosis of familial hypokalemic periodic paralysis—invasive versus surface determination. *Muscle & nerve*, 17(8):898–905.

[49] der Hoeven, J. H., Zwarts, M. J., and Van Weerden, T. W. (1993). Muscle fiber conduction velocity in amyotrophic lateral sclerosis and traumatic lesions of the plexus brachialis. *Electroencephalography and Clinical Neurophysiology/Evoked Potentials Section*, 89(5):304–310.

[50] Dewire, J., Khurram, I. M., Pashakhanloo, F., Spragg, D. D., Marine, J. E., Berger, R. D., Ashikaga, H., Rickard, J., Zimmerman, S. L., Zipunnikov, V., Calkins, H., and Nazarian, S. (2014). The association of pre-existing left atrial fibrosis with clinical variables in patients referred for catheter ablation of atrial fibrillation. *Clinical Medicine Insights: Cardiology*, 8:25–30.

[51] Dokos, S., Celler, B., and Lovell, N. (1996). Ion currents underlying sinoatrial node pacemaker activity: a new single cell mathematical model. *J Theor Biol*, 181(3):245–272.

[52] Du Bois-Reymond, E. H. (1849). *Untersuchungen über thierische elektricität,*. Untersuchungen über thierische elektricität. G. Reimer.

[53] Dubois, R., Shah, A. J., Hocini, M., Denis, A., Derval, N., Cochet, H., Sacher, F., Bear, L., Duchateau, J., Jais, P., and Haissaguerre, M. (2015). Non-invasive cardiac mapping in clinical practice: Application to the ablation of cardiac arrhythmias. *Journal of Electrocardiology*, 48(6):966–974.

[54] Durran, D. R. (2013). *Numerical methods for wave equations in geophysical fluid dynamics*, volume 32. Springer Science & Business Media.

[55] Eberstein, A. and Beattie, B. (1985). Simultaneous measurement of muscle conduction velocity and emg power spectrum changes during fatigue. *Muscle & Nerve*, 8(9):768–773.

[56] Einthoven, W. (1908). Weiteres über das Elektrokardiogramm. *Pflüger, Archiv für die Gesamte Physiologie des Menschen und der Tiere*, 122(12):517–584.

[57] El Haddad, M., Taghji, P., Phlips, T., Wolf, M., Demolder, A., Choudhury, R., Knecht, S., Vandekerckhove, Y., Tavernier, R., Nakagawa, H., and Duytschaever, M. (2017). Determinants of Acute and Late Pulmonary Vein Reconnection in Contact Force-Guided Pulmonary Vein Isolation. *Circulation: Arrhythmia and Electrophysiology*, 10(4).

[58] Farina, D., Arendt-Nielsen, L., Merletti, R., and Graven-Nielsen, T. (2004). Effect of experimental muscle pain on motor unit firing rate and conduction velocity. *Journal of neurophysiology*, 91(3):1250–1259.

[59] Farina, D. and Merletti, R. (2004). Methods for estimating muscle fibre conduction velocity from surface electromyographic signals. *Medical and biological Engineering and Computing*, 42(4):432–445.

[60] Farina, D. and Negro, F. (2007). Estimation of muscle fiber conduction velocity with a spectral multidip approach. *IEEE Transactions on Biomedical Engineering*, 54(9):1583–1589.

[61] Farina, D., Negro, F., Gazzoni, M., and Enoka, R. M. (2008a). Detecting the Unique Representation of Motor-Unit Action Potentials in the Surface Electromyogram. *Journal of Neurophysiology*, 100(3):1223–1233.

[62] Farina, D., Yoshida, K., Stieglitz, T., and Koch, K. P. (2008b). Multichannel thin-film electrode for intramuscular electromyographic recordings. *Journal of Applied Physiology*, 104(3):821–827.

[63] Feichtinger, H. G. and Strohmer, T. (2012). *Gabor analysis and algorithms: Theory and applications*. Springer Science & Business Media.

[64] Fenton, F. H., Cherry, E. M., Hastings, H. M., and Evans, S. J. (2002). Multiple mechanisms of spiral wave breakup in a model of cardiac electrical activity. *Chaos: An Interdisciplinary Journal of Nonlinear Science*, 12(3):852–892.

[65] Fitzgerald, T. N., Brooks, D. H., and Triedman, J. K. (2005). Identification of cardiac rhythm features by mathematical analysis of vector fields. *IEEE transactions on bio-medical engineering*, 52(1):19–29.

[66] Fourier, J.-B.-J. (1808). Mémoire sur la propagation de la chaleur dans les corps solides. *Nouveau Bulletin des Sciences de la Société Philomathique de Paris*, 6:112–116.

[67] Frohlich, C. (1998). *Fundamentals of geophysics*, volume 79. Cambridge University Press, second edition.

[68] Galvani, L. (1791). *De viribus electricitatis in motu musculari commentarius*, volume 7. Ex Typographia Instituti Scientiarium.

[69] Gepstein, L., Hayam, G., Shpun, S., Cohen, D., and Ben-Haim, S. A. (1999). Atrial Linear Ablations in Pigs. *Circulation*, 100(4):419 LP – 426.

[70] Go, A. S., Mozaffarian, D., Roger, V. L., Benjamin, E. J., Berry, J. D., Borden, W. B., Bravata, D. M., Dai, S., Ford, E. S., Fox, C. S., Franco, S., Fullerton, H. J., Gillespie, C., Hailpern, S. M., Heit, J. A., Howard, V. J., Huffman, M. D., Kissela, B. M., Kittner, S. J., Lackland, D. T., Lichtman, J. H., Lisabeth, L. D., Magid, D., Marcus, G. M., Marelli, A., Matchar, D. B., McGuire, D. K., Mohler, E. R., Moy, C. S., Mussolino, M. E., Nichol, G., Paynter, N. P., Schreiner, P. J., Sorlie, P. D., Stein, J., Turan, T. N., Virani, S. S., Wong, N. D., Woo, D., and Turner, M. B. (2013). Heart disease and stroke statistics-2013 update: A Report from the American Heart Association. *Circulation*, 127(1).

[71] Goldberger, E. (1942a). A simple, indifferent, electrocardiographic electrode of zero potential and a technique of obtaining augmented, unipolar, extremity leads. *American Heart Journal*, 23(4):483–492.

[72] Goldberger, E. (1942b). The aVl, aVr, and aVf leads: A simplification of standard lead electrocardiography. *American Heart Journal*, 24(3):378–396.

[73] Grady, L. J. and Polimeni, J. R. (2010). *Discrete Calculus*. Springer London, London.

[74] Grassi, F., Perraudin, N., and Ricaud, B. (2016). Tracking time-vertex propagation using dynamic graph wavelets. In *2016 IEEE Global Conference on Signal and Information Processing (GlobalSIP)*, pages 351–355. IEEE.

[75] Griffa, A., Ricaud, B., Benzi, K., Bresson, X., Daducci, A., Vandergheynst, P., Thiran, J.-p., and Hagmann, P. (2017). Transient networks of spatio-temporal connectivity map communication pathways in brain functional systems. *NeuroImage*, 155(April):490–502.

[76] Gröchenig, K. (2001). *Foundations of Time-Frequency Analysis*. Applied and Numerical Harmonic Analysis. Birkhäuser Boston, Boston, MA.

[77] Guille, A., Hacid, H., and Zighed, D. A. (2013). Information Diffusion in Online Social Networks : A Survey. *ACM SIGMOD Record*, 42(June):12.

[78] Gustafson, K. and Harary, F. (1985). The curl of graphs and networks. *Mathematical Modelling*, 6(2):145–155.

[79] Haissaguerre, M., Hocini, M., Shah, A. J., Derval, N., Sacher, F., Jais, P., and Dubois, R. (2013). Noninvasive panoramic mapping of human atrial fibrillation mechanisms: A feasibility report. *Journal of Cardiovascular Electrophysiology*, 24(6):711–717.

[80] Haïssaguerre, M., Jaïs, P., Hocini, M., Sanders, P., Hsu, L.-F., Scavee, C., Weerasooriya, R., Shah, D. C., Garrigue, S., and Clementy, J. (2003). Macro reentrant atrial flutter following ablation of pulmonary veins, tricuspid and mitral isthmuses. *PACE*, 26:970.

[81] Haïssaguerre, M., Jaïs, P., Shah, D. C., Takahashi, A., Hocini, M., Quiniou, G., Garrigue, S., Le Mouroux, A., Le Métayer, P., and Clémenty, J. (1998). Spontaneous Initiation of Atrial Fibrillation by Ectopic Beats Originating in the Pulmonary Veins. *New England Journal of Medicine*, 339(10):659–666.

[82] Haldar, S. K., Magtibay, K., Porta-Sanchez, A., Massé, S., Mitsakakis, N., Lai, P. F. H., Azam, M. A., Asta, J., Kusha, M., Dorian, P., Ha, A. C. T., Chauhan, V., Deno, D. C., and Nanthakumar, K. (2017). Resolving Bipolar Electrogram Voltages During Atrial Fibrillation Using Omnipolar Mapping. *Circulation. Arrhythmia and electrophysiology*, 10(9):e005018.

[83] Hammond, D. K., Vandergheynst, P., and Gribonval, R. (2011). Wavelets on graphs via spectral graph theory. *Applied and Computational Harmonic Analysis*, 30(2):129–150.

[84] Hansson, A., Holm, M., Blomstrom, P., Johansson, R., Luhrs, C., Brandt, J., and Olsson, S. B. (1998). Right atrial free wall conduction velocity and degree of anisotropy in patients with stable sinus rhythm studied during open heart surgery. *European heart journal*, 19(2):293–300.

[85] Harvey, M., Kim, Y.-H., Sousa, J., El-Atassi, R., Morady, F., Calkins, H., and Langberg, J. J. (1992). Impedance monitoring during radiofrequency catheter ablation in humans. *Pacing and clinical electrophysiology : PACE*, 15(1):22–27.

[86] Heeringa, J., van der Kuip, D. A. M., Hofman, A., Kors, J. A., Van Herpen, G., Stricker, B. H. C., Stijnen, T., Lip, G. Y. H., and Witteman, J. C. M. (2006). Prevalence, incidence and lifetime risk of atrial fibrillation: the Rotterdam study. *European Heart Journal*, 27(8):949–953.

[87] Hermens, H. J., Bruggen, T. A. M. v., Baten, C. T. M., Rutten, W. L. C., and Boom, H. B. K. (1992). The median frequency of the surface EMG power spectrum in relation to motor unit firing and action potential properties. *Journal of Electromyography and Kinesiology*, 2(1):15–25.

[88] Hodgkin, A. L. and Huxley, A. F. (1939). Action Potentials Recorded from Inside a Nerve Fibre. *Nature*, 144(3651):710–711.

[89] Huang, W., Goldsberry, L., Wymbs, N. F., Grafton, S. T., Bassett, D. S., and Ribeiro, A. (2015). Graph frequency analysis of brain signals. *IEEE Journal of Selected Topics in Signal Processing*, 10(Section VI):1189–1203.

[90] Husser, D., Stridh, M., Sornmo, L., Geller, C., Klein, H. U., Olsson, S. B., and Bollmann, A. (2005). Time-frequency analysis of the surface electrocardiogram for monitoring antiarrhythmic drug effects in atrial fibrillation. *The American journal of cardiology*, 95(4):526–528.

[91] Issa, Z., Miller, J. M., and Zipes, D. P. (2008). *Clinical Arrhythmology and Electrophysiology: A Companion to Braunwald's Heart Disease*. Elsevier Saunders, 1 edition.

[92] Isufi, E., Loukas, A., Simonetto, A., and Leus, G. (2016). Separable Autoregressive Moving Average Graph-Temporal Filters. In *EUSIPCO*, pages 200–204. IEEE.

[93] Isufi, E., Loukas, A., Simonetto, A., and Leus, G. (2017). Autoregressive Moving Average Graph Filtering. *IEEE Transactions on Signal Processing*, 65(2):274–288.

[94] Itoh, T., Kimura, M., Sasaki, S., Owada, S., Horiuchi, D., Sasaki, K., Ishida, Y., Takahiko, K., and Okumura, K. (2014). High correlation of estimated local conduction velocity with natural logarithm of bipolar electrogram amplitude in the reentry circuit of atrial flutter. *Journal of Cardiovascular Electrophysiology*, 25(4):387–394.

[95] Jacquemet, V. and Henriquez, C. S. (2009). Genesis of complex fractionated atrial electrograms in zones of slow conduction: a computer model of microfibrosis. *Heart rhythm*, 6(6):803–810.

[96] January, C. T., Wann, L. S., Alpert, J. S., Calkins, H., Cigarroa, J. E., Cleveland, J. C., Conti, J. B., Ellinor, P. T., Ezekowitz, M. D., Field, M. E., Murray, K. T., Sacco, R. L., Stevenson, W. G., Tchou, P. J., Tracy, C. M., and Yancy, C. W. (2014). 2014 AHA/ACC/HRS Guideline for the Management of Patients With Atrial Fibrillation: A Report of the American College of Cardiology/American Heart Association Task Force on Practice Guidelines and the Heart Rhythm Society. *Circulation*, 130(23):e199–e267.

[97] Ju, W., Yang, B., Chen, H., Zhang, F., Zhai, L., Cao, K., and Chen, M. (2011). Localized reentry as a novel type of the proarrhythmic effects of linear ablation in the left atrium. *Pacing and clinical electrophysiology : PACE*, 34(8):919–926.

[98] Juel, C. (1988). Muscle action potential propagation velocity changes during activity. *Muscle & nerve*, 11(7):714–719.

[99] Kaiser, J. F. (1990). On a simple algorithm to calculate the energy of a signal. In *Acoustics, Speech, and Signal Processing, 1990. ICASSP-90., 1990 International Conference on*, volume 2, pages 381–384.

[100] Kalman, J., Fitzpatrick, A. P., Olgin, J. E., Chin, M. C., Lee, R. J., Scheinman, M. M., and Lesh, M. D. (1997). Biophysical characteristics of radiofrequency lesion formation in vivo: dynamics of catheter tip-tissue contact evaluated by intracardiac echocardiography. *American heart journal*, 133(1):8–18.

[101] Kalofolias, V. (2016). How to learn a graph from smooth signals. In *AISTATS*, volume 13.

[102] Kanagaratnam, L., Tomassoni, G., Schweikert, R., Pavia, S., Bash, D., Beheiry, S., Lesh, M. D., Niebauer, M., Saliba, W., Chung, M., Tchou, P. J., and Natale, A. (2001). Empirical pulmonary vein isolation in patients with chronic atrial fibrillation using a three-dimensional nonfluoroscopic mapping system: long-term follow-up. *Pacing and clinical electrophysiology : PACE*, 24(12):1774–1779.

[103] Kannel, W. B., Wolf, P. A., Benjamin, E. J., and Levy, D. (1998). Prevalence, incidence, prognosis, and predisposing conditions for atrial fibrillation: population-based estimates. *The American Journal of Cardiology*, 82(7):2N–9N.

[104] Kautzner, J., Neuzil, P., Lambert, H., Peichl, P., Petru, J., Cihak, R., Skoda, J., Wichterle, D., Wissner, E., Yulzari, A., and Kuck, K.-H. (2015). EFFICAS II: optimization of catheter contact force improves outcome of pulmonary vein isolation for paroxysmal atrial fibrillation. *Europace*, 17(8):1229–1235.

[105] Kautzner, J. and Peichl, P. (2014). Contact Force Assessment In Catheter Ablation Of Atrial Fibrillation. *Journal of Atrial Fibrillation*, 6(6):1047.

[106] Keller, M. (2014). *Formation of Intracardiac Electrograms under Physiological and Pathological Conditions*. Karlsruhe transactions on biomedical engineering. KIT Scientific Publishing, Karlsruhe.

[107] Kermack, W. O. and McKendrick, A. G. (1927). A Contribution to the Mathematical Theory of Epidemics. *Proceedings of the Royal Society A: Mathematical, Physical and Engineering Sciences*, 115(772):700–721.

[108] Khurram, I. M., Beinart, R., Zipunnikov, V., Dewire, J., Yarmohammadi, H., Sasaki, T., Spragg, D. D., Marine, J. E., Berger, R. D., Halperin, H. R., Calkins, H., Zimmerman, S. L., and Nazarian, S. (2014). Magnetic resonance image intensity ratio, a normalized measure to enable interpatient comparability of left atrial fibrosis. *Heart Rhythm*, 11(1):85–92.

[109] Kivelä, M., Arenas, A., Barthelemy, M., Gleeson, J. P., Moreno, Y., and Porter, M. A. (2014). Multilayer networks. *Journal of Complex Networks*, 2(3):203–271.

[110] Klabunde, R. E. (2011). *Cardiovascular Physiology Concepts*. Lippincott Williams & Wilki, 2 edition.

[111] Kleber, A. G. and Rudy, Y. (2004). Basic mechanisms of cardiac impulse propagation and associated arrhythmias. *Physiological reviews*, 84(2):431–488.

[112] Knowles, B. R., Caulfield, D., Cooklin, M., Rinaldi, C. A., Gill, J. S., Bostock, J., Razavi, R., Schaeffter, T., and Rhode, K. S. (2010). 3-D visualization of acute RF ablation lesions using MRI for the simultaneous determination of the patterns of necrosis and edema. *IEEE Transactions on Biomedical Engineering*, 57(6):1467–1475.

[113] Kojodjojo, P., Kanagaratnam, P., Markides, V., Davies, D. W., and Peters, N. (2006). Age-related changes in human left and right atrial conduction. *Journal of cardiovascular electrophysiology*, 17(2):120–127.

[114] Kolipaka, A., Chatzimavroudis, G. P., White, R. D., O'Donnell, T. P., and Setser, R. M. (2004). Segmentation of non-viable myocardium in delayed enhancement magnetic resonance images. *The International Journal of Cardiovascular Imaging*, 21:303–311.

[115] Kovačević, J. and Chebira, A. (2007). Life Beyond Bases: The Advent of Frames (Part I). *IEEE Signal Process. Mag.*, 24(4):86–104.

[116] Kuck, K.-H. (2008). Comparison of catheter stability between magnetically guided and manual cooled-tip ablation catheters. *Heart Rhythm*, 5(5):S438–S466.

[117] Kumar, S., Barbhaiya, C. R., Balindger, S., John, R. M., Epstein, L. M., Koplan, B. A., Tedrow, U. B., Stevenson, W. G., and Michaud, G. F. (2015). Better Lesion Creation And Assessment During Catheter Ablation. *Journal of Atrial Fibrillation*, 8(3):1189.

[118] Kumar, S., Chan, M., Lee, J., Wong, M. C. G., Yudi, M., Morton, J. B., Spence, S. J., Halloran, K., Kistler, P. M., and Kalman, J. (2014). Catheter-tissue contact force determines atrial electrogram characteristics before and lesion efficacy after antral pulmonary vein isolation in humans. *Journal of Cardiovascular Electrophysiology*, 25:122–129.

[119] Kupa, E. J., Roy, S. H., Kandarian, S. C., and De Luca, C. J. (1995). Effects of muscle fiber type and size on EMG median frequency and conduction velocity. *Journal of Applied Physiology*, 79(1):23–32.

[120] Latcu, D. G. and Saoudi, N. (2014). How fast does the electrical impulse travel within the myocardium? the need for a new clinical electrophysiology tool: The conduction velocity mapping. *Journal of Cardiovascular Electrophysiology*, 25(4):395–397.

[121] Lenis, G., Pilia, N., Loewe, A., Schulze, W. H., and Dössel, O. (2017). Comparison of Baseline Wander Removal Techniques considering the Preservation of ST Changes in the Ischemic ECG: A Simulation Study. *Computational and Mathematical Methods in Medicine*, 2017.

[122] Levkov, C., Mihov, G., Ivanov, R., Daskalov, I., Christov, I., and Dotsinsky, I. (2005). Removal of power-line interference from the ECG: A review of the subtraction procedure. *BioMedical Engineering Online*, 4:1–18.

[123] Lim, L.-H. L.-h. (2015). Hodge Laplacians on graphs. *ArXiv e-prints*, pages 1–38.

[124] Linz, D., Ukena, C., Mahfoud, F., Neuberger, H. R., and Böhm, M. (2014). Atrial autonomic innervation: A target for interventional antiarrhythmic therapy? *Journal of the American College of Cardiology*, 63(3):215–224.

[125] Loukas, A. and Cattani, M. (2015). Graph Scale-Space Theory for Distributed Peak and Pit Identification. In *2015 14th International Conference on Information Processing in Sensor Networks (IPSN 2015)*, pages 118–129. ACM/IEEE.

[126] Loukas, A. and Foucard, D. (2016). Frequency Analysis of Temporal Graph Signals. In *2016 IEEE Global Conference on Signal and Information Processing (GlobalSIP)*, pages 346–350.

[127] Loukas, A., Simonetto, A., and Leus, G. (2015). Distributed Autoregressive Moving Average Graph Filters. *IEEE Signal Processing Letters*, 22(11):1931–1935.

[128] Lowery, M., Nolan, P., and O'Malley, M. (2002). Electromyogram median frequency, spectral compression and muscle fibre conduction velocity during sustained sub-maximal contraction of the brachioradialis muscle. *Journal of Electromyography and Kinesiology*, 12(2):111–118.

[129] Luo, S. and Johnston, P. (2010). A review of electrocardiogram filtering. *Journal of Electrocardiology*, 43(6):486–496.

[130] Marieb, E. N. and Hoehn, K. (2012). *Human Anatomy & Physiology*. Pearson, 9 edition.

[131] Marques, A. G., Segarra, S., Leus, G., and Ribeiro, A. (2016). Stationary Graph Processes and Spectral Estimation. *arXiv preprint arXiv:1603.04667*.

[132] Mason, J. C. and Handscomb, D. C. (2002). *Chebyshev Polynomials*. CRC Press.

[133] Massé, S., Magtibay, K., Jackson, N., Asta, J., Kusha, M., Zhang, B., Balachandran, R., Radisic, M., Deno, D. C., and Nanthakumar, K. (2016). Resolving myocardial activation with novel omnipolar electrograms. *Circulation: Arrhythmia and Electrophysiology*, 9(7).

[134] Matteucci, C. and Savi, P. (1844). *Traité des phénomènes électrophysiologiques des animaux*. Nineteenth Century Collections Online: Science, Technology, and Medicine: 1780-1925, Part II. Masson éditeurs.

[135] McGann, C. J., Kholmovski, E. G., Oakes, R. S., Blauer, J. J. E., Daccarett, M., Segerson, N., Airey, K. J., Akoum, N. W., Fish, E., Badger, T. J., DiBella, E. V. R., Parker, D., MacLeod, R. S., and Marrouche, N. F. (2008). New Magnetic Resonance Imaging-Based Method for Defining the Extent of Left Atrial Wall Injury After the Ablation of Atrial Fibrillation. *Journal of the American College of Cardiology*, 52(15):1263–1271.

[136] Mei, J. and Moura, J. M. F. (2015). Signal processing on graphs: Estimating the structure of a graph. In *2015 IEEE International Conference on Acoustics, Speech and Signal Processing (ICASSP)*, pages 5495–5499. IEEE.

[137] Menne, M. J., Durre, I., Vose, R. S., Gleason, B. E., and Houston, T. G. (2012). An Overview of the Global Historical Climatology Network-Daily Database. *Journal of Atmospheric and Oceanic Technology*, 29(7):897–910.

[138] Merletti, R., Knaflitz, M., and De Luca, C. J. (1990). Myoelectric manifestations of fatigue in voluntary and electrically elicited contractions. *Journal of applied physiology*, 69(5):1810–1820.

[139] Merris, R. (1994). Laplacian matrices of graphs: a survey. *Linear Algebra and its Applications*, 197:143–176.

[140] Methenitis, S., Karandreas, N., Spengos, K., Zaras, N., Stasinaki, A.-N., and Terzis, G. (2016). Muscle Fiber Conduction Velocity, Muscle Fiber Composition, and Power Performance. *Medicine and science in sports and exercise*, 48(9):1761–1771.

[141] Miz, V., Benzi, K., Ricaud, B., and Vandergheynst, P. (2017). Wikipedia graph mining: dynamic structure of collective memory. *ArXiv e-prints*.

[142] Moe, G. K. (1962). On the multiple wavelet hypothesis of atrial fibrillation. *Arch.Int.Pharmacodyn.Ther.*, 140:183–188.

[143] Mohan, P., Padmanabhan, V. N., and Ramjee, R. (2008). TrafficSense : Rich Monitoring of Road and Traffic Conditions using Mobile Smartphones. In *Proceedings of the 6th ACM conference on Embedded network sensor systems*, pages 1–29. ACM.

[144] Moler, C. (1994). Jordan's Canonical Form Just Doesn't Compute.

[145] Nair, G. M., Nery, P. B., Redpath, C. J., and Birnie, D. H. (2014). The Role Of Renin Angiotensin System In Atrial Fibrillation. *Journal of Atrial Fibrillation*, 6(6):972.

[146] Narasimhan, T. N. (1999). Fourier's heat conduction equation: History, influence, and connections. *Proceedings of the Indian Academy of Sciences, Earth and Planetary Sciences*, 108(3):117–148.

[147] Narayan, S. M., Krummen, D. E., and Rappel, W. J. (2012). Clinical mapping approach to diagnose electrical rotors and focal impulse sources for human atrial fibrillation. *Journal of Cardiovascular Electrophysiology*, 23(5):447–454.

[148] Oakes, R. S., Badger, T. J., Kholmovski, E. G., Akoum, N. W., Burgon, N. S., Fish, E. N., Blauer, J. J. E., Rao, S. N., Dibella, E. V. R., Segerson, N. M., Daccarett, M., Windfelder, J., McGann, C. J., Parker, D., MacLeod, R. S., and Marrouche, N. F. (2009). Detection and quantification of left atrial structural remodeling with delayed-enhancement magnetic resonance imaging in patients with atrial fibrillation. *Circulation*, 119(13):1758–1767.

[149] Odinaka, I., Lai, P. H., Kaplan, A. D., O'Sullivan, J. A., Sirevaag, E. J., Kristjansson, S. D., Sheffield, A. K., and Rohrbaugh, J. W. (2010). ECG biometrics: A robust short-time frequency analysis. In *2010 IEEE International Workshop on Information Forensics and Security, WIFS 2010*, pages 1–6.

[150] Otomo, K., Uno, K., Fujiwara, H., Isobe, M., and Iesaka, Y. (2010). Local unipolar and bipolar electrogram criteria for evaluating the transmurality of atrial ablation lesions at different catheter orientations relative to the endocardial surface. *Heart Rhythm*, 7(9):1291–1300.

[151] Pagana, G., Galleani, L., Grossi, S., Roch, M. R., Pastore, E., Poggio, M., and Quaranta, G. (2012). Time-Frequency Analysis of the Endocavitarian Signal in Paroxysmal Atrial Fibrillation. *IEEE Transactions on Biomedical Engineering*, 59(10):2838–2844.

[152] Pan, J. and Tompkins, W. J. (1985). A real-time qrs detection algorithm. *Biomedical Engineering, IEEE Transactions on*, BME-32(3):230–236.

[153] Pappone, C., Cappato, R., Oreto, G., Shpun, S., Calabrò, M. P., Conversano, A., Vicedomini, G., Lamberti, F., Rillo, M., Loricchio, M. L., Ben-Haim, S. A., Chierchia, S., Vicedomini, G., Loricchio, M. L., Shpun, S., Rillo, M., Calabrò, M. P., Conversano, A., Ben-Haim, S. A., Cappato, R., and Chierchia, S. (1999). Catheter ablation of paroxysmal atrial fibrillation using a 3D mapping system. *Circulation*, 100(11):1203–1208.

[154] Pappone, C., Rosanio, S., Oreto, G., Tocchi, M., Gugliotta, F., Vicedomini, G., Salvati, A., Dicandia, C., Mazzone, P., Santinelli, V., Gulletta, S., and Chierchia, S. (2000). Circumferential Radiofrequency Ablation of Pulmonary Vein Ostia. *Circulation*, 102(21):2619 LP – 2628.

[155] Pappone, C. and Santinelli, V. (2005). Atrial Fibrillation Ablation: State of the Art. *American Journal of Cardiology*, pages 59–64.

[156] Pappone, C., Vicedomini, G., Manguso, F., Gugliotta, F., Mazzone, P., Gulletta, S., Sora, N., Sala, S., Marzi, A., Augello, G., Livolsi, L., Santagostino, A., and Santinelli, V. (2006). Robotic Magnetic Navigation for Atrial Fibrillation Ablation. *Journal of the American College of Cardiology*, 47(7):1390–1400.

[157] Park, C.-I. I., Lehrmann, H., Keyl, C., Weber, R., Schiebeling, J., Allgeier, J., Schurr, P., Shah, A., Neumann, F.-J. J., Arentz, T., and Jadidi, A. S. (2014). Mechanisms of Pulmonary Vein Reconnection After Radiofrequency Ablation of Atrial Fibrillation: The Deterministic Role of Contact Force and Interlesion Distance. *Journal of Cardiovascular Electrophysiology*, 25(7):701–708.

[158] Pastor-Satorras, R., Castellano, C., Van Mieghem, P., and Vespignani, A. (2015). Epidemic processes in complex networks. *Reviews of Modern Physics*, 87(3):925–979.

[159] Perraudin, N., Kalofolias, V., Shuman, D., and Vandergheynst, P. (2016a). UNLocBoX: A MATLAB convex optimization toolbox for proximal-splitting methods. *ArXiv e-prints*, pages 1–15.

[160] Perraudin, N., Paratte, J., Shuman, D. I., Kalofolias, V., Vandergheynst, P., and Hammond, D. K. (2014). GSPBOX: A toolbox for signal processing on graphs. *ArXiv e-prints*, pages 1–8.

[161] Perraudin, N., Ricaud, B., Shuman, D. I., and Vandergheynst, P. (2016b). Global and Local Uncertainty Principles for Signals on Graphs. *arXiv preprint arXiv:1603.03030*, pages 1–36.

[162] Perraudin, N. and Vandergheynst, P. (2016). Stationary signal processing on graphs. *IEEE Trans. Signal Process.*, PP(99):1.

[163] Phillips, G. M. (2003). *Interpolation and Approximation by Polynomials*. CMS Books in Mathematics. Springer.

[164] Piccini, J. P., Hammill, B. G., Sinner, M. F., Jensen, P. N., Hernandez, A. F., Heckbert, S. R., Benjamin, E. J., and Curtis, L. H. (2012). Incidence and Prevalence of Atrial Fibrillation and Associated Mortality Among Medicare Beneficiaries: 1993–2007. *Circulation: Cardiovascular Quality and Outcomes*, 5(1):85–93.

[165] Piorkowski, C., Eitel, C., Rolf, S., Bode, K., Sommer, P., Gaspar, T., Kircher, S., Wetzel, U., Parwani, A. S., Boldt, L.-H., Mende, M., Bollmann, A., Husser, D., Dagres, N., Esato, M., Arya, A., Haverkamp, W., and Hindricks, G. (2011). Steerable versus nonsteerable sheath technology in atrial fibrillation ablation: a prospective, randomized study. *Circulation. Arrhythmia and electrophysiology*, 4(2):157–165.

[166] Pontecorboli, G., Figueras I Ventura, R. M., Carlosena-Remírez, A., Benito, E. M., Prat-Gonzales, S., Padeletti, L., and Mont, L. (2016). Use of delayed-enhancement magnetic resonance imaging for fibrosis detection in the atria: a review. *Europace : European pacing, arrhythmias, and cardiac electrophysiology : journal of the working groups on cardiac pacing, arrhythmias, and cardiac cellular electrophysiology of the European Society of Cardiology*, 155(5):469–473.

[167] Průša, Z., Søndergaard, P. L., Holighaus, N., Wiesmeyr, C., and Balazs, P. (2014). The Large Time-Frequency Analysis Toolbox 2.0. In Aramaki, M., Derrien, O., Kronland-Martinet, R., and Ystad, S., editors, *Sound, Music, and Motion: 10th International Symposium, CMMR 2013, Marseille, France, October 15-18, 2013. Revised Selected Papers*, volume 8905, pages 419–442. Springer International Publishing, Cham.

[168] Rahman, F., Kwan, G. F., and Benjamin, E. J. (2014). Global epidemiology of atrial fibrillation. *Nat Rev Cardiol*, 11(11):639–54.

[169] Rajappan, K., Kistler, P. M., Earley, M. J., Thomas, G., Izquierdo, M., Sporton, S. C., and Schilling, R. J. (2008). Acute and chronic pulmonary vein reconnection after atrial fibrillation ablation: a prospective characterization of anatomical sites. *Pacing and clinical electrophysiology : PACE*, 31(12):1598–1605.

[170] Ravazzi, C., Coluccia, G., and Magli, E. (2017). Curl-Constrained Gradient Estimation for Image Recovery From Highly Incomplete Spectral Data. *IEEE Transactions on Image Processing*, 26(6):2656–2668.

[171] Reddy, V. Y., Dukkipati, S. R., Neuzil, P., Natale, A., Albenque, J.-P., Kautzner, J., Shah, D., Michaud, G. F., Wharton, M., Harari, D., Mahapatra, S., Lambert, H., and Mansour, M. (2015). A Randomized Controlled Trial of the Safety and Effectiveness of a Contact Force Sensing Irrigated Catheter for Ablation of Paroxysmal Atrial Fibrillation: Results of the TOCCASTAR Study. *Circulation*.

[172] Reddy, V. Y., Shah, D., Kautzner, J., Schmidt, B., Saoudi, N., Herrera, C., Jais, P., Hindricks, G., Peichl, P., Yulzari, A., Lambert, H., Neuzil, P., Natale, A., and Kuck, K.-H. (2012). The relationship between contact force and clinical outcome during radiofrequency catheter ablation of atrial fibrillation in the TOCCATA study. *Heart rhythm*, 9(11):1789–1795.

[173] Romero, I., Fleck, E., and Kriatselis, C. (2011). Frequency analysis of atrial fibrillation surface and intracardiac electrograms during pulmonary vein isolation. *Europace*, 13(9):1340–1345.

[174] Roney, C. H., Cantwell, C. D., Qureshi, N. A., Ali, R. L., Chang, E. T. Y., Lim, P. B., Sherwin, S. J., Peters, N. S., Siggers, J. H., and Ng, F. S. (2014). An automated algorithm for determining conduction velocity, wavefront direction and origin of focal cardiac arrhythmias using a multipolar catheter. *2014 36th Annual International Conference of the IEEE Engineering in Medicine and Biology Society, EMBC 2014*, pages 1583–1586.

[175] Rudelson, M. (1999). Random vectors in the isotropic position. *Journal of Functional Analysis*, 164(1):1–12.

[176] Sameni, R. (2012). A linear Kalman Notch Filter for Power-Line Interference Cancellation. In *The 16th CSI International Symposium on Artificial Intelligence and Signal Processing (AISP 2012)*, pages 604–610.

[177] Sanchez, J. E., Kay, G. N., Benser, M. E., Hall, J. A., Walcott, G. P., Smith, W. M., and Ideker, R. E. (2003). Identification of transmural necrosis along a linear catheter ablation lesion during atrial fibrillation and sinus rhythm. *Journal of Interventional Cardiac Electrophysiology*, 8(1):9–17.

[178] Sanders, P., Berenfeld, O., Hocini, M., Jaïs, P., Vaidyanathan, R., Hsu, L. F., Garrigue, S., Takahashi, Y., Rotter, M., Sacher, F., Scavée, C., Ploutz-Snyder, R., Jalife, J., and Haïssaguerre, M. (2005). Spectral analysis identifies sites of

high-frequency activity maintaining atrial fibrillation in humans. *Circulation*, 112(6):789–797.

[179] Sandryhaila, A. and Moura, J. M. F. (2013). Discrete Signal Processing on Graphs. *IEEE Transactions on Signal Processing*, 61(7):1644–1656.

[180] Sandryhaila, A. and Moura, J. M. F. (2014a). Big data analysis with signal processing on graphs: Representation and processing of massive data sets with irregular structure. *IEEE Signal Processing Magazine*, 31(5):80–90.

[181] Sandryhaila, A. and Moura, J. M. F. (2014b). Discrete signal processing on graphs: Frequency analysis. *IEEE Transactions on Signal Processing*, 62(12):3042–3054.

[182] Sawa, A., Shimizu, A., Ueyama, T., Yoshiga, Y., Suzuki, S., Sugi, N., Oono, M., Oomiya, T., and Matsuzaki, M. (2008). Activation patterns and conduction velocity in posterolateral right atrium during typical atrial flutter using an electro-anatomic mapping system. *Circulation journal : official journal of the Japanese Circulation Society*, 72(3):384–391.

[183] Shah, D. C., Lambert, H., Nakagawa, H., Langenkamp, A., Aeby, N., and Leo, G. (2010). Area Under the Real-Time Contact Force Curve (Force-Time Integral) Predicts Radiofrequency Lesion Size in an In Vitro Contractile Model. *Journal of Cardiovascular Electrophysiology*, 21(9):1038–1043.

[184] Shahid, N., Grassi, F., and Vandergheynst, P. (2016a). Multilinear Low-Rank Tensors on Graphs & Applications. *ArXiv e-prints*.

[185] Shahid, N., Perraudin, N., Kalofolias, V., Puy, G., Vandergheynst, P., Puy, G., and Vandergheynst, P. (2016b). Fast robust pca on graphs. *IEEE Journal on Selected Topics in Signal Processing*, 10(4):740–756.

[186] Shuman, D. I., Narang, S. K., Frossard, P., Ortega, A., and Vandergheynst, P. (2013a). The emerging field of signal processing on graphs: Extending high-dimensional data analysis to networks and other irregular domains. *Signal Process. Mag., IEEE*, 30(3):83–98.

[187] Shuman, D. I., Ricaud, B., and Vandergheynst, P. (2012). A Windowed Graph Fourier Transform Signal Processing on Graphs on Graphs Processing Signals. In *Statistical Signal Processing Workshop (SSP), 2012 IEEE*, pages 133–136. Ieee.

[188] Shuman, D. I., Ricaud, B., and Vandergheynst, P. (2013b). Vertex-Frequency Analysis on Graphs. *Applied and Computational Harmonic Analysis*, 40(2):260–291.

[189] Shuman, D. I., Vandergheynst, P., and Frossard, P. (2011). Chebyshev polynomial approximation for distributed signal processing. In *2011 International Conference on Distributed Computing in Sensor Systems and Workshops (DCOSS)*, pages 1–8. IEEE, IEEE.

[190] Shuman, D. I., Wiesmeyr, C., Holighaus, N., and Vandergheynst, P. (2015). Spectrum-adapted tight graph wavelet and vertex-frequency frames. *IEEE Transactions on Signal Processing*, 63(16):4223–4235.

[191] Silverthorn, D. U. (2013). *Human Physiology: An Integrated Approach*. Pearson, 6 edition.

[192] Smeets, J. L., Allessie, M. A., Lammers, W. J., Bonke, F. I., and Hollen, J. (1986). The wavelength of the cardiac impulse and reentrant arrhythmias in isolated rabbit atrium. The role of heart rate, autonomic transmitters, temperature, and potassium. *Circulation research*, 58(1):96–108.

[193] Smith, K., Ricaud, B., Shahid, N., Rhodes, S., Starr, J. M., Ibanez, A., Parra, M. A., Escudero, J., and Vandergheynst, P. (2016). The Physiological Underpinnings of Visual Short-Term Memory Binding using Graph Modular Dirichlet Energy: Evidence from Healthy Subjects. *arXiv preprint*, pages 1–13.

[194] Smith, K., Spyrou, L., and Escudero, J. (2017). Graph-Variate Signal Analysis: Framework and Applications. *ArXiv e-prints*.

[195] Smola, A. A. J. and Kondor, R. (2003). Kernels and Regularization on Graphs. In Schölkopf, B. and Warmuth, M., editors, *Machine Learning*, volume 2777, pages 1–15. Springer.

[196] Sohns, C., Karim, R., Harrison, J., Arujuna, A., Linton, N., Sennett, R., Lambert, H., Leo, G., Williams, S. E., Razavi, R. S., Wright, M., Schaeffter, T., O'Neill, M., and Rhode, K. (2014). Quantitative magnetic resonance imaging analysis of the relationship between contact force and left atrial scar formation after catheter ablation of atrial fibrillation. *Journal of Cardiovascular Electrophysiology*, 25(2):138–145.

[197] Solomon, J. (2015). PDE Approaches to Graph Analysis. *CoRR*, abs/1505.0.

[198] Sörnmo, L. and Laguna, P. (2005). *Bioelectrical Signal Processing in Cardiac and Neurological Applications*. Academic Press series in biomedical engineering. Elsevier Academic Press.

[199] Spach, M. S. and Dolber, P. C. (1986). Relating extracellular potentials and their derivatives to anisotropic propagation at a microscopic level in human cardiac muscle. Evidence for electrical uncoupling of side-to-side fiber connections with increasing age. *Circulation research*, 58(3):356–371.

[200] Strang, G. (1999). The Discrete Cosine Transform. *Socitey of Industrial and Applied Mathematics*, 41(1):135–147.

[201] Stridh, M., Sornmo, L., Meurling, C., and Olsson, S. (2001). Characterization of atrial fibrillation using the surface ECG: time-dependent spectral properties. *IEEE Transactions on Biomedical Engineering*, 48(1):19–27.

[202] Stulen, F. B. and De Luca, C. J. (1981). Frequency parameters of the myoelectric signal as a measure of muscle conduction velocity. *IEEE Transactions on Biomedical Engineering*, BME-28(7):515–523.

[203] Tao, S., Way, S. F., Garland, J., Chrispin, J., Ciuffo, L. A., Balouch, M. A., Nazarian, S., Spragg, D. D., Marine, J. E., Berger, R. D., Calkins, H., and Ashikaga, H. (2017). Ablation as targeted perturbation to rewire communication network of persistent atrial fibrillation. *PLoS ONE*, 12(7):1–18.

[204] Thanou, D., Shuman, D. I., and Frossard, P. (2014). Learning Parametric Dictionaries for Signals on Graphs. *IEEE Transactions on Signal Processing*, 62(15):3849–3862.

[205] Ullah, W., Hunter, R. J., Baker, V., Dhinoja, M. B., Sporton, S. C., Earley, M. J., and Schilling, R. J. (2014). Target indices for clinical ablation in atrial fibrillation: insights from contact force, electrogram, and biophysical parameter analysis. *Circulation. Arrhythmia and electrophysiology*, 7(1):63–68.

[206] Ullah, W., Hunter, R. J., Baker, V., Dhinoja, M. B., Sporton, S. C., Earley, M. J., and Schilling, R. J. (2015). Factors affecting catheter contact in the human left atrium and their impact on ablation efficacy. *Journal of cardiovascular electrophysiology*, 26(2):129–136.

[207] Valdivia, P., Dias, F., Petronetto, F., Silva, C. T., and Nonato, L. G. (2015). Wavelet-based visualization of time-varying data on graphs. In *2015 IEEE Conference on Visual Analytics Science and Technology (VAST)*, pages 1–8. IEEE.

[208] Vaquero, M., Calvo, D., and Jalife, J. (2008). Cardiac fibrillation: from ion channels to rotors in the human heart. *Heart Rhythm*, 5(6):872–879.

[209] Vershynin, R. (2012). How Close is the Sample Covariance Matrix to the Actual Covariance Matrix? *Journal of Theoretical Probability*, 25(3):655–686.

[210] Wang, T. J., Larson, M. G., Levy, D., Vasan, R. S., Leip, E. P., Wolf, P. A., D'Agostino, R. B., Murabito, J. M., Kannel, W. B., and Benjamin, E. J. (2003). Temporal Relations of Atrial Fibrillation and Congestive Heart Failure and Their Joint Influence on Mortality: The Framingham Heart Study. *Circulation*, 107(23):2920–2925.

[211] Weber, F. M., Luik, A., Schilling, C., Seemann, G., Krueger, M. W., Lorenz, C., Schmitt, C., and Dossel, O. (2011). Conduction velocity restitution of the human atriuman-An efficient measurement protocol for clinical electrophysiological studies. *IEEE Transactions on Biomedical Engineering*, 58(9):2648–2655.

[212] Weber, F. M., Schilling, C., Seemann, G., Luik, A., Schmitt, C., Lorenz, C., and Dossel, O. (2010). Wave Direction and Conduction Velocity Analysis from Intracardiac Electrograms - A Single-Shot Technique. *IEEE transactions on bio-medical engineering*, 57(10):45–45.

[213] Weiss, J. P., May, H. T., Bair, T. L., Crandall, B. G., Cutler, M. J., Day, J. D., Osborn, J. S., Mallender, C., and Bunch, T. J. (2016). A Comparison of Remote Magnetic Irrigated Tip Ablation versus Manual Catheter Irrigated Tip Catheter Ablation With and Without Force Sensing Feedback. *Journal of cardiovascular electrophysiology*, 27 Suppl 1:S5–S10.

[214] Welch, P. (1967). The use of fast Fourier transform for the estimation of power spectra: a method based on time averaging over short, modified periodograms. *IEEE Transactions on Audio and Electroacoustics*, 15:70–73.

[215] Wiener, N. (1930). Generalized harmonic analysis. *Acta Mathematica*, 55(1):117–258.

[216] Wijffels, M. C. E. F., Kirchhof, C. J. H. J., Dorland, R., and Allessie, M. A. (1995). Atrial fibrillation begets atrial fibrillation. A study in awake chronically instrumented goats. *Circulation*, 92(7):1954–68.

[217] Wilson, F. N., Johnston, F. D., Macleod, A. G., and Barker, P. S. (1934). Electrocardiograms that represent the potential variations of a single electrode. *American Heart Journal*, 9(4):447–458.

[218] Wilson, F. N., Macleod, A. G., and Barker, P. S. (1931). The potential variations produced by the heart beat at the apices of Einthoven. *American Heart Journal*, 7(2):207–211.

[219] Wolowacz, S. E., Samuel, M., Brennan, V. K., Jasso-Mosqueda, J.-G., and Van Gelder, I. C. (2011). The cost of illness of atrial fibrillation: a systematic review of the recent literature. *Europace : European pacing, arrhythmias, and cardiac electrophysiology : journal of the working groups on cardiac pacing, arrhythmias, and cardiac cellular electrophysiology of the European Society of Cardiology*, 13(10):1375–85.

[220] Xie, Y., Garfinkel, A., Weiss, J. N., and Qu, Z. (2009). Cardiac alternans induced by fibroblast-myocyte coupling: mechanistic insights from computational models. *American Journal of Physiology - Heart and Circulatory Physiology*, 297(2):H775—-H784.

[221] Yushkevich, P. A., Piven, J., Cody Hazlett, H., Gimpel Smith, R., Ho, S., Gee, J. C., and Gerig, G. (2006). User-Guided {3D} Active Contour Segmentation of Anatomical Structures: Significantly Improved Efficiency and Reliability. *Neuroimage*, 31(3):1116–1128.

[222] Zhang, C., Florêncio, D., and Chou, P. A. (2015). Graph signal processing–a probabilistic framework. Technical report, Microsoft Research Lab - Redmond.

[223] Zhou, X., Lv, W., Zhang, W., Ye, Y., Li, Y., Zhou, Q., Xing, Q., Zhang, J., Lu, Y., Zhang, L., Wang, H., Qin, W., and Tang, B. (2017). Impact of contact force technology on reducing the recurrence and major complications of atrial fibrillation ablation: A systematic review and meta-analysis. *Anatolian journal of cardiology*, 17(2):82–91.

[224] Zlochiver, S., Yamazaki, M., Kalifa, J., and Berenfeld, O. (2008). Rotor meandering contributes to irregularity in electrograms during atrial fibrillation. *Heart Rhythm*, 5(6):846–854.

Appendix A

Harmonic Analysis on Graphs

A.1 Proof of Lemma 1

Proof. The adjacency matrix of the Cartesian product graph G is given by the matrix Cartesian product:

$$\boldsymbol{W}_{\times} = \boldsymbol{W}_1 \times \boldsymbol{W}_2 = \boldsymbol{W}_1 \otimes \boldsymbol{I}_2 + \boldsymbol{I}_1 \otimes \boldsymbol{W}_2$$

With this definition of the adjacency matrix, it is possible to write the degree matrix of the Cartesian product graph as Cartesian product of the factor degree matrices:

$$\begin{aligned}
\boldsymbol{d}_{\times} &= \boldsymbol{W}_{\times}(\mathbf{1}_1 \otimes \mathbf{1}_2) = (\boldsymbol{W}_1 \otimes \boldsymbol{I}_2 + \boldsymbol{I}_1 \otimes \boldsymbol{W}_2)(\mathbf{1}_1 \otimes \mathbf{1}_2) \\
&= (\boldsymbol{W}_1 \otimes \boldsymbol{I}_2)(\mathbf{1}_1 \otimes \mathbf{1}_2) + (\boldsymbol{I}_1 \otimes \boldsymbol{W}_2)(\mathbf{1}_1 \otimes \mathbf{1}_2) \\
&= (\boldsymbol{W}_1 \mathbf{1}_1) \otimes (\boldsymbol{I}_2 \mathbf{1}_2) + (\boldsymbol{I}_1 \mathbf{1}_1) \otimes (\boldsymbol{W}_2 \mathbf{1}_2) \\
&= \boldsymbol{d}_1 \otimes \mathbf{1}_1 + \mathbf{1}_2 \otimes \boldsymbol{d}_2
\end{aligned}$$

where we have used the following property

$$(\boldsymbol{A}_1 \otimes \boldsymbol{B}_1)(\boldsymbol{A}_2 \otimes \boldsymbol{B}_2) = (\boldsymbol{A}_1 \boldsymbol{A}_2) \otimes (\boldsymbol{B}_1 \boldsymbol{B}_2).$$

This implies the following matrix equality:

$$\boldsymbol{D} = \boldsymbol{D}_1 \otimes \boldsymbol{I}_2 + \boldsymbol{I}_1 \otimes \boldsymbol{D}_2 = \boldsymbol{D}_1 \times \boldsymbol{D}_2$$

The **combinatorial** Laplacian of the cartesian product is:

$$\begin{aligned}\boldsymbol{L}_{\times} &= \boldsymbol{D}_{\times} - \boldsymbol{W}_{\times} = \boldsymbol{D}_1 \times \boldsymbol{D}_2 - \boldsymbol{W}_1 \times \boldsymbol{W}_2 \\ &= (\boldsymbol{D}_1 \otimes \boldsymbol{I}_2 + \boldsymbol{I}_1 \otimes \boldsymbol{D}_2) - (\boldsymbol{W}_1 \otimes \boldsymbol{I}_2 + \boldsymbol{I}_1 \otimes \boldsymbol{W}_2) \\ &= (\boldsymbol{D}^1 - \boldsymbol{W}^1) \otimes \boldsymbol{I}_2 + \boldsymbol{I}_1 \otimes (\boldsymbol{D}_2 - \boldsymbol{W}_2) \\ &= \boldsymbol{L}_1 \otimes \boldsymbol{I}_2 + \boldsymbol{I}_1 \otimes \boldsymbol{L}_2 = \boldsymbol{L}_1 \times \boldsymbol{L}_2\end{aligned}$$

The Laplacian matrices can be decomposed as

$$\begin{aligned}\boldsymbol{L}_1 &= \boldsymbol{U}_1 \boldsymbol{\Lambda}_1 \boldsymbol{U}_1^* \\ \boldsymbol{L}_2 &= \boldsymbol{U}_2 \boldsymbol{\Lambda}_2 \boldsymbol{U}_2^*\end{aligned}$$

The Kronecker product of the two eigenvectors basis $\boldsymbol{U}_1$ and $\boldsymbol{U}_2$ diagonalize the joint Laplacian with eigenvalues equal to the sum of all the pairs $(\lambda_{\ell_1}, \lambda_{\ell_2})$[139]:

$$\begin{aligned}\boldsymbol{L}_{\times} &= \boldsymbol{L}_1 \otimes \boldsymbol{I}_2 + \boldsymbol{I}_1 \otimes \boldsymbol{L}_2 \\ &= (\boldsymbol{U}_1 \boldsymbol{\Lambda}_1 \boldsymbol{U}_1^*) \otimes \boldsymbol{I}_2 + \boldsymbol{I}_1 \otimes (\boldsymbol{U}_2 \boldsymbol{\Lambda}_2 \boldsymbol{U}_2^*) \\ &= (\boldsymbol{U}_1 \otimes \boldsymbol{U}_2)(\boldsymbol{\Lambda}_1 \times \boldsymbol{\Lambda}_2)(\boldsymbol{U}_1 \otimes \boldsymbol{U}_2)^* = \boldsymbol{U}_{\times} \boldsymbol{\Lambda}_{\times} \boldsymbol{U}_{\times}^*\end{aligned}$$

□

Appendix B

Time-Vertex Harmonic Analysis

B.1 Heat equation

The discrete heat diffusion equation on the graph G with Laplacian $\boldsymbol{L}_G$ is

$$\boldsymbol{x}_t - \boldsymbol{x}_{t-1} = -s\boldsymbol{L}_G\boldsymbol{x}_t$$

whose closed form solution at time t can be written as

$$\boldsymbol{x}_t = (\boldsymbol{I} - s\boldsymbol{L}_G)^{t-1}\boldsymbol{x}_1. \tag{B.1}$$

Using the spectral theorem, we can rewrite the previous equation as

$$\boldsymbol{x}_t = \boldsymbol{U}_G(\boldsymbol{I} - s\boldsymbol{\Lambda}_G)^{t-1}\boldsymbol{U}_G^*\boldsymbol{x}_1$$

which allows us to decouple the equations in the graph spectral domain

$$\begin{aligned}
\tilde{\boldsymbol{x}}_t &= (\boldsymbol{I} - s\boldsymbol{\Lambda}_G)^{t-1}\tilde{\boldsymbol{x}}_1 \\
\tilde{\boldsymbol{x}}_t(\lambda_\ell) &= (1 - s\lambda_\ell)^{t-1}\tilde{\boldsymbol{x}}_1(\lambda_\ell) \\
\widetilde{\boldsymbol{X}}(\ell,t) &= (1 - s\lambda_\ell)^{t-1}\tilde{\boldsymbol{x}}_1(\lambda_\ell)
\end{aligned}$$

where $\left\{\widetilde{\boldsymbol{X}}(\ell,t)\right\}_{t=1}^{T}$ can be interpreted as a time series for each λ_ℓ. Computing the DFT, we obtain

$$\widehat{\boldsymbol{X}}(\ell,k) = \sum_{t=1}^{T}(1-s\lambda_\ell)^{t-1}\tilde{\boldsymbol{x}}_1(\lambda_\ell)\mathrm{e}^{-\mathrm{j}\omega_k t}$$

Denoting $a(\lambda_\ell,\omega_k) = (1-s\lambda_\ell)\,\mathrm{e}^{-\mathrm{j}\omega_k}$ and $\boldsymbol{Z}(\ell,k) = \widetilde{\boldsymbol{x}_1}(\ell)\,\boldsymbol{U}_T^*(k,1)$, the geometric sum has solution

$$\widehat{\boldsymbol{X}}(\ell,k) = \frac{1}{\sqrt{T}}\frac{a(\lambda_\ell,\omega_k)^T-1}{a(\lambda_\ell,\omega_k)-1}\boldsymbol{Z}(\ell,k). \tag{B.2}$$

B.2 Wave equation

In the continuous setting, the wave equation is

$$\partial_{tt}u - \Delta u = 0$$

where $u\colon \mathbb{R}\times\mathbb{R}^d \to \mathbb{C}$ is a function of both time $t\in\mathbb{R}$ and space $x\in\mathbb{R}^d$, with Δ being the Laplacian operator. Even though being a second order PDE, the equation can be rewritten as a first order system defining $v(t) := \partial_t u(t)$. The pair $(u(t),v(t))$ evolves now according to the system

$$\begin{cases} \partial_t u(t) = v(t) \\ \\ \partial_t v(t) = \Delta u(t) \end{cases} \tag{B.3}$$

Assuming vanishing initial velocity $v(0)=0$, the solution $u(t)$ is given via functional calculus by [54]

$$u(t) = \cos(t\sqrt{-\Delta})u(0) \tag{B.4}$$

where $\cos(t\sqrt{-\Delta})$ is called *propagator operator*.

To obtain a discrete wave equation evolving on a graph, we approximate the second order time derivative with its stencil approximation and the continuous Laplacian Δ with the graph Laplacian $\boldsymbol{L}_G$ with reversed sign:

$$\boldsymbol{X}\boldsymbol{L}_T = s\boldsymbol{L}_G\boldsymbol{X}, \tag{B.5}$$

where $s > 0$ is the speed of propagation. The wave equation is a hyperbolic differential equation and several difficulties arise in discretizing it for the numerical computation of the solution [54]. Moreover, the graph being an irregular domain, the solution of the above equation is not any more a smooth wave after a few iterations. Nevertheless, we assume as in the case of the heat diffusion Eq. (B.1) that the solution can be written as

$$\boldsymbol{x}_t = K_s(\boldsymbol{L}_G, t)\boldsymbol{x}_1 = \boldsymbol{K}_{t,s}\boldsymbol{x}_1, \tag{B.6}$$

where $\boldsymbol{K}_{t,s} = K_s(\boldsymbol{L}_G, t)$ is a matrix obtained applying the function $K_s(\boldsymbol{L}_G, t)$ to the scaled Laplacian $s\boldsymbol{L}_G$ and parametrized by the time t. We will call the operator $\boldsymbol{K}_{t,s}$ "the discrete analogue of the wave propagator" of Eq. (B.4). Therefore, the matrix

$$\boldsymbol{X} = [\boldsymbol{K}_{t,s}\boldsymbol{x}_1]_{t=1}^{T} = \boldsymbol{K}_s\{\boldsymbol{x}_1\}$$

is obtained by stacking the vectors $\boldsymbol{x}_t$ of Eq. (B.6) along the columns. Substituting (B.6) into (B.5), we obtain $\boldsymbol{K}_s\{\boldsymbol{x}_1\}\boldsymbol{L}_T = s\boldsymbol{L}_G\boldsymbol{K}_s\{\boldsymbol{x}_1\}$ which in the graph spectral domain is

$$\widetilde{\boldsymbol{K}_s}\{\tilde{\boldsymbol{x}}_1\}\boldsymbol{L}_T = s\boldsymbol{\Lambda}_G\widetilde{\boldsymbol{K}_s}\{\tilde{\boldsymbol{x}}_1\}, \tag{B.7}$$

where $\widetilde{\boldsymbol{K}_{t,s}} = K_s(\boldsymbol{\Lambda}_G, t)$. Equation (B.7) is formally analogous to the eigendecomposition of the operator $\boldsymbol{L}_T$, therefore, the ℓ-th row of $\widetilde{\boldsymbol{K}_s}\{\tilde{\boldsymbol{x}}_1\}$ must be an eigenvector of $\boldsymbol{L}_T$ with eigenvalue λ_ℓ, for every ℓ. It has been proved in [200] that the eigenvectors $\boldsymbol{U}_T(t,k) = \cos(tk\pi/T)$ form also the discrete Fourier basis. Using Eq. (7.8), we obtain

$$K_s(\lambda_\ell, t) = \cos\left(t \arccos\left(1 - \frac{s\lambda_\ell}{2}\right)\right) = \cos(t\vartheta_\ell), \tag{B.8}$$

with $\vartheta_\ell = \arccos(1 - \frac{s\lambda_\ell}{2})$. Since the $\arccos(x)$ is defined only for $x \in [-1, 1]$, to guarantee stability the parameter s must satisfy $s < 4/\lambda_{max}$. We remark that this result is in agreement with the stability analysis of the numerical solver for the discrete wave equation presented in [54].

Taking the DFT of the wave kernel in Eq. (B.8), we obtain

$$\widehat{K}_s(\lambda_\ell, \omega_k) = \sum_t \cos(t\vartheta_\ell)\mathrm{e}^{-\mathrm{j}\omega_k t}$$

Therefore, the solution in the joint spectral domain can be written as

$$\widehat{\boldsymbol{X}}(\ell,k) = \widehat{K}_s(\lambda_\ell, \omega_k)\boldsymbol{Z}(\ell,k),$$

where $\boldsymbol{Z}(\ell,k) = \widetilde{\boldsymbol{x}_1}(\ell)\,\boldsymbol{U}_T^*(k,1)$. Note that there exists a closed form solution for the function $\widehat{K}_s$:

$$\widehat{K}_s(\lambda_\ell, \omega_k) = \begin{cases} \dfrac{\delta(\omega_k + \vartheta_\ell) + \delta(\omega_k - \vartheta_\ell)}{2}, & \text{if } T\vartheta_\ell/2\pi \text{ integer} \\ \dfrac{1}{2}\left(\dfrac{1-\mathrm{e}^{-\mathrm{j}T(\omega_k+\vartheta_\ell)}}{1-\mathrm{e}^{-\mathrm{j}(\omega_k+\vartheta_\ell)}} + \dfrac{1-\mathrm{e}^{-\mathrm{j}T(\omega_k-\vartheta_\ell)}}{1-\mathrm{e}^{-\mathrm{j}(\omega_k-\vartheta_\ell)}}\right), & \text{otherwise} \end{cases}$$

B.3 Joint time-vertex frame

B.3.1 Theorem 2

Let $\{h_z(\lambda,\omega)\}_{z\in\mathscr{Z}_\lambda\times\mathscr{Z}_\omega}$ be the kernels of a time-vertex dictionary $\mathscr{D}_h$, and set

$$A = \min_{l,k}\sum_z |h_z(\lambda_\ell,\omega_k)|^2,$$
$$B = \max_{l,k}\sum_z |h_z(\lambda_\ell,\omega_k)|^2.$$

If $0 < A \le B < \infty$, then D_h is a frame in the sense:

$$A\|\boldsymbol{X}\|_F^2 \le \|D_h\{\boldsymbol{X}\}\|_F^2 \le B\|\boldsymbol{X}\|_F^2$$

for any time-vertex signal $\boldsymbol{X} \in \mathbb{R}^{N\times T}$.

Proof. In the joint spectral domain we can write:

$$
\begin{aligned}
\|\{D_h\{\boldsymbol{X}\}\}\|_F^2 &= \sum_{m,\tau,z} |\{D_h\{\boldsymbol{X}\}\}(m,\tau,z)|^2 \\
&= \sum_{z,m,\tau} \left(\sum_{\substack{\ell,k \\ n,t}} \boldsymbol{X}(n,t) h_z(\lambda_\ell,\omega_k) \boldsymbol{u}_\ell^*(n) \boldsymbol{u}_\ell(m) \mathrm{e}^{-\mathrm{j}\omega_k(t-\tau)} \right) \\
&\left(\sum_{\substack{\ell',k' \\ n',t'}} \boldsymbol{X}(n',t') h_z(\lambda_{\ell'},\omega_{k'}) \boldsymbol{u}_{\ell'}^*(n') \boldsymbol{u}_{\ell'}(m) \mathrm{e}^{-\mathrm{j}\omega_{k'}(t'-\tau)} \right)^* \\
&= \sum_{z,\ell,k} h_z(\lambda_\ell,\omega_k) \widehat{h}_z^*(\lambda_\ell,\omega_k) \widehat{\boldsymbol{X}}(\ell,k) \widehat{\boldsymbol{X}}^*(\ell,k) \\
&= \sum_{z,\ell,k} |h_z(\lambda_\ell,\omega_k)|^2 |\widehat{\boldsymbol{X}}(\ell,k)|^2 = \sum_z \langle |h_z|^2, |\widehat{\boldsymbol{X}}|^2 \rangle,
\end{aligned}
$$

where the equality holds due to the orthogonality of the eigenvectors. Finally, each element in the sum can be lower bounded and upper bounded by the minimum and maximum value that every filter takes over ℓ and k. Using the Parseval relation (7.6), the theorem holds. □

B.4 Joint stationarity

B.4.1 Theorem 3

If a joint process $\boldsymbol{X}$ is JWSS, then it is both TWSS and VWSS.

Proof. It is straightforward to see that $\boldsymbol{L}_J \mathbb{E}[\boldsymbol{x}] = \boldsymbol{0}_{NT}$ if and only if both $\boldsymbol{L}_T \mathbb{E}[\boldsymbol{x}_t] = \boldsymbol{0}_T$ and $\boldsymbol{L}_G \mathbb{E}\left[\boldsymbol{x}^i\right] = \boldsymbol{0}_N$, hold for all t and n. We still need to show that the second-order moment properties of TWSS and VWSS are equivalent to that of JWSS. If a process is joint stationary, the covariance matrix is the linear operator associated to a joint filter $\boldsymbol{\Sigma} = h(\boldsymbol{L}_G, \boldsymbol{L}_T)$. Denoting

$$
\gamma_\tau(\lambda_\ell) = \frac{1}{T} \sum_{k=1}^{T} h(\lambda_\ell,\omega_k) \mathrm{e}^{\mathrm{j}\omega_k\tau},
$$

the covariance matrix can be written as

$$\boldsymbol{\Sigma}_{t_1,t_2} = \boldsymbol{U}_G \boldsymbol{\gamma}_\tau(\boldsymbol{\Lambda}) \boldsymbol{U}_G^* = \boldsymbol{\gamma}_\tau(\boldsymbol{L}_G).$$

Therefore, the process is both VWSS and TWSS. Conversely, if the process $\boldsymbol{X}$ is TWSS and VWSS, we have

$$\boldsymbol{\Sigma}_{t_1,t_2} = \boldsymbol{\gamma}_{t_1,t_2}(\boldsymbol{L}_G) = \boldsymbol{\gamma}_\tau(\boldsymbol{L}_G)$$

with $\tau = t_1 - t_2 + 1$. The covariance matrix can be written as a joint filter $h(\boldsymbol{L}_G, \boldsymbol{L}_T)$, defined as

$$h(\lambda_\ell, \omega_k) = \sum_{\tau}^{T} \gamma_{\tau=1}(\lambda_\ell) \mathrm{e}^{\mathrm{j}\omega_k \tau}.$$

Hence, it satisfies the second property of the JWSS processes.

□

B.4.2 Theorem 4

When a joint filter $f(\boldsymbol{L}_G, \boldsymbol{L}_T)$ is applied to a JWSS process $\boldsymbol{X}$, the result $\boldsymbol{Y}$ remains JWSS with mean $f(0,0)\,\mathbb{E}[\boldsymbol{X}]$ and JPSD satisfying

$$h_{\boldsymbol{y}}(\lambda, \omega) = f^2(\lambda, \omega)\, h_{\boldsymbol{x}}(\lambda, \omega).$$

Proof. The output of a filter $f(\boldsymbol{L}_G, \boldsymbol{L}_T)$ can be written in vector form as $\boldsymbol{y} = f(\boldsymbol{L}_G, \boldsymbol{L}_T)$. If the input signal $\boldsymbol{x}$ is JWSS, the first moment of the filter output is

$$\mathbb{E}[f(\boldsymbol{L}_G, \boldsymbol{L}_T)\boldsymbol{x}] = f(\boldsymbol{L}_G, \boldsymbol{L}_T)\mathbb{E}[\boldsymbol{x}] = f(0,0)\mathbb{E}[\boldsymbol{x}],$$

which is constant as $\mathbb{E}[\boldsymbol{x}]$ is constant by hypothesis. The last equality follows from the fact that by definition $\mathbb{E}[\boldsymbol{x}]$ is in the null space of $\boldsymbol{L}_J$. The computation of the

second moment gives

$$\begin{aligned}\boldsymbol{\Sigma}_{\boldsymbol{y}} &= \mathbb{E}\left[f(\boldsymbol{L}_G,\boldsymbol{L}_T)\boldsymbol{x}\,(f(\boldsymbol{L}_G,\boldsymbol{L}_T)\boldsymbol{x})^*\right] - \mathbb{E}\left[h(\boldsymbol{L}_G,\boldsymbol{L}_T)\boldsymbol{x}\right]\mathbb{E}\left[(f(\boldsymbol{L}_G,\boldsymbol{L}_T)\boldsymbol{x})^*\right] \\ &= f(\boldsymbol{L}_G,\boldsymbol{L}_T)\mathbb{E}\left[\boldsymbol{x}\boldsymbol{x}^*\right] f(\boldsymbol{L}_G,\boldsymbol{L}_T) - f(\boldsymbol{L}_G,\boldsymbol{L}_T)\mathbb{E}\left[\boldsymbol{x}\right]\mathbb{E}\left[\boldsymbol{x}^*\right] f(\boldsymbol{L}_G,\boldsymbol{L}_T)^* \\ &= f(\boldsymbol{L}_G,\boldsymbol{L}_T)\,\boldsymbol{\Sigma}_{\boldsymbol{x}} f(\boldsymbol{L}_G,\boldsymbol{L}_T)^* \\ &= \boldsymbol{U}_J\left(f^2(\boldsymbol{\Lambda}_G,\boldsymbol{\Omega})\,h_{\boldsymbol{x}}(\boldsymbol{\Lambda}_G,\boldsymbol{\Omega})\right)\boldsymbol{U}_J^*,\end{aligned}$$

which is JWSS as it is diagonalizable by $\boldsymbol{U}_J$. □